

# DAMAGE IN COMPOSITE MATERIALS

K. L. Reifsnider, *editor*



# DAMAGE IN COMPOSITE MATERIALS: BASIC MECHANISMS, ACCUMULATION, TOLERANCE, AND CHARACTERIZATION

A symposium  
sponsored by ASTM  
Committees E-7 on  
Nondestructive Testing  
and E-9 on Fatigue  
Bal Harbour, Fla., 13-14 Nov. 1980

ASTM SPECIAL TECHNICAL PUBLICATION 775  
K. L. Reifsnider, Virginia Polytechnic  
Institute and State University, editor

ASTM Publication Code Number (PCN)  
04-775000-30



1916 Race Street, Philadelphia, Pa. 19103

**Copyright © by AMERICAN SOCIETY FOR TESTING AND MATERIALS 1982**  
**Library of Congress Catalog Card Number: 81-70760**

**NOTE**

**The Society is not responsible, as a body,  
for the statements and opinions  
advanced in this publication.**

**Printed in Baltimore, Md.  
June 1982**

# Foreword

The symposium on **Damage in Composite Materials**, sponsored by ASTM Committees E-7 on Nondestructive Testing and E-9 on Fatigue, was held in Bal Harbour, Fla., on 13–14 Nov. 1980. J. T. Fong, National Bureau of Standards, and K. L. Reifsnider, Virginia Polytechnic Institute and State University, served as symposium chairmen. K. L. Reifsnider also edited this publication.

## **Related ASTM Publications**

**Joining of Composite Materials, STP 749 (1981), 04-749000-33**

**Statistical Analysis of Fatigue Data, STP 744 (1981), 04-744000-30**

**Fatigue Crack Growth Measurement and Data Analysis, STP 738 (1981),  
04-738000-30**

**Test Methods and Design Allowables for Fibrous Composites, STP 734  
(1981), 04-734000-33**

**Fatigue of Fibrous Composite Materials, STP 723 (1981), 04-723000-33**

**Eddy-Current Characterization of Materials and Structures, STP 722 (1981),  
04-722000-22**

**Real-Time Radiologic Imaging: Medical and Industrial Applications,  
STP 716 (1980), 04-716000-22**

**Effect of Load Variables on Fatigue Crack Initiation and Propagation,  
STP 714 (1980), 04-714000-30**

**Nondestructive Testing Standards—A Review, STP 624 (1977), 04-624000-22**

## A Note of Appreciation to Reviewers

This publication is made possible by the authors and, also, the unheralded efforts of the reviewers. This body of technical experts whose dedication, sacrifice of time and effort, and collective wisdom in reviewing the papers must be acknowledged. The quality level of ASTM publications is a direct function of their respected opinions. On behalf of ASTM we acknowledge with appreciation their contribution.

*ASTM Committee on Publications*

## Editorial Staff

Jane B. Wheeler, *Managing Editor*  
Helen M. Hoersch, *Senior Associate Editor*  
Helen P. Mahy, *Senior Assistant Editor*  
Allan S. Kleinberg, *Assistant Editor*  
Virginia M. Barishek, *Assistant Editor*

# Contents

<b>Introduction</b>	<b>1</b>
<b>DAMAGE MECHANISMS: ACCUMULATION AND NONDESTRUCTIVE INVESTIGATION</b>	
<b>Toward the Nondestructive Characterization of Fatigue Damage in Composite Materials—L. MORDFIN</b>	<b>7</b>
<b>Damage Documentation in Composites by Stereo Radiography— G. P. SENDECKYJ, G. E. MADDUX, AND E. PORTER</b>	<b>16</b>
<b>Fractographic Studies of Graphite/Epoxy Fatigue Specimens— G. E. MORRIS AND C. M. HETTER</b>	<b>27</b>
<b>An Investigation of Cumulative Damage Development in Quasi-Isotropic Graphite/Epoxy Laminates—J. E. MASTERS AND K. L. REIFSNIDER</b>	<b>40</b>
<b>Effects of Moisture, Residual Thermal Curing Stresses, and Mechanical Load on the Damage Development in Quasi-Isotropic Laminates— R. D. KRIZ AND W. W. STINCHCOMB</b>	<b>63</b>
<b>DAMAGE MECHANISMS: TOLERANCE AND CHARACTERIZATION</b>	
<b>Mechanisms of Fatigue Damage in Boron/Aluminum Composites— W. S. JOHNSON</b>	<b>83</b>
<b>Stiffness-Reduction Mechanisms in Composite Laminates— A. L. HIGHSMITH AND K. L. REIFSNIDER</b>	<b>103</b>
<b>The Dependence of Transverse Cracking and Delamination on Ply Thickness in Graphite/Epoxy Laminates—F. W. CROSSMAN AND A. S. D. WANG</b>	<b>118</b>
<b>Characterization of Delamination Onset and Growth in a Composite Laminate—T. K. O'BRIEN</b>	<b>140</b>

<b>Characterizing Delamination Growth in Graphite-Epoxy—D. J. WILKINS, J. R. EISENMANN, R. A. CAMIN, W. S. MARGOLIS, AND R. A. BENSON</b>	<b>168</b>
<b>Compression Fatigue Behavior of Composites in the Presence of Delaminations—R. L. RAMKUMAR</b>	<b>184</b>
<b>Effect of Stacking Sequence on Damage Propagation and Failure Modes in Composite Laminates—M. M. RATWANI AND H. P. KAN</b>	<b>211</b>
<b>Damage Mechanism and Life Prediction of Graphite/Epoxy Composites—R. BADALIANE AND H. D. DILL</b>	<b>229</b>
<b>What Is Fatigue Damage?—J. T. FONG</b>	<b>243</b>

#### SUMMARY

<b>Summary</b>	<b>269</b>
<b>Index</b>	<b>277</b>

# Introduction

---

It is well established that the micro-events which reduce the strength and stiffness, and determine the life of composite laminates (commonly referred to as “damage”) are complex, various, and intricately related to a variety of failure modes under different circumstances. The study of individual details of damage is certainly of academic interest. However, it was the objective of the symposium which formed the basis for this book to provide a forum for the general discussion of the specific nature of damage in composite materials as a collective condition, what might be called a “damage state.” The symposium was sponsored by Subcommittees E09.03 on Fatigue of Composite Materials and E09.01 on Research, in Committee E-9 on Fatigue. Committee E-7 on Nondestructive Testing also contributed in a formal way. The symposium material was chosen and organized to specifically serve three groups of people.

1. Materials scientists and nondestructive evaluation practitioners: For this group, the symposium was intended to provide an opportunity to establish the mechanisms which create damage in composite materials, to discuss the experimental methods that can be used to investigate those mechanisms, and to study the relationship of these mechanisms to loads, strains, and other environments.

2. Fatigue researchers in composite materials: For this group, whether they consider composites to be structural materials or models for studying microscopic damage of complex material systems such as metal alloys, ceramics, semi-crystalline polymers, etc., it was intended that the symposium provide an attempt to establish the nature of damage accumulation, and to identify and characterize cumulative damage states as collective entities as an approach to anticipating the residual properties and response of such materials. This emphasis included an effort to develop modeling methods and analytical techniques which can be used to represent damage states and to anticipate response in unfamiliar circumstances.

3. Designers and others primarily concerned with the application of composite materials to engineering structures and with the nondestructive testing of those structures: The symposium was intended to provide information to

## 2 DAMAGE IN COMPOSITE MATERIALS

this group which could be used to assess the damage tolerance of various composite laminates and structures in terms of their subsequent strength, life and stiffness following the formation of damage states.

The material the Symposium Committee chose to include in the symposium and in this book was based on these criteria.

In a more general sense, the contents of this book should serve a variety of technical people in a variety of ways. Engineers who only want to consider damage mechanisms and damage development to the extent that they can use those concepts in design will find that several papers deal specifically with relationships between damage development and life (see papers by Badaliance and Dill, Ramkumar, Wilkins et al, and O'Brien). Engineers and others on the "design side" will also find discussions of property reductions due to damage development and the influence of environment on damage development and subsequent property reductions (see papers by Highsmith and Reifsnider, Kriz and Stinchcomb, and Masters and Reifsnider). Technical people with a nonspecialist interest will find an excellent review of the "state-of-the-art" in the sense that virtually all major damage mechanisms are discussed from the standpoint of detection, characterization and modeling, and finally from the standpoint of their influence on engineering behavior.

But perhaps the book has the most to offer those investigators who are vitally involved in the study of damage as such. For that group, this book is the most complete collection of information, knowledge, and philosophy which deals with damage in composite materials currently available. Moreover, the book bridges the gap between micro-observations and macro-behavior, the most critical and difficult step in the process of attempting to make technical and scientific progress in this area. And experimentalists will be especially glad to find that investigative techniques are discussed (some quite new) in sufficient detail to allow direct adoption by the reader (see papers by Mordfin; Sendekyj, Maddux, and Porter; Masters and Reifsnider; Highsmith and Reifsnider; and Wilkins et al).

Perhaps one last point should be made in our introductory comments. One overriding question is at the heart of many of the investigations described herein, and was the central issue that motivated the symposium associated with this book. Basically, that question is, "What philosophy and rational analysis can we use to describe and explain damage development in composite laminates so that we can anticipate their residual strength, stiffness, and life under engineering conditions?" In a general sense, this question requires a replacement for the single crack problem (and fracture mechanics) in homogeneous isotropic materials. The discovery and development of such a philosophy is the ultimate goal of our efforts to study damage. Without such a development the practical application of composite materials will be a desultory effort which produces a random array of limited successes and

costly failures. With such a development as a foundation, a rational exploitation of the widely recognized advantages of composite materials for many engineering purposes is possible and probable.

*K. L. Reifsnider*

Department of Engineering Science and Mechanics, Virginia Polytechnic Institute and State University, Blacksburg, Va. 24060; symposium cochairman and editor.

# **Damage Mechanisms: Accumulation and Nondestructive Investigation**

L. Mordfin<sup>1</sup>

# Toward the Nondestructive Characterization of Fatigue Damage in Composite Materials

---

**REFERENCE:** Mordfin, L., "Toward the Nondestructive Characterization of Fatigue Damage in Composite Materials," *Damage in Composite Materials, ASTM STP 775*, K. L. Reifsnider, Ed., American Society for Testing and Materials, 1982, pp. 7-15.

**ABSTRACT:** This paper is based upon introductory remarks presented at the opening of the ASTM Symposium on Damage in Composite Materials. The cooperation between specialists in fatigue and in nondestructive testing, in the organization and implementation of the symposium, is marked as a noteworthy milestone in an era in which closer cooperation between these two groups will be needed in order to achieve enhanced quality in materials and manufactured products.

Experiences with an unusual form of damage in pultruded guys for antenna support systems are described to show that the development of meaningful test methods for composites may benefit from unconventional approaches. It is suggested, furthermore, that the development of voluntary standards for the nondestructive characterization of composite materials will succeed only to the extent that individuals with the relevant competences are encouraged to contribute to this important activity.

**KEY WORDS:** composite materials, damage, fatigue, guys, mechanical testing, non-destructive testing, pultrusions, standards

Few ASTM symposia have titles which are as long or as specific as the title of this symposium (*Damage in Composite Materials: Basic Mechanisms, Accumulation, Tolerance, and Characterization*). In choosing this title the symposium organizing committee felt that it was important to specify precisely the kind of information which it wanted to acquire and to disseminate. To a large extent the committee was successful in this endeavor, but not entirely so. Note that the symposium is sponsored by ASTM Committees E-7 on Nondestructive Testing and E-9 on Fatigue but that neither "nondestructive testing" nor "fatigue" appears in the symposium title. I think it is safe to infer that where the title says *Damage* it is supposed to imply *Fatigue Damage* primarily, and where it says *Characterization* it is supposed to imply *Nondes-*

<sup>1</sup> Acting chief, Office of Nondestructive Evaluation, National Bureau of Standards, Washington, D. C. 20234.

*tructive Characterization* primarily, although other kinds of damage and other kinds of characterization were not excluded from the program.

The nondestructive characterization of fatigue damage—in this case for composite materials—is the theme of mutual interest that brought Committees E-7 and E-9 together in this cooperative effort. That is a significant event because these two committees have not joined forces very often in the past. Upon consulting my outdated membership lists for the two committees I think I discovered the reason for this. As of 1978 Committee E-7 had 288 members, Committee E-9 had 257 members, but only three individuals held membership in both committees! Those statistics suggest that the members of the two committees have generally different interests.<sup>2</sup> If that is, indeed, the case, then I am hopeful that this symposium will show that the differences are not as great as once might have been perceived. The advances that have been achieved over the past decade in our understanding of fracture mechanics and fatigue crack propagation show us, beyond question, that cooperation between specialists in fatigue and in nondestructive testing is vital if we are to succeed in our national quest for enhanced quality in materials and manufactured products.

An immediate requirement for such cooperation is represented by our need for standard methods for nondestructively characterizing fatigue damage in composite materials. Committee E-9 has recognized this need for some time but Committee E-7 has not yet responded to this need. This is not meant as an indictment, but rather to point out that the development of test methods for composite materials may require some radical departures from the approaches that we have used so successfully in the past for conventional materials.

The brief narrative that follows may clarify this point. Several years ago I had the privilege of leading a research program, in the old Engineering Mechanics Section of the National Bureau of Standards, to characterize the mechanical behavior of pultruded rod products. The rods we worked on were fabricated from polyester resin, heavily reinforced in the axial direction with continuous fiberglass roving. These rods are used widely for guying communications towers and arrays all over the world. Literally miles of the rod are employed in applications of this kind, as shown in Fig. 1, as well as for insulators on cross-country power lines. The rods are coated with an epoxy formulation for enhanced environmental resistance.

Our work, which was supported by a number of government agencies<sup>3</sup> which have responsibilities for the design, erection, or maintenance of such systems, was concerned with evaluating the mechanical properties and per-

<sup>2</sup> Those statistics also explained to me how I was selected to serve on the organizing committee for the symposium; I am one of the three.

<sup>3</sup> Air Force Materials Laboratory, Army Electronics Command, National Bureau of Standards, Naval Facilities Engineering Command, Rome Air Development Center, U. S. Coast Guard, and U. S. Information Agency.

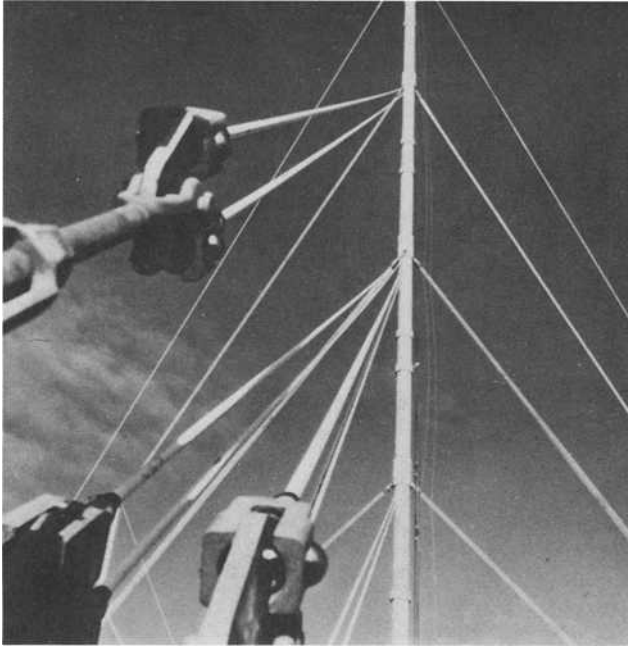


FIG. 1—*Pultruded guys support an antenna mast.*

formance of the rods under the kinds of operational and environmental conditions that they might be expected to see in service [1-5].<sup>4</sup> This was not a problem of trivial concern because failures of antenna guys can and do lead to catastrophic failures of the structures which they support.

Because of our involvement it was not uncommon that, when failures of rods occurred in service, the failed pieces were sent to us for examination. It was in this way that we became aware of a very unusual failure mode that sometimes appeared. Figure 2 shows one of these, in which the rod fractured near one of its end fittings. Note the surprisingly smooth fracture surfaces normal to the fiber direction. This failure mode is entirely different from anything we had seen in the laboratory, where fracture surfaces were invariably jagged and involved considerable brooming of the fibers.

Figure 3 shows a pultruded guy which had failed at some distance from its end fittings. The fracture surface normal to the fibers again looks as though it had been made with a fine saw. Upon closer examination, however, it became clear, as shown in Fig. 4, that the fracture surface through the epoxy coating was, in fact, considerably smoother than the fracture surface through the fibers.

We could not explain this mode of failure. We conducted tension, torsion,

<sup>4</sup>The italic numbers in brackets refer to the list of references appended to this paper.

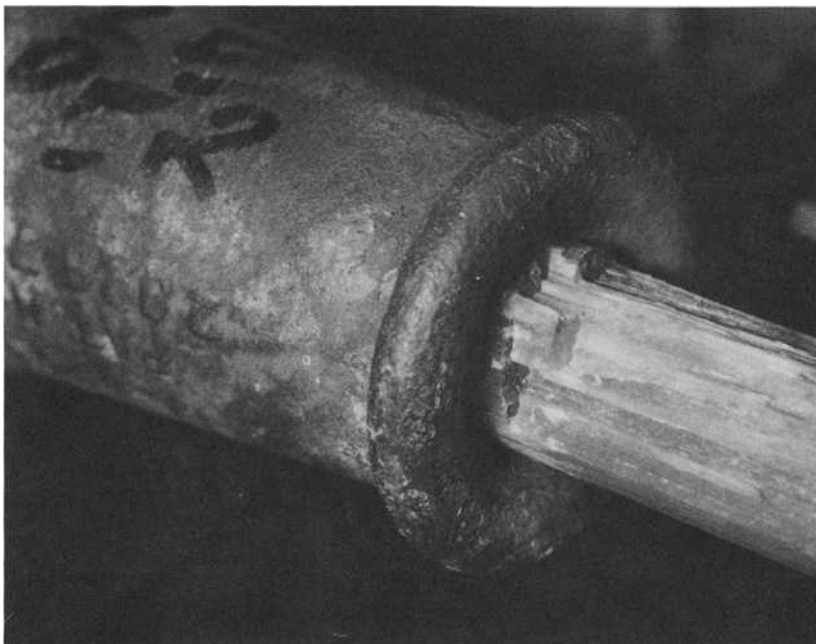


FIG. 2.—*Pultruded guy which failed near one of its end fittings.*

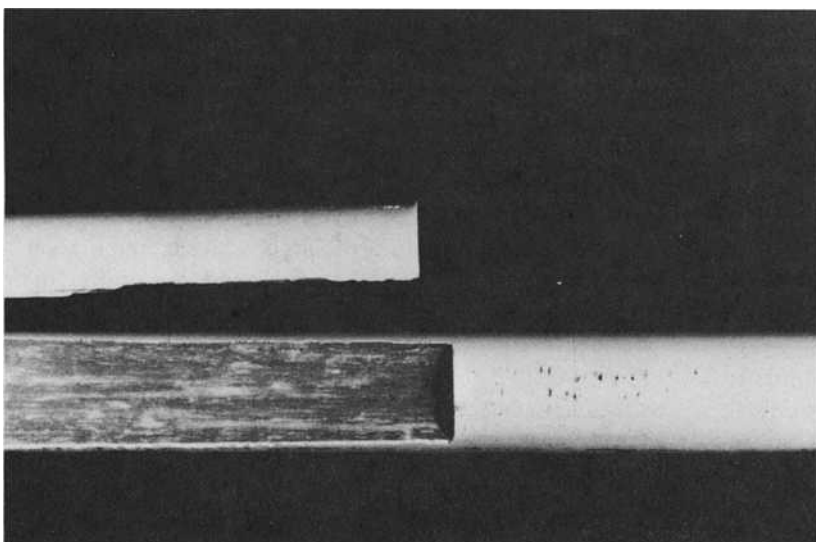


FIG. 3.—*Pultruded guy which failed at some distance from its end fittings.*

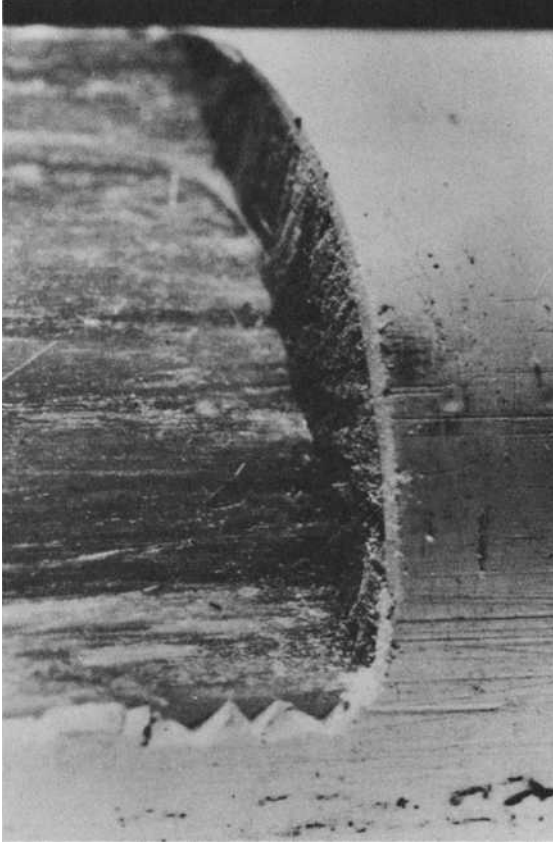


FIG. 4—Fracture surface on the pultruded guy shown in Fig. 3.

bending and buckling tests, and we conducted fatigue and creep rupture tests in all types of simulated environments, but we were unable to reproduce this failure mode in the laboratory. Then, one day, we received from the field the failed rod shown in Fig. 5. This rod exhibited the same type of fracture surface normal to the fibers, but it showed us something we had not noted previously—a series of hairline cracks normal to the rod axis. This led us to suspect that the hairline cracks represented a form of damage which, if undetected, could propagate into relatively smooth transverse fractures. But what caused the hairline cracks?

A pultrusion manufacturer suggested that transverse hairline cracks could be produced by shock tension loads such as might be experienced by certain guy configurations in the field under sudden wind gusts. We mounted a piece of rod in an electro-hydraulic testing machine and applied a tensile load to it at an extremely high rate of loading to a level just short of the nominal

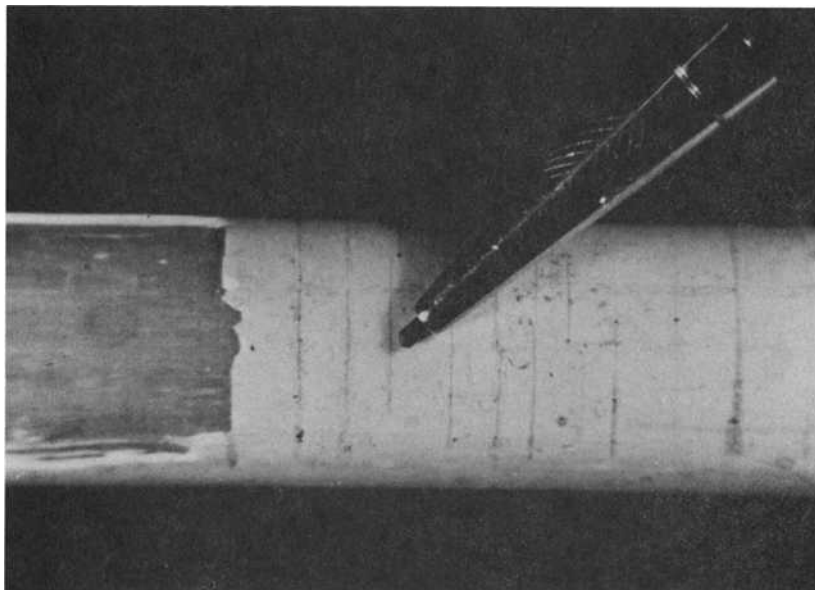


FIG. 5—Pultruded guy which failed at some distance from its end fittings, exhibiting transverse hairline cracks.

breaking load. Then we unloaded it and carefully examined it for transverse hairline cracks. We found nothing.

The next morning one of our technicians went to remove the rod from the testing machine and found, to our surprise, three transverse hairline cracks in the specimen, as seen in Fig. 6. By applying a gradually increasing tensile load to the rod in this condition, the hairline cracks began to propagate into transverse fractures, shown in Fig. 7, of the kind we had been seeking to generate for so long. In subsequent work we were able to show that the kind of damage represented by the hairline cracks could be produced in certain kinds of coated pultruded rod by a shock tension load followed by an incubation period of several minutes or hours.

This unusual two-stage test method has since been incorporated into the national specifications for coated pultruded rod for guying applications [6, 7], but that is not the point of this story. It is easy now, with hindsight, to postulate mechanisms that explain damage of this kind in pultruded rod. But we didn't think of such mechanisms before, probably because we—my associates and I—had spent most of our careers until then doing research on metals and metal structures, and we were not accustomed, at that time, to thinking in terms of the *different* things that can happen with composites. I suggest that when you are dealing with inhomogeneous, anisotropic, and viscoelastic materials like organic-matrix composites, your intuition may well be better off without a strong background of experience with metals. We have seen, for example, that many of the mechanical test methods for composites have been developed by ASTM Committees D-20 on Plastics and

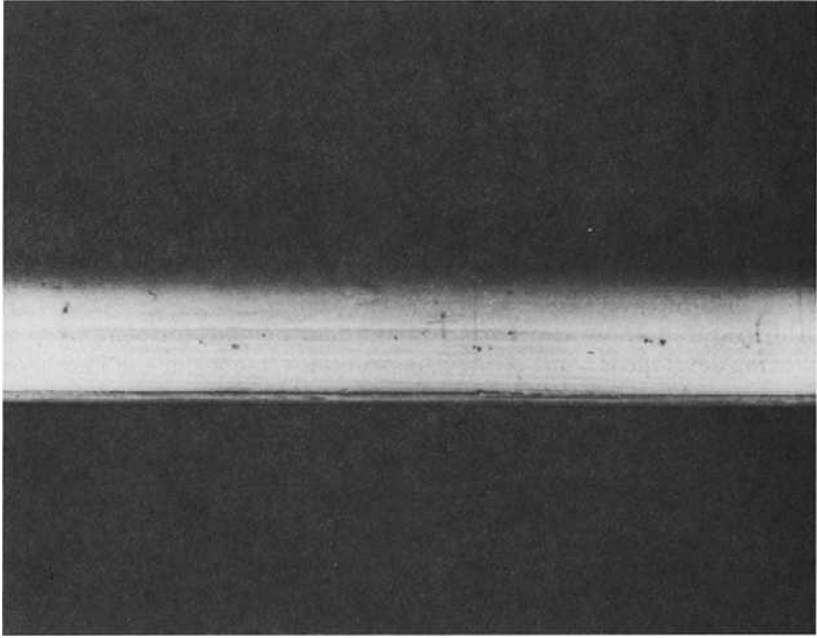


FIG. 6—Pultruded rod specimen with three transverse hairline cracks that were produced in the laboratory by a shock tension load followed by an incubation period. (The horizontal black line along the lower surface of the specimen is a scuff mark.)

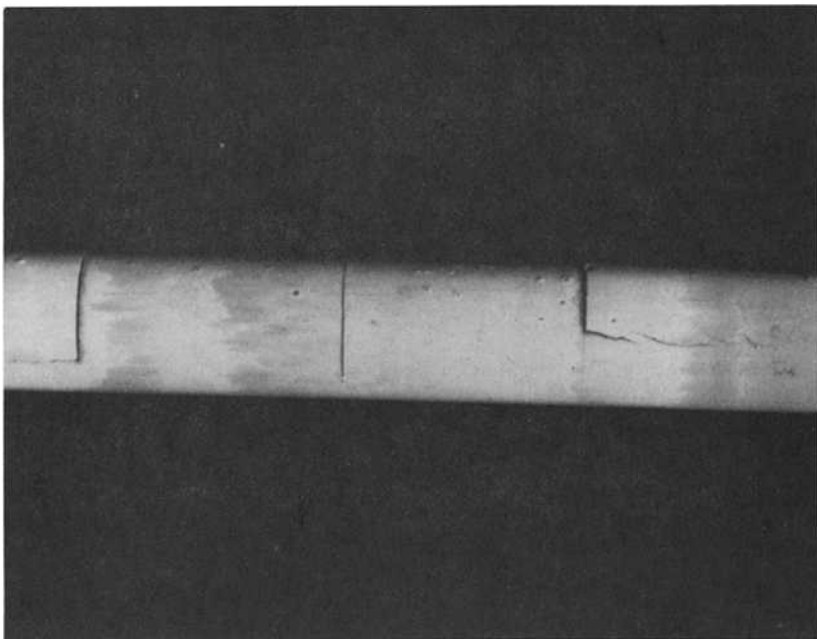


FIG. 7—The pultruded rod specimen from Fig. 6 during a subsequent tension test.

D-30 on High Modulus Fibers and Their Composites, involving people who, for the most part, have not been similarly involved in Committee E-28 on Mechanical Testing.

This hypothesis is relevant to the situation we now face wherein Committee E-7 on Nondestructive Testing has not yet satisfied the needs of Committee E-9 on Fatigue for standard nondestructive methods for characterizing damage in composite materials. I submit that the difficulty may lie in the fact that the active membership of Committee E-7, while unquestionably competent, consists primarily of individuals with strong backgrounds in the non-destructive testing of *metals*.

This is not to imply that nondestructive test methods for composites are not being developed. Some of the papers in this symposium and in other recent symposia and conferences show that such methods *are* being developed. But the developers have not pursued the standardization of their methods. I maintain that until they have taken that step they have not completed their developments. Examples have been cited elsewhere [8] which show that the most advantageous time to pursue the standardization of a test method is during the development of the testing methodology itself. Attempts to retrofit standards to accommodate already well-developed test methods often result in less satisfactory compromises.

Let me summarize. I think that the cooperative effort here between specialists in fatigue and in nondestructive testing is significant, and I am hopeful that this symposium will mark the beginning of an era of increasing cooperation between these two groups. I think that the development of test methods for composite materials can benefit from the ingenuity of young minds and fresh approaches that are unencumbered by long experience with the testing of traditional materials. And, finally, let me encourage those of you who are developing nondestructive test methods for composite materials to become involved in the standardization activities of Committee E-7 on Nondestructive Testing. I can assure you of a warm welcome and, more importantly, you will be taking a significant step toward giving the whole nation the benefit of your accomplishments.

## References

- [1] Halsey, N., Mitchell, R. A. and Mordfin, L., "Evaluation of GRP Rod and Rope Materials and Associated End Fittings," Report NBSIR 73-129, National Bureau of Standards, Washington, D. C., Dec. 1972.
- [2] Halsey, N. and Mordfin, L., "Environmental Effects on the Strength of Glass Fiber-Reinforced-Plastic Rod Material," Report NBSIR 76-1069, National Bureau of Standards, Washington, D. C., March 1976.
- [3] Sushinsky, G. F. and Mordfin, L., "Nondestructive Examination of Glass-Reinforced-Plastic Rod End Fittings," Report NBSIR 76-1084, National Bureau of Standards, Washington, D. C., April 1976.
- [4] Halsey, N., Marlowe, D. E., Mitchell, R. A. and Mordfin, L., "Non-Metallic Antenna-Support Materials: Pultruded Rods for Antenna Guys, Catenaries and Communications Structures," Report AFML-TR-76-42, Air Force Materials Laboratory, Wright-Patterson Air Force Base, Ohio, May 1976.

- [5] Mordfin, L. and Halsey, N., "Failure Analysis of Fiberglass Insulator Rods," Report NBSIR 76-1136, National Bureau of Standards, Washington, D. C., July 1976.
- [6] "Rods, Aramid Fiber/Polyester Resin, Coated, Pultrusion," Aerospace Material Specification ANSI/SAE AMS 3811-1978, Society of Automotive Engineers, Warrendale, Pa., 15 April 1978.
- [7] "Rods, Glass Fiber/Polyester Resin, Coated, Pultrusion," Aerospace Material Specification ANSI/SAE AMS 3812-1978, Society of Automotive Engineers, Warrendale, Pa., 15 April 1978.
- [8] Mordfin, L., and Berger, H. in *Nondestructive Evaluation in the Nuclear Industry—1980*, American Society for Metals, Metals Park, Ohio, 1981, pp. 303-318.

G. P. Sendeckyj,<sup>1</sup> G. E. Maddux,<sup>1</sup> and E. Porter<sup>2</sup>

# Damage Documentation in Composites by Stereo Radiography

---

**REFERENCE:** Sendeckyj, G. P., Maddux, G. E., and Porter, E., "Damage Documentation in Composites by Stereo Radiography," *Damage in Composite Materials, ASTM STP 775*, K. L. Reifsnider, Ed., American Society for Testing and Materials, 1982, pp. 16-26.

**ABSTRACT:** The results of an experimental study of penetrant enhanced stereo X-ray radiography for damage documentation in resin-matrix composite materials are presented. The results show that penetrant enhanced stereo radiography can describe accurately the spatial distribution of matrix cracks and delaminations. Presence of fiber fractures can be inferred from the matrix cracking patterns.

**KEY WORDS:** stereo X-ray radiography, tetrabromoethane, composite materials, graphite/epoxy composites, delaminations, matrix cracks, fiber fractures, nondestructive evaluation

An accurate description of the state of damage as a function of fatigue loading is required for successful development of procedures for predicting the residual strength and fatigue life of composite structures. The state of damage in composites can be documented by using nondestructive evaluation (NDE) techniques. Of the available NDE methods, only penetrant enhanced X-ray radiography has the resolution capability to record matrix cracks, delaminations, and fiber bundle fractures [1,2].<sup>3</sup> Unfortunately, the X-ray procedure used by the composites community does not provide through-the-thickness information on the state of damage. In an attempt to overcome this deficiency, we have adopted a three-dimensional X-ray technique used by the medical profession. While sophisticated X-ray techniques (such as computer aided tomography and multiple film laminography) are in everyday use in medicine, classical stereo X-ray radiography is more than adequate for the documentation of the state of damage in resin-matrix composites. Herein, we will describe the penetrant enhanced stereo X-ray method that we have been using, describe a simple procedure for constructing the

<sup>1</sup> Aerospace engineers, Structural Integrity Branch, Structures and Dynamics Division, Flight Dynamics Laboratory, Air Force Wright Aeronautical Laboratories (AFSC), Wright-Patterson Air Force Base, Ohio 45433.

<sup>2</sup> Nondestructive testing engineer, Universal Technology Corp., Dayton, Ohio 45432.

<sup>3</sup> The italic numbers in brackets refer to the list of references appended to this paper.

three-dimensional image of the damage, and present some typical examples of stereo X-ray radiographs of damage in graphite/epoxy test specimens.

### Penetrant Enhanced Stereo X-ray Radiography Procedure

Stereo radiography is a well established X-ray procedure, described in reference books [3-5]. The standard procedure consists of making two X-ray radiographs of an object from slightly different orientations. This can be done by translating the X-ray source relative to the object/film combination by moving either the X-ray tube or the film and object. In either case, the amount of permissible translation is limited by the characteristics of the cone of X-rays emanating from the X-ray tube. To overcome this difficulty, we adopted a different procedure for making the X-ray stereo radiographs. The procedure makes use of a special fixture for properly positioning the film and object being X-rayed. The fixture, shown on edge in Fig. 1, consists of a "bed" that can be precisely rotated with respect to the X-ray source. The bed consists of a lead foil (to absorb the X-rays that penetrate the film) mounted on a foam rubber cushion which is in turn mounted on a wooden plate that can be rotated about an axis in its plane. The foam rubber cushion and lead foil are slightly smaller than the test section to avoid difficulties in maintaining intimate contact between the film pack and specimen caused by the load introduction tabs on the specimen. When positioned directly under the X-ray source, the bed can be rotated through any desired angle with the specimen at the center of the cone of X-rays. The angle of rotation is controlled by a positioning pin system.

The following procedure was used in making the stereo X-ray radiographs presented herein:

1. The specimen was treated with tetrabromoethane (TBE), an X-ray opaque penetrant, to bring out the details of the damage. The penetrant was necessary to provide sufficient contrast between the damage and the graphite/epoxy so that the damage could be observed. The TBE was applied continuously to the surfaces of the specimen in the damaged region for 30 min to give it sufficient time to penetrate into all of the matrix cracks and delaminations. After it had fully saturated the damage regions, the excess TBE was

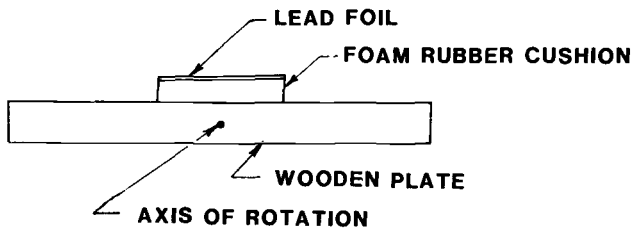


FIG. 1—Cross-section view of specimen holding fixture.

removed from the surfaces of the specimen with absorbent towels. Note that other penetrants, such as zinc iodide in an alcohol solution or diiodobutane (DIB), can be used just as easily and more safely. We used the TBE because we had a supply of it on hand.

2. The saturated specimen was placed on top of a Kodak<sup>4</sup> Type R single-coat industrial film pack placed on the lead foil in the fixture. The fixture was positioned precisely under the X-ray source by using a laser positioning system mounted on the X-ray machine. The fixture then was set to give the desired viewing angle. A small-focal-spot Norelco 150 X-ray unit, set at a focal film distance of 91.4 cm and operating at 25 kV and 5 mA, was used to expose the film. The film was exposed for 1.5 min.

3. Step 2 was repeated for each desired viewing angle. We used three viewing angles ( $-15$ ,  $0$ , and  $15$  deg) to give three possible stereo pair combinations.

4. The X-ray negatives were printed at  $\times 4$  magnification on high contrast paper. This was done to bring out the fine details in the damage region.

Initially, we tried using Type R double-coat film because of a shorter required exposure time. This proved to be unsatisfactory for our purposes because the X-ray images on the two emulsions are slightly displaced, resulting in a double image on the film. This leads to loss of resolution in the stereo image constructed from the stereo pair.

### Reconstruction of Stereo X-ray Pairs

The perception of three-dimensionality in a scene involves a complex interactive relationship between the brain and the eyes. The eyes, operating at a fixed distance apart, each provide a slightly different view. The brain combines this sensory information with years of observations involving all of the senses to reach a conclusion about the scene. If the scene is photographed by a pair of cameras having the same angular separation from it as a pair of eyes would have, the resulting images can be used to reconstruct a reasonably accurate three-dimensional view. This view exists only in the mind of the viewer. This is accomplished by placing the images in such a way that the left eye can see only the left image and the right eye the right image. A number of ways for accomplishing this have been developed since the introduction of stereo photography in the 19th century [6].

The most popular instrument for viewing stereo pair images is the stereoscope invented by Brewster in 1844. It consists of a pair of convex lenses mounted in a hand-held frame which allows the images to be moved to compensate for variations in the user's eyesight. Unfortunately, many viewers do not have the same degree of nearsightedness or farsightedness in both eyes

<sup>4</sup> Reference to a company or product name does not imply approval or recommendation of the product by the Air Force Wright Aeronautical Laboratories to the exclusion of others that may be suitable.

and the viewing position is a compromise. It was, and still is, awkward to look through optical elements of any sort with eyeglasses on. A more convenient device, called the telestereoscope, was invented by Helmholtz in 1857. It has a more sophisticated set of optics, which permit individual focusing of each eyepiece, adjustable distance between eyepieces, and variable magnification. It has an additional advantage in that much larger pictures can be viewed. The telestereoscope has been used for interpreting aerial photographs and is still being manufactured. If the viewer suffers from astigmatism, he must still use his glasses and the stereo optics.

The aforementioned difficulties and the requirement to have a display unit which also could be used in routine examination of specimens led to the construction of the viewer used in this effort. The unit is designed so that it could be used by a number of viewers, one at a time, with no intervening adjustments. The concept is actually the oldest, being invented by Whetstone in 1838. The present device shown in Fig. 2 consists of an enclosure, an internal light source, two front surface mirrors, and a frame for holding the photographs. The viewer positions himself so that he is centered on the intersection of the two mirrors and close enough to the unit so that the left eye can see only what is reflected from the left mirror and the right eye can see only the reflection from the right mirror. The viewer can do so comfortably with his glasses on. As can be seen from the ray trace diagram in Fig. 3, the two separate images appear to merge in the center, behind the mirror. The angle between the mirrors is somewhat arbitrary. Once it is chosen, the angular position and location of the photograph planes can be determined. The angle was chosen for our unit so that a conveniently sized display box could be fabricated.

The brain assembles the information from the superimposed images and is convinced that there is a three-dimensional object located behind the mirrors. Owing to the fact that the reflections in the mirrors are reversed left to right, the perspective of the scene is reversed. It is as though one is looking

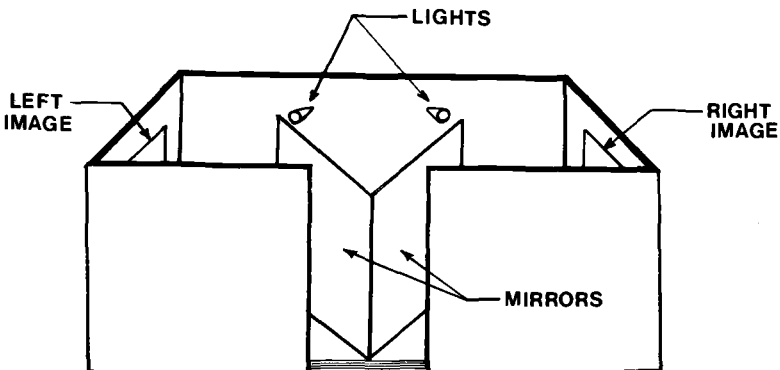


FIG. 2—Device for viewing X-ray stereo pair photographs.

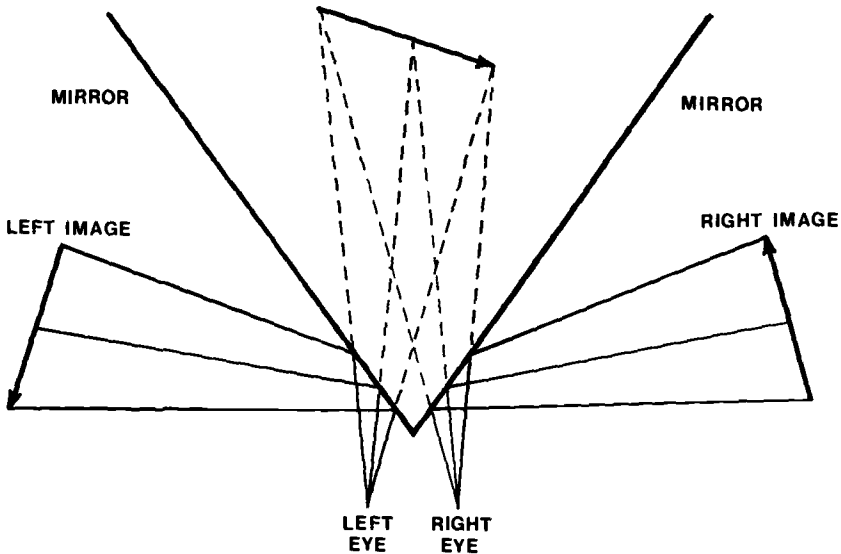


FIG. 3—Ray trace diagram illustrating reconstruction of three-dimensional image from stereo pair photographs.

through the back surface toward the front. This can be corrected by reversing the photographs during printing or exchanging the left photograph for the right one. Since identifying X-ray opaque markers are normally placed on the reference surface(s), it really does not make any difference in which direction the reconstruction is viewed. It is interesting to note that the length of time it takes to see a three-dimensional view ranges from almost instantly to a few seconds, from individual to individual. Once the reconstructed three-dimensional image is perceived, the point of attention can wander around the image without losing the depth perception. Even though the present viewing unit can be used successfully by people who cannot use the telestereoscope, there are a few people who cannot merge the stereo pairs. This inability is possibly due to strabismus or some other malfunction.

At the outset of this section, we mentioned that the recording cameras normally are located at the same angular separation as the eyes. Quite satisfactory reconstructions can be obtained using larger angles. The effect in the reconstruction is to change the perspective or perception of depth. In the case of stereo radiography, the resulting reconstruction is an arrangement of abstract objects in space. Since the brain has no prior experience of having encountered a view like this, it does not care whether the object appears to be a fraction of an inch in depth or an inch or more. The stereo recording geometry thus can be varied to yield the most information. For the purpose of damage documentation in composites, the primary interest is in the relative location of damage artifacts as opposed to determining the exact depth-wise separation between the artifacts. Automated photogrammetry procedures can be used to obtain precise spatial information [5].

The process of taking the radiographs, converting them to 20.3 by 25.4 cm (8 by 10 in.) photographs, and locating them in the viewing box is not very convenient for laboratory use. The radiographs could be back lighted and projected onto the photo plane. An even more interesting, but much more expensive, approach might be to view the backlighted radiographs with video cameras. Television monitors could then replace the photographs. With appropriate zoom lenses and positioning apparatus, the entire specimen could be examined first and then an enlargement of an area of interest made. In addition, the contrast of selected areas could be greatly enhanced to bring out subtle details.

### Examples of Application to Damage Documentation

The penetrant enhanced X-ray stereo radiography procedure described in the previous sections was used to document the fatigue induced damage accumulation process in the  $[(0/\pm 45/90)_S]_2$  T300/5208 graphite/epoxy specimens used in Ref 2. The specimens were 25.4 mm wide and contained a centrally located circular hole with 4.75 mm diameter. The reader is referred to Ref 2 for a detailed description of the specimen geometry. The specimens were subjected to 150 000 cycles of constant amplitude fatigue loading at a frequency of 5 Hz. The maximum and minimum cyclic loads were 13.3 kN and 1.33 kN, respectively. Note that the maximum cyclic load used is approximately 86 percent of the static tensile strength of the specimens.

#### *Specimen AB-100*

A penetrant enhanced stereo X-ray triple of the fatigue induced damage in Specimen AB-100 is shown in Fig. 4. The left, center, and right views in the figure were obtained by using  $-15$ ,  $0$ , and  $15$ -deg viewing angles, respectively, in making the X-ray photographs. The viewing angles are defined in

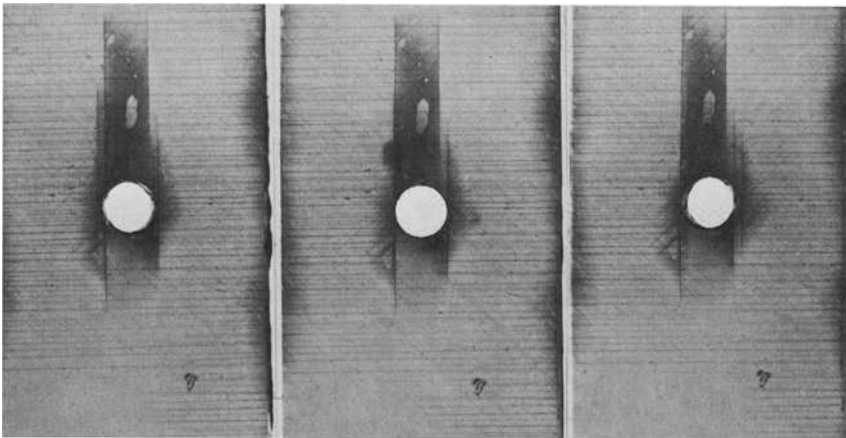


FIG. 4—Penetrant enhanced X-ray stereo triplet of damage in Specimen AB-100.

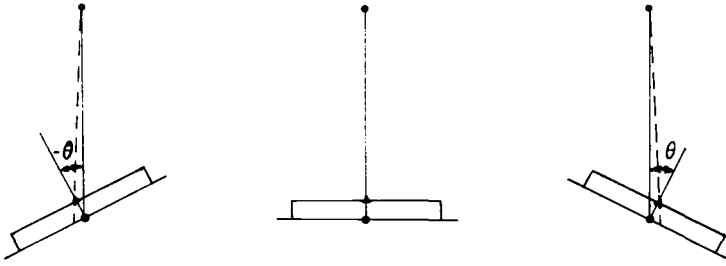


FIG. 5—Sketch showing the orientation of specimen and film relative to X-ray source and the resulting relative location of artifacts on film.

Fig. 5. Any two of the three views can be used to reconstruct a stereo image of the damage in the specimen. Since details can be lost in the printing process, stereo sketches of interesting damage features were prepared from enlarged photographs of the views in Fig. 4. A typical stereo triplet sketch, illustrating a number of damage indications, is shown in Fig. 6.

As can be seen from the stereo views in Figs. 4 and 6, the fatigue loading has caused matrix cracking in the vicinity of the hole in all the 0-deg plies. The depth location of these matrix cracks can be determined from either the stereo image of the damage or the relative location of the matrix crack indications (dark vertical lines in the two figures) in the different views. If the stereo image is used, the depth perception of the damage details depends on how the different views are merged to form the stereo image. If the views are merged with the aid of an optical device like the stereoscope, the left eye sees the left view and the right eye sees the right one. This type of image merging is referred to as conventional stereo viewing. If the stereo pairs are viewed without optical aids, the depth perception depends on whether the stereo pairs are merged conventionally or cross-eyed. In cross-eyed viewing, the left

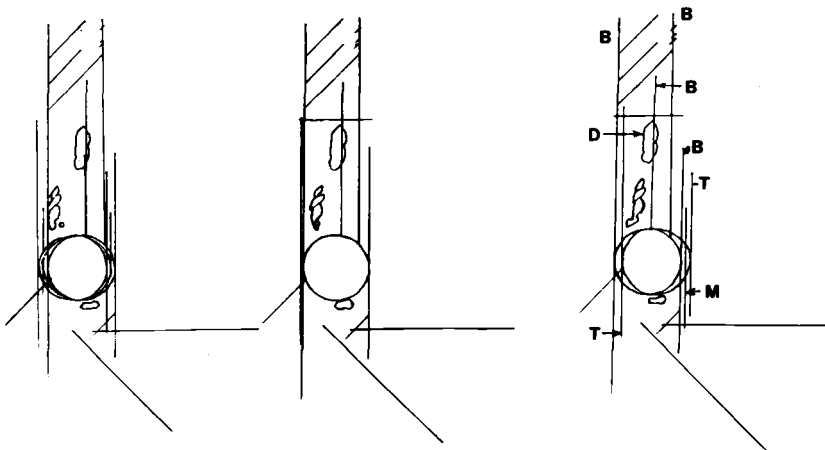


FIG. 6—Stereo triplet sketch of selected damage features from Fig. 4.

eye sees the right image and the right eye sees the left one. As a result, the depth perception is reversed from that in conventional merging. In cross-eyed viewing, images further apart than the eye separation can be merged, while in conventional unaided viewing the images have to be located closer to each other than the eye separation.

When the relative location of the crack indications in the different views is used to determine the depth of the cracks, the matrix cracks in the bottom surface 0-deg ply (the ply adjacent to the film pack during the X-raying process) have essentially zero relative displacement in the different views. The matrix cracks in the middle and top surface 0-deg plies are displaced to the left in the left-hand view and to the right in the right-hand one relative to their location in the center view. The magnitude of the relative displacement indicates the depth location of the matrix cracks. The matrix cracks with the largest relative displacement in the views are in the top surface 0-deg ply, while those with an intermediate relative displacement are in the subsurface plies. This procedure for determining the depth location of damage features was used to determine the spatial location of the matrix cracks in the 0-deg plies. The depth location of these matrix cracks is indicated in the right-hand view in Fig. 6 by letters *B*, *M*, and *T* (standing for the bottom, middle, and top, respectively). The depth location of the matrix cracks in the off-axis plies and delaminations between plies also can be determined by this procedure. Thus, the matrix cracks in the 45-deg plies shown in the sketches in Fig. 6 are in the 45-deg ply adjacent to the back surface 0-deg ply. These matrix cracks are initiated by the matrix cracks in the back surface 0-deg ply. Whether they are associated with fiber fractures in the 45-deg ply cannot be determined from the present results. The delamination feature, indicated by the letter *D* in Fig. 6, is between the back surface 0-deg ply and the adjacent subsurface 45-deg ply. This delamination feature is a region in which the penetrant evaporated out due to the presence of the matrix cracking. Similarly, the delamination feature just above the hole is between the top surface 0-deg ply and the adjacent subsurface 45-deg ply. With these preliminary considerations out of the way, we can form the following description of the fatigue induced damage in the specimen:

1. Matrix cracks are present in the vicinity of the hole in all the 0-deg plies. The matrix cracks in the middle 0-deg plies occur at the edges of and are tangent to the hole. The matrix cracks in the surface 0-deg plies occur at these and a number of other locations. The matrix cracks tangent to the hole are due to the stress concentration at the edge of the hole. The other matrix cracks are due to the presence of delaminations between the surface and subsurface plies.

2. Matrix cracks are present in the 45-deg plies in the vicinity of the hole and along the specimen edges. These have the appearance of dark 45-deg lines in the different views in Fig. 4. The matrix cracks in the 45-deg plies in

the vicinity of the hole are in the 45-deg plies adjacent to the surface 0-deg plies. They were initiated by the matrix cracks in the surface 0-deg plies. This can be inferred from the short matrix cracks sketched above the hole in Fig. 6. The matrix cracks in the 45-deg plies near the specimen edges are associated with the matrix cracks in the -45-deg plies. These matrix cracks are in the 45-deg plies nearest to the 90-deg plies and were initiated by the matrix cracks in the -45-deg plies.

3. An extensive pattern of matrix cracks in the 90-deg plies can be seen in the views in Fig. 4. Most of these cracks were initiated at the free edges of the specimen and have propagated towards the specimen center. This can be confirmed by the horizontal crack indications (horizontal dark lines) in Fig. 4 that terminate inside the specimen. Evidence of matrix cracks in the 90-deg plies that did not initiate at the specimen edges can be seen in the views in Fig. 4. One such crack associated with the extensive matrix cracking in the -45-deg ply in its vicinity has been sketched above the hole in Fig. 6.

4. An extensive pattern of matrix cracks in the -45-deg plies can be seen near the specimen edges. The cracks are associated with the matrix cracks in the 90-deg plies. Most of these cracks run towards the specimen center, but do not cross the specimen width. The exception to this is the cracks intersecting the circular hole. Thus, the matrix cracks in the -45-deg plies were initiated at the free edges by the matrix cracks in the 90-deg plies.

5. Delaminations are present near the hole and along the specimen edges. The delaminations have the appearance of dark regions with diffuse edges and lighter colored splotches in their interiors. The delaminations near the hole are between the surface 0-deg plies and the subsurface 45-deg plies. Whether delaminations between the other plies are also present near the hole cannot be determined from the photographs. The delaminations along the specimen edges are between the interior 90-deg plies and the adjacent -45-deg plies.

### *Specimen AB-97*

A penetrant enhanced stereo X-ray triple of the fatigue induced damage in Specimen AB-97 is shown in Fig. 7. As can be seen by comparing this figure with Fig. 4, the damage features in Specimen AB-97 are similar to those in Specimen AB-100. The extent of the delaminations near the hole is the only difference.

### **Conclusions and Recommendations**

The experimental results lead to the following conclusions:

1. Penetrant enhanced stereo X-ray radiography gives detailed information on the nature and spatial distribution of damage in graphite/epoxy composites. It can find fiber fractures [1,2], matrix cracks, and delaminations.

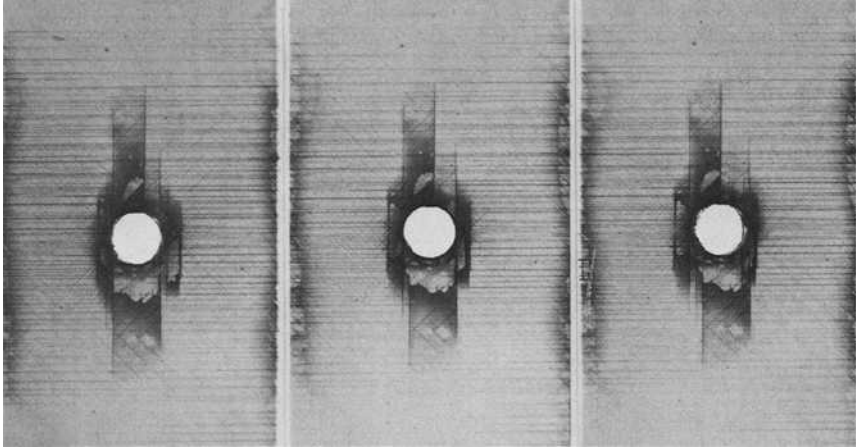


FIG. 7—Penetrant enhanced X-ray stereo triplet of damage in Specimen AB-97.

2. Fatigue loading of  $[(0/\pm 45/90)_s]_2$  specimens with a center hole causes extensive matrix cracking in the 90-deg and the  $\pm 45$ -deg plies. It also causes matrix cracks in the 0-deg plies near the hole. The extensive matrix cracking is believed to cause the delaminations resulting from the fatigue loading.

Based on our experience with TBE enhanced stereo X-ray radiography, we offer the following recommendations:

1. A procedure for obtaining more detailed information on the damage associated with the delaminations should be developed. We believe that this can be done by varying the time between the introduction of the penetrant into the damage regions and taking of the stereo radiographs.
2. A procedure for rapidly quantifying the spatial distribution of the damage should be developed. This may be done by using either laminography or photogrammetry.

#### *Acknowledgment*

This paper is based on inhouse work performed at the Flight Dynamics Laboratory of the Air Force Wright Aeronautical Laboratories under the Solid Mechanics Project funded by the Air Force Office of Scientific Research.

#### **References**

- [1] Sendekyj, G. P., Maddux, G. E., and Tracy, N. A. in *Proceedings of the 1978 International Conference on Composite Materials*, B. Noton, R. Signorelli, K. Street, and L. N. Phillips, Eds., American Institute of Mining, Metallurgical, and Petroleum Engineers, 1978, pp. 1037-1056.

- [2] Maddux, G. E. and Sendeckyj, G. P. in *Nondestructive Evaluation and Flaw Criticality for Composite Materials*, ASTM STP 696, American Society for Testing and Materials, 1979, pp. 26-44.
- [3] McMaster, R. C., *Nondestructive Testing Handbook*, The Ronald Press Co., New York, 1963, pp. 20.46-20.49.
- [4] *Radiography in Modern Industry*, Eastman Kodak Co., Rochester, N.Y., 1970.
- [5] Halbert, B., *X-Ray Photogrammetry, Basic Geometry and Quality*, Elsevier Publishing Co., Amsterdam, 1970.
- [6] Clerc, L. P., *Photography, Theory and Practice*, Sir Isaac Pitman & Sons, Ltd., London, 1954.

# Fractographic Studies of Graphite/Epoxy Fatigue Specimens

---

**REFERENCE:** Morris, G. E., and Hetter, C. M., "Fractographic Studies of Graphite/Epoxy Fatigue Specimens," *Damage in Composite Materials, ASTM STP 775*, K. L. Reifsnider, Ed., American Society for Testing and Materials, 1982, pp. 27-39.

**ABSTRACT:** Techniques have been developed for determining fracture directions and locating fracture origins for graphite/epoxy (Gr/Ep) laminates that fail by overload. These techniques have used the scanning electron microscope (SEM) to identify failed epoxy component topographic features (hackles) that characterize overload failures. Now, the hackle interpretation technique is used to trace hackles back to fracture origin locations on the fracture surfaces of tensile failed Gr/Ep test coupons and structures.

Recently, these SEM studies have been expanded to include fatigue tested cross-ply Gr/Ep specimens. Patterns of arrest marks (striations) have been associated with tension-compression fatigue crack propagation for some Gr/Ep test specimens. The striation features are distinctly different in appearance from hackles; therefore, they present a promising topographic feature to differentiate tension-compression fractures from overload fractures in Gr/Ep composites. Visual, nondestructive testing, and SEM techniques that were used to identify the striation topographic features are described. Progress to date is presented on attempts to correlate observed striation patterns with fatigue damage growth in Gr/Ep test specimens.

**KEY WORDS:** composite materials, fatigue, fracture (materials), fractography, failure analysis, graphite/epoxy, hackles, striations

Aircraft and automobile components, as well as sporting equipment, are being fabricated of graphite/epoxy (Gr/Ep) composites. There are no standardized fractographic techniques for conducting failure analyses for this material. The techniques that are most often used for analyzing these failures have been primarily mathematical and can only speculate as to where fracture origins are located; they have not identified the initiating mode of failure. Current visual and scanning electron microscope (SEM) examination techniques for Gr/Ep fractures include assessing the degree of fiber pull-out or the profiles of fracture surfaces. Many of these studies have been confined to unidirectional composites that do not necessarily duplicate the fracture characteristics of cross-ply laminates.

<sup>1</sup> Unit chief and engineer, respectively, Materials and Physics Laboratories, McDonnell Aircraft Co., McDonnell Douglas Corp., St. Louis, Mo. 63166.

One technique has been reported for determining fracture directions and locating fracture origins for Gr/Ep laminates that fail by overload.<sup>2</sup> When Gr/Ep composites fail, the fracture surfaces are comprised of the graphite fiber and epoxy matrix components. For overload failures, the fractured epoxy matrix most often has a characteristic overlapping platelet topographic feature, shown in Fig. 1, that has been termed both hackles and lacerations.<sup>3</sup> The way that hackles overlap has been interpreted to determine the fracture directions for the various exposed plies of a failed Gr/Ep composite. In addition, the fracture directions have been traced back to fracture origin locations. These are the first two required steps for conducting a failure analysis of metals,<sup>4</sup> graphite/epoxy, or any other failed material. Graphite/epoxy components are subjected to the same static and cyclic service loads as the

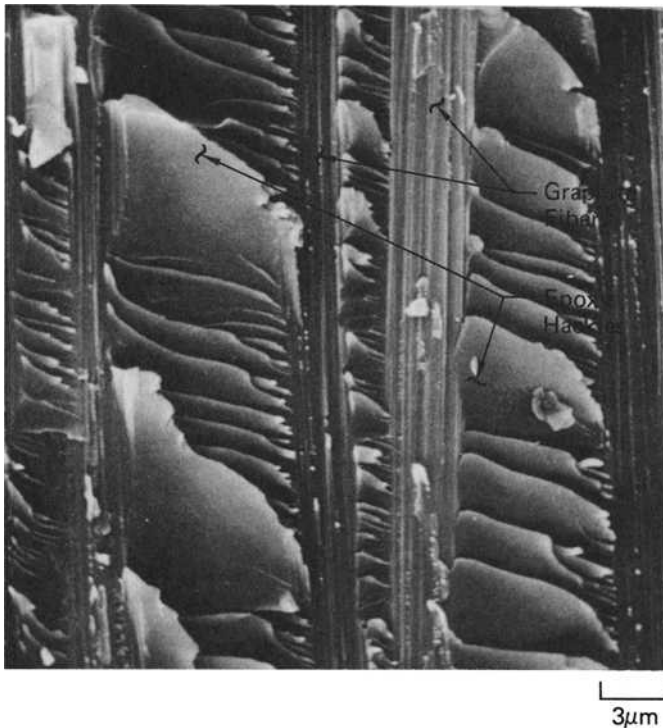


FIG. 1—Hackles (fractured epoxy) and graphite topographic features on an overload fracture surface of graphite/epoxy composite.

<sup>2</sup> Morris, G. E. in *Nondestructive Evaluation and Flaw Criticality for Composite Materials*, ASTM STP 696, American Society for Testing and Materials, 1979, pp. 274–297.

<sup>3</sup> Chamis, C. C. and Sinclair, J. H., "Mechanical Behavior and Fracture Characteristics of Off-Axis Fiber Composites II—Theory and Comparisons," NASA Technical Paper 1082, National Aeronautics and Space Administration, Washington, D. C., Jan. 1978.

<sup>4</sup> *Fractography and Atlas of Fractographs*, ASM Metals Handbook, Vol. 9, American Society for Metals, Metals Park, Ohio, 1974.

metal components to which they are attached. Because hackles characterize static failures, it also was considered necessary to study fatigue failed Gr/Ep specimens to detect topographic features that could define this fracture mode.

This report describes recent SEM studies that have been conducted to characterize constant amplitude fatigue failed Gr/Ep cross-plyed laminates.

## Procedure

### Equipment

All fatigue testing was conducted at constant amplitude using an MTS load frame. A JOEL Model JSM-2 scanning electron microscope was used to study and document the topographic features of the failed Gr/Ep test specimen fracture surfaces. Stereo viewing of stereo pairs of SEM fractographs, taken at  $+5$  and  $-5$  deg, was considered the best way to study and interpret the fracture surface topographic features of the failed specimens.

### Specimen Fabrication

Twenty-five ply-thick Gr/Ep (AS/3501-6, MMS-549 Type II) laminates were fabricated for this examination. Panel P1 was a 48/48/4 fiber dominated laminate with a  $[+45, -45, 0, 0]_3, 90, [0, 0, -45, +45]_3$  layup, and Panel P2 was a 16/80/4 matrix dominated laminate with a  $[+45, -45, 0, +45, -45]_2, +45, -45, 90, -45, +45, [-45, +45, 0, -45, +45]_2$  layup. The panels were cured in an autoclave for 2 h at a maximum temperature of  $177^\circ\text{C}$  ( $350^\circ\text{F}$ ) at  $0.69\text{ N/m}$  ( $100\text{ lbs/in.}$ ), and subsequently were post-cured at the same temperature for 8 h in an air-circulating oven. Test specimens measuring  $3.81\text{ cm}$  ( $1.50\text{ in.}$ ) wide by  $17.8\text{ cm}$  ( $7\text{ in.}$ ) long, shown in Fig. 2, were machined from each panel with diamond impregnated tools using established machining techniques for graphite/epoxy. A  $0.64\text{-cm}$  ( $0.250\text{-in.}$ )-diameter hole was machined at the center of each specimen. Ultrasonic "C" scan inspection of the laminates and all test specimens, after the completion of machining, indicated that all specimens were acceptable.

### Test Procedure

The initial study was conducted on a 16/80/4 specimen that was tension-compression constant amplitude fatigue tested at room temperature in air

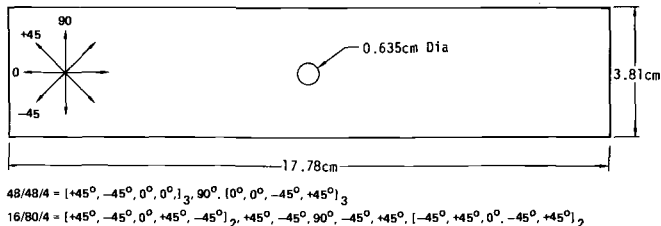


FIG. 2—Graphite/epoxy fatigue specimen.

using an MTS load frame operating at 5 Hz according to the following schedule:

Number of Cycles	Cumulative Number of Cycles	Maximum Load Tension,		Maximum Load Tension,		Specimen Condition <sup>a</sup>
		kN	(lbs)	kN	(lbs)	
500	500	57.0	(12 820)	-57.0	(-12 820)	NF-NDT
2 500	3 000	43.9	(9 870)	-43.9	(-9 870)	NF-NDT
2 500	5 500	43.9	(9 870)	-43.9	(-9 870)	NF-NDT
1 370	6 870	43.9	(9 870)	-43.9	(-9 870)	fail

<sup>a</sup>NF = No failure; specimen supported loads. NDT = Enhanced penetrant radiographic inspection.

The Radiographic Inspection Procedure (NDT) enhanced radiographic inspections indicated in the test schedule were conducted using tetrabromothane (TBE) enhanced Z1-22A Magnflux penetrant in a ratio of one part TBE to three parts of Z1-22A. The penetrant was applied to the hole surface and to the outside edge surfaces during each test stoppage. Enhanced radiographs were taken to document the extent and location of any damage progression that occurred during each test interval. Figure 3 presents four views of a failed specimen. The  $\pm 45$ -deg oriented surface plies are obviously delaminated, and the right and left edge views show several obvious splits between variously oriented subsurface plies. Figure 4 shows how the fatigue damage progression was monitored with the enhanced radiographs.

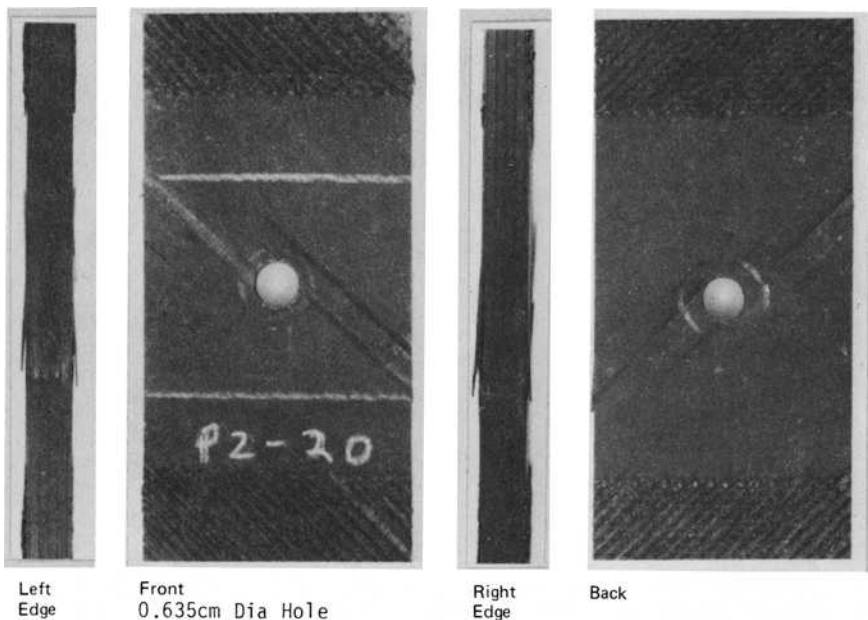
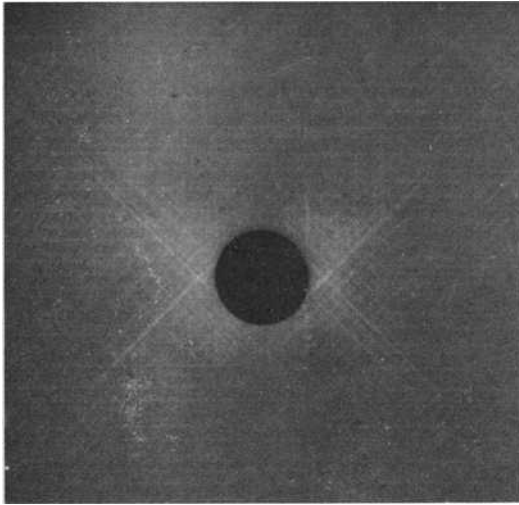
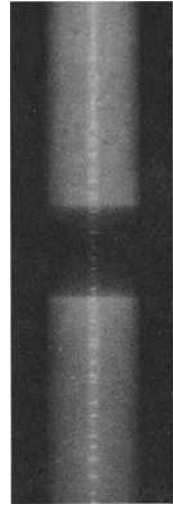


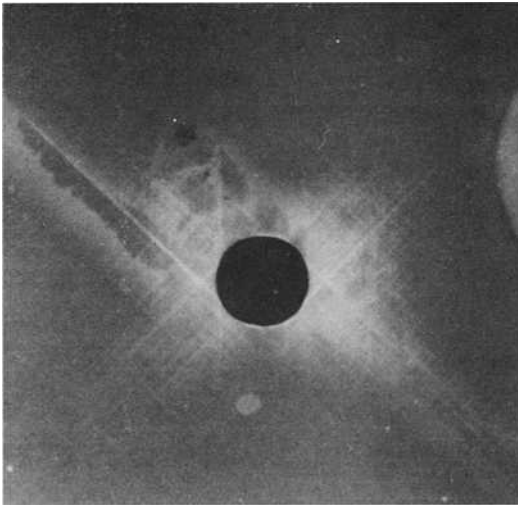
FIG. 3—Four views of the failed graphite/epoxy tension-compression fatigue specimen.



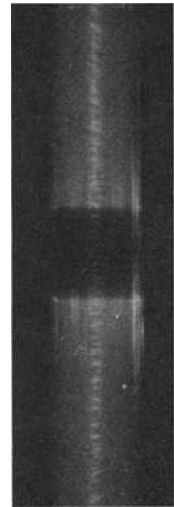
3,000 Cycles



3,000 Cycles



5,500 Cycles



5,500 Cycles

FIG. 4—Enhanced radiographs showing damage growth (white lines) during tension-compression fatigue testing of a graphite/epoxy specimen.

To examine the fracture surface topographic features, the outside +45-deg oriented surface ply was peeled from the specimen. A distinct texture variation was obvious between the fatigue incurred damage and the delaminated overload zone that resulted from peeling the surface ply from the specimen, shown in Fig. 5. The delaminated fracture surface that resulted during fatigue testing had a mottled appearance that was comprised of alternate light and dark bands. The created fracture surface appeared uniformly black. Because the fluorescent penetrant used during the enhanced radiographic inspections had dried, it was decided to examine several of the exposed fracture surfaces under a black light. The dried penetrant on the mating fracture surfaces between the second and third plies fluoresced as shown in Fig. 6, and differentiated the fatigue created surfaces from the overload created surfaces.

It is anticipated this technique can be applied to any failed Gr/Ep component to examine the extent of test or of in-service incurred damage. Removal of the dried fluorescent penetrant has proven to be somewhat difficult using standard acetone solvents in an ultrasonic cleaning tank. Various solvents are being evaluated to solve this problem.

A SEM was used to detect and document topographic features that would characterize fatigue fractures of Gr/Ep composites. Prior to SEM examination, gold was sputtered onto the fracture surface of each specimen ply to obtain optimum resolution of the topographic features and to minimize static charging by the SEM electron beam.

### *Test Results and Discussion*

During SEM examination there were distinct differences in the topographic features between the fracture surface in the mottled and uniformly black

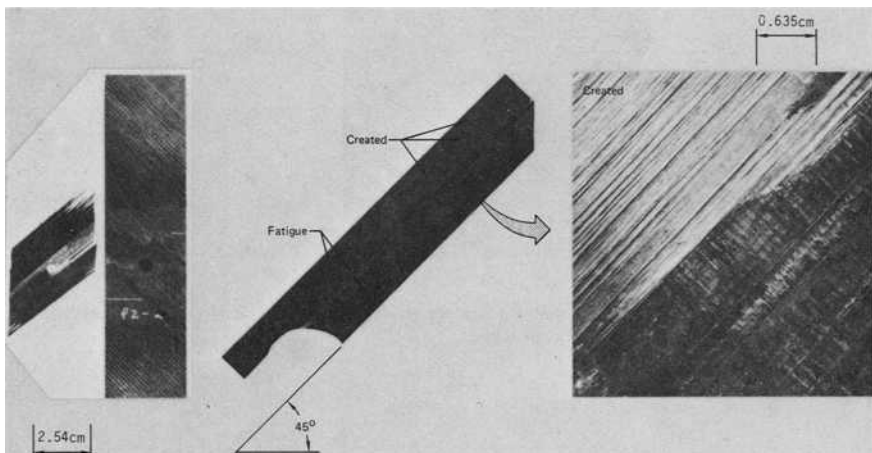


FIG. 5—Surface texture variations between fatigue (mottled) and created (uniformly black) zone in graphite/epoxy.

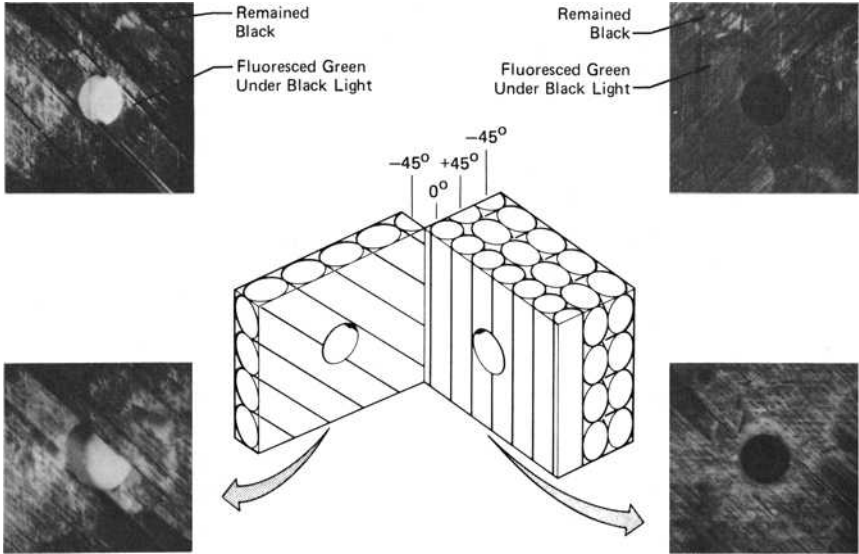


FIG. 6—Comparison between white light (top) and black light (bottom) appearances of mating fracture surfaces of a graphite/epoxy tension-compression fatigue specimen.

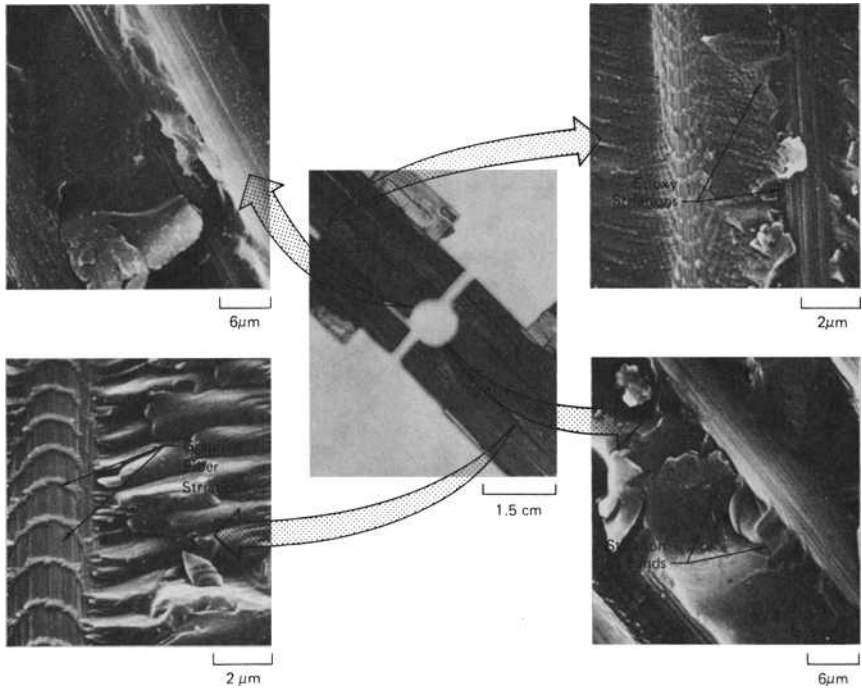
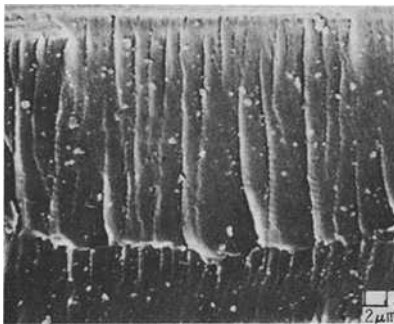


FIG. 7—Variations in fatigue striation morphology.

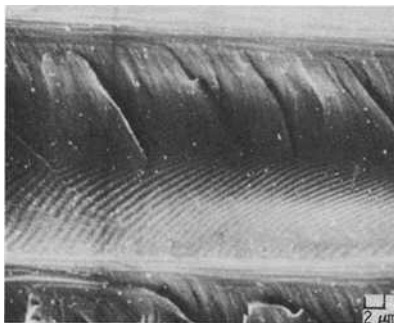
areas. In the SEM, the uniformly black, manually created, fracture surfaces consisted of relatively clean graphite fibers and hackles—topographic features that characterize overload failures (Fig. 1). The mottled areas exhibited several topographic features. However, striations were the most commonly observed feature that typified the fatigue created zones. Striations appeared with several variations, as shown in Fig. 7. Proximate to the fastener hole and on opposite sides of the hole, individual striations could not be detected. However, what appeared to be concave bands of striations were detected in the epoxy component; the adjacent graphite fibers appeared relatively clean. Striations with two configurations were detected away from the hole. Graphite fiber striations were located on the fibers and were oriented normal to the fiber axes and convex to the hole. Epoxy striations were oriented more nearly parallel to the fiber axes. The epoxy striations appeared to be more numerous and closer spaced than the fiber striations. However, at some locations, the epoxy striations were extensions of the fiber striations. A relationship between the number of striations and the cyclic fatigue loading could not be determined. Because of the adjacent composite plies and different orientations, the spacing and orientation of the fiber striations apparently



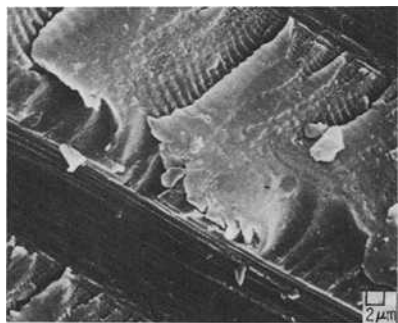
a) Epoxy Striations Propagating From Adjacent Fibers Toward Each Other



b) Epoxy Striations Propagating From the Top of One Fiber to the Base of the Adjacent Fiber



c) Combined Striation and Hackle Propagation



d) Striations on Hackle-Like Features

FIG. 8—Various fatigue striation configurations.

are influenced by the orientations of the fibers on which they are located and the relative orientation of the applied fatigue loads. Fiber and epoxy striations were detected on fibers of +45, -45, 0 and 90-deg plies.

Striations similar to those observed on the graphite fibers have been reported previously for cyclic debonding of unidirectional composite bonded to aluminum sheet for constant-amplitude loading. The striations spacing reportedly reflected the debonding rate that was monitored using a photoelastic coating technique. A correspondence between the debonding rate or striation spacing with respect to the application of one or more fatigue cycles apparently was not included in the test regime. Roderick et al did not attempt to explain the formation of individual striations.<sup>5</sup>

TABLE 1—Test conditions for constant amplitude fatigue specimens.

Specimen Layup	Fatigue Conditions <sup>a</sup>			Cycles to Failure
	Percentage 0/45/90 Plies	Maximum Stress, MPa (ksi)	Minimum Stress, MPa (ksi)	
48/48/4	443 (64.3)	-443 (-64.3)	-1	6 690
48/48/4	445 (64.5)	-445 (-64.5)	-1	7 000
48/48/4	439 (63.7)	-439 (-63.7)	-1	4 890
48/48/4	378 (54.8)	-378 (-54.8)	-1	30 840
48/48/4	287 (41.6)	-287 (-41.6)	-1	279 350
48/48/4	233 (33.8)	-467 (-67.7)	-2	11 910
48/48/4	188 (27.2)	-375 (-54.4)	-2	377 770
48/48/4	233 (33.8)	-467 (-67.7)	-2	12 550
48/48/4	0 (0)	-465 (-67.4)	-∞	535 960
48/48/4	0 (0)	-460 (-66.7)	-∞	431 520
48/48/4	375 (54.4)	-375 (-54.4)	-1	75 030
16/80/4	291 (42.2)	-291 (-42.2)	-1	170
16/80/4	292 (42.3)	-292 (-42.3)	-1	40
16/80/4	248 (35.9)	-248 (-35.9)	-1	1 150
16/80/4	192 (27.8)	-192 (-27.8)	-1	11 650
16/80/4	0 (0)	-309 (-44.8)	-∞	570
16/80/4	0 (0)	-247 (-35.8)	-∞	28 810
16/80/4	148 (21.5)	-297 (-43.0)	-2	110
16/80/4	123 (17.9)	-246 (-35.7)	-2	2 220
16/80/4	121 (17.6)	-243 (-35.2)	-2	3 160
16/80/4	99 (14.4)	-199 (-28.8)	-2	226 190
16/80/4	234 (33.9)	-234 (-33.9)	-1	4 850
16/80/4	226 (32.7)	-226 (-32.7)	-1	5 060
16/80/4	202 (29.3)	-202 (-29.3)	-1	20 140
16/80/4	246 (35.6)	-246 (-35.6)	-1	1 120

<sup>a</sup> 100 MPa = 14.50 ksi.

<sup>5</sup> Roderick, G. L., Everett, R. A., and Crews, J. H., "Cyclic Debonding of Unidirectional Composite Bonded to Aluminum Sheet for Constant-Amplitude Loading," NASA Technical Note TN D-8126, National Aeronautics and Space Administration, Washington, D. C., Jan. 1976.

Some other configurations of striations that were observed during the examination are presented in Fig. 8. These SEM fractographs were studied using stereo pairs and the striations had the following appearances. Figure 8a shows striations in the epoxy propagating from adjacent fibers in opposite directions toward each other. The striations were concave to the nearest fibers and propagated such that one set of striations overlapped at the fracture surface created by the other set of striations. In Fig. 8b, epoxy striations initiated at the common sides of each fiber and propagated in a common direction toward the adjacent fiber. They propagated away from the top of each fiber and terminated near the bottom of the adjacent fiber. In Fig. 8c, a similar fracture propagation sequence occurred, but instead of propagating completely to the adjacent fiber by epoxy striation formation, the epoxy appeared to fracture initially by fatigue (striations) and finally by overload, as evidenced by hackle formation during the latter 40 to 50 percent of the inter-fiber crack propagation. In Fig. 8d, striations were observed on the surfaces of hackle-like topographic features.

In an attempt to understand what kinds of fatigue test conditions resulted

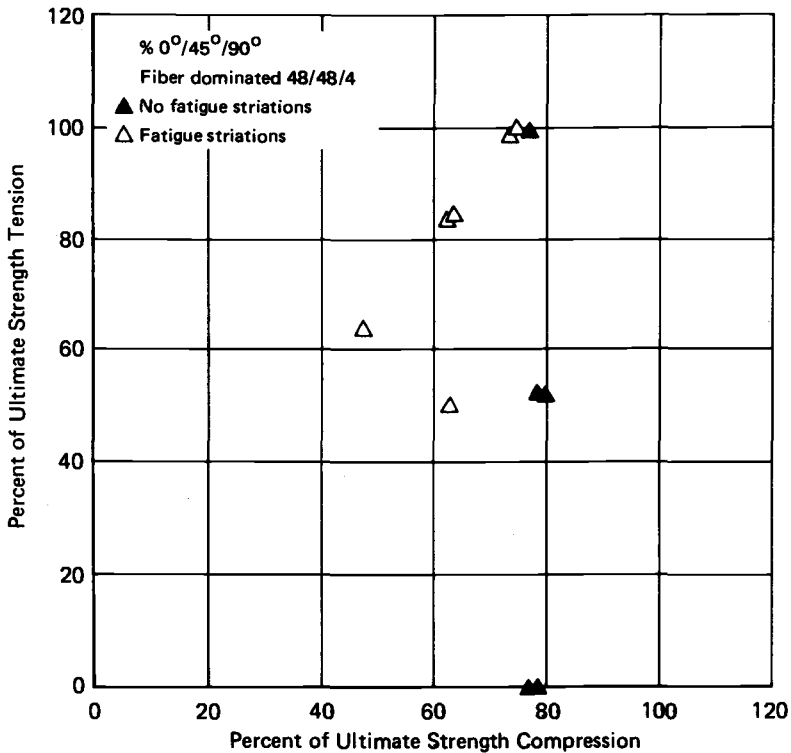


FIG. 9—Graph showing the presence or absence of striation topographic features for fiber dominated fatigue test specimens.

in the formation of striations, numerous test specimens that had been tested in tension-tension, tension-compression, or compression-compression constant amplitude fatigue at room temperature, in air, at 5 Hz, in an MTS loading frame were dissected and examined.

Table 1 shows the test conditions for the failed fatigue specimens that were studied. Each failed specimen was examined using the procedures described for the initial 16/80/4 specimen. The specimens were classified as either "exhibiting" or "not exhibiting" striation topographic features. Figure 9 shows the results of the study that was concluded on 48/48/4 fiber dominated specimens. The clear triangles represent specimens that exhibited striations with the SEM and the dark triangles present specimens for which striations were not detected. The axes represent applied stresses as a percent of the ultimate tensile strengths and percent of the ultimate compressive strengths. This plot, although lacking data points below about 50 percent of the ultimate compressive strength, still indicates that the maximum compressive strengths that resulted in striation formation were somewhere between 65 and 80 percent of the ultimate compressive stress.

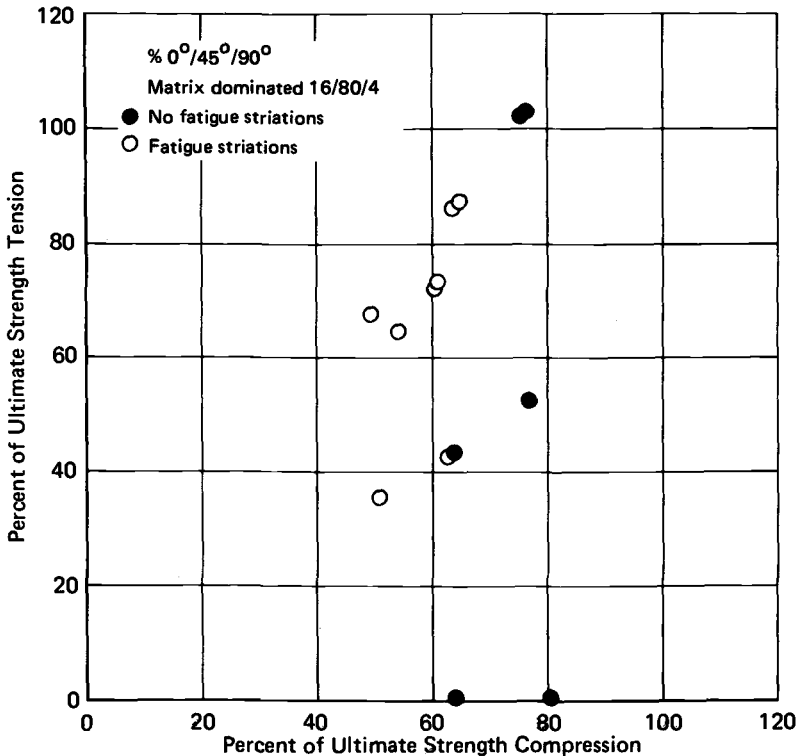


FIG. 10—Graph showing the presence or absence of striation topographic features for matrix dominated fatigue test specimens.

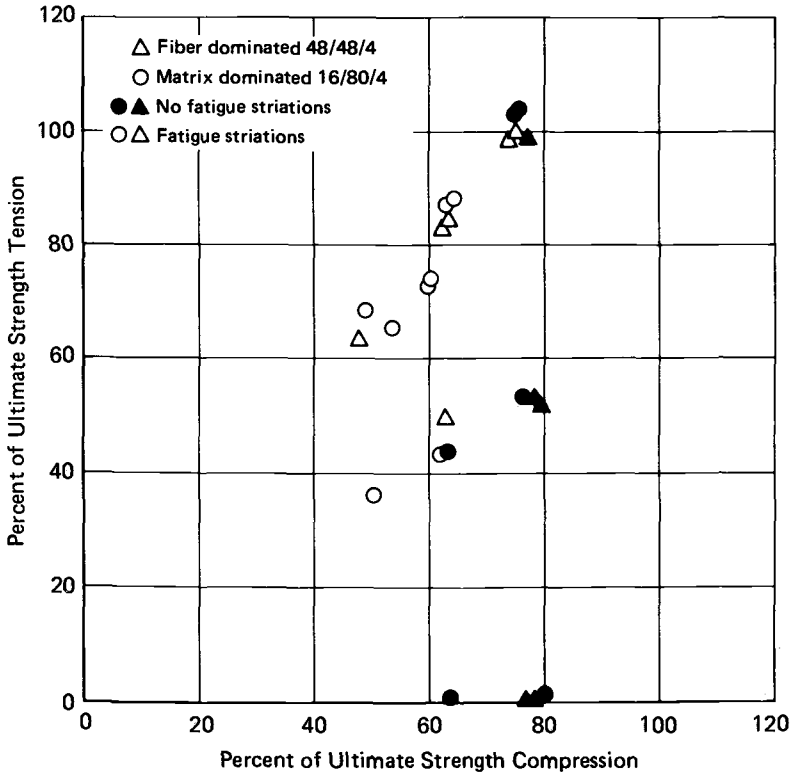


FIG. 11—Plot of combined fiber and matrix dominated fatigue test specimens.

Figure 10 shows the results that were obtained for a 16/80/4 matrix dominated layup. Again an apparent zone existed between 60 and 70 percent of the ultimate compressive stress above which striations were not observed.

When the preceding specimens were plotted together, as shown in Fig. 11, a common boundary area at about 65 to 70 percent of the tensile compressive strength appeared to be present to separate the striation containing specimens from those that did not exhibit striations. These plots represent preliminary data, however, and additional tests are going to be conducted to correlate further the formation of striations with the combination of applied tensile and compressive stresses. If this correlation can be accomplished, it possibly can provide design and strength engineers with data that can be used for future applications of graphite/epoxy.

**Summary**

The examination of Gr/Ep element specimens failed by known modes has resulted in the identification of microscopic topographic features associated with the different modes of failure. In past studies, hackles have been associ-

ated with fracture direction in overload Gr/Ep specimens. In this study, striations have been associated with fatigue damage growth in tension-compression loaded Gr/Ep specimens. Preliminary test results indicate that the formation of striations may be limited, and will not occur in Gr/Ep fatigue specimens in which more than 70 percent of the ultimate compressive strength of the specimen has been applied.

# An Investigation of Cumulative Damage Development in Quasi-Isotropic Graphite/Epoxy Laminates

---

**REFERENCE:** Masters, J. E. and Reifsnider, K. L., "An Investigation of Cumulative Damage Development in Quasi-Isotropic Graphite/Epoxy Laminates," *Damage in Composite Materials*, ASTM STP 775, K. L. Reifsnider, Ed., American Society for Testing and Materials, 1982, pp. 40-62.

**ABSTRACT:** Results of an experimental investigation of cumulative damage development in two unnotched quasi-isotropic graphite/epoxy laminates subjected to quasi-static tension and tension-tension fatigue are presented. Damage development in the form of transverse cracking in all off-axis laminae, longitudinal cracking, and delamination was monitored via the surface replication technique. Results of the study include a detailed description of the chronology of damage development prior to failure. Evidence also is presented in support of a damage model based on the concept of a characteristic damage state.

**KEY WORDS:** transverse cracking, saturation spacing, characteristic damage state, monotonic tension, tension-tension fatigue, composite materials

The ability to predict the strength of high performance composite materials under complex loading conditions is a necessary ingredient for rational design with such materials. Similarly, because composite materials are frequently used in structures subjected to dynamic loads, it is also important that their response to cyclic loads be well known and understood.

Pipes states that no unified failure model has emerged to date; rather, a multitude of models are being developed to describe a multimode failure process [1].<sup>3</sup> Similarly, Stinchcomb states that our current understanding of the failure of composite materials is incomplete [2]. Although we can detect, identify, and monitor damage details during the process of failure, we do not understand how the individual details combine to form the damage state

<sup>1</sup> Senior research scientist, General Dynamics Corp., P.O. Box 748, Fort Worth, Tex. 76101.

<sup>2</sup> Professor, Department of Engineering Science and Mechanics, Virginia Polytechnic Institute and State University, Blacksburg, Va. 24060.

<sup>3</sup> The italic numbers in brackets refer to the list of references appended to this paper.

which controls the fracture of the materials. Stinchcomb further states that only through assiduous investigations of mechanics and materials interactions throughout the loading history can we hope to characterize flaws more completely and understand their relationships to material response.

This report will detail the results of an investigation of cumulative damage development in laminated graphite epoxy plates. It will begin by describing the material system examined and the experimental procedures employed. This will be followed by a qualitative description of the cumulative damage development observations. Finally, quantitative experimental results will be presented, followed by a brief outline of the proposed characteristic damage state model.

### Materials and Experimental Procedures

The specimens studied in this investigation were constructed of Hercules Type AS/3501-5 graphite/epoxy prepreg. Two quasi-isotropic configurations were studied:  $[0/+45/-45/90]_s$  (referred to as Type I) and  $[0/90/+45/-45]_s$  (referred to as Type II). The Type I laminates had a 28 percent resin content, and the Type II laminates had a 31 percent resin content. The specimen geometry is illustrated in Fig. 1. These two layups are of particular interest because even though large differences in laminate properties exist, laminate plate theory predicts identical in-plane stresses ( $\sigma_x$ ,  $\sigma_y$ , and  $\tau_{xy}$ ). The through-the-thickness normal stresses ( $\sigma_z$ ), however, are quite different for these two laminates. Applying the Pipes and Pagano analysis [3] indicates that under axial tensile loading the  $\sigma_z$  stresses in the Type I laminates are tensile throughout the thickness at the laminate edges, while the largest  $\sigma_z$  stresses in the Type II laminates are compressive [4].

Tests were conducted in quasi-static tension and constant amplitude tension-tension fatigue. All the fatigue tests and a portion of the quasi-static tension tests were run on a 222 400 N (50 000 lb) MTS testing machine. The remaining quasi-static tests were run on a Model 1125 Instron testing machine. The 89 000 N (20 000 lb) capacity machine was run at a constant cross-head displacement rate of 1.3 mm/min (0.05 in./min). All specimens were held using 89 000 N (20 000 lb) Instron wedge grips.

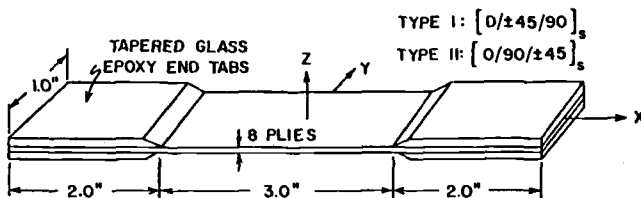


FIG. 1—Specimen configuration.

The general approach was to apply nondestructive test techniques to interrogate the specimens during loading. The goal of the study was to define the physical mechanisms which lead to ultimate failure of the material. Damage development in the form of transverse cracking in all off-axis laminates, longitudinal cracking, and delamination was monitored throughout the tests. Results of the study include a detailed description of the chronology of events leading to failure of the two specimen types.

The bulk of the data reported in this paper was obtained through the microscopic examination of surface replicas. This technique was first used to monitor damage in composite material by Masters and Stalnaker [4,5]. With this procedure it was possible to obtain quickly highly detailed permanent records of the entire specimen edge while the specimen was held at load. This was important because, in the unnotched specimens studied, damage (transverse cracking) was dispersed along the entire specimen edge. A thorough discussion of the technique can be found in Ref 6.

The experimental procedure employed in the monotonic tension tests was quite straightforward. The specimen was mounted in the Instron wedge grips, and an 1100 N (250 lb) tensile load was applied to open any initial cracks which may have resulted from thermal curing or handling. An initial surface replica then was made. (Experience has indicated that these cracks may go undetected if a slight tensile load is not applied first.) Once the initial crack pattern was recorded, tensile ramp loading was continued. The loading subsequently was halted periodically so replicas could be made. The specimen was held at load for approximately 5 min during these periods. Again, once the replication was completed, the ramp loading continued until the next load level was reached, and the replication process was repeated. Loading continued in this manner until specimen failure occurred.

There is no experimental evidence to indicate that this procedure adversely affected the observations. Ultrasonic attenuation remained unchanged and there was no acoustic emission during replication periods.

Fatigue specimens were subjected to 1 000 000 cycles of tension-tension fatigue ( $R = 0.1$ ). These tests were conducted at 15 Hz with a maximum stress level of 275.7 MPa (40 ksi). This stress level was chosen since it would be an upper bound design level, the stress at which first ply failure would occur if thermal residual stresses were neglected. The average ultimate stress measured for Type I laminates was 602 MPa (87 ksi). The average Type II value was 532 MPa (77 ksi).

The experimental procedure for these tests was similar to the static test procedure. The specimen was mounted in the wedge grips, an 1100 N (250 lb) tensile load was placed on the specimen, and an initial replica was made. The specimen was then loaded to mean load ( $P$  mean) and cycled in tension-tension fatigue. As in the static tests, loading was interrupted periodically for surface replication.

### Cumulative Damage Development

Results of the surface replica observations indicate that two distinct damage patterns develop in the specimens depending on the stacking sequence; that is, the damage states in Type I ( $[0/+45/-45/90]_s$ ) and Type II ( $[0/90/+45/-45]_s$ ) materials were reproducible from specimen to specimen and were distinctly different according to specimen type. Surface replication results also indicated that the same damage patterns developed under monotonic tension and tension-tension fatigue loading.

Figure 2 illustrates typical segments of Type I ( $[0/\pm 45/90]_s$ ) and Type II ( $[0/90/\pm 45]_s$ ) laminates at advanced quasi-static load levels. A phenomenological description of the damage development will be presented in this section. Quantitative results will be discussed in a later section.

In the case of both Type I and Type II specimens, damage appeared first in the form of transverse cracking of the 90-deg laminae. These transverse cracks were arrested initially at the lamina interfaces and did not propagate to adjacent plies. As the load increased, cracks appeared almost solely within the 90-deg laminae. From this point on, however, the sequence of events differed.

In the  $[0/+45/-45/90]_s$  (Type I) laminates, the number of transverse cracks in the 90-deg lamina increased until a uniform pattern of periodically spaced cracks was formed over the entire length of the specimen. As the load increased, transverse cracks appeared in the  $-45$ -deg laminae (terminating at the lamina interfaces), again reaching a saturation crack spacing (Fig. 2).

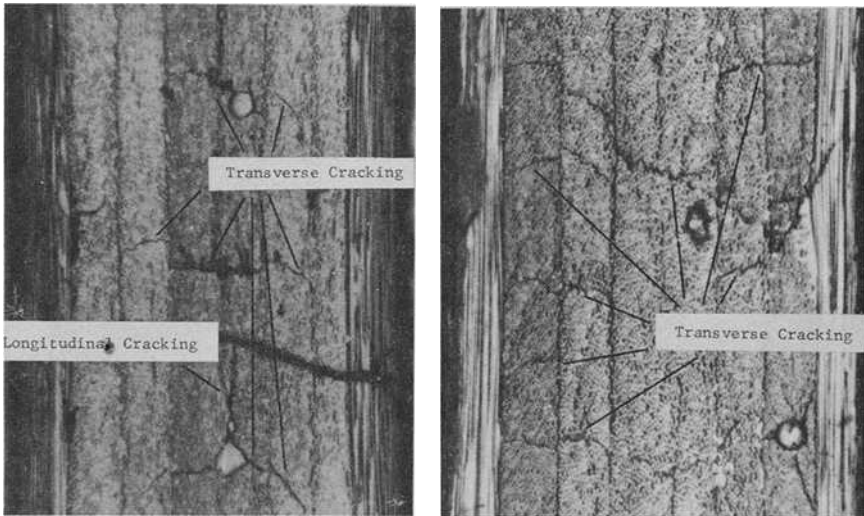


FIG. 2—Photomicrographs of replicas showing details of damage development: (left)  $[0/\pm 45/90]_s$  laminate and (right)  $[0/90/\pm 45]_s$  laminate.

Coincident to this transverse crack extension into the  $-45$ -deg laminae, longitudinal cracks grew from transverse cracks in the  $90$ -deg lamina (Fig. 2). These longitudinal cracks appeared at several locations along the specimen length and propagated axially with increased load. They eventually joined together, linking all  $90$ -deg lamina transverse cracks, and formed one continuous edge delamination which spanned the entire specimen length. The only new damage that appeared from this point to failure was the formation of a few cracks in the  $+45$ -deg laminae. In extending over the specimen length, the longitudinal cracks occasionally "jogged" to the  $90/-45$ -deg interface and then "jogged" back to the interior of a  $90$ -deg lamina or to the central  $90/90$ -deg lamina interface, as shown in Fig. 3. As the loading was increased, the central delamination opened further; that is, it extended from the edges toward the center of the specimen. This delamination never fully propagated across the specimen width prior to failure, however.

Damage in the  $[0/90/+45/-45]_s$  (Type II) specimens also began with transverse cracking that initially spanned only the  $90$ -deg lamina. These cracks were much more numerous (that is, the saturation spacing was much smaller) in the Type II specimens than in the Type I specimens. As load increased, transverse cracks appeared in all of the remaining off-axis laminae. This was particularly evident at elevated load levels (Fig. 2).

In general, each off-axis lamina in the Type II specimens appeared to seek independently to achieve a saturation crack spacing before ultimate specimen failure occurred. In contrast to the Type I specimens, negligible longitudinal cracking appeared in the Type II specimens. It existed only in short segments at one or two locations in the  $90$ -deg laminae along the specimen length (Fig. 2) and has been attributed to local material defects [7].

As stated earlier, comparable damage states developed under quasi-static tension and tension-tension fatigue. The sequence of damage development in the fatigue specimens follows the description given previously. Examination of the surface replicas indicates that comparable damage states existed in fa-

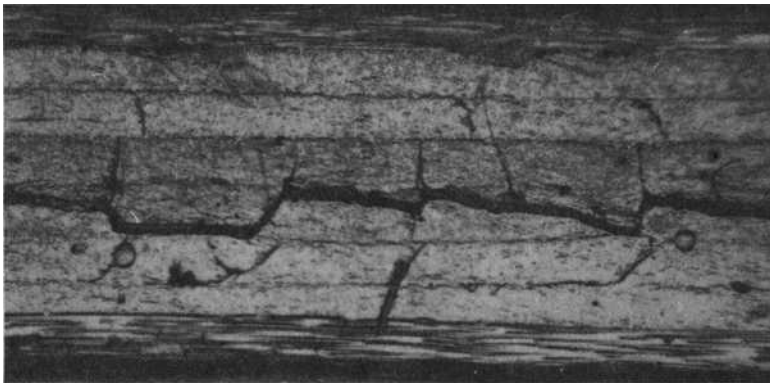


FIG. 3—Longitudinal cracking in  $[0/\pm 45/90]_s$  laminate.

tigue specimens after one-half cycle (that is, when loaded from zero to  $P_{max}$ ) and in statically loaded specimens at equivalent load levels. However, when fatigue cycling continued, additional cracks formed as a function of additional cycles of loading. The type of cracks that form (that is, the type of laminae that develop cracks) is controlled by the load level, but the number of cracks increases for successive cycles of loading at that level until a saturation number of cracks is reached in the individual laminae.

There were, however, two significant features in the Type I fatigue damage sequence that did not appear in the static loading case. The first was the presence of significant damage in the +45-deg laminae. No significant damage was noted in these laminae in the static tests. It should be noted, however, that although significant numbers of cracks appeared in these laminae and crack spacing values appeared to be stabilizing, saturation was not attained at 1 000 000 cycles. The second difference was the presence of delamination at the +45/-45-deg lamina interfaces, shown in Fig. 4. While a "forked" crack-+45/-45-deg delamination pattern was noted in the static results, the delaminations caused by fatigue loading were much longer.

Similarly, although no significant delaminations or longitudinal cracks appeared in the statically loaded Type II specimens, delaminations at the +45/-45-deg lamina interfaces were evident in the fatigue loaded specimens, shown in Fig. 5. These delaminations were seen in several segments along the specimen edge and appeared to grow from a transverse crack in one 45-deg lamina to a transverse crack in the adjacent 45-deg lamina. In many instances, these delaminations were the final link in a crack pattern that extended from one 90-deg lamina to the other, crossing the whole laminate edge [8].

Figure 6 presents a diiodobutate (DIB) enhanced radiograph of Specimen I-15 after it has been subjected to 1 000 000 fatigue cycles. It illustrates sev-

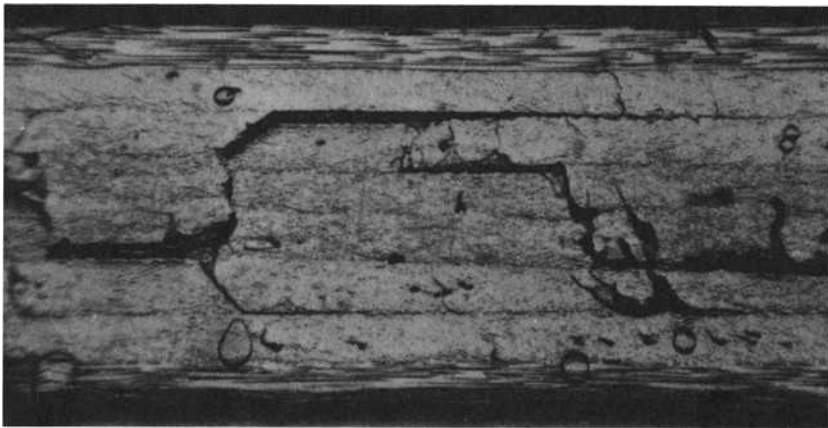


FIG. 4—Fatigue damage features in  $[0/\pm 45/90]_s$  laminate.

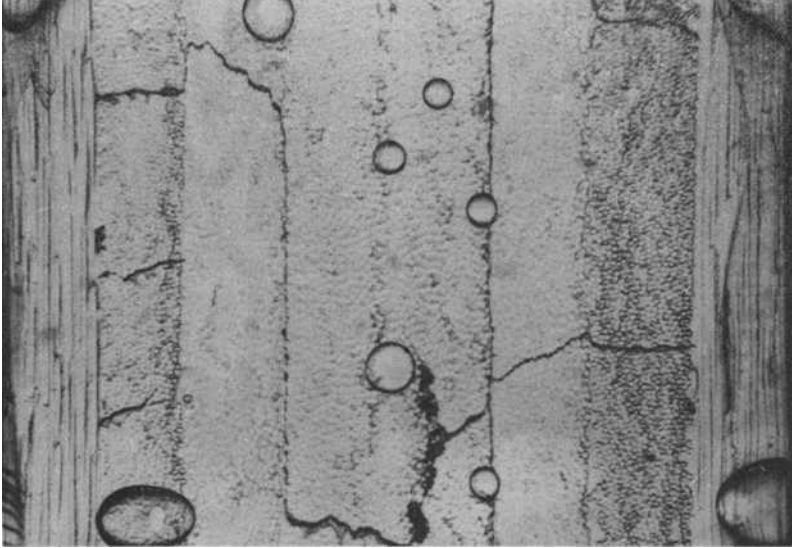


FIG. 5—Fatigue damage features in  $[0/90/\pm 45]_s$  laminate.

eral key features which confirm damage development observations made via the edge replication technique. The existence of a characteristic damage state is verified by the uniform damage pattern observed over the whole specimen length. A periodic crack spacing is seen in all of the off-axis (that is,  $90$ ,  $+45$ , and  $-45$ -deg) laminae. The extent of delamination from the specimen edge into the center is also evident. Transverse cracks are oriented at  $90$ ,  $+45$ , and  $-45$ -deg, indicating that they propagate along the fibers (that is, fibers are not broken in this stage of damage development). This has been verified through microscopic investigation of sectioned specimens [6]. The radiograph also shows that these cracks transverse the entire specimen width, indicating that the damage observed at the specimen edge via surface replication is representative of damage in the specimen interior.

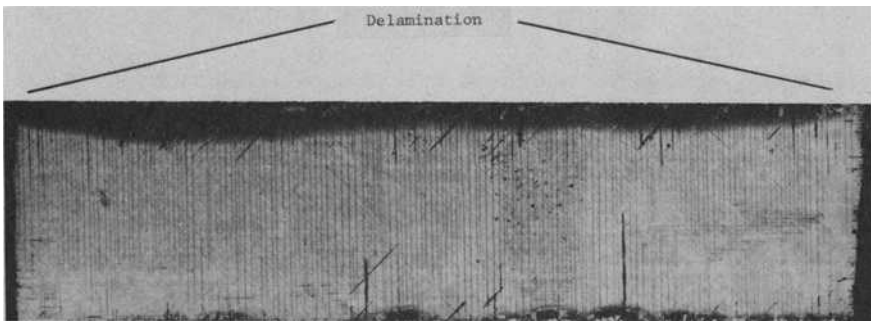


FIG. 6—DIB enhanced X-ray radiograph of  $[0/\pm 45/90]_s$  fatigue specimen.

**Static Test Results**

A quantitative description of the cumulative damage/saturation spacing development observed in quasi-static tension tests will be presented in this section. Information defining the observed cumulative damage development is reported in terms of crack spacing. This can be interpreted physically as the average distance between transverse cracks. These values were obtained by scanning the replicas of the specimen edges on a metallograph and counting the number of transverse cracks in each lamina. The average crack spacing distance then was computed by dividing the lamina length by the total number of transverse cracks in the lamina. This is equivalent to physically measuring the distance between each crack and taking the numerical average. To simplify the data presentation, the numerical average of the two crack spacing values obtained (one for each 90, +45, and -45-deg lamina) will be reported. Data which demonstrate the validity of these procedures is available in Ref 6. Due to space limitations, it will not be presented here.

Figure 7 illustrates the damage development in  $[0/\pm 45/90]_s$  Specimen I-6. Loading was halted at 520 MPa (76 ksi) and the specimen was sectioned so that the internal damage could be recorded. Several fundamental characteristics of damage development in tensile loaded  $[0/\pm 45/90]_s$  laminates can be seen in the figure. First, there was no appreciable damage in the +45-deg lamina. This was true of all specimens tested, even those loaded to failure. The figure also demonstrates that transverse cracks appear first in the 90-deg lamina and that, in the 90-deg lamina, spacing values near the final saturation spacing values are attained very early in the loading. Saturation was attained at 415 MPa (60 ksi), but at 277 MPa (40 ksi) the crack spacing was 90

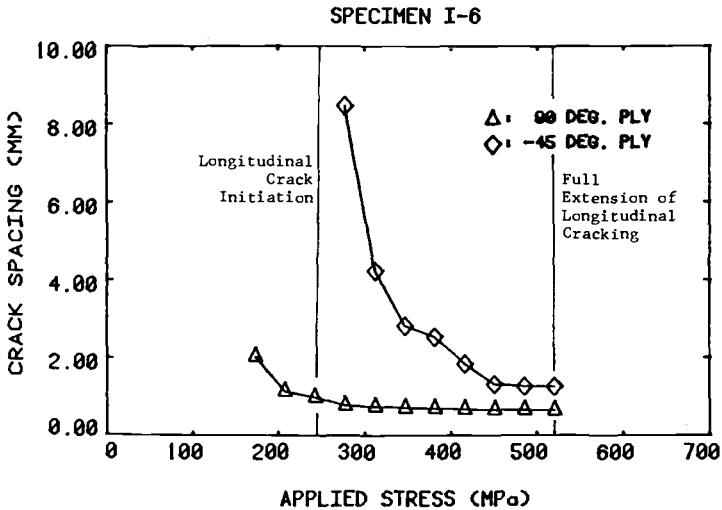


FIG. 7—Damage development in  $[0/\pm 45/90]_s$  Specimen I-6.

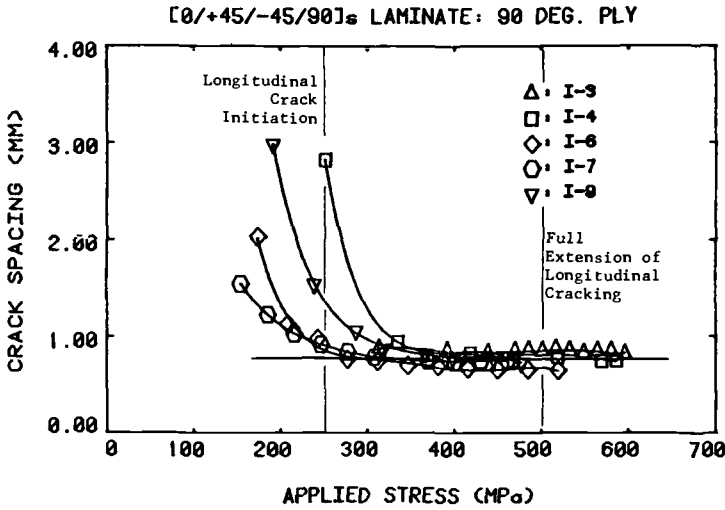


FIG. 8—Damage development in 90-deg plies of  $[0/\pm 45/90]_s$  laminates.

percent of the saturation level. Saturation spacing was not attained in the  $-45$ -deg lamina until 450 MPa (65 ksi). The replicas also indicated that longitudinal cracking was first evident at 242 MPa (35 ksi). When loading was halted at 520 MPa (76 ksi), it had just reached full extension over the entire specimen length.

To demonstrate the reproducibility of the damage development, the crack spacing versus applied stress histories of five  $[0/\pm 45/90]_s$  (Type I) specimens have been plotted in Figs. 8 and 9. Two of the specimens were tested under controlled load. The remaining three were tested under controlled displace-

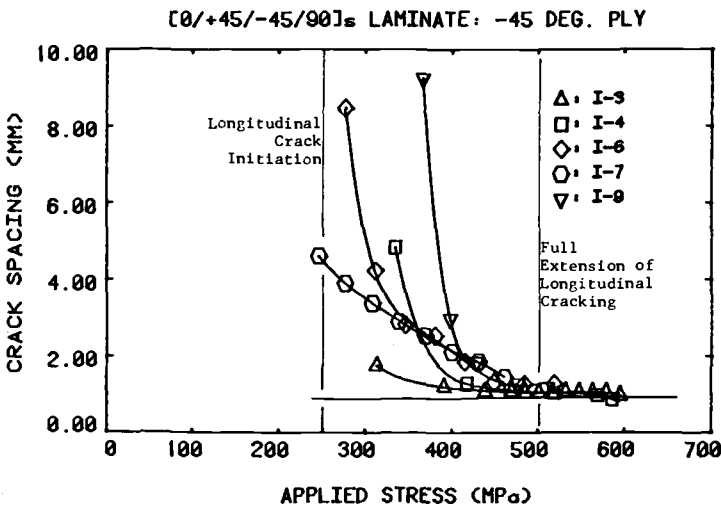


FIG. 9—Damage development in  $-45$ -deg plies of  $[0/\pm 45/90]_s$  laminates.

ment. The horizontal lines in each figure represent values predicted earlier by Reifsnider using a modified shear-lag analysis [9]. This analysis will be discussed further in the Appendix.

Figure 8 illustrates the results obtained for the 90-deg laminae. Saturation spacing was attained in all specimens. The initial portions of the curves differ in slope, and crack spacing values differ at low stress levels. (The stress level at which cracking begins in each lamina was not determined.) However, all the curves coalesced to the same approximate crack spacing. The average spacing was  $0.756 \pm 0.06$  mm ( $0.029 \pm 0.002$  in.). This spacing was obtained at an average stress level of  $402 \pm 8$  MPa (58 ksi). Figure 9 shows the crack spacings in the -45-deg laminae for the same five Type I specimens. The same observations apply; despite initial variances, the curves coalesced to a common value. The average saturation spacing in the -45-deg lamina was  $1.12 \pm 0.17$  mm ( $0.044 \pm 0.006$  in.) attained at an average stress level of  $485 \pm 70$  MPa (70 ksi).

Also shown in the figures are the average stress levels for longitudinal crack initiation and complete crack extension. The initiation level,  $247 \pm 35$  MPa (36 ksi), is defined as the average stress level at which longitudinal cracks first appeared, initiating at 90-deg transverse cracks (Fig. 2). The full extension level,  $493 \pm 71$  MPa (71 ksi), is the average stress level at which these separate longitudinal cracks first join together to form a continuous edge delamination. The investigators did not observe any influence of this longitudinal cracking/delamination on the transverse crack development. However, this possibility was not thoroughly investigated.

We now turn our attention to the Type II,  $[0/90/+45/-45]_s$  laminates. Figure 10 traces the development of the saturation spacings for the 90, +45,

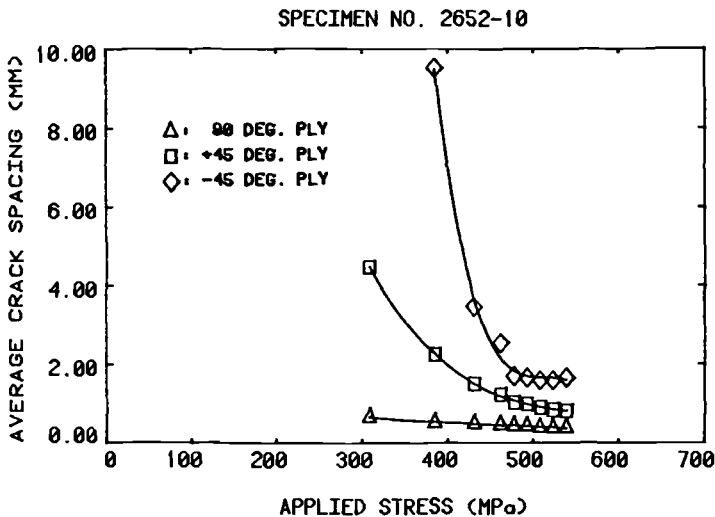


FIG. 10—Damage development in  $[0/90/\pm 45]_s$  Specimen 2652-10.

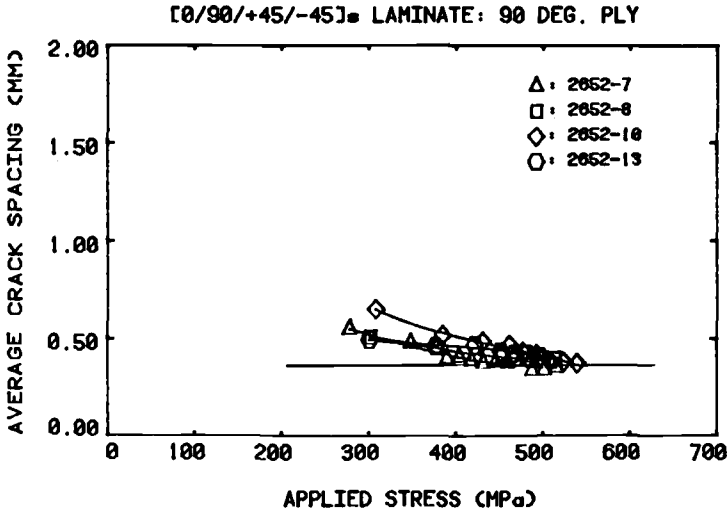


FIG. 11—Damage development in 90-deg plies of  $[0/90/\pm 45]_s$  laminates.

and  $-45$ -deg laminae of Specimen 2652-10 [loaded to failure at 570 MPa (83 ksi)]. The figure demonstrates that transverse cracking again appears first in the 90-deg laminae, and shows that saturation spacing was achieved for the 90 and  $-45$ -deg fiber orientations. The 90-deg lamina curves are quite flat, indicating that crack spacings comparable to saturation values were attained early in the loading. The curves for the other two ply orientations demonstrate that although cracking appears at higher loads, it rapidly approaches saturation.

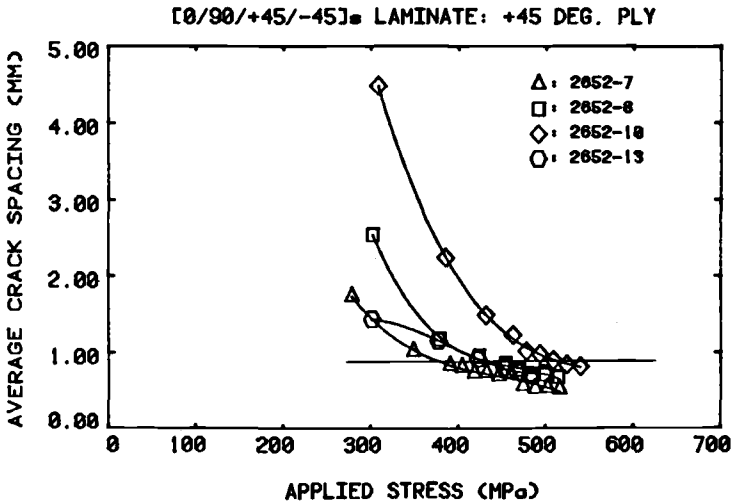


FIG. 12—Damage development in  $+45$ -deg plies of  $[0/90/\pm 45]_s$  laminates.

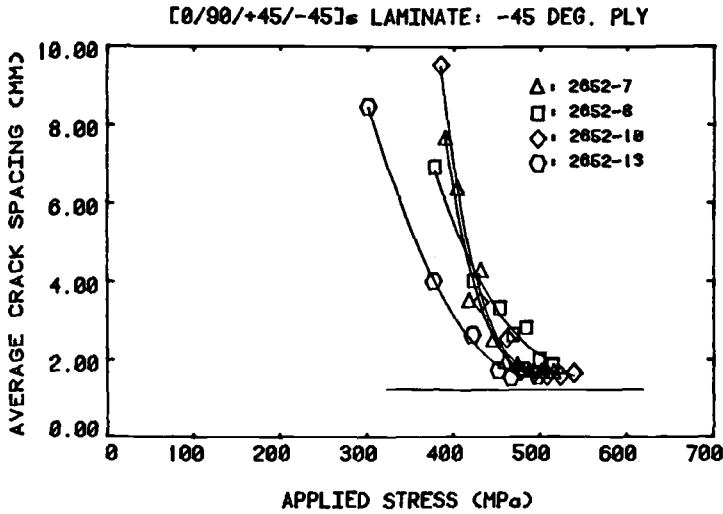


FIG. 13—Damage development in -45-deg plies of [0/90/±45]<sub>s</sub> laminates.

The results of four typical quasi-static tension tests are plotted in Figs. 11, 12, and 13. All laminates were loaded to failure. The average ultimate stress was  $532 \pm 24$  MPa (77 ksi). The horizontal lines in each figure represent the values predicted from the modified shear lag analysis [9]. Again the figures demonstrate the consistency of the characteristic saturation spacing values from specimen to specimen. Although some variance is seen in the initial portions of the curves, crack spacing values coalesce to the characteristic crack spacing values for the 90 and -45-deg lamina. The average crack spacings were  $0.393 \pm 0.016$  mm ( $0.0154 \pm 0.0006$  in.) and  $1.64 \pm 0.10$  mm ( $0.0645 \pm 0.004$  in.), respectively. The saturation spacings in the +45-deg lamina were disrupted by crack growth from ply to ply prior to failure.

As in the case of the Type I specimens, it must be emphasized that in the Type II 90-deg lamina, crack spacing values near to saturation values were attained at relatively low loads. Although cracking first appears in the 90-deg lamina of both specimen types, a comparison of these average stress levels also reveals that damage occurs at a much lower stress level in the Type I 90-deg lamina than in the Type II 90-deg lamina. The average saturation stress level was 471.5 MPa (68 ksi) for Type II specimens versus 402.2 MPa (58 ksi) for Type I specimens. The average saturation stress levels for the -45-deg lamina were similar, however, with 485.6 MPa (70 ksi) for Type I and 473 MPa (69 ksi) for Type II specimens.

**Fatigue Test Results**

As noted earlier, the fatigue specimens demonstrated damage development sequences which were very similar to those observed in the static specimens.

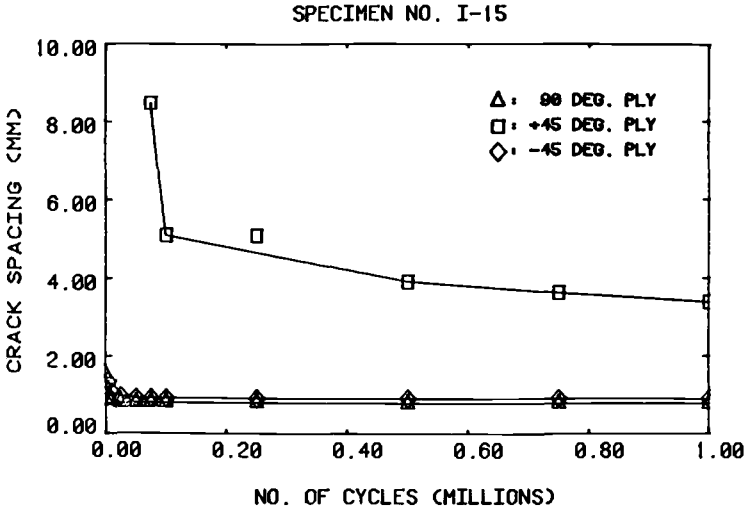


FIG. 14—Fatigue damage development in  $[0/\pm 45/90]_s$  Specimen I-15.

The data in Fig. 14 represent typical crack development in a Type I laminate subjected to tension-tension fatigue loading. The figure shows that the crack spacings in the 90 and  $-45$ -deg plies again reach a saturation spacing. The crack spacing in the 90-deg plies for three Type I,  $[0/\pm 45/90]_s$  specimens has been plotted versus cycles of loading in Fig. 15. The ordinate has been expanded to impart a better representation of the relative scatter of the data. While a small variability is seen in the data for the early parts of the tests, the crack spacings of each specimen remain stable through the majority

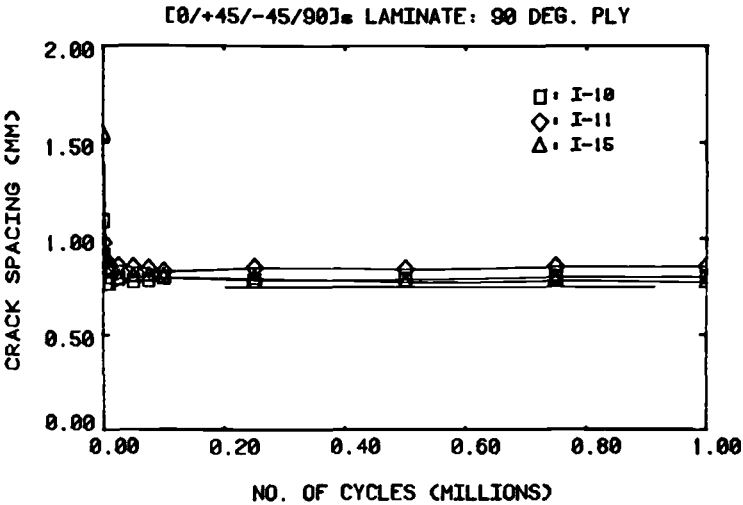


FIG. 15—Fatigue damage development in 90-deg plies of  $[0/\pm 45/90]_s$  laminates.

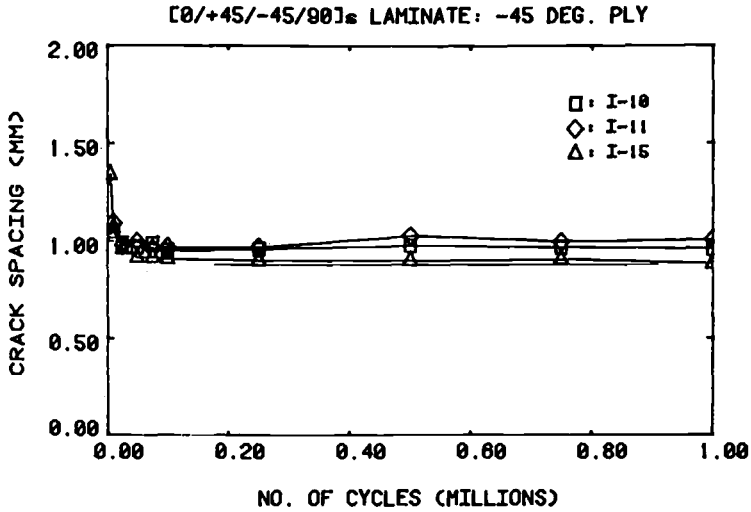


FIG. 16—Fatigue damage development in -45-deg plies of  $[0/\pm 45/90]_s$  laminates.

of the fatigue life. The average final crack spacing value was  $0.802 \pm 0.08$  mm ( $0.032 \pm 0.003$  in.). Figure 16 is a similar plot for the -45-deg plies of the same specimens. The same observations as to the stability of the saturation crack spacing at advanced cycles may be made for this data [the average value here was  $0.959 \pm 0.13$  mm ( $0.0377 \pm 0.005$  in.)]. Finally, the same general behavior was noted in the +45-deg lamina data shown in Fig. 17. When cycling was halted at 1 000 000 cycles, an equilibrium spacing was not achieved. However, the test data again show good consistency [the average

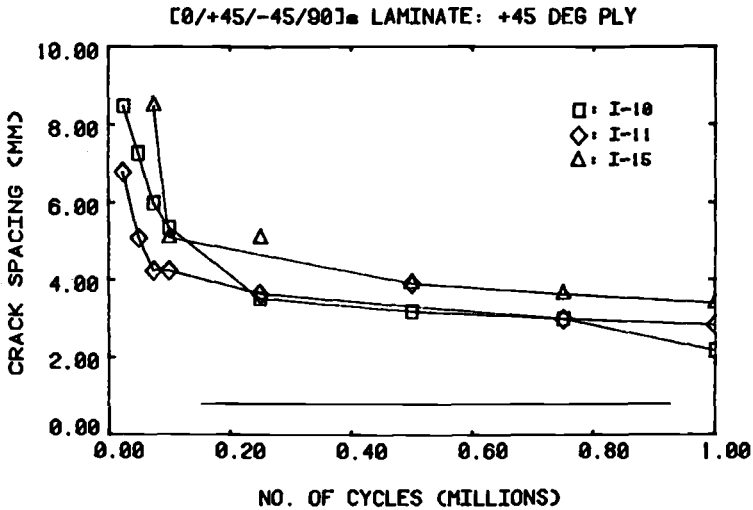


FIG. 17—Fatigue damage development in +45-deg plies of  $[0/\pm 45/90]_s$  laminates.

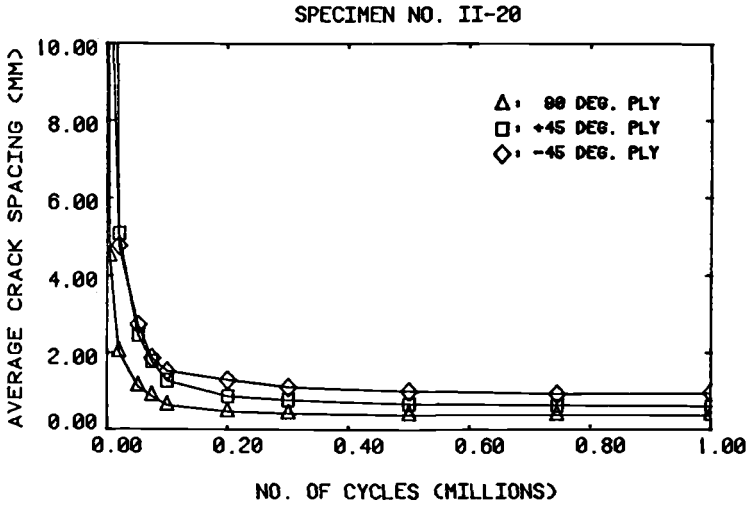


FIG. 18—Fatigue damage development in  $[0/90/\pm 45]_s$  Specimen II-20.

spacing was  $3.20 \pm 0.20$  mm ( $0.126 \pm 0.0078$  in.). The predicted saturation spacing is below the data since the crack spacing is still changing.

Consider now the  $[0/90/\pm 45]_s$  laminates. Figure 18 displays the crack development history of a typical Type II laminate subjected to tension-tension fatigue loading. All three off-axis plies reach a stable (regular) crack spacing. To compare the crack spacings in the various lamina of three specimens, the values again have been separated and plotted versus the number of cycles. These plots are seen in Figs. 19 through 21. The horizontal lines in these figures represent the analytically predicted saturation spacings. The saturation crack spacing varies little from specimen to specimen. The average values

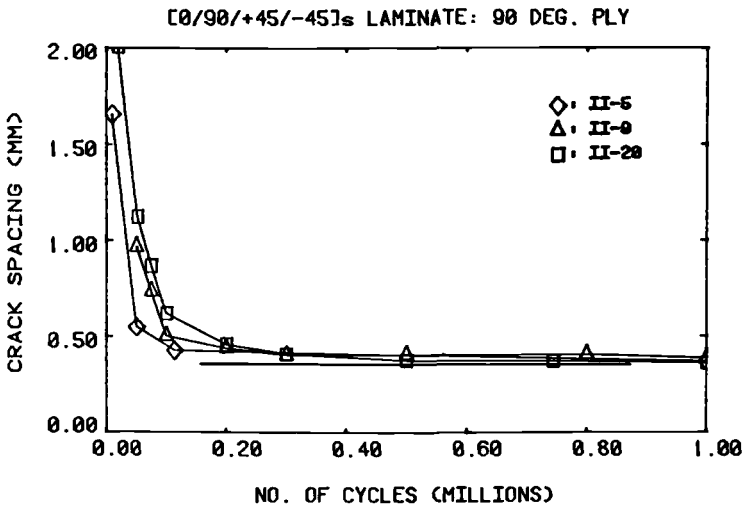


FIG. 19—Fatigue damage development in 90-deg plies of  $[0/90/\pm 45]_s$  laminates.

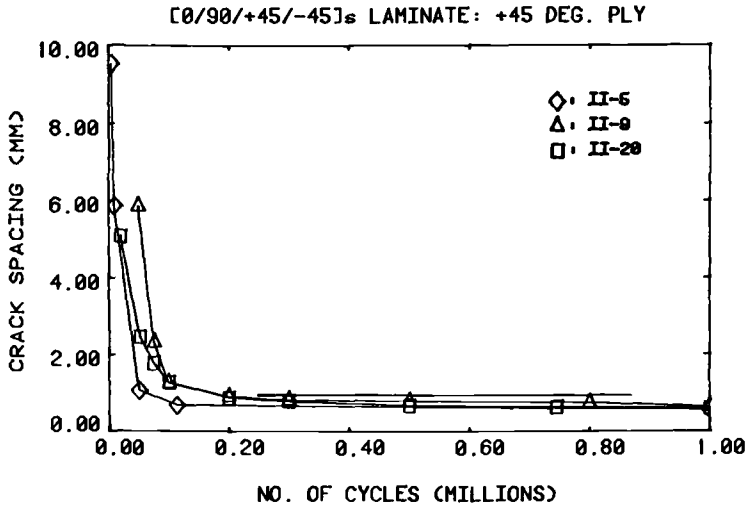


FIG. 20—Fatigue damage development in +45-deg plies of [0/90/±45]<sub>s</sub> laminates.

are  $0.380 \pm 0.018$  mm ( $0.0149 \pm 0.0007$  in.),  $0.639 \pm 0.093$  mm ( $0.0252 \pm 0.0004$  in.), and  $1.06 \pm 0.120$  mm ( $0.0419 \pm 0.0047$  in.) for the 90, +45, and -45-deg lamina, respectively.

**Summary of Experimental Results**

The significant feature observed consistently throughout this investigation was, in the opinion of the authors, the development of the unique saturation crack spacing in the off-axis laminae. Table 1 lists the average saturation

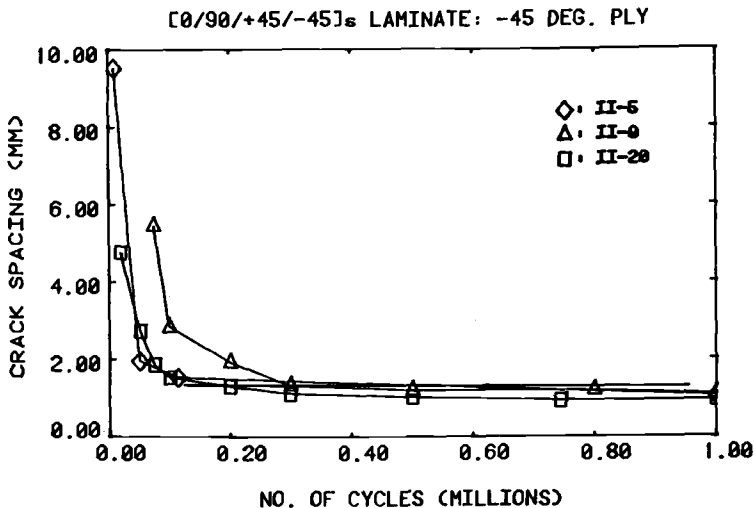


FIG. 21—Fatigue damage development in -45-deg plies of [0/90/±45]<sub>s</sub> laminates.

TABLE 1—Saturation crack spacing, mm.

	Lamina	Type Loading		Predicted Value
		Quasi-Static	Fatigue	
Type I	[0/+45/-45/90] <sub>s</sub>			
	90	0.756 ± 0.06	0.802 ± 0.08	0.760
	+45	... <sup>a</sup>	3.201 ± 0.20	0.755
	-45	1.12 ± 0.17	0.959 ± 0.13	0.879
Type II	[0/90/+45/-45] <sub>s</sub>			
	90	0.393 ± 0.016	0.380 ± 0.018	0.363
	+45	0.737 ± 0.059	0.639 ± 0.093	0.875
	-45	1.64 ± 0.10	1.06 ± 0.120	1.21

<sup>a</sup> Negligible damage observed, spacing not computed.

crack spacings attained under both quasi-static and fatigue loading for all the specimens studied. Several observations can be made from this table relevant to the nature of damage development in the laminates. The variance in the experimentally determined saturation spacing values is generally quite small, indicating that the values were reproducible from specimen to specimen. A second observation is that the saturation spacing values for the two laminates ([0/±45/90]<sub>s</sub> and [0/90/±45]<sub>s</sub>) are distinctly different. Finally, the table demonstrates that equivalent saturation spacings were developed under quasi-static tension and tension-tension fatigue in both laminates.

Further evidence of the reproducibility of this saturation spacing phenomenon is seen in Figs. 22 and 23. The figures demonstrate the insensitivity of the saturation spacing to cyclic load frequency. These figures compare the crack spacing versus applied fatigue cycle data obtained in this study with data from Stalnaker's study [4]. In that study, specimens identical to those used for the present study were cycled to the same 275 MPa (40 ksi) stress level in tension-tension fatigue ( $R = 0.1$ ) but at a frequency of 1 Hz (versus 15 Hz used in this study). The figures demonstrate that equivalent crack spacings were observed in both studies. However, these crack spacings were reached after (1000 cycles in Stalnaker's 1 Hz tests as compared to 1 000 000 cycles in this study). This indication of a fatigue frequency effect on the rate of damage development is consistent with the observations of Sendeckyj [10], Sun [11], and Reifsnider et al [12,13].

## Conclusions

The cumulative damage data developed in this study indicated that the [0/±45/90]<sub>s</sub> and [0/90/±45]<sub>s</sub> graphite epoxy laminates developed two distinctly different crack patterns. These patterns were created by the formation of transverse cracks with a regular spacing (a saturation spacing) in each off-axis lamina. Examination of the data reveals that this spacing is unique for

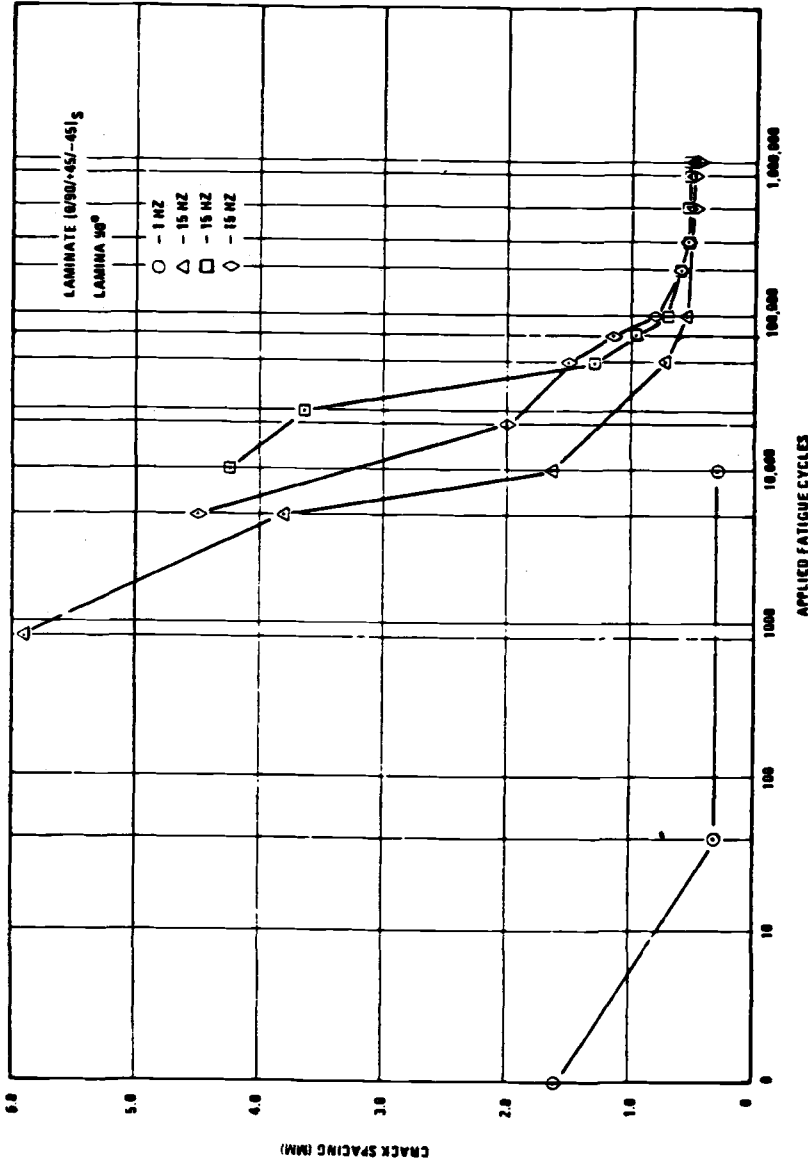


FIG. 22—Frequency dependence of damage development in 90-deg plies of [0/90/±45]<sub>s</sub> laminates.

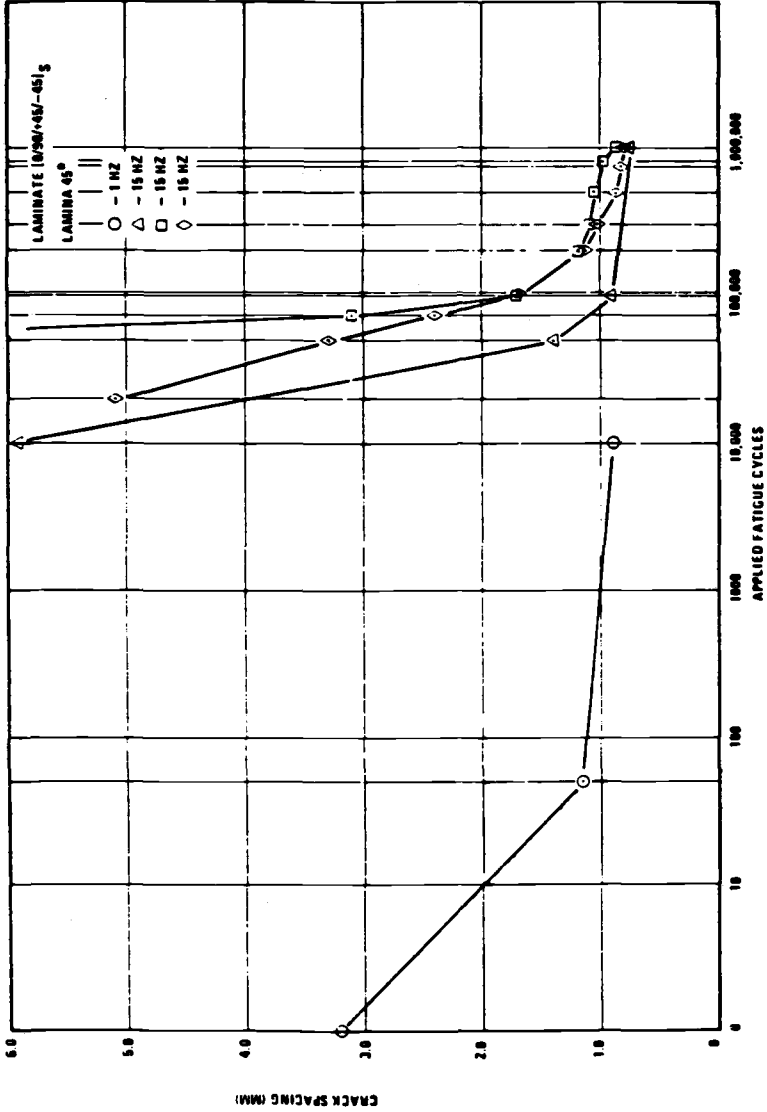


FIG. 23—Frequency dependence of damage development in 45-deg plies of [0/90/±45]<sub>s</sub> laminates.

each lamina in the laminate. The data also show that the saturation spacing values are highly reproducible from specimen to specimen.

This spacing is not merely a characteristic of fiber orientation. Laminae in  $[0/\pm 45/90]_s$  specimens had saturation crack spacing values that differed from the values observed in corresponding laminae in  $[0/90/\pm 45]_s$  specimens (for example, saturation spacings in 90-deg plies of Type I and Type II laminates were quite different). The crack spacings were different even though laminated plate theory predicts identical stresses in the individual plies.

A comparison of the edge replicas of specimens subjected to quasi-static tension and tension-tension fatigue indicated that the saturation crack spacings are independent of load history. Identical damage states were formed under high static stresses and repeated cycles at lower stress levels.

The saturation crack patterns observed are characteristic damage states in the sense that they are well-defined, unique damage patterns that are characteristic of a given laminate, independent of loading history. Such a well-defined physical situation is amenable to well-set modeling, as we have suggested by comparisons to a simple model published earlier. However, the characteristic damage state is a wholly physical situation which our observations suggest is generic for the type of matrix cracking discussed in this investigation of this type of graphite epoxy composite laminates.

## APPENDIX

A brief summary of the one-dimensional analysis used to predict saturation crack spacings cited in the text is presented below.

Figure 24 shows an edge view of a laminate divided into three regions. The center region of width  $a$  represents a cracked ply; the regions on either side of width  $c$  represent

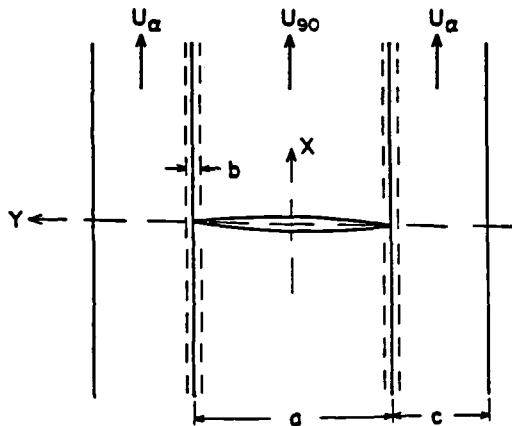


FIG. 24—Schematic diagram of a crack in the center plies of a laminate (edge view).

the adjacent region of influence, and the remainder of the specimen thickness consists of the material beyond these two regions. For purposes of illustration, we take the broken region to be the 90-deg plies of a  $[0/\pm 45/90]_s$  graphite epoxy laminate. Consider the equilibrium of an element  $dx$  long, with unit thickness, representing a region just above or below the crack plane in Fig. 24. A simple force balance is written including only stress components thought to be important, with two shear stress components on either side of the element representing the action of the constraint layers and an axial normal stress component within the element in this case. The resulting equation is

$$aE_{x90} \frac{d^2 U_{90}}{dx^2} + 2G \left( \frac{U_{45} - U_{90}}{b} \right) = 0 \quad (1)$$

where  $E_{x90}$  is the uniaxial engineering stiffness of the 90-deg ply in the  $x$  direction,  $G$  is the engineering shear stiffness of the matrix material,  $U_{90}$  is the average  $X$  displacement of the 90-deg ply at a given point, and the stress transfer region dimension  $b$  has been used to write the constraining forces in difference form. For the constraint layers, an equilibrium element also can be constructed having width  $c$  and axial displacement  $U$  as shown in Fig. 24. The resulting equilibrium equation is

$$CE_{x\alpha} \frac{d^2 U_\alpha}{dx^2} + \frac{G}{b} (U_{90} + U^0 - 2U_\alpha) = 0 \quad (2)$$

where  $E_{x\alpha}$  is the uniaxial engineering stiffness of the constraint layer,  $U^0$  is the undisturbed laminate displacement, and  $U$  is the average displacement in the constraint layer. In normalized form Eqs 1 and 2 take the form

$$A \frac{d^2 U_{90}}{dx^2} + U_\alpha - U_{90} = 0 \quad \text{and} \quad B = \frac{d^2 U_\alpha}{dx^2} + U_{90} + x - 2U_\alpha = 0 \quad (3)$$

where

$$A = \frac{b}{2a} \frac{E_{x90}}{E_{LM}} \quad \text{and} \quad B = \frac{bc}{a^2} \frac{E_{x\alpha}}{E_{LM}}$$

for this case where  $E_{LM}$  is the laminate modulus. The appropriate boundary conditions require that

$$\frac{dU_{90}}{dx} (x \rightarrow \infty) = 1 \quad \frac{dU_\alpha}{dx} (x \rightarrow \infty) = 1 \quad (4)$$

$$\frac{dU_{90}}{dx} (x = 0) = 0 \quad U_\alpha (x = 0) = 0 \quad (5)$$

Solutions to Eqs 4, as well as a large class of similar equations, are obtained easily and are available from such familiar situations as the coupled oscillator problem. For our purpose, we choose solutions of the form

$$U_{90} = x + C_1 e^{-\alpha x} + C_2 e^{-\beta x} \quad \text{and} \quad U_\alpha = x + D_1 C_1 e^{-\alpha x} + D_2 C_2 e^{-\beta x} \quad (6)$$

From these results, the normal stress in the plies and the shear stress can be approximated. A normalized plot of the normal stress in the broken ply is shown in Fig. 25. Beginning from a vanishing value at the free face of the crack, the stress rises to the level of stress that existed in the unbroken material. The saturation crack spacing is estimated by postulating that the shortest distance from the existing crack to a position where a new crack can form is the distance from the existing crack to the position where the normal stress just reaches the undisturbed value (which formed the

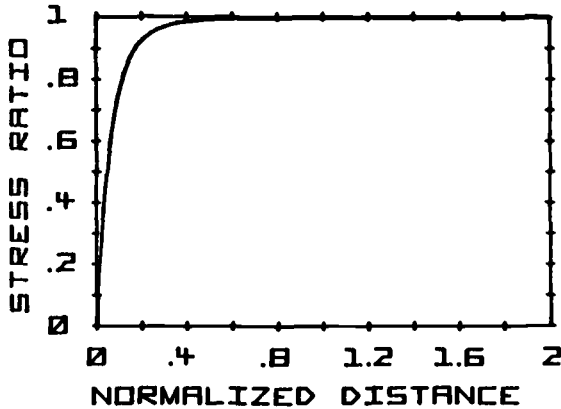


FIG. 25—Stress distributions in a cracked  $[0/\pm 45/90]_s$  laminate.

first crack). Such a position is suggested by a dotted line in Fig. 25. Since that distance is the shortest such distance possible, when crack spacings reach that level they should become stable, corresponding to the saturation spacings observed. Correlations with experimental data have been published previously [4-6,9,14]. Other formulations including a three-dimensional finite difference analysis are discussed in other sources [8,15].

## References

- [1] Pipes, R. B. in *Nondestructive Evaluation and Flaw Criticality for Composite Materials*, ASTM STP 696, American Society for Testing and Materials, 1979, pp. 1-2.
- [2] Stinchcomb, W. W. in *Nondestructive Evaluation and Flaw Criticality for Composite Materials*, ASTM STP 696, American Society for Testing and Materials, 1978, pp. 355-356.
- [3] Pipes, R. B. and Pagano, N. J., *Journal of Composite Materials*, Oct. 1970, pp. 538-548.
- [4] Stalnaker, D. O. and Stinchcomb, W. W. in *Composite Materials: Testing and Design (Fifth Conference)*, ASTM STP 674, American Society for Testing and Materials, 1979, pp. 620-641.
- [5] Reifsnider, K. L. and Masters, J. E., "Investigation of Characteristic Damage States in Composite Laminates," American Society of Mechanical Engineers (ASME) Winter Annual Meeting, San Francisco, Calif., 1978.
- [6] Masters, J. E., "An Experimental Investigation of Cumulative Damage Development in Graphite Epoxy Laminates," Ph.D. dissertation, Materials Engineering Science Department, Virginia Polytechnic Institute, 1980.
- [7] Reifsnider, K. L., Henneke, E. G., and Stinchcomb, W. W. in *Composite Materials: Testing and Design (Fourth Conference)*, ASTM STP 617, American Society for Testing and Materials, 1977, pp. 93-105.
- [8] Reifsnider, K. L. and Talug, A., *International Journal of Fatigue*, Nov. 1979, pp. 3-11.
- [9] Reifsnider, K. L., "Some Fundamental Aspects of the Fatigue and Fracture Response of Composite Materials," *Proceedings of the 14th Annual Meeting of Society of Engineering Science*, Lehigh University, Bethlehem, Pa., 14-16 Nov. 1977.
- [10] Sendeckyj, G. P. and Stalnaker, H. D. in *Composite Materials: Testing and Design (Fourth Conference)*, ASTM STP 617, American Society for Testing and Materials, 1977, pp. 39-52.
- [11] Sun, C. T. and Chan, W. S. in *Composite Materials: Testing and Design (Fifth Conference)*, ASTM STP 674, American Society for Testing and Materials, 1979, pp. 418-430.
- [12] Reifsnider, K. L., Stinchcomb, W. W., and O'Brien, T. K. in *Fatigue of Filamentary Composite Materials*, ASTM STP 636, American Society for Testing and Materials, 1977, pp. 171-184.

- [13] Reifsnider, K. L. and Henneke, E. G. in *Stochastic Problems in Mechanics*, University of Waterloo Press, 1974, pp. 355-367.
- [14] Reifsnider, K. L., Henneke, E. G., and Stinchcomb, W. W., "Defect-Property Relationships in Composite Laminates," AFML Technical Report 76-81, Final Report, Air Force Materials Laboratory, June 1979.
- [15] Reifsnider, K. L. and Highsmith, A. in *Materials Experimentation and Design: Fatigue '81*, Wesbury House, 1981, pp. 246-260.

# Effects of Moisture, Residual Thermal Curing Stresses, and Mechanical Load on the Damage Development in Quasi-Isotropic Laminates

---

**REFERENCE:** Kriz, R. D. and Stinchcomb, W. W., "Effects of Moisture, Residual Thermal Curing Stresses, and Mechanical Load on the Damage Development in Quasi-Isotropic Laminates," *Damage in Composite Materials, ASTM STP 775*, K. L. Reifsnider, Ed., American Society for Testing and Materials, 1982, pp. 63-80.

**ABSTRACT:** This investigation demonstrates how moisture absorbed in [0/±45/90]<sub>s</sub> and [0/90/±45]<sub>s</sub> graphite epoxy laminates significantly alters the stress state and chronology of damage development along the laminate edge during static tension and tension-tension cyclic loading.

Emphasis is placed on using reasonable approximations for wet and dry elastic properties, including out-of-plane properties ( $\nu_{23}$  and  $G_{23}$ ), since these properties are required by finite element and shear lag models to predict the stress state at the laminate edge.

Moisture was observed to alter the dry edge stress state in the 90-deg plies of the [0/±45/90]<sub>s</sub> laminate such that delaminations occurred at a lower load and transverse cracks occurred at a higher load. A model was developed which predicted the differences in loads required to initiate damage in the 90-deg plies of the two laminates in the wet and dry conditions.

Although moisture can alter the chronology of damage development, the damage state in each laminate observed prior to fracture appeared to be independent of moisture content.

**KEY WORDS:** composite materials, graphite epoxy, damage, characteristic damage state, moisture absorption

Recent emphasis on environmental degradation of graphite epoxy fiber-reinforced composites is due to the increased use of these materials in structures exposed to atmospheric moisture. The accumulative moisture absorbed by graphite epoxy when exposed to in-service environments [1]<sup>3</sup> is significant

<sup>1</sup> Postdoctoral research associate, Fracture and Deformation Division, Department of Commerce, National Bureau of Standards, Boulder, Colo. 80303.

<sup>2</sup> Professor, Department of Engineering Science and Mechanics, Virginia Polytechnic Institute and State University, Blacksburg, Va. 24061.

<sup>3</sup> The italic numbers in brackets refer to the list of references appended to this paper.

in terms of reduced lamina properties which are related to the degradation of the matrix and fiber/matrix interface [2,3].

The experimental and analytic techniques used in this investigation are based on observations from previous investigations [4,5,6], which are that damage first occurs at the laminate edge and that the subsequent development of damage at the edge prior to fracture can be characterized as a stable pattern of ply cracks. The concept of a characteristic damage state (CDS), defined as a predictable pattern of ply cracks, first was introduced by Reifsnider et al [7,8,9] as a laminate property which exists prior to fracture. Definition of the CDS is facilitated by a shear lag model which predicts the spacing of cracks that develop after the first ply failure. The damage state observed prior to failure is unique for each laminate stacking sequence.

Variations in stacking sequence can have a substantial effect on the laminate strength as demonstrated by Crossman [10]. From a damage state viewpoint, these variations in laminate strengths are related to the stress concentration of each unique damage state on the unbroken 0-deg ply.

Moisture not only affects the strength of individual plies, but also can have a unique influence on the laminate strength by altering the dry residual stress state such that, when quasi-statically loaded, the first formation of damage and subsequent CDS development could be altered and change the 0-deg ply stress concentration.

Although it is necessary to investigate further the influence of the CDS on laminate fracture strength, the effort in this investigation is to define the CDS better with respect to the effects of moisture.

From a damage state viewpoint the objective of this investigation was to demonstrate how moisture can alter the dry residual stress state and the development of a CDS in  $[0/\pm 45/90]_s$  (Type I) and  $[0/90/\pm 45]_s$  (Type II) laminates fabricated from Narmco T300/5208 graphite epoxy.

Differences in wet and dry damage free stress states uniquely influence the free edge damage which developed when mechanically loaded. Using a previously established replica technique [4], damage at the laminate edge is recorded by replicating an image of damage from the edge onto the surface of an acetate strip, while the load is held constant. The chronology of damage events can be observed during the static and cyclic tests by incrementally stopping the test, taking a replica, and viewing the damage with a microfiche card reader at  $\times 50$  magnification.

### Analytic Methods

Since a mechanistic approach is emphasized in this investigation, the stress state predicted near the laminate edge is compared with the damage process as observed on the replicas.

*Damage Free Stress State*

The stress state existing prior to the first formation of damage observed on replicas is predicted by a finite element model (FEM) and a linear elastic thin laminated plate analysis (LPA).

If the stress state prior to the formation of damage is substantially altered by moisture absorption, then accurate wet and dry elastic properties, including out-of-plane properties ( $\nu_{23}$  and  $G_{23}$ ), should be utilized when predicting this change in stress.

Transversely isotropic fiber properties and dry epoxy properties listed in Table 1 were extrapolated from experimental data [11]. Elastic lamina properties listed in Table 1 were calculated using the formulation of Hashin [12] such that the dry epoxy Young's modulus and shear modulus were reduced 25 percent and 27 percent, respectively, owing to absorbed moisture of 1.2 percent by weight gain. Fiber elastic properties were assumed to be unaffected by absorbed moisture. Lamina elastic properties calculated in this manner reflect the change of constituent properties, due to absorbed moisture, without including the inherent statistical variations of experimental data. Laminate Young's modulus,  $E_x$ , was calculated using a laminate plate analysis with the lamina elastic properties listed in Table 1. For the dry state both Type I and Type II laminates have a Young's modulus of 51.1 GPa (7.4 Msi) and for the wet state 49.5 GPa (7.2 Msi). Elastic property subscripts correspond to coordinate systems defined in Fig. 1.

A dry shear transfer layer modulus,  $G_{SL}$ , of 4.48 GPa (0.65 Msi), predicted by Reifsnider et al [7], was calculated using Hashin's equation [12] for  $G_{12}$  at a fiber volume fraction of 42 percent. A reduced shear transfer layer modulus of 3.36 GPa (0.49 Msi) was calculated similarly using the wet epoxy shear modulus listed in Table 1.

The wet and dry laminate, shear transfer layer, and lamina elastic properties listed in Table 1 provide a consistent set of elastic properties to be used in

TABLE 1—Wet and dry elastic properties.

Type	Material	Elastic Properties—Dry/Wet, (Percent Difference)					
Matrix	Epoxy	$E_m$ , GPa		$G_m$ , GPa		$\nu_m$	
	5208 <sup>a</sup>	5.35/3.96 (-25)		1.95/1.43 (-27)		0.353/0.388 (+10)	
Fiber	Graphite	$E_{FL}$ , GPa	$E_{FT}$ , GPa	$G_{FLT}$ , GPa	$G_{FTT}$ , GPa	$\nu_{FLT}$	$\nu_{FTT}$
	T300 <sup>a</sup>	232.0/232.0 (0)	15.0/15.0 (0)	24.0/24.0 (0)	5.02/5.02 (0)	0.290/0.290 (0)	0.490/0.490 (0)
Lamina	T300/5208 <sup>a</sup>	$E_1$ , GPa	$E_2$ , GPa	$G_{12}$ , GPa	$G_{23}$ , GPa	$\nu_{12}$	$\nu_{23}$
	Graphite/ Epoxy	130./129.6 (-0.5)	9.72/8.69 (-11)	5.39/4.16 (-23)	3.25/2.83 (-13)	0.308/0.323 (+4.6)	0.492/0.323 (-8.1)
	$V_f = 0.55^b$						

<sup>a</sup>Trade name: NARMCO T300/5208 graphite/epoxy.

<sup>b</sup> $V_f$  = fiber volume fraction percent.

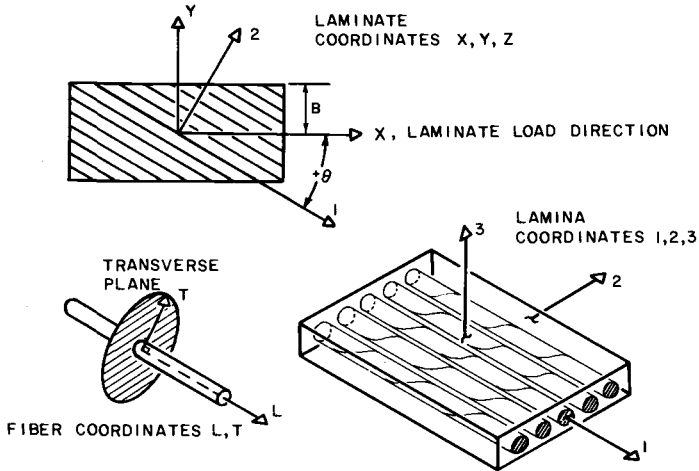


FIG. 1—Coordinate system definition.

the FEM, LPA, and shear lag models to predict differences in the wet and dry laminate stress states.

Coefficients of thermal expansion ( $\alpha_i$ ) shown below were the same as used by Nagarkar and Herakovich [6], and moisture coefficients ( $\beta_i$ ) were obtained by curve fitting experimental data reported by Crossman et al [5] assuming a moisture threshold,  $C_v$ , of 0.4 percent.

$$\alpha_1 = -0.41 \mu\epsilon/^\circ\text{C} (-0.23 \mu\epsilon/^\circ\text{F}); \quad \alpha_2 = 26.8 \mu\epsilon/^\circ\text{C} (14.9 \mu\epsilon/^\circ\text{F}) = \alpha_3$$

$$\beta_1 = 0; \quad \beta_2 = 5560 \mu\epsilon/\text{percent weight} = \beta_3 \text{ when } C_v = 0.4 \text{ percent weight}$$

The same wet and dry properties were consistently used in the FEM and LPA models except the value of  $\beta_2$  used by the FEM was recalculated to give the same total swelling strain at  $\Delta M = 1.2$  percent when  $C_v = 0$  percent.

$$\beta_2 = 3710 \mu\epsilon/\text{percent weight} = \beta_3 \text{ when } C_v = 0 \text{ percent weight}$$

The current version of the FEM (NONCOM III) used in this investigation was developed at Virginia Polytechnic Institute and State University. The general formulation of this FEM is reported in the most recent reference [15]. The FEM represents the laminate  $Y$ - $Z$  plane in a state of plane strain along the laminate load ( $X$ ) direction using constant strain triangular elements. The FEM used 768 elements to model the symmetric four-layer quarter-plane with 96 elements at the laminate edge. Although the sizes of the elements near the edge were reduced in order to model the stress gradients, the size of the smallest edge element (centroid at  $Y/B = 0.998$ ) included at least 15 fibers in order to maintain the idealization of homogeneity.

An approximation of the stresses,  $\sigma_i$ , in the plane of a thin laminate is calculated using the LPA model assuming plane stress. The combined effect of a mechanical load,  $N_x$ , and residual stresses,  $\sigma_i^R$ , on the individual ply

stresses,  $\sigma_i$ , is shown in Eq 1 using the notation of Kim and Hahn [13].

$$\sigma_i = Q_{ij}A_{jk}^{-1}N_k + \sigma_i^R \quad (1)$$

where

$Q_{ij}$  = reduced ply stiffnesses,  
 $A_{jk}$  = laminate stiffnesses, and  
 $N_k$  = equivalent stress resultants

The residual ply stresses,  $\sigma_i^R$ , can be represented in terms of differences between lamina ( $\alpha\Delta T$ ,  $\beta\Delta M$ ) and laminate ( $\bar{\alpha}\Delta T$ ,  $\bar{\beta}\Delta M$ ) thermal and moisture strains.

$$\sigma_i^R = Q_{ij}(\bar{\alpha}_j - \alpha_j)\Delta T + Q_{ij}(\bar{\beta}_j - \beta_j)\Delta M \quad (2)$$

The percent moisture weight gained,  $\Delta M$ , was measured as 1.2 percent in the fully saturated state and a temperature change,  $\Delta T$ , of  $-82.2^\circ\text{C}$  ( $-180^\circ\text{F}$ ) was chosen using the approximation of  $121^\circ\text{C}$  ( $250^\circ\text{F}$ ) for the stress free temperature [14].

Based on observations from previous investigations [4,5,13], damage first occurs in the 90-deg plies of Type I and Type II dry laminates in the form of ply cracks transverse to the direction of the laminate tension load,  $N_x$ . Since cracks first occur in the 90-deg plies, stresses in this ply are calculated using Eq 1 where the shear stress in the 90-deg ply is zero.

$$\sigma_1 = \frac{Q_{12}A_{yy} - Q_{11}A_{xy}}{A_{xx}A_{yy} - A_{xy}^2} N_x + \sigma_1^R; \quad \sigma_2 = \frac{Q_{22}A_{yy} - Q_{12}A_{xy}}{A_{xx}A_{yy} - A_{xy}^2} N_x + \sigma_2^R \quad (3)$$

The initial crack in the 90-deg ply is labeled FPF for first ply failure and the corresponding load is labeled,  $N_x^{FPF}$ . Although  $\sigma_1$  and  $\sigma_2$  both exist in the 90-deg ply at FPF, the  $\sigma_2$  stress is equal to the transverse strength,  $T$ , while  $\sigma_1$  is much lower than the longitudinal strength. Therefore, a maximum stress failure criterion (MSC) can be used which assumes FPF occurs when the value of  $\sigma_2$  is equal to the transverse strength,  $T$ , of a [90<sub>8</sub>] specimen

$$N_x^{FPF} = \frac{A_{xx}A_{yy} - A_{xy}^2}{Q_{22}A_{yy} - Q_{12}A_{xy}} (T - \sigma_2^R) \quad (4)$$

where the wet and dry transverse strengths were measured.

$$T_{DRY} = 44.6 \text{ MPa (6.47 ksi)} \quad \text{and} \quad T_{WET} = 32.7 \text{ MPa (4.74 ksi)}$$

Using the previously defined wet and dry properties the residual 90-deg ply stress and the FPF laminate loads are calculated and listed here.

$$\sigma_{DRY}^R = 23.6 \text{ MPa (3.43 ksi)}; \quad \sigma_{2WET}^R = -13.5 \text{ MPa (-1.96 ksi)}$$

$$N_{xDRY}^{FPF} = 1380 \text{ N/cm (789 lb/in.)}; \quad N_{xWET}^{FPF} = 3330 \text{ N/cm (1900 lb/in.)}$$

Note that the FPF laminate loads predicted by LPA for both laminate types are identical since changing the stacking sequence has no effect on  $\sigma_2^R$ .

Although the 90-deg ply stress,  $\sigma_2$ , was singled out for use in FPF calculations, all 0, 90, and 45-deg in-plane ply stresses in the wet and dry state were calculated and compared with the in-plane stresses predicted by the FEM, as a check, using the same wet and dry FPF laminate loads predicted by the LPA.

The stress state in finite width quasi-isotropic laminates is not uniform through the width as assumed by LPA [15]. FEM stress analysis demonstrates that the out-of-plane stresses, which are negligible away from the laminate edge, can exceed ply strengths within a thin boundary layer near the edge [15]. Depending on stacking sequence, the magnitude of these out-of-plane stresses can contribute to the formation of interply cracks (delaminations) at the edge [4]. Table 2 provides a comparison of the predicted FEM 90-deg ply stresses and edge damage as observed at 445 N (100 lb) load intervals.

*Characteristic Damaged Stress State (CDS)*

Since the pattern of ply cracks is the basis of the CDS, the effects of moisture on the mechanics of predicting the crack spacing, using the shear lag model, will be demonstrated. The shear lag model is presented in Ref 7 in sufficient detail such that only basic principles are restated below.

The shear lag model assumes that after a FPF crack forms in the 90-deg ply, the  $\sigma_x$  stress is recovered from zero at the crack surface to the unbroken ply stress ( $\sigma_x = 0.999 T$ ) as shown in Fig. 2. The  $\sigma_x$  stress near the crack no

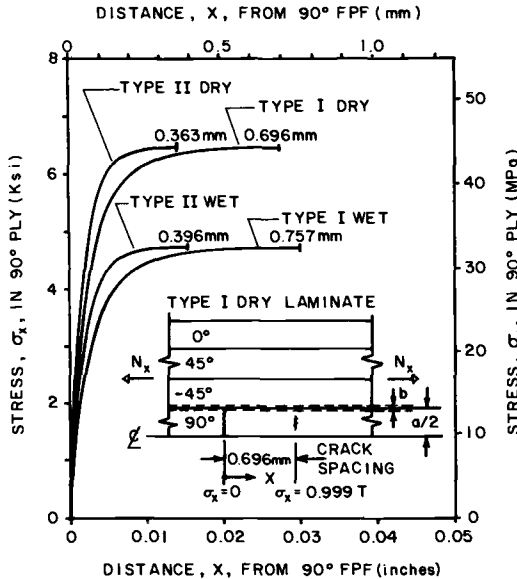


FIG. 2—Influence of wet and dry elastic properties on crack spacing.

TABLE 2—Damage development.

Laminate Configuration/ Environmental Condition	Predicted FEM 90-deg Ply Stresses $Y/B = 0.998$ (Edge/Interior)		90-deg Ply Damage		Predicted/Observed ECS, mm (Percent Difference)
	$\sigma_x$ , MPa	$\sigma_z$ , MPa	Predicted (LL) <sup>a</sup>	Observed (LL) <sup>a</sup>	
Type I/Dry	(+63.6/+43.2)	(+36.2/0)	T(8), D(?)	T(5 to 6), ECS(12), D(18 to 20)	0.696/0.706 (+1.4)
Type I/Wet	(+63.9/+31.4)	(+52.7/0)	T(19), D(?)	T(11 to 12), ECS(17), D(11 to 12)	0.757/1.59 (+100)
Type II/Dry	(+55.4/+43.2)	(+19.8/0)	T(8), ND	T(7 to 8), ECS(14), ND	0.363/0.325 (-10.4)
Type II/Wet	(+42.2/+31.4)	(+11.8/0)	T(19), ND	T(15 to 16), ECS(30), ND	0.396/0.330 (-16.7)

NOTE—Stresses in 90-deg ply calculated by FEM using the first ply failure laminate loads;  $N_{x, FPF} = 1380$  N/cm (789 lb/in.);  $N_{x, FWT} = 3330$  N/cm (1900 lb/in.).

<sup>a</sup> Abbreviations: T = transverse crack (first ply failure); D = delamination; ECS = equilibrium crack spacing; ND = no delamination; LL = load level in 100 lb/in. where 100 lb/in. = 175 N/cm; and ? = no prediction.

longer can be carried by the cracked ply but is transferred through a thin [ $b = 0.015 \text{ mm}$  ( $6 \times 10^{-4} \text{ in.}$ )] interply shear layer to the adjacent plies. When the  $\sigma_x$  stress has recovered 99.9 percent of the ply strength,  $T$ , the formation of a second crack is possible. Cracks continue to form in this manner with increasing laminate load,  $N_x$ , until no new cracks are observed (equilibrium crack spacing, ECS). The crack spacing is said to be characteristic of the laminate since the ply and laminate elastic properties are used together with the ply strengths to calculate ECS. ECS is typically nonuniform within a ply due to variations in ply strengths distributed along the ply length. Typically the standard deviation reported by Masters [16] is 0.21 mm when an average ECS of 0.665 mm was measured. Therefore, an average ECS is usually reported by dividing the length of the ply by the total number of cracks.

The increase in the predicted wet ECS, shown in Fig. 2, is largely due to the factor  $(E_x/G_{SL})^{1/2}$  shown in Eq 9 of the Appendix. Recall the shear transfer layer modulus,  $G_{SL}$ , was calculated at a fiber volume of 42 percent and is an epoxy dominated property compared with the fiber dominated laminate Young's modulus,  $E_x$ . As a consequence,  $G_{SL}$  will decrease with respect to  $E_x$  when the laminate absorbs moisture, causing an increase in the predicted ECS.

## Experimental Program

### *Environmental Conditioning*

A total of 72 Type I, 72 Type II, 12  $[0_8]$ , and 12  $[90_8]$  specimens were fabricated from the same batch of Narmco T300/5208 graphite epoxy. All specimens were 2.54 cm (1 in.) wide and 30.5 cm (12 in.) long. Half of the specimens of each type were exposed to 95 percent relative humidity (RH) at 70°C (158°F) until no additional weight gain due to moisture could be measured (wet condition). The remaining specimens were dried in a dry nitrogen gas oven at 65°C (149°F) until no additional loss of weight due to deabsorption could be measured (dry condition). The edges of ten Type I and ten Type II laminates were polished and replicated as outlined in Ref 4 prior to wet and dry conditioning.

### *Experimental Procedures*

Seventeen wet and seventeen dry unpolished laminates (gage length, 10.2 cm) of each stacking sequence were quasi-statically loaded in tension to fracture using an MTS hydraulic load controlled system with an MTS extensometer to measure strains. The wet and dry  $[0_8]$  and  $[90_8]$  specimens were quasi-statically loaded in tension to fracture using an Instron load frame. The strains transverse and parallel to the load were measured at the center of each specimen using biaxial strain gages.

Fracture strengths, Young's moduli, and Poisson's ratios were determined

for each specimen in a wet or dry condition. However, a series of strengths was obtained from each  $[90_8]$  specimen by testing the remaining sections after each failure. Using a minimum specimen length of 3.81 cm (1.5 in.), up to eight values of strength could be measured from each 30.5-cm (12-in.)  $[90_8]$  specimen. Testing the  $[90_8]$  specimens in this manner allows the experimentalist to isolate the first or "weakest link" strength from the subsequent higher strengths.

Nine wet and nine dry laminates from each stacking sequence without polished edges were quasi-statically loaded in tension to maximum stress of 345 MPa (50 ksi) and cyclically loaded at 10 Hz with  $R = 0.1$ . Residual strengths were measured after 100 K cycles by a quasi-static load to fracture.

All wet and dry laminates with polished edges were loaded in increments of 445 N (100 lb) in order to replicate the damage process up to 8900 N (2000 lb). From this group of tests one wet and one dry laminate from each stacking sequence continued with replicas from 8900 N (2000 lb) in increments of 890 N (200 lb) to fracture. The remaining wet and dry laminates with polished edges were cyclically loaded at 10 Hz with a stress ratio of  $R = 0.1$  and a maximum stress of 345 MPa (50 ksi). Replicas were obtained at 5 K, 10 K, 50 K, 100 K and 1 M cycles. Residual strengths were measured after 100 K and 1 M cycles with replicas taken at 890 N (200 lb) load increments.

## Results

A summary of residual and static strengths for all wet and dry specimens which were quasi-statically loaded in tension to fracture is shown in Fig. 3. A comparison of these strengths with the wet and dry laminate stress state is provided in Fig. 4 by using the LPA model to equate  $[0_8]$  and  $[90_8]$  strengths with their respective 0 and 90-deg ply stress in the laminate. As a consequence, the maximum stress failure criterion (MSC) used to predict FPF in the 90-deg ply is graphically represented in Fig. 4. For comparison, the values of stress corresponding to FPF observed on replicas within a 175 N/cm (100 lb/in.) load interval are included in Fig. 4. The wet and dry static strengths for both laminate types along with the wet and dry  $[0_8]$  strengths also are oriented with respect to the laminate stress axis as shown in Fig. 4. Figure 4 provides some perspective on how moisture can alter the in-plane stresses and shift the damage events in a laminate.

The difference between the Type I and Type II laminate mean strengths in a wet or dry condition, shown in Figs. 3 and 4, is not due to the random nature of a small sample size ( $n = 17$ ) but can be shown to be statistically significant using the Student's  $t$  distribution [17] at a 99 percent confidence level. A Chi-square test [18] demonstrated that a larger specimen size ( $n = 30$ ) was needed to determine more accurately the type of distribution function. At best, with an interval sample size of six, the Type I and Type II dry laminate strengths fit the Weibull distribution [18], shown in Fig. 5, with

Data Description	Mat'l Condition		Average Strength $\pm$ Std. Dev. (MPa)	
[0,±45,90] <sub>s</sub> Type I Static Tensile Strengths	Ref. (14) Dry			
	Dry			502 $\pm$ 26
	Wet			525 $\pm$ 29
[0,90,±45] <sub>s</sub> Type II Static Tensile Strengths	Wet		578 $\pm$ 30	
	Dry		589 $\pm$ 24	
	Ref. (10) Dry			
Type I Residual Strength 100K Cycles	Dry		498 $\pm$ 23	
	Wet		477 $\pm$ 28	
Type II Residual Strength 100K Cycles	Wet		554 $\pm$ 35	
	Dry		554 $\pm$ 34	
[0 <sub>g</sub> ] Static Tensile Strengths	Dry		1470 $\pm$ 179	
	Wet		1420 $\pm$ 145	
[90 <sub>g</sub> ] Weakest Link Static Tensile Strengths	D R Y	1	44.6 $\pm$ 5.5	
		2	50.6 $\pm$ 4.4	
		3	52.7 $\pm$ 4.1	
		4	54.6 $\pm$ 4.7	
		5	52.9 $\pm$ 2.5	
		6	50.9 $\pm$ 0.7	
		7	56.3	
		8	49.1	
	Break No.			
	W E T	1	32.7 $\pm$ 7.0	
		2	34.3 $\pm$ 3.3	
		3	32.4 $\pm$ 5.4	
		4	35.4 $\pm$ 5.4	
		5	32.1 $\pm$ 4.0	
		6	35.4 $\pm$ 5.2	
		7	34.7 $\pm$ 6.0	
		8	37.6 $\pm$ 0.4	
9		36.7		

FIG. 3—Summary of strength data.

a Chi-square of 1.128 and 2.616, respectively. In summary, the difference between the Type I and Type II dry mean strengths, which is reduced by moisture absorption, is small but statistically significant.

The chronological sequence of 90-deg ply damage events observed on replicas is summarized in Table 2 and compared with nonzero FEM edge stresses. FEM edge stresses were calculated using first ply failure laminate loads of 1380 N/cm (789 lb/in.) for the dry condition and 3330 N/cm (1900 lb/in.) for the wet condition.

As previously discussed, due to swelling, moisture reduces the inplane residual 90-deg ply stress [ $\sigma_{2DRY}^R = 23.6$  MPa (3.43 ksi);  $\sigma_{2WET}^R = -13.5$  MPa (-1.96 ksi)] such that the laminate load required to produce FPF is increased, as shown in Fig. 4, even though the transverse strength is reduced by moisture, as shown in Fig. 3. Conversely, the predicted FEM out-of-plane stress,  $\sigma_z$ , as shown in Table 2, is increased with moisture such that a lower load in the Type I laminate is required to produce delaminations between the 90-deg plies. Using the replica technique, dry Type I FPF was observed to occur within the laminate load increment 876 to 1050 N/cm (500 to 600 lb/in.), and wet FPF laminate load was observed to increase to 1930 to 2100 N/cm (1100 to 1200 lb/in.). The laminate load required to cause delamina-

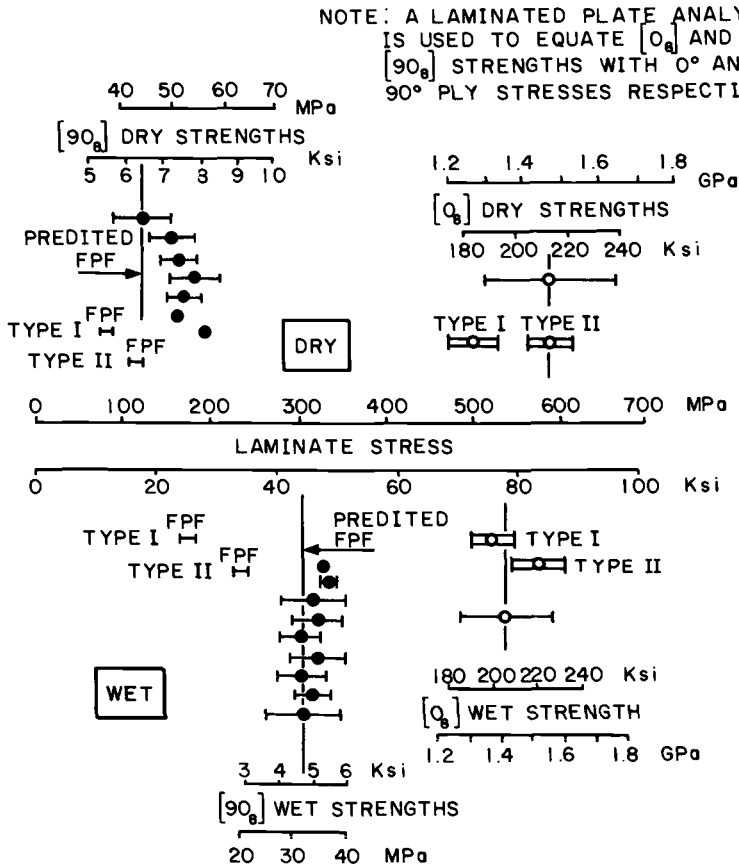


FIG. 4—Correlation of wet and dry  $[0_a]$  and  $[90_a]$  strengths with 0/90 laminate ply stresses.

tions in Type I laminates was observed to decrease from 3150 to 3500 N/cm (1800 to 2000 lb/in.), for the dry case to 1930 to 2100 N/cm (1100 to 1200 lb/in.), for the wet case. As a result of moisture absorption, FPF and delaminations in Type I laminates were observed to occur simultaneously near 1930 N/cm (1100 lb/in.) as shown in Fig. 6.

A comparison of ECS predicted by the shear lag model and the ECS observed on the replicas is summarized in Table 2. For both laminate types moisture increases the ECS as predicted, except the ECS for the Type I wet laminate was twice as large as predicted. Delaminations occurring at the same load with FPF alter the boundary conditions assumed by the shear lag model to predict the wet ECS. In summary, moisture has altered the sequence of damage events in the Type I laminate such that the ECS in the wet 90-deg ply is increased.

Although moisture can alter the chronology of the damage process, the

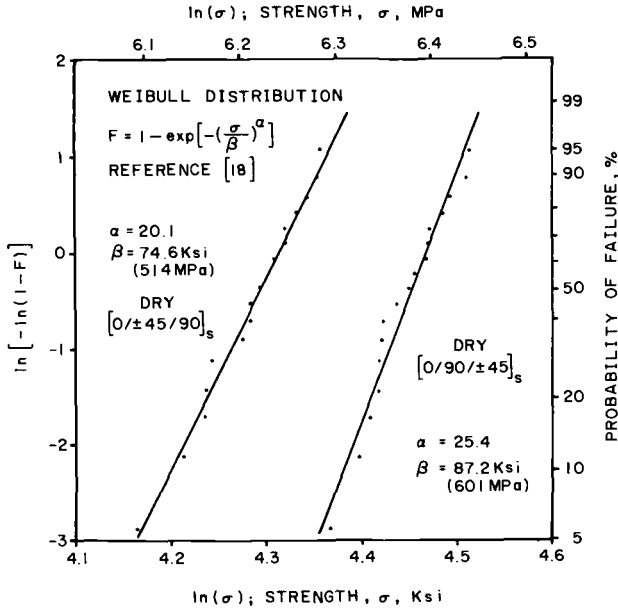


FIG. 5—Weibull plot of  $[0/\pm 45/90]_s$  strengths.

fully developed crack pattern (CDS) of the wet Type I laminate prior to fracture was observed to be similar to the CDS of the dry Type I laminate, as shown in Fig. 7. Similar crack patterns were observed after 100 K cycles for both wet and dry conditioned Type I laminates. Except for a 2 percent increase in the ECS of the wet 90-deg plies, identical crack patterns were observed prior to fracture for all Type II laminates in the wet or dry state.

Except for the Type II dry laminate, the FPF, observed in Fig. 4, occurred at lower laminate loads than predicted by MSC. An increase in the  $\sigma_x$  and  $\sigma_z$  FEM stresses predicted near the laminate edge shown in Table 2 is most likely a factor to be considered with respect to the lower FPF laminate loads

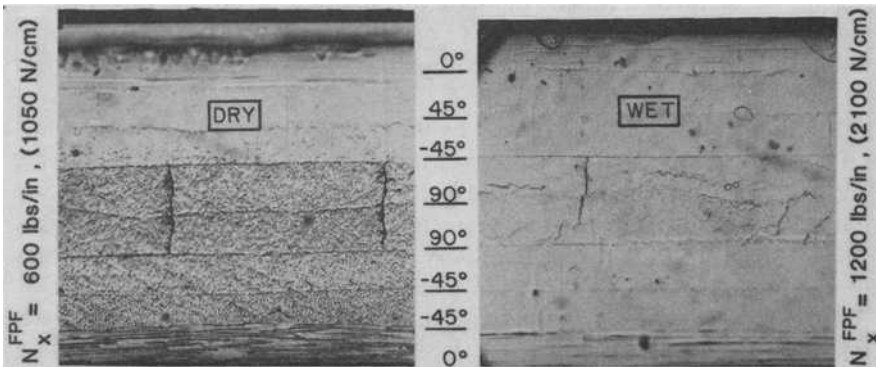


FIG. 6—Wet and dry 90-deg ply cracks ( $\times 50$ ) at  $N_x = 1100$  lb/in. (1930 N/cm).

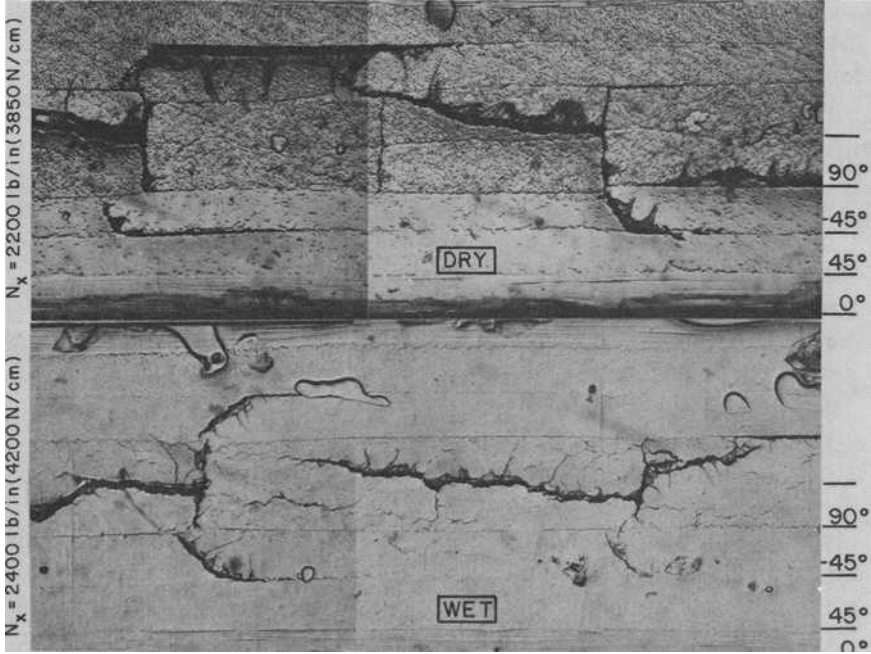


FIG. 7—Wet and dry characteristic damage state at the  $[0/\pm 45/90]$  laminate edge ( $\times 50$ ).

shown in Fig. 4. It is interesting to note that the smallest predicted increase of  $\sigma_x$  and  $\sigma_z$  occurs near the edge of the Type II dry laminate. Based on these observations, a model is developed which predicts the first formation of damage near the edge of the 90-deg ply in any stacking sequence.

It is tempting to use this predicted increase of FEM edge stresses together with some failure criteria in order to account for the differences in the FPF laminate loads,  $N_x^{FPF}$ , as previously discussed. Crossman et al [5] point out that only trends in the predicted FEM edge stress can be realized when the material can no longer be modeled as homogeneous at one or two fiber diameters from the edge and when the elastic properties in the lamina 2-3 plane are assumed. Improved predictions of  $\sigma_x$  and  $\sigma_z$  stresses are obtained in this study by using better approximations for the wet and dry elastic properties in the lamina 2-3 plane. From a continuum viewpoint, Crossman et al [5] suggest that FEM stresses evaluated at five fiber diameters from the edge ( $Y/B \approx 0.998$ ) are more realistic than stresses predicted at  $7 \mu\text{m}$  ( $2.8 \times 10^{-4}$  in.) from the edge. Although a few improvements in FEM stresses near the edge can be realized, a model is needed which can predict failure without reference to an exact prediction of an experimental stress within the region of stress concentration.

Whitney and Nuismer [19] demonstrated that the localized nature of a stress concentration near a hole of radius,  $R$ , in a quasi-isotropic laminate

can be empirically modeled by evaluating a characteristic distance,  $d_o$ , from the elasticity given by Eq 5. The stress ratio  $\sigma_y/\bar{\sigma}$  is redefined in terms of experimental notched,  $\sigma_n$ , and unnotched,  $\sigma_o$ , laminate strengths

$$\sigma_y(\xi)/\bar{\sigma} = 2/(2 + \xi^2 + 3\xi^4) = \sigma_n/\sigma_o \quad (5)$$

where

- $\xi = R/(R + d_o)$ ,
- $R =$  hole radius,
- $d_o =$  distance from the edge of hole,
- $\sigma_y =$  stress within region of stress concentration,
- $\bar{\sigma} =$  far-field stress,
- $\sigma_n =$  notched strength, and
- $\sigma_o =$  unnotched strength.

Although a critical stress at some distance,  $d_o$ , is realized as some lower notch strength,  $\sigma_n$ , changes in  $\sigma_n$  can be predicted for different hole radii,  $R$ , without requiring that this critical stress be a prediction of an actual experimental stress at some distance,  $d_o$ , within the stress concentration. This same philosophy can be extended to edge damage events corresponding to stress concentrations existing in individual plies near the laminate edge.

The objective of the proposed model is to predict cracking at the edge of the 90-deg ply without requiring that some critical stress state, which is predicted by the FEM at some distance,  $a_o = 1 - Y/B$ , from the edge, be numerically equal to the actual experimental stress state. The model requires only that the variations in the 90-deg ply stresses at some point near the edge, due to variation in stacking sequence in the wet or dry state, be accurately predicted by the FEM. The nonzero-90-deg ply FEM stresses averaged at the centroid ( $Y/B = 0.998$ ;  $a_o = 0.002$ ) of the 90-deg ply edge element are summarized in Table 2. When these nonzero FEM stresses are substituted into the tensor polynomial failure criterion, outlined in Ref 15, the surviving terms are written as follows:

$$2\sigma_x/T - 2\sigma_z/T - (\sigma_x/T)^2 - (\sigma_z/T)^2 = ff \quad (6)$$

where the transverse strengths in the lamina 2-3 plane are assumed equal ( $F_2 = F_3 = 2T$ ;  $F_{22} = F_{33} = 1/T^2$ ) and  $ff = 1$  since the FEM stresses, located at  $a_o = 0.002$ , are calculated using  $N_x^{FPF}$  as observed on replicas.

The model uses Eq 6 to empirically evaluate the parameter,  $T$ , which effectively represents the crack formation in a 90-deg ply.

$$T_{eff} = \sigma_x + \sigma_z \pm [(\sigma_x + \sigma_z)^2 - \sigma_x^2 - \sigma_z^2]^{1/2} \quad (7)$$

The parameter,  $T_{eff}$ , is not an exact measure of ply strength, in the same sense that  $d_o$  used by Whitney and Nuismer [19] is not the exact location from the hole where some critical stress initiates damage leading to fracture. The empirical parameters ( $T_{eff}$ ,  $d_o$ ) are based on experimental observations

and are used only to predict changes in laminate loads which result in a damage event due to a change in a stress concentration.

The linear relationships between the laminate load,  $N_x$ , and the parameter,  $T_{eff}$ , for both laminate types in the wet and dry state are plotted in Fig. 8 along with the experimental FPF laminate loads,  $N_x^{FPF}$ . Based on the experimental observations in this investigation, it appears that  $T_{eff}$  can be used as a parameter to predict changes in the  $N_x^{FPF}$  due to changes in stacking sequence. Because of the replica load interval, FPF is observed to occur when the numerical value of  $T_{eff}$  is within the intervals of 23.1 to 28.3 MPa (3.35 to 4.10 ksi) for dry laminates and 15.6 to 18.7 MPa (2.26 to 2.71 ksi) for wet laminates. Using acoustic emission to detect FPF [13] and including other laminate stacking sequences may provide additional information to evaluate the proposed model critically.

The model, as shown in Fig. 8, verifies that the difference between the Type I wet  $N_x^{FPF}$  and Type II wet  $N_x^{FPF}$  can be predicted as a result of a change in the stress concentration near the edge which is modeled by empirically evaluating the parameter,  $T_{eff}$ .

A final comparison of edge stresses, shown in Fig. 9, demonstrates the effect that the experimental FPF laminate loads have on the nonzero 90-degree FEM stresses at  $Y/B = 0.998$ . Of particular interest is the near equality of Type I wet  $\sigma_x$  and  $\sigma_z$  stresses predicted using the experimental values of  $N_x^{FPF}$ . A picture of the replica taken at  $N_x^{FPF}$  for the Type I wet laminate, as shown in Fig. 6, demonstrates that both FPF and delaminations occur simultaneously, which validates the approximation of equating transverse strengths in the lamina 2-3 plane, at least for wet 90-degree plies.

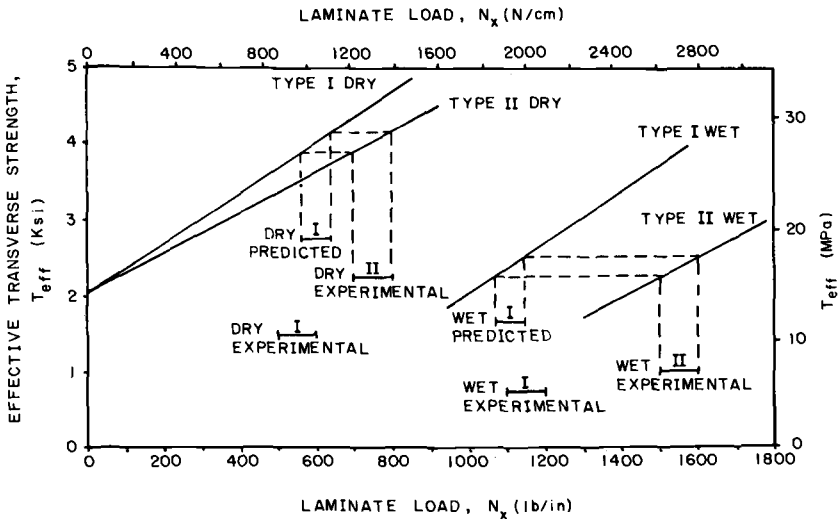


FIG. 8—Comparison of effective transverse edge strengths with experimental observations.

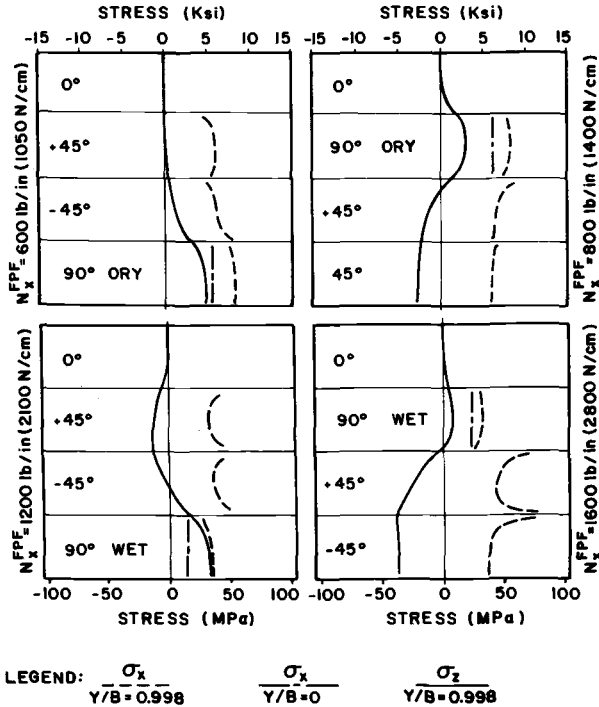


FIG. 9—Comparison of wet and dry nonzero laminate edge stresses at load corresponding to first ply failure.

**Conclusions**

1. In general, moisture tends to reduce moduli, strengths, and scatter of strengths for specimens tested in this investigation. Moisture also reduces the difference between Type I,  $[0/\pm 45/90]_s$ , and Type II,  $[0/90/\pm 45]_s$ , laminate strengths.

2. Edge damage, which is recorded using acetate replicas, can be viewed on a microfiche card reader with sufficient magnification such that the damage process can be interpreted conveniently during the test.

3. Moisture was observed to significantly alter the Type I dry laminate edge residual FEM stresses such that delaminations are predicted to occur at lower loads, and first 90-deg ply failures (FPF) are predicted to occur at higher loads. These predicted trends due to moisture absorption were verified experimentally using the replica technique.

4. For the Type I wet laminate, delaminations were observed to occur simultaneously and interact with transverse cracks in the 90-deg ply such that ECS was twice the value observed for the Type I dry laminate.

5. The absorption of moisture was observed and predicted to cause less than a 2 percent increase in the ECS of the Type II laminate.

6. By using an empirically evaluated parameter,  $T_{eff}$ , it was possible to model the observed difference in FPF laminate loads.

7. Differences in observed FPF laminate loads were accounted for by the model as predictable changes in the nonzero FEM values of stresses near the laminate edge, due to changes in the wet or dry stress gradients near the edge.

8. Although moisture was shown to alter significantly the first formation of damage in the 90-deg plies, the fully developed dry crack patterns prior to fracture (dry CDS), which develop from static or cyclic loads, were similar to the wet crack patterns (wet CDS). Consequently, the difference between the redistributed stresses in damaged wet and dry laminates prior to fracture will be small; as a result, these differences will have a small influence on the laminate strength. This observation was verified statistically as small but significant differences between wet and dry laminate strengths.

*Acknowledgments*

This report represents a portion of the work accomplished under National Aeronautics and Space Administration (NASA) Grant NGR47-004-129. Appreciation is extended gratefully to E. G. Henneke, C. T. Herakovich, and K. L. Reifsnider for many valuable discussions. Special appreciation is given to D. R. Tenney for serving as NASA advisor during the experimental portion of this investigation.

**APPENDIX**

The ECS in the 90-deg ply for the Type I laminate may be predicted by calculating a value for  $X$  when the normalized strain,  $dU_{90}/dx$ , reaches a value of 0.999.

$$U_{90} = a\sigma(x + c_1e^{-\alpha x} + c_2e^{-\beta x})/(E_x G_{SL})^{1/2} \tag{8}$$

and

$$X = xa (E_x/G_{SL})^{1/2} \tag{9}$$

where

- $\alpha, \beta = [(B + A)/(2AB) \pm (B^2 + 4A^2)^{1/2}/(2AB)]^{1/2}$ ,
- $A = (bE_{90})/(2aE_x)$ ,  $B = (bcE_{45})/(a^2E_x)$ ,
- $C_1 = -D_2/(\beta D_1 - \alpha D_2)$ ,  $C_2 = D_1/(\beta D_1 - \alpha D_2)$ ,
- $D_1 = 1 - A\alpha^2$ ,  $D_2 = 1 - A\beta^2$ ,
- $x$  = normalized distance from crack surface,
- $X$  = distance from crack surface,
- $\sigma$  = laminate stress,
- $E_x$  = laminate modulus,
- $E_{90}$  = 90-deg ply modulus,
- $E_{45}$  = 45-deg ply modulus,
- $G_{SL}$  = transfer layer shear modulus,

- $a$  = 90-deg ply thickness,  
 $b$  = shear transfer layer thickness, and  
 $c$  = 45-deg ply thickness.

## References

- [1] Unnam, J. and Tenney, D. R., "Analytical Prediction of Moisture Absorption/Desorption in Resin Matrix Composites Exposed to Aircraft Environments," American Institute of Aeronautics and Astronautics, Paper No. 77-400, March 1977.
- [2] Browning, C. E., Husman, G. E., and Whitney, J. M. in *Composite Materials: Testing and Design (Fourth Conference)*, ASTM STP 617, American Society for Testing and Materials, 1977, pp. 481-496.
- [3] Kaeble, D. H., Dynes, P. J., Crane, L. W., and Maus, L., *Journal of Adhesion*, Vol. 7, 1975, pp. 25-54.
- [4] Stalnaker, D. O. and Stinchcomb, W. W. in *Composite Materials: Testing and Design (Fifth Conference)*, ASTM STP 674, American Society for Testing and Materials, 1979, pp. 620-641.
- [5] Crossman, F. W., Mauri, R., and Warren, W., "Hygrothermal Damage Mechanisms in Graphite-Epoxy Composites, Final Report No. LMSC-D626480," Lockheed Palo Alto Research Laboratory, Lockheed Missiles and Space Co., Inc., Palo Alto, Calif., June 1978.
- [6] Herakovich, C. T., Nagarkar, A., and O'Brien, D. A. in *Modern Developments in Composite Materials and Structures*, American Society of Mechanical Engineers Conference, New York, 1979.
- [7] Reifsnider, K. L., Henneke, E. G., and Stinchcomb, W. W., "Defect-Property Relationships in Composite Materials," AFML-TR-76-81, Part IV, Air Force Materials Laboratory, Wright-Patterson Air Force Base, Ohio, June 1979.
- [8] Reifsnider, K. L. and Masters, J. E., "Investigation of Characteristic Damage States in Composite Laminates," American Society of Mechanical Engineers Paper No. 78-WA/Aero-4, Winter Annual Meeting, 1978.
- [9] Talug, A., "Analysis of Stress Fields in Composite Laminates with Interior Cracks," Doctoral Dissertation, Department of Engineering Science and Mechanics, College of Engineering, Virginia Polytechnic Institute and State University, Blacksburg, Va., Aug. 1978.
- [10] Crossman, F. W., "Analysis of Free Edge Induced Failure of Composite Laminates," *Proceedings of United States-Union of Soviet Socialist Republics Conference on Fracture of Composite Materials*, Riga, Latvia, Union of Soviet Socialist Republics, Sept. 1978.
- [11] Kriz, R. D. and Stinchcomb, W. W., *Experimental Mechanics*, Vol. 19, No. 2, Feb. 1979, pp. 41-49.
- [12] Hashin, Z., "Theory of Fiber Reinforced Materials," NASA-CR-1974, National Aeronautics and Space Administration, Langley Research Center, March 1972.
- [13] Kim, R. Y. and Hahn, H. T., *Journal of Composite Materials*, Vol. 13, 1979, p. 2.
- [14] Pagano, N. J. and Hahn, H. T. in *Composite Materials: Testing and Design (Fourth Conference)*, ASTM STP 617, American Society for Testing and Materials, 1977, pp. 317-329.
- [15] Nagarkar, A. P. and Herakovich, C. T., "Nonlinear Temperature Dependent Failure Analysis of Finite Width Composite Laminates," Virginia Polytechnic Institute and State University, VPI-E-79-36, Sept. 1979.
- [16] Masters, J. E., "Damage Development in Graphite Epoxy Laminates," Doctoral Dissertation, Department of Engineering Science and Mechanics, College of Engineering, Virginia Polytechnic Institute and State University, Blacksburg, Va., 1980.
- [17] *A Guide for Fatigue Testing and the Statistical Analysis of Fatigue Data*, ASTM STP 91-A, 2nd ed., American Society for Testing and Materials, 1963.
- [18] Park, W. J., "Basic Concepts of Statistics and Their Applications in Composite Materials," AFML-TR-79-4070, Air Force Materials Laboratory, Wright-Patterson Air Force Base, Ohio, June 1979.
- [19] Whitney, J. M. and Nuismer, R. J., *Journal of Composite Materials*, Vol. 8, July 1974, p. 253.

# **Damage Mechanisms: Tolerance and Characterization**

# Mechanisms of Fatigue Damage in Boron/Aluminum Composites

---

**REFERENCE:** Johnson, W. S., "Mechanisms of Fatigue Damage in Boron/Aluminum Composites," *Damage in Composite Materials, ASTM STP 775*, K. L. Reifsnider, Ed., American Society for Testing and Materials, 1982, pp. 83-102.

**ABSTRACT:** Fatigue damage mechanisms have been investigated using a series of tension fatigue tests on several laminates of boron/aluminum (6061-0). This study focuses on four aspects of the fatigue response. First, in laminates with 0-deg fibers on the outside, an analysis that identifies "shakedown" conditions is shown to predict the stress amplitude below which no fatigue damage accumulates. Second, a simple fatigue damage accumulation model which relates matrix fatigue cracking and the overall laminate properties is described. A model for the saturation damage stage development is presented. Third, data illustrate that identical laminates, tested in directions 90-deg apart (such that one layup has 90-deg outer plies and the other 0-deg), have different fatigue behaviors due to the stacking sequence. The 90-deg plies on the surface develop cracks earlier than predicted by shakedown. An attempt is made to explain this stacking sequence effect. Finally, variable load history effects on the fatigue damage response are investigated by simple tests. These tests reveal that for a given stress ratio the specimen seeks the saturation damage state for the largest stress range to which it is subjected. It also was found that little damage is generated by shifting a given stress range down, whereas significant damage may be created by shifting it upward.

**KEY WORDS:** boron-aluminum composites, metal matrix composites, fatigue damage mechanisms, fatigue, stacking sequence, saturation damage state, load history, shakedown analysis, composite materials

## Nomenclature

- $a$  Half length of crack, mm
- $E^f$  Fiber elastic modulus, MPa
- $E^m$  Matrix elastic modulus, MPa
- $E_{eff}^m$  Effective modulus of the matrix in the loading direction, MPa
- $E_N$  Unloading elastic modulus of the  $N$ th cycle, MPa
- $E_o$  Unloading elastic modulus of the first cycle, MPa
- $R$  Stress ratio

<sup>1</sup> Research engineer, National Aeronautics and Space Administration, Langley Research Center, Hampton, Va. 23665.

$S_{max}$	Maximum laminate stress, MPa
$S_{min}$	Minimum laminate stress, MPa
$S_{11}$	Laminate stress in the 0-deg fiber direction, MPa
$S_{22}$	Laminate stress in the 90-deg fiber direction, MPa
$S_{33}$	Laminate stress in the thickness direction, MPa
$V_f$	Fiber volume fraction
$Y$	Cyclic hardened yield stress, corresponds to one half the matrix fatigue limit for $R = 0$ , MPa
$\Delta\epsilon$	Laminate strain range associated with the saturation damage state
$\Delta\epsilon_{comp}^m$	Compressive strain range of the matrix material in the loading direction
$\Delta K$	Stress intensity range, $\text{MN} \cdot \text{m}^{-3/2}$
$\Delta K_{th}$	Threshold stress intensity range, $\text{MN} \cdot \text{m}^{-3/2}$
$\Delta S$	Laminate stress range, MPa
$\Delta S_R$	Experimentally determined stress range that causes no fatigue damage, MPa
$\Delta S_{sh}$	Calculated maximum stress range that causes no fatigue damage, MPa
$\Delta\sigma_e$	Stress required to grow an embedded flaw, MPa
$\Delta\sigma_s$	Stress required to grow a surface flaw, MPa
$\nu^f$	Poisson's ratio of the boron fiber
$\nu^m$	Poisson's ratio of the matrix material
$\phi$	Correction factor to account for the effect of laminate stacking sequence

In recent years, fatigue damage and failure of metal-matrix fibrous composites have been studied extensively [1-11].<sup>2</sup> Most studies were tests to determine S-N curves. Such tests indicate only the number of cycles that a composite laminate can sustain for constant maximum and minimum load levels; they do not indicate the mechanical degradation due to fatigue, nor do they give much insight into the complex fatigue damage mechanisms that occur in these materials. Most fatigue tests of metal matrix composites were conducted under constant amplitude loading; thus, variable amplitude loading effects, which are prominent in most structural applications, are not well understood.

The objective of this paper is to describe the results of tests in which the fatigue damage mechanisms of continuous boron fibers in a 6061 aluminum matrix were studied. Four areas of metal matrix fatigue are discussed: (1) correlation of laminate fatigue damage threshold with the matrix cyclic yield stress; (2) presentation of a simple model that describes damage that leads to a damage saturation state; (3) the effect of ply stacking sequence on fatigue damage accumulation; and (4) the effect of variable load history on fatigue damage.

<sup>2</sup>The italic numbers in brackets refer to the list of references appended to this paper.

TABLE 1—Composite constituents mechanical properties.

	Boron Fiber [12], 0.142 mm dia	6061 Aluminum [16]
Elastic modulus	$E^f = 40.0 \times 10^4 \text{ MPa}$ ( $58.0 \times 10^6 \text{ psi}$ )	$E^m = 7.25 \times 10^4 \text{ MPa}$ ( $10.5 \times 10^6 \text{ psi}$ )
Poisson's ratio	$\nu^f = 0.200$	$\nu^m = 0.33$

## Fatigue of Composite Laminates

### Specimen Preparation and Testing

The material for the boron-aluminum composite specimens was manufactured in the form of 300 by 230 mm (12 by 9 in.) plates. The matrix was 6061 aluminum; fibers were 0.14-mm (5.6-mils)-diameter boron.

Table 1 presents material properties for the boron fiber and aluminum constituents, and Table 2 shows the six laminates that were tested. Plates were cut with a diamond saw into rectangular specimens 102 mm (4.0 in.) long and 12.7 mm (0.50 in.) wide. All specimens were annealed at 413°C (775°F) for 2 h and cooled at the rate of about 28°C (50°F) per hour from the annealing temperature to 260°C (500°F), then oven cooled to room temperature. Ultrasonic C-scan was used to screen out the specimens containing detectable defects [13, 14]. This screening eliminates most of the fatigue scatter such that the data presented are significant. Glass-epoxy end tabs were bonded to each composite specimen. Tab dimensions were 3.2 mm (0.125 in.) thick, 28.6 mm (1.125 in.) long, and 12.7 mm (0.50 in.) wide. All fatigue failures occurred in the gage section, none in the tab area.

The specimens were tested at a cyclic frequency of 10 Hz using an MTS closed-loop hydraulic machine, in a load-controlled tension-tension mode. Standard wedge grips were used. The specimen strains were measured with an MTS extensometer of 25.4 mm (1.0 in.) gage length, designed for fatigue testing. The stress-strain response, during quasi-static loading cycles, was recorded using an  $x$ - $y$  plotter at various intervals during the fatigue test.

### Boron-Aluminum Composite Test Results

The stress-strain response of each specimen was recorded at various intervals during the cyclic life to determine the changes in the longitudinal modu-

TABLE 2—Predicted and experimental laminated composite behavior.

Layup	$V_f$	$E_c \times 10^5$ MPa	$\Delta S_{sh}/Y$	Shakedown Stress Range, $\Delta S_{sh}$		$\phi$ , $\Delta S_R / \Delta S_{sh}$
				Predicted	Experimental	
$[0]_8$	0.45	2.200	6.10	429	481	1.12
$[0/90]_{2s}$	0.50	1.840	3.13	220	214	0.97
$[90/0]_{2s}$	0.50	1.840	3.13	220	173	0.79
$[0/\pm 45/90]_s$	0.33	1.264	2.60	183	166	0.91
$[90/\pm 45/0]_s$	0.30	1.210	2.57	181	123	0.68
$[0/\pm 45/90/0/\pm 45/90]_s$	0.45	1.514	2.71	191	196	1.03

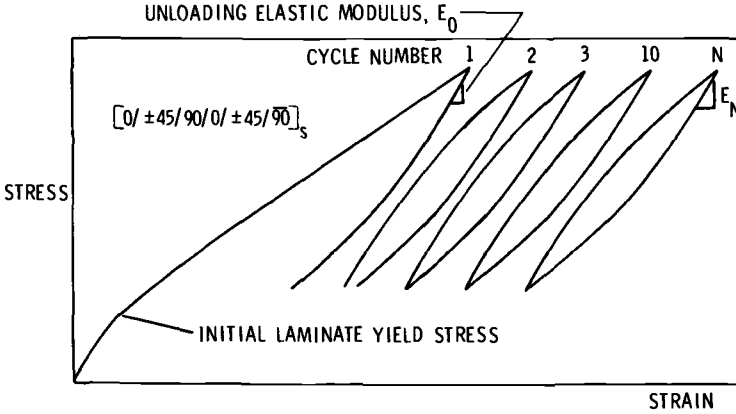


FIG. 1—Example of stress-strain recording of a boron-aluminum laminated composite specimen.

lus due to fatigue damage. These changes in modulus will be shown to be caused primarily by fatigue cracks developing in the matrix material. Figure 1 shows a typical stress-strain response of a boron-aluminum laminate loaded at  $R = 0.3$ . The unloading elastic modulus,  $E_N$ , was measured for each recorded cycle. It is known that the secant modulus is affected by matrix hardening as well as fatigue damage [13, 14]. Since the unloading elastic modulus is not affected, it is a more direct indicator of fatigue damage.

An example of the fatigue damage accumulation as a function of number of applied cycles and stress is presented in Fig. 2 for a  $[0/\pm 45/90/0/\pm 45/90]_s$  laminate. The damage is expressed in terms of  $E_N/E_0$ , the percent of the initial unloading elastic modulus remaining after  $N$  cycles. All of the data shown are for specimens that survived at least 2 000 000 cycles, after which

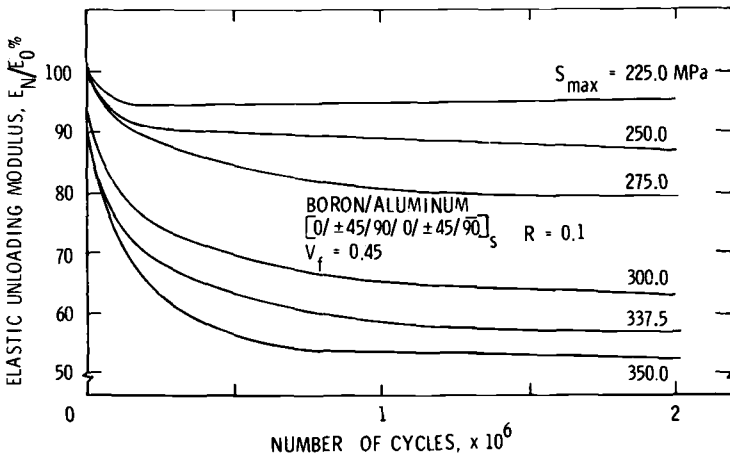


FIG. 2—Change in elastic modulus of  $[0/\pm 45/90/0/\pm 45/90]_s$ . Specimens tested at different values of  $S_{max}$ .

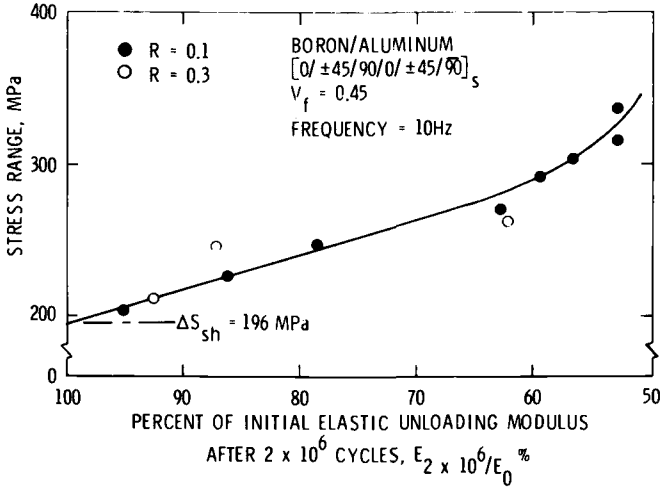


FIG. 3—Change in elastic modulus of  $[0/\pm 45/90/0/\pm 45/90]_s$ . Specimens related to applied stress range  $\Delta S$ .

the tests were terminated. Notice that each specimen appears to reach a stabilized value of  $E_N/E_o$ , herein referred to as a “saturation damage state” (SDS). All of the specimens shown in Fig. 2 were cyclic loaded below the 375 MPa (54 ksi) fatigue limit. S-N data and the associated fatigue limits are presented in Ref 14 for all six laminates. The SDS implies that the laminate will neither accumulate more damage nor fail under the present loading condition.

Figure 3 presents the SDS as a function of stress range by plotting the  $E_N/E_o$  values after 2 000 000 cycles. This figure includes data for stress ratios of  $R = 0.1$  and  $0.3$ . The constant amplitude SDS seems to be a function of stress range and independent of mean stress. (This will be explained by the simple fatigue damage model.) The data can be extrapolated, using a regression analysis, to 100 percent of  $E_N/E_o$  (that is, no change in elastic unloading modulus) to determine the stress range below which no fatigue damage accumulates. This range was referred to as the shakedown range  $\Delta S_R$ . The type of data presented previously were generated for all six laminates. The corresponding  $\Delta S_R$  values are presented in Table 2. Notice that the laminates with a 90-deg ply on the surface have lower  $\Delta S_{sh}$  values than similar laminates with 0-deg surface plies. Hence, the stress level required to produce fatigue damage is lower for laminates with 90-deg outer plies than for those with 0-deg outer plies. This stacking sequence effect will be discussed later.

**Shakedown Analysis**

The possible relationship between fatigue and shakedown stress range in metal matrix composites was first suggested by Dvorak and Tarn [15] and

related to the available experimental data, obtained primarily for unidirectional boron-aluminum materials. Since only S-N data were available for analysis, they tried to relate the shakedown stress to the fatigue limit. This relationship, however, does not hold generally, as was demonstrated when additional data became available. In this paper, the relationship between the fatigue damage initiation stress (not fatigue limit) and shakedown is examined analytically and experimentally for both unidirectional and cross-plyed boron-aluminum composites.

If fatigue damage in general is to be avoided, and low cycle fatigue failures in particular, the cyclic applied load must produce only elastic strains in all constituents. However, local plastic straining can be permitted in the composite during the first few load cycles, provided that the composite “shakes down” during these few cycles. The shakedown state is reached if the matrix cyclically hardens to a cyclic yield stress  $Y$  such that only elastic deformation occurs under the subsequent load cycles. Previous tests on annealed aluminum have shown that the fatigue limit coincides with the stable cyclic yield stress [16]; that is, the cyclic range was elastic. This is in accordance with Melan’s theorem [17] as well as others [18–20].

The application of Melan’s theorem to shakedown of unidirectional composites was presented in Ref 21, and the extension to laminate plates was discussed in Ref 13. These and other related results [22–24] describe a procedure for the determination of initial yield surfaces for composite laminates. The translation of these surfaces in the load space during plastic loading and their relation to shakedown envelopes also are described.

Figure 4 shows the ply yield surfaces for the case of a boron-aluminum plate under biaxial in-plane stresses  $S_{11}$  and  $S_{22}$ ;  $Y$  is the cyclic hardened

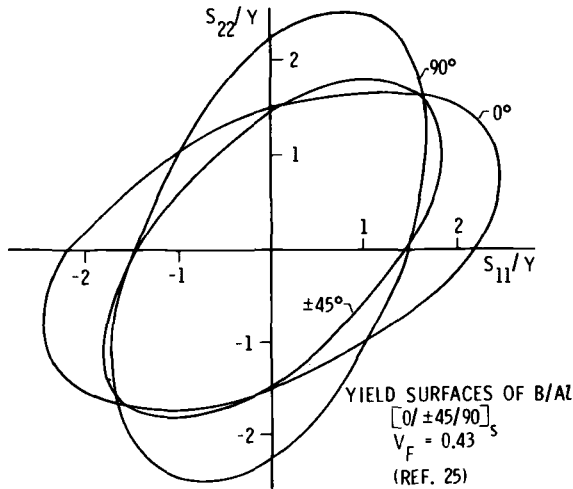


FIG. 4—Yield surfaces for plies of a boron-aluminum laminate. The  $S_{11}$  direction coincides with 0-deg fiber direction.

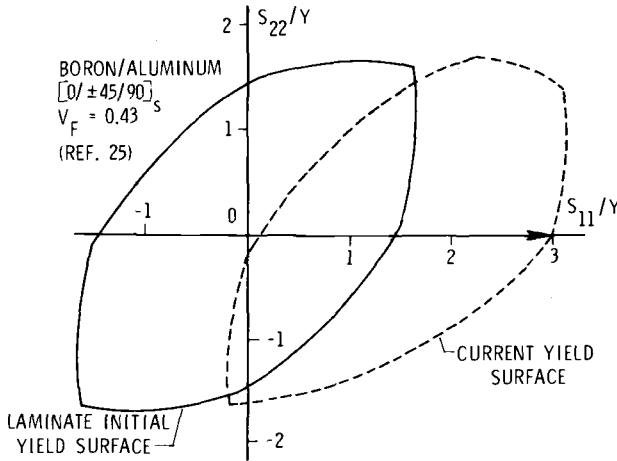


FIG. 5—Initial and current yield surfaces of a boron-aluminum laminate. The  $S_{11}$  direction coincides with 0-deg fiber direction.

yield strength of the aluminum matrix. Each of the plies has its own elliptical yield surface, constructed analytically from the ply matrix stresses and the Mises yield condition. The overall yield surface of the laminate is an internal envelope of the yield surfaces of individual plies.

Figure 5 shows this internal envelope (that is, the laminate initial yield surface) and the translation and deformation of this yield surface in the process of plastic loading to  $S_{11}/Y = 3.0$ . The deformation of the laminate yield surface is the result of the relative translation of the three ply yield surfaces in the biaxial loading plane. Each of the ply surfaces translates, according to its own hardening rule [23–25]. After loading to  $S_{11}/Y = 3.0$ , the composite will remain elastic for any loading path within the current yield surface. In the case of cyclic loading, the current yield surface will be the shakedown envelope, such as the envelope shown in Fig. 5. The shakedown stress range,  $\Delta S_{sh}$ , is the width of the shakedown envelope in the uniaxial loading direction.

$\Delta S_{sh}/Y$  is the dimensionless width of the internal envelope of the yield surfaces along the  $S_{11}$  load axis in Figs. 4 and 5. The analytically predicted magnitudes of  $\Delta S_{sh}/Y$  are listed in Table 2. In each case, the load applied is applied in the 0-deg fiber direction.

Unreinforced 6061–0 aluminum specimens were fatigue tested to determine the extent of cyclic hardening and the appropriate value for  $Y$  that may be expected for the matrix of the composite specimens. The average initial yield stress of six specimens was found to be 58.0 MPa (8.42 ksi). The maximum elastic stress range corresponded to the fatigue limit, which was 141 MPa (20.4 ksi) at  $2 \times 10^6$  cycles. The magnitude of matrix yield stress  $Y$  to be used in shakedown limit calculations was assumed to be 70.3 MPa (10.2 ksi), that is, to one half of the fatigue limit at  $R \approx 0.10$ . This  $R$  value is not quite

ideal because the matrix, within a composite containing 0-deg fibers, cycles between its tensile and compressive yield stress,  $Y$ , at  $R = -1.0$ . Assuming kinematic hardening behavior for the matrix material, the stress ratio effect is minimal. More details are available in Refs 13 and 14.

Table 2 presents the analytical shakedown range,  $\Delta S_{sh}$ , and the range determined from the regression analysis of the experimental data,  $\Delta S_R$ . The correlation is within 10 percent except for those laminates with 90-deg outer plies. This suggests that a stacking sequence effect exists.

### Simple Fatigue Damage Model

The decrease in elastic unloading modulus observed during fatigue cycling could be caused by matrix cracking, or fiber breakage, or both. Specimens were optically examined for fiber failure and matrix cracking after gradual etching of the surface layers of aluminum matrix in a 30 percent hydrochloric acid (HCl) solution in distilled water. Fiber failure was detected only in specimens subjected to stresses that approached the fatigue limit. However, substantial laminate modulus changes were detected well below this stress level. Those specimens that sustained modulus loss without failure had long matrix cracks which grew parallel to the fibers in the off-axis layers of the laminate. These cracks appeared to be mostly within the individual off-axis plies. They did not extend beyond the nearest layer of fibers that were not parallel to the matrix crack direction. Almost all of the observed modulus decrease is likely to be attributable to cracks in the matrix of the off-axis plies, since such cracks were the only observed damage of consequence. No split fibers were observed in specimens which failed by fatigue. The only split fibers observed were under the conditions described in the next section.

Figure 6 shows the matrix cracks in the 45-deg layer of a  $[0/\pm 45/90/0/\pm 45/90]_s$  specimen tested at  $S_{max} = 375$  MPa (54 ksi),  $R = 0.3$ , for  $2 \times 10^6$  cycles. The cracks are partially hidden behind the few remaining 0-deg (vertical) fibers (oriented in the vertical direction in Fig. 6). No matrix cracks were seen on the outer surface, other than an occasional H-crack [9,13] associated with a random broken 0-deg fiber.

Figure 7 reveals the matrix cracking in the second ply of a  $[0/90]_{2s}$  laminate specimen tested at  $S_{max} = 500$  MPa (72.5 ksi),  $R = 0.1$  for  $2 \times 10^6$  cycles.

A simple analysis was developed to relate the decrease in laminate unloading elastic modulus to the matrix damage. The off-axis plies were assumed to develop cracks during cyclic loading (above the shakedown stress range) so that the cracks opened during tensile loading; thus, the modulus is reduced under tensile loads in the matrix. However, for compressive loading the cracks close, so the modulus is unchanged. Figure 8 illustrates this behavior in terms of the applied laminate stress and the corresponding stresses in the matrix and 0-deg fibers. The laminate has an ideally elastic-plastic matrix

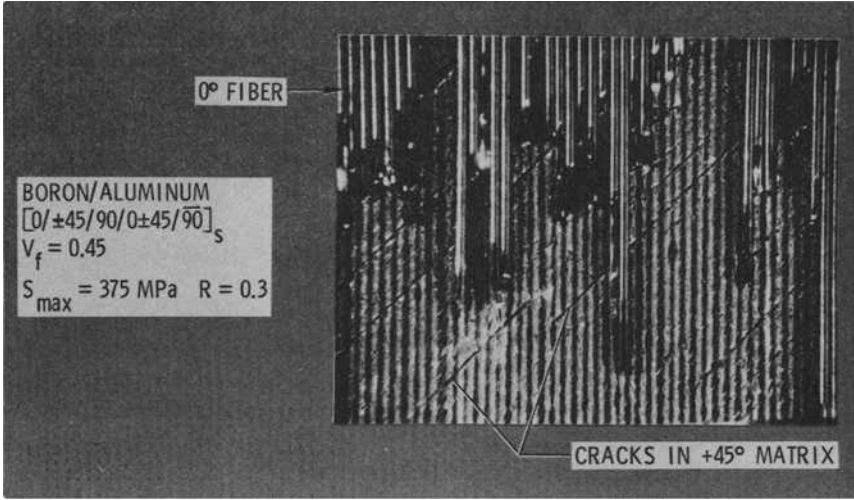


FIG. 6—Cracks in the +45-deg lamina matrix material.

(for illustration of the model and simplicity of presentation) and is subjected to a constant cyclic stress range,  $\Delta S$ . The matrix stress was assumed to cycle between  $+Y$  and  $-Y$  as shown in Fig. 8. The dashed lines in this figure represent the initial loading response. Accordingly, the first load cycle causes the matrix and 0-deg fiber stresses to follow the dashed loops. With subsequent cycling, the matrix cracks effectively decrease the overall matrix tensile modulus until an SDS is reached (that is, the matrix stiffness contribution is

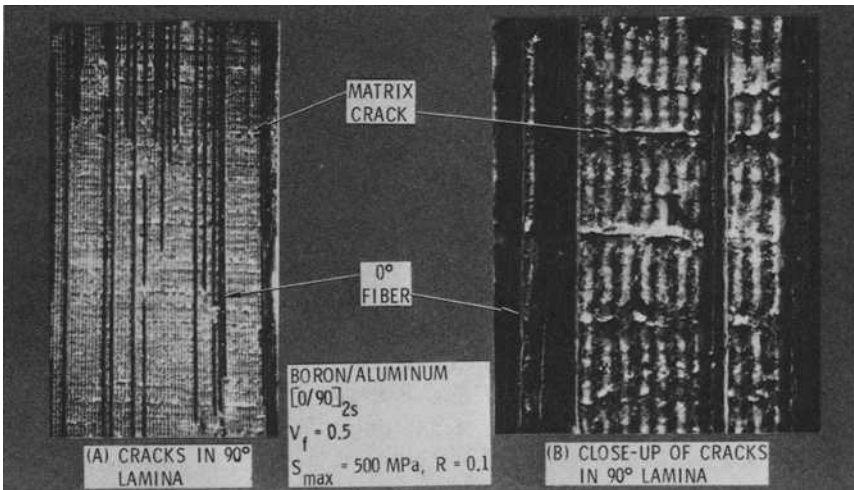


FIG. 7—Cracks in 90-deg lamina matrix material.

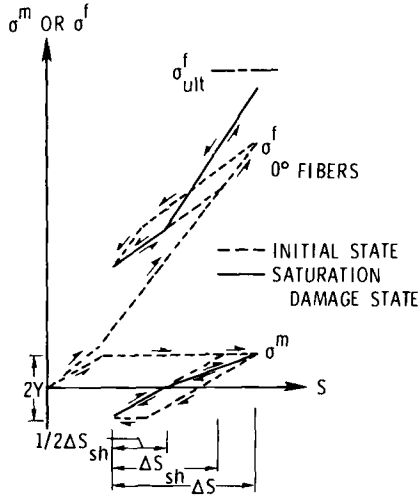


FIG. 8—Decreasing tensile matrix response and increasing 0-deg fiber stress as the laminate attains a saturation damage state.

lowered). The dashed loops narrow to zero-width loops, shown as solid lines; the lines represent the SDS. The SDS develops when the matrix cracking causes transfer of load to the 0-deg fibers, thus relieving the matrix from undergoing additional damaging plastic deformation. If the stress range,  $\Delta S$ , were increased, the effective tensile modulus of the matrix must decrease to again reach an SDS, which implies that more fatigue damage must occur by growing existing cracks and/or initiating new ones. The laminate elastic unloading modulus would then decrease even more. If the load transferred to the 0-deg fiber due to matrix cracking and overall laminate load causes the 0-deg fiber stress to exceed the fiber's endurance strength,  $\sigma_{ult}^f$ , no saturation damage state will develop; the laminate will fail. Notice in Fig. 8 that the required matrix damage for the SDS is independent of stress ratio, and is only a function of  $\Delta S$ .

The drop in matrix modulus in the load direction due to fatigue damage now will be evaluated. Figure 9 depicts the stress-strain curve of the saturation damage state that has developed in a hypothetical laminate. The strain in the matrix and laminate is plotted versus the matrix stress,  $\sigma^m$ , and laminate stress,  $S$ , respectively. The damage state has an associated cyclic strain range,  $\Delta \epsilon$ , that remains constant during an SDS [14]. If this cyclic strain range is known, an effective tensile modulus  $E_{eff}^m$  of the off-axis matrix material can be estimated. Note that  $E_{eff}^m$  is the modulus in the loading (0-deg fiber) direction. The compressive strain range of the matrix,  $\Delta \epsilon_{comp}^m$ , was approximated by

$$\Delta \epsilon_{comp}^m = \frac{\Delta S_{sh}}{2E_o} \tag{1}$$

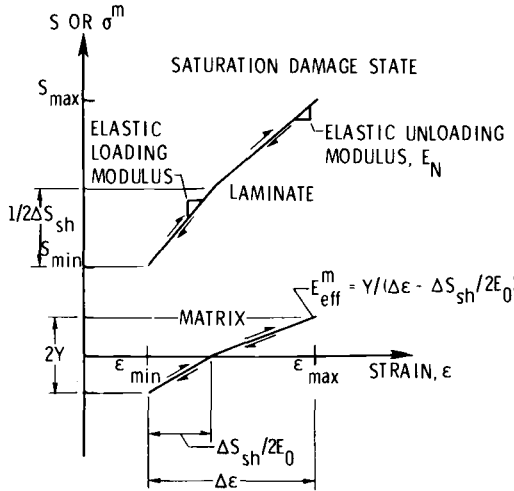


FIG. 9—Composite laminate and matrix stress-strain response for a saturation damage state.

where  $\Delta S_{sh}$  and  $E_o$  are the calculated shakedown stress range and initial laminate unloading elastic modulus, respectively. The effective tensile modulus of the off-axis matrix material now can be approximated by dividing  $Y$  by the cyclic strain minus the compressive portion

$$E_{eff}^m = Y / \left( \Delta\epsilon - \frac{\Delta S_{sh}}{2E_o} \right) \tag{2}$$

where  $Y = 70.3 \text{ MPa}$  (10.2 ksi) for laminates with 0-deg outer laminae, which correlated well with the shakedown analysis; however

$$E_{eff}^m = Y\phi / \left( \Delta\epsilon - \frac{\Delta S_{sh}}{2E_o} \right) \tag{3}$$

For the laminates with off-axis laminae on the outside the factor  $\phi$  is introduced to correct for the effects of stacking sequence on the shakedown stress range, and is defined as

$$\phi = \frac{\Delta S_R}{\Delta S_{sh}} \tag{4}$$

Notice that the values of  $\phi$  in Table 2 are near unity for laminates with 0-deg fibers on the surface, but are much smaller for laminates with off-axis laminae on the outside. The validity of the above assumptions and model can be evaluated for other arbitrary laminates that have developed an SDS by measuring the cyclic strains. The  $E_{eff}^m$  values can be calculated from the data in Tables 2 and 3 and the preceding equations.

The  $E_{eff}^m$  values were used as the matrix modulus in lamination theory (using the computer program AGLPLY [25]) to calculate the unloading elas-

TABLE 3—Saturation damage state predictions.

Layup	$S_{max}$ , MPa	$R$	$\Delta\epsilon \times 10^{-3}$	$E_{Al}^{eff}$ , MPa	$E_N/E_o$	
					Predicted	Experimental
[0] <sub>8</sub>	900	0.3	2.96	36 653	91	96
	800	0.1	3.40	29 813	89	94
[0/90] <sub>2s</sub>	450	0.1	2.88	24 410	71	63
	350	0.1	1.58	44 494	84	82
[90/0] <sub>2s</sub>	450	0.1	3.60	17 826	67	66
	250	0.1	1.70	46 029	85	83
[0/±45/90] <sub>s</sub>	225	0.1	2.10	47 954	79	76
	200	0.1	1.60	72 450	100	89
[90/±45/0] <sub>s</sub>	180	0.1	1.70	39 287	70	75
	160	0.1	1.40	49 712	80	83
[0±45/90/0/±45/90] <sub>s</sub>	350	0.1	3.7	22 802	42	51
	275	0.1	2.0	50 831	83	79

tic modulus of the composite in its SDS. All the fibers were assumed to be intact, and matrix damage was assumed to be characterized by its lower modulus,  $E_{eff}^m$ . Although such a formulation implicitly assumes that the matrix modulus is reduced isotropically, the reduction really is orthotropic. However, since we are interested in the laminate modulus in the loading direction only, the assumption should not introduce excessive error. Table 3 presents the results obtained at two cyclic stress levels for each laminate. The predicted and experimental  $E_N/E_o$  values are presented for comparison. The good correlation between these experimental and predicted values lends validity to the model illustrated by Figs. 8 and 9. Therefore, if the cyclic strain range is known for a particular metal matrix composite laminate, a good quantitative approximation of the matrix fatigue damage in terms of elastic modulus reduction can be calculated.

It is suggested further that an SDS can be maintained only within laminate specimens that contain 0-deg or near 0-deg laminae. The 0-deg laminae enable the matrix to reach a damage state such that the matrix stresses,  $\sigma^m$ , are low enough that damage no longer accumulates. In other words, it is expected that an angle-ply laminate specimen, such as  $(\pm 45)_s$ , would fail at approximately the laminate shakedown stress range since, once the fatigue damage starts, it could end only in failure of the laminate. Menke and Toth [7] present S-N data for  $\pm 45$ -deg cross-ply boron-aluminum 6061 specimens, with  $V_f = 0.60$ . The fatigue limit, at  $2 \times 10^6$  cycles and  $R = 0.0$ , was 138 MPa (20 ksi). The S-N curve was very flat. The initial yield surface of this laminate was calculated, as discussed earlier in this paper, and resulted in a shakedown range of 2.14  $Y$ . Assuming the  $Y$  for Menke and Toth's matrix is equal to the matrix material tested in this program, the shakedown range for a  $\pm 45$  laminate with  $V_f \approx 0.6$  is  $\Delta S_{sh} = 150$  MPa (21.7 ksi), which agrees well with the experimental data (that is, 138 MPa). Therefore, the angle-ply laminate specimens probably do not reach a saturation damage state, but fail

at approximately the laminate shakedown stress range due to matrix cracking.

**Stacking Sequence Effect**

As shown earlier, laminates with 90-deg outer plies tends to accumulate fatigue damage at a lower stress level than a similar laminate with 0-deg outer plies (Table 3). An examination of the behavior of  $[0/90]_{2s}$  and  $[90/0]_{2s}$  laminate specimens cut from the same plate will now illustrate this.

Figure 10 presents curves depicting modulus loss, due to  $2 \times 10^6$  cycles of fatigue, versus the cyclic stress range for both  $[0/90]_{2s}$  and  $[90/0]_{2s}$ . Notice that the  $[90/0]_{2s}$  accumulates damage at a lower fatigue stress range. However at the high stress, that is, 400 MPa (58 ksi), the damage is nearly equal for both laminates.

Further evidence of the stacking sequence effect is found in a series of micrographs of  $[90/0]_{2s}$  specimens, shown in Fig. 11. The micrographs are of the failure surface with the 90-deg fibers in the plane of the page. Each specimen presented was tested at a different stress level for  $2 \times 10^6$  fatigue cycles and then pulled for residual strength. Notice in Fig. 11a [ $\Delta S = 202.5$  MPa (29 ksi)] that the 90-deg fibers are split longitudinally in all of the 90-deg plies. The 90-deg fibers split through the tungsten core, which is sometimes visible as a line in the middle of the fiber. This is an indication of very little fatigue damage in the matrix before the residual strength test. The transverse static strength of the boron fiber appears to be less than the undamaged matrix material. Merke and Toth [7] have made similar observations. The speci-

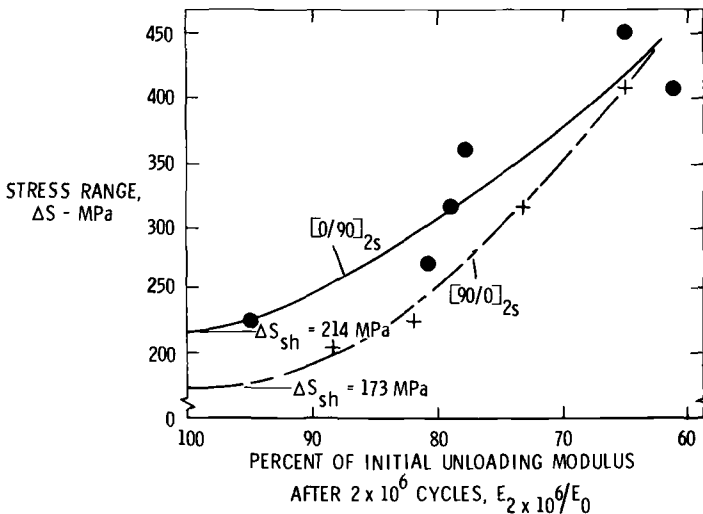


FIG. 10—Change in elastic unloading modulus of  $[0/90]_{2s}$  and  $[90/0]_{2s}$  specimens for a range of applied stress.

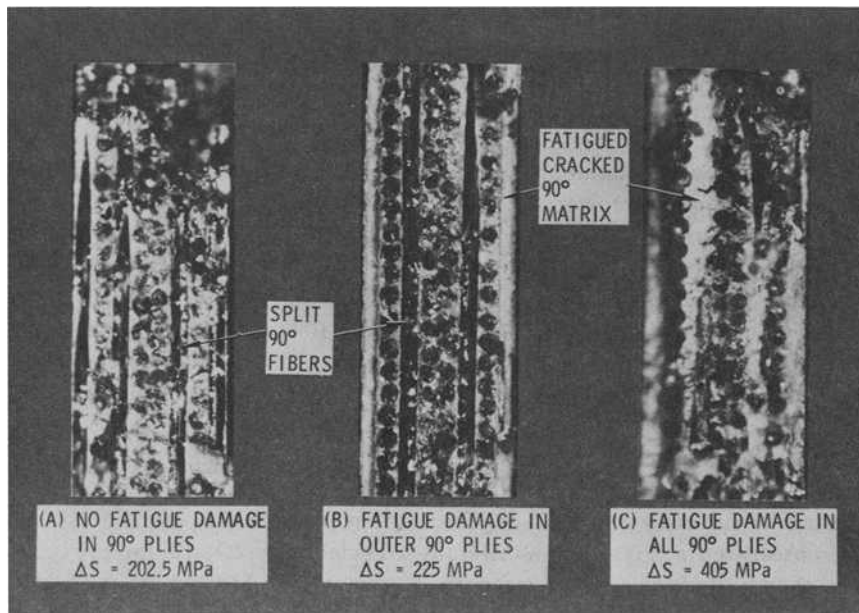


FIG. 11—Fracture surfaces indicating the degree of fatigue cracking present,  $[90/0]_{2s}$ ,  $R = 0.1$ .

men shown in Fig. 11b [ $\Delta S = 225$  MPa (33 ksi)] indicates cracks in the outer 90-deg plies, since the inner 90-deg plies still failed through the fibers, whereas the outer plies failed through the weaker cracked matrix. These cracks in the outer 90-deg plies also were visible on the surface. [Notice in Fig. 10 that at a stress range equal to 225 MPa (33 ksi) the  $[90/0]_{2s}$  laminate had lost 18 percent of the initial modulus, whereas the  $[0/90]_{2s}$  laminate lost only 5 percent. When examined, the  $[0/90]_{2s}$  specimen revealed no significant surface damage, fiber damage, or cracks in internal ply matrices.] Figure 11c [ $\Delta S = 405$  MPa (59 ksi)] shows extensive matrix damage in all four 90-deg plies. A  $[0/90]_{2s}$  specimen tested at the same stress level also showed as much damage.

Hancock [5] stated that the fatigue damage in a composite laminate could initiate from surface imperfections. However, as previously discussed, the microscopic examinations showed that the only surface cracking found on the 0-deg outer layer were the H-cracks that were associated with broken 0-deg fibers. The microscopic examination further revealed that the 0-deg lamina had a crack arresting capacity for cracks growing other than parallel to the fibers. Long matrix cracks in the +45 and 90-deg lamina (Figs. 6 and 7) grew to the edge of the 0-deg fibers without causing 0-deg fiber failure or growing past the 0-deg fibers to the free surface. Therefore, if potential crack initiation sites existed on the free surface, it is doubtful that they could initiate and grow because of the restraint of the 0-deg fibers.

However, with the 90-deg fibers on the free surface, the surface defects could indeed cause early crack initiation and growth. Figure 11*b* illustrates the crack growth in the outer 90-deg surface as opposed to little or no cracking in the inner two 90-deg plies. This can be explained by the use of fracture mechanics. Assume that there exist two tiny flaws of the same dimension  $a$ , one of the free surface in the form of a “thumbnail” type flaw, and one in the form of a “penny” shaped flaw embedded in the matrix of an inner 90-deg lamina, as shown in Fig. 12. The stress intensity range,  $\Delta K$ , for these two types of flaws are as follows

Surface “thumbnail” flaw [26]

$$\Delta K_{th} = 1.1 \Delta\sigma_s \sqrt{\pi a} \tag{5}$$

where  $\Delta K_{th}$  is the threshold stress intensity range, below which no crack growth will occur, and  $\Delta\sigma_s$  is the corresponding threshold stress.

Embedded “penny” shaped flaw [27]

$$\Delta K_{th} = \frac{2 \Delta\sigma_e \sqrt{a}}{\sqrt{\pi}} \tag{6}$$

The preceding equations were solved for the threshold stress ratio to obtain

$$\frac{\Delta\sigma_e}{\Delta\sigma_s} = \frac{\frac{\Delta K_{th}}{2\sqrt{a}}}{\frac{\Delta K_{th}}{1.1\sqrt{\pi a}}} = 1.73 \tag{7}$$

This implies that the stress required to grow an embedded flaw in the inner 90-deg lamina is 1.73 greater than the stress required to grow a surface flaw of the same size. Thus a  $[90/0]_{2s}$  laminate would develop fatigue damage at a lower stress in the outer ply than a  $[0/90]_{2s}$  laminate in the inner ply. This explanation, which pertains to homogeneous isotropic materials, is not intended to apply rigorously to the composites in question, since they are anisotropic in nature, but to suggest a qualitative trend.

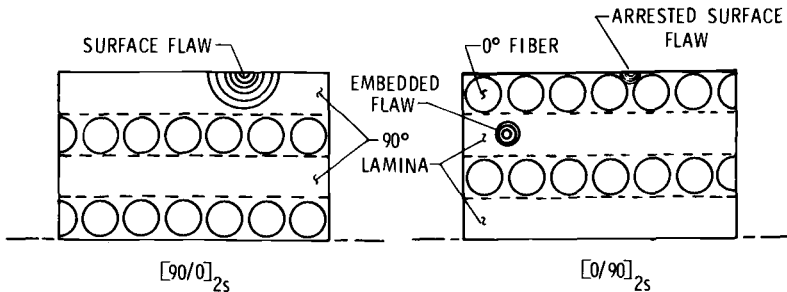


FIG. 12—Schematic of possible crack initiation sites.

In summary, it appears that the crack initiations on the free surface have little effect if the 0-deg fibers are on the outer plies, due to the crack arresting capabilities of the fibers and the lower matrix stress. In this case, the cracks initiate within the inner, off-axis lamina matrix. However, if off-axis plies (such as 90-deg) are on the outside, surface flaws may grow at stresses lower than those predicted from shakedown. Results similar to those discussed in this section were found for  $[0/\pm 45/90]$ , and  $[90/\pm 45/0]$ , laminates [14].

### Load History Effect

Three  $[0/\pm 45/90/0/\pm 45/\overline{90}]$ , specimens were subjected to simple load variations; the corresponding fatigue damage in terms of unloading elastic modulus loss was monitored. Figure 13 presents results from a single specimen tested at  $R = 0.1$  when  $S_{max}$  was increased stepwise. The cycling at a given level was continued until a relatively stable value of damage was reached (that is, no significant drop in modulus with additional cycling). For reference, the data previously presented in Fig. 5 are shown as dashed lines in Fig. 13. The test was conducted first at maximum stress ( $S_{max}$ ) of 210 MPa (30 ksi); this resulted in a modulus drop to about 97 percent. This loss seems to be consistent with the dashed line for 225 MPa (33 ksi). The  $S_{max}$  then was raised to 275 MPa (40 ksi), which resulted in a loss to about 73 percent (slightly lower than the dashed 275 MPa data). The test specimen then was subjected to  $S_{max} = 337$  MPa (49 ksi), which caused further drop in modulus to about 58 percent, which is slightly above the dashed line for 350 MPa (51 ksi). The test results of Fig. 13 imply that a laminate will seek the SDS associated with the current value of  $S_{max}$  if  $S_{max}$  is the largest in the loading history.

The response of a laminate subjected to a constant stress range [that is, 225 MPa (33 ksi)], but with varying values of  $S_{max}$  was investigated. Figure 14 indicates that the modulus drops when  $S_{max}$  is shifted upward. As expected, the modulus did not decrease when  $S_{max}$  was lowered from 325 to 275 MPa (47 to 40 ksi).

Additional data are presented in Fig. 15. Again the stress range was constant [ $\Delta S = 225$  MPa (33 ksi) until the last loading segment]. The shift from  $S_{max} = 325$  to 300 MPa (47 to 44 ksi) resulted in a gradual modulus decrease of approximately 2 percent. The 300 to 325 MPa (44 to 47 ksi) shift upward in Fig. 14 resulted in a decrease of more than 4 percent. No detectable damage was created by decreasing  $S_{max} = 300$  to 250 MPa (44 to 36 ksi). The  $S_{max}$  then was increased to 325 MPa (47 ksi), and additional damage resulted. Finally, this maximum stress then was held at 325 MPa (47 ksi), and the stress range increased such that  $R = 0.1$ . The damage resulted in a modulus loss of approximately 36 percent, which is close to what one might expect from Fig. 5.

From observations of these three tests, two phenomena seem obvious:

1. For a given stress ratio, the specimen seeks the SDS for the largest  $S_{max}$

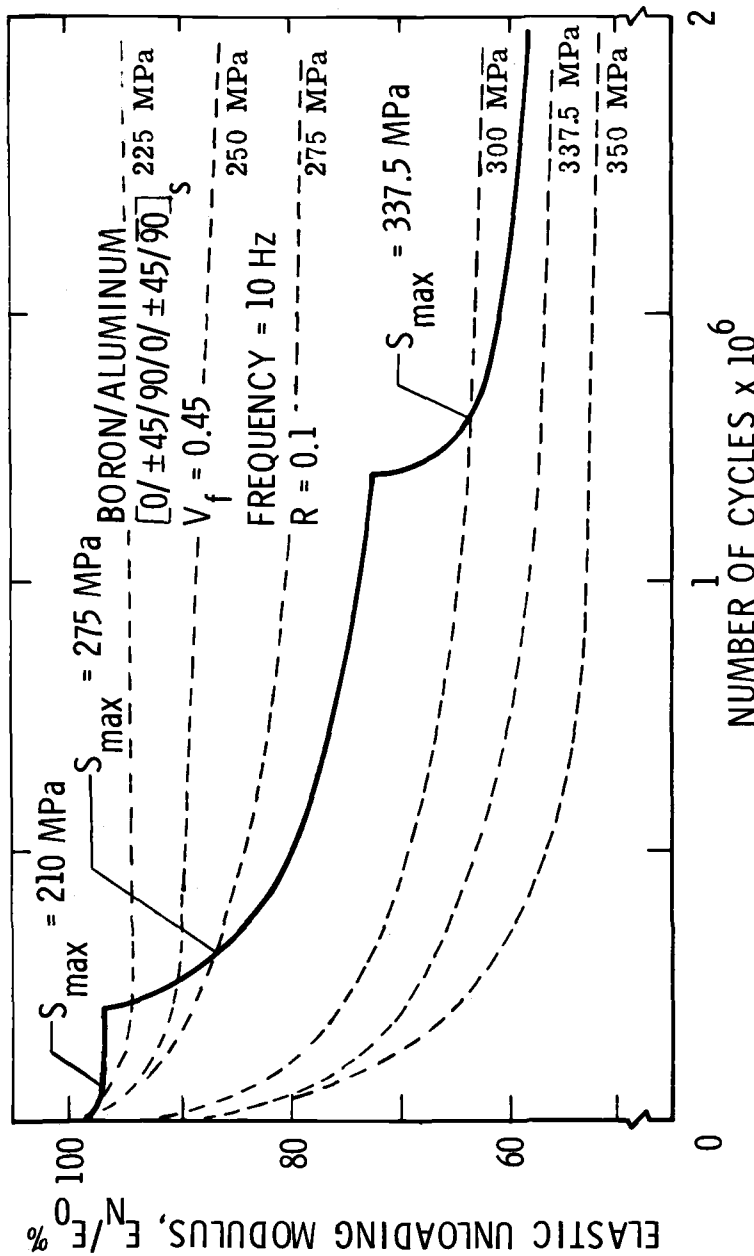


FIG. 13—Change in elastic unloading modulus of a  $[0/\pm 45/90/0/\pm 45/90]_S$  specimen with increasing  $S_{max}$  at a constant  $R = 0.1$ .

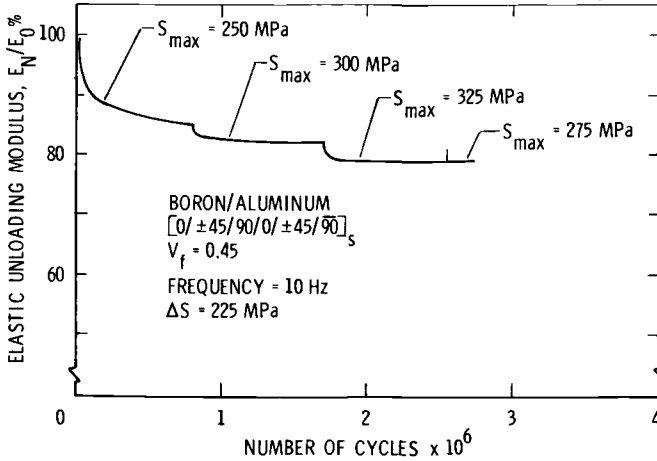


FIG. 14—Change in elastic unloading modulus under constant stress range and varying maximum stress (primarily increasing  $S_{max}$ ).

to which it is subjected. The simple damage accumulation model in Fig. 8 may be used to give a possible explanation of this phenomenon. An increase in the cyclic stress range above the shakedown range must result in an increase in the amount of matrix fatigue damage to re-establish a new saturation damage state. Once the new saturation damage state is established, reducing the stress range within the  $\Delta S$  range on Fig. 9 clearly will result in no additional damage.

2. For a constant stress range, relatively negligible modulus drop is generated by shifting the mean stress downward, whereas significant loss may be created by shifting the mean stress upward. This second phenomenon is attributed to the tensile plastic deformation and the opening and extension of

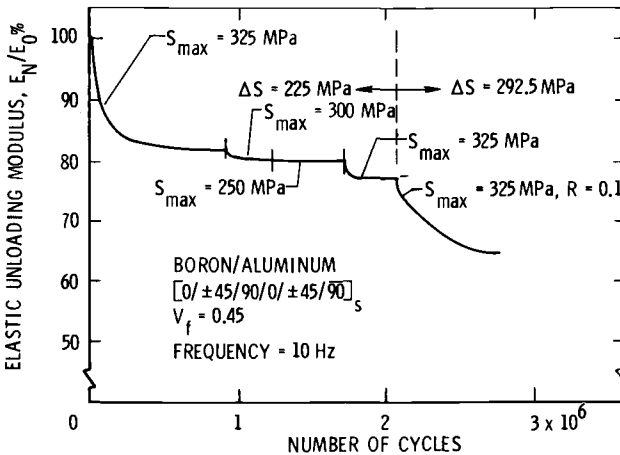


FIG. 15—Change in elastic unloading modulus under a variable loading program.

the existing cracks during the upward shift of the stress range. The previously presented model, Fig. 8 and 9, does not account for this drop in modulus due to increasing the mean stress. It is clear, however, from Fig. 8 that a downward shift of the stress range would result in a compressive yielding of the matrix, which would not serve to open or extend the present cracks further. Thus, raising the cyclic mean stress would be more damaging than lowering it.

Although the variable load history tests were simple, they revealed some interesting implications for fatigue response under complex spectrum loads. For example, Miner's cumulative damage would not apply. For constant amplitude tests the fatigue damage was found to be a function of stress range, but not mean stress. However, if one were to use the shakedown stress range and randomly change the mean, fatigue damage would result from the plastic deformation required each time the mean was shifted. In this manner, it is not so much the cyclic load causing the damage as the plastic excursion between cyclic levels.

### **Concluding Remarks**

A shakedown analysis for annealed matrix, metal matrix composites was shown to predict the stress amplitude below which no fatigue damage accumulated in laminate with 0-deg fibers on the outside.

A simple fatigue damage accumulation analysis was presented which adequately described the relationship between matrix modulus drop due to matrix fatigue cracks and overall laminate properties. A method for predicting changes in the laminate properties was developed. It is based upon a model that envisions an SDS to be able to exist during constant amplitude fatigue loading.

Data were presented to show the difference in fatigue response of laminates that differed only in stacking sequence; some laminates had 0-deg plies on the surface, whereas the others had 90-deg plies on the outside surface. The 90-deg plies on the surface developed cracks earlier than predicted by shakedown. An attempt was made to explain this stacking sequence effect.

Variable load history effects on the fatigue damage response were investigated by simple tests. These tests revealed that, for a given stress ratio, the specimen seeks the SDS for the largest stress range to which it is subjected. It also was found that relatively negligible modulus loss results when shifting a given cyclic stress range down, whereas significant damage may be created by shifting upward.

### *Acknowledgment*

Most of this work was conducted by the author at Duke University under the supervision of G. J. Dvorak, presently at the University of Utah, and

sponsored by the Army Research Office. The C-scan equipment at Virginia Polytechnic Institute and State University was used for the ultrasonic inspections.

## References

- [1] Baker, A. A., *Journal of Materials Science*, Vol. 3, 1968, pp. 412-423.
- [2] Baker, A. A., Braddick, D. M., and Jackson, P. W., *Journal of Materials Science*, Vol. 7, 1972, pp. 747-762.
- [3] Jackson, P. W., Baker, A. A., and Braddick, D. M., *Journal of Materials Science*, Vol. 6, 1971, pp. 427-438.
- [4] Shimizu, H. and Dolowy, J. F., Jr. in *Composite Materials: Testing and Design, ASTM STP 460*, American Society for Testing and Materials, 1969, pp. 192-202.
- [5] Hancock, J. R. in *Composite Materials*, Vol. 5, *Fracture and Fatigue*, L. J. Broutman, Ed., Academic Press, New York, 1974.
- [6] Toth, I. J. in *Composite Materials: Testing and Design, ASTM STP 460*, American Society for Testing and Materials, 1969, pp. 236-253.
- [7] Menke, G. D. and Toth, I. J., "The Time Dependent Mechanical Behavior of Metal Matrix Composites," AFML-TR-71-102, Air Force Materials Laboratory, Sept. 1971.
- [8] Christian, J. L. in *Fatigue of Composite Materials, ASTM STP 569*, American Society for Testing and Materials, 1975, pp. 280-294.
- [9] Gouda, M., Prewo, K. M., and McEvily, A. J. in *Fatigue of Fibrous Composite Materials, ASTM STP 723*, American Society for Testing and Materials, 1981, pp. 101-115.
- [10] White, M. K. and Wright, M. A., *Journal of Material Science*, Vol. 14, 1979, pp. 653-662.
- [11] Stinchcomb, W. W., Reifsnider, K. L., Marcus, L. A., and Williams, R. S. in *Fatigue of Composite Materials, ASTM STP 569*, American Society for Testing and Materials, 1975, pp. 115-129.
- [12] Mayfield, J., *Aviation Week and Space Technology*, 8 Jan. 1979, pp. 35-41.
- [13] Dvorak, G. J. and Johnson, W. S., *International Journal of Fracture*, Vol. 16, No. 6, Dec. 1980, pp. 585-607.
- [14] Johnson, W. S., "Characterization of Fatigue Damage Mechanisms in Continuous Fiber Reinforced Metal Matrix Composites," Ph.D. dissertation, Duke University, Dec. 1979.
- [15] Dvorak, G. J. and Tarn, J. Q. in *Fatigue of Composite Materials, ASTM STP 569*, American Society for Testing and Materials, 1975, pp. 145-168.
- [16] VanHorn, K. R., Ed., *Aluminum*, Vol. 1, American Society for Metals, Metals Park, Ohio, 1967, p. 183.
- [17] Melan, E., "Zur Plastizität des Räumlichen Kontinuums," *Ingenieur-archiv Gesellschaft fuer Angewandte Mathematik und Mechanik* (Berlin), Vol. 9, 1938, p. 116.
- [18] Symonds, P. S., *Journal of Applied Mechanics*, Vol. 18, 1951, p. 85.
- [19] Maier, G., *Meccanica*, Vol. 4, 1969, p. 250.
- [20] Koiter, W. T., *Proceedings of the Koninklijke Akademie van Wetenschappen te Amsterdam*, Amsterdam, Series B59, No. 1, 1956, p. 24.
- [21] Tarn, J. Q., Dvorak, G. J., and Rao, M. S. M., *International Journal of Solids and Structures*, Vol. 11, 1975, pp. 751-764.
- [22] Dvorak, G. J., Rao, M. S. M., and Tarn, J. Q., *Journal of Applied Mechanics*, Vol. 4, 1974, pp. 249-253.
- [23] Dvorak, G. J. and Bahei-El-Din, Y. A., "Plasticity of Composite Laminates," *Proceedings of Research Workshop on Mechanics of Composite Materials*, Duke University, 17-18 Oct. 1978.
- [24] Bahei-El-Din, Y. A. and Dvorak, G. J. in *Modern Developments in Composite Materials and Structures*, J. R. Vinson, Ed., American Society of Mechanical Engineers, New York, 1979, pp. 123-147.
- [25] Bahei-El-Din, Y. A., "Plastic Analysis of Metal-Matrix Composite Laminates," Ph.D. dissertation, Duke University, July 1979.
- [26] Johnson, W. S. in *Part-Through Crack Fatigue Life Prediction, ASTM STP 687*, American Society for Testing and Materials, 1979, pp. 143-155.
- [27] Tada, H., Paris, P. C., and Irwin, G. R., *The Stress Analysis of Cracks Handbook*, Del Research Corp., Hellertown, Pa., 1973, p. 24.1.

# Stiffness-Reduction Mechanisms in Composite Laminates

---

**REFERENCE:** Highsmith, A. L. and Reifsnider, K. L., "Stiffness-Reduction Mechanisms in Composite Laminates," *Damage in Composite Materials, ASTM STP 775*, K. L. Reifsnider, Ed., American Society for Testing and Materials, 1982, pp. 103-117.

**ABSTRACT:** It now is recognized widely that stiffness changes during the service loading of composite laminates can be significantly large, especially as those changes affect deflections, dimensional changes, vibration characteristics, and load or stress distributions. Several generic sources of stiffness change can be identified, in various degrees, in fibrous composite materials. The source which occurs quite early in the life of a specimen or component is matrix cracking, the subject of this paper. While most laboratories now report stiffness changes, very little systematic philosophy has been developed to account for and explain such stiffness changes. The complexity of this situation requires systematic study, and motivates the search for a model, or models, which can describe the behavior and predict unfamiliar response. The present paper reports the results of an experimental program and an analytical modelling exercise which indicate that much of the observed matrix cracking can be predicted and the effects on stiffness calculated with various degrees of accuracy depending upon the sophistication of the model used.

**KEY WORDS:** composite materials, stiffness, matrix (transverse) cracking, crack density, characteristic damage state (CDS), laminate

One of the primary differences between the mechanical response of fiber reinforced composite laminates and that of more conventional structural materials, such as aluminum and steel, is that the damage that develops in such composites is generally much more complex. In traditional engineering materials, one particular flaw usually accounts for failure. In laminated composites, numerous defects above the atomic level but still microscopic in nature may contribute to the eventual failure of the material, including transverse cracking, delamination, fiber breakage, and fiber-matrix debonding. This investigation studies degradation of the mechanical response of composite materials, as determined via stiffness measurements, resulting from transverse cracking.

The three most important mechanical properties of structural materials are strength, stiffness, and life. Measurement of strength or life during dam-

<sup>1</sup> Graduate research assistant and professor, respectively, Engineering Science and Mechanics Department, Virginia Polytechnic Institute and State University, Blacksburg, Va. 24061.

age development in a material is not feasible, because only one such measurement can be made for one specimen, and as yet it is very difficult to compare damage states between two specimens. On the other hand, stiffness can be measured frequently during damage development, and can be measured without further degrading the material. Therefore, stiffness is a potential nondestructive test parameter which could be used to monitor the damage which develops in a component during service, and to establish residual strength and life. Numerous such applications of stiffness change as a measure of damage development have been cited in the literature [1].<sup>2</sup>

Previous investigations in which stiffness as well as other parameters, such as ultrasonic attenuation and acoustic emission, were monitored during damage development were primarily qualitative in nature [2]. With regard to transverse cracking, the most important discovery was that of the characteristic damage state (CDS). It was noticed that after sufficient loading the off-axis plies in a laminate reach a saturation state, wherein the distance between consecutive cracks in a particular ply is nearly uniform throughout the specimen. Hence, the cracking which appears in all off-axis plies in this state forms a distinctive pattern, and is referred to as the characteristic damage state; this pattern can be predicted by a shear lag analysis [3].

This study is the quantitative extension of previous work. After obtaining considerable insight into the physics of the problem, relationships (not merely trends) between crack density and stiffness were sought. One of the first difficulties to be overcome was that in the previous studies, axial behavior was so dominated by the 0-deg plies that laminate stiffness changes were small. For this investigation,  $[0,90_3]_s$ ,  $[90_3,0]_s$ ,  $[0,90]_s$ , and  $[0,\pm 45]_s$  glass-epoxy laminates were studied. A glass-epoxy material system was chosen because the ratio of transverse to longitudinal moduli for a lamina ( $E_2/E_1$ ) for this material is large in comparison to that of other advanced composites. The laminate load carried by off-axis plies, particularly 90-deg plies, is significant, and stiffness changes resulting from transverse cracking in these situations also will be significant. And while the first two laminates listed may not be of great practical value, their stiffness changes due to cracking are large enough to provide a critical test for an analysis, and also to allow a check for stacking sequence dependence. The remaining two laminates provide different constraint cases and different off-axis plies to further test our analysis.

Finally, a long term goal is the ability to both classify and quantify damage in a composite laminate. Since the three principal damage modes—transverse cracking, delamination, and fiber breakage—may all contribute to the degradation of the mechanical response of the laminate, no single stiffness measurement will suffice even to classify the damage. In addition, structural designs may depend on several stiffness components. Therefore, to

<sup>2</sup>The italic numbers in brackets refer to the list of references appended to this paper.

achieve the desired goal, information concerning the degradation of several components of stiffness with increasing damage will be required to determine fully the damage state of the material.

### Analysis

In order to determine how transverse cracking in off-axis plies affects the stiffness of the overall laminate, the stress state in the vicinity of such cracks must be found. Talug has formulated a finite difference solution to such a problem [4]. The laminate is assumed to be symmetric and infinite in width (the  $y$  direction). The  $x$ -axis is chosen to be the load direction, and the  $z$ -axis is chosen through the thickness, with  $z = 0$  at the midplane. The finite difference solution is applied to the first quadrant of the  $x$ - $z$  plane, with cracks inserted along  $x = 0$ . The principal reason for using this technique is that it yields a full-field solution; all six stress components are determined throughout the laminate in the presence of a crack. One then can determine the distance from the crack over which the stresses in the  $x$ - $y$  plane are redistributed to reach essentially laminate analysis values. Also, the out of plane stresses  $\sigma_z$ ,  $\tau_{xz}$ , and  $\tau_{yz}$ , stresses which may initiate delamination, are determined in the vicinity of a crack. To determine the precise nature of damage propagation and crack growth into adjacent plies, such a full-field solution is essential.

The finite difference solution does present some difficulties. Due to the large core requirements for the solution of the resulting algebraic equations, a computer implemented solution is limited to relatively simple laminates. In our case, Talug's numerical solution can analyze symmetric laminates of no more than eight plies. Further, with the discovery of the characteristic damage state it is unnecessary to know all of the details of the stress field, as it is unnecessary to know the precise details of crack growth throughout the laminate.

Reifsnider has developed a one-dimensional model which can approximate normal stress in the load direction  $\sigma_x$  in the various plies of a cracked laminate [2]. Careful examination of edge replicas of crack patterns in specimens of various materials shows that shear deformations in any given ply are restricted to a thin region in the vicinity of interfaces of that ply with adjacent plies. Further, this region tends to be resin-rich, and thus is less stiff in response to shear loads than the central portion of the lamina. Transverse cracks extend up to this region, but usually do not extend into it. In the one dimensional model that follows, this thin region is assumed to be a shear transfer region. This approach is similar to that used by Zweben in modeling the strength of notched laminates [5].

Figure 1 shows a typical one-dimensional equilibrium element for a ply within a laminate, Ply  $i$ . The thickness of the ply is  $a_i$ , and the thickness of the shear transfer region is  $b$ ; in the figure, the ply is shown to be cracked. At a crack surface, the stress in the ply is zero, but away from the crack, the

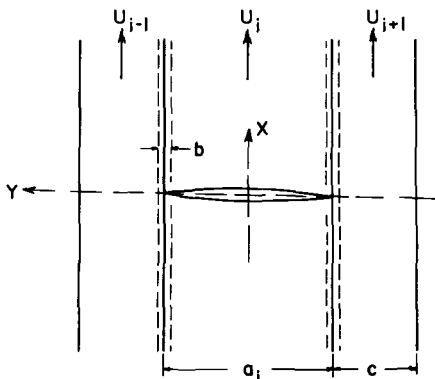


FIG. 1.—Equilibrium element used in formulation of shear lag model.

stress is nonzero; load is transferred back into the middle Ply  $i$  from the constraining Plies  $i - 1$  and  $i + 1$  via shear transfer across the thickness  $b$ . The equilibrium equation for such a ply is

$$a_i E_i \frac{d^2 U_i}{dx^2} - \frac{2G}{b} (U_i - U_{i-1}) - \frac{2G}{b} (U_i - U_{i+1}) = 0 \tag{1}$$

where  $E_i$  is the longitudinal modulus of the middle ply,  $G$  is the shear modulus in the shear transfer region, and  $U_{i-1}$ ,  $U_i$ , and  $U_{i+1}$  are displacements in Plies  $i - 1$ ,  $i$ , and  $i + 1$ , respectively. If the substitutions  $x = b\xi$ ,  $U_i = bu_i$ ,  $U_{i-1} = bu_{i-1}$ , and  $U_{i+1} = bu_{i+1}$  are made, Eq 1 can be written in nondimensional form as

$$\frac{E_i a_i}{2Gb} \frac{d^2 u_i}{d\xi^2} + u_{i-1} - 2u_i + u_{i+1} = 0 \tag{2}$$

There are two special cases of Eq 1 which need to be considered. Suppose Ply  $i$  is an exterior ply of a laminate, so that there is no Ply  $i - 1$  to constrain it. Then the shear lag contribution from Ply  $i - 1$ ,  $(2G/b)(U_i - U_{i-1})$ , must be eliminated from Eq 1, since the left surface of Ply  $i$  is a free surface. The resulting equation written in nondimensional form is

$$\frac{E_i a_i}{2Gb} \frac{d^2 u_i}{d\xi^2} - u_i + u_{i+1} = 0 \tag{3}$$

The other special case arises when one surface of Ply  $i$  is the midplane of a symmetric laminate. For example, if Plies  $i$  and  $i - 1$  are plies on either side of the midplane of such a laminate, then  $(2G/b)(U_i - U_{i-1}) = 0$  from symmetry, since  $U_i = U_{i-1}$ . This result yields an equation which is identical to that which was obtained for an exterior ply.

The assembly of the governing equations discussed previously for the plies

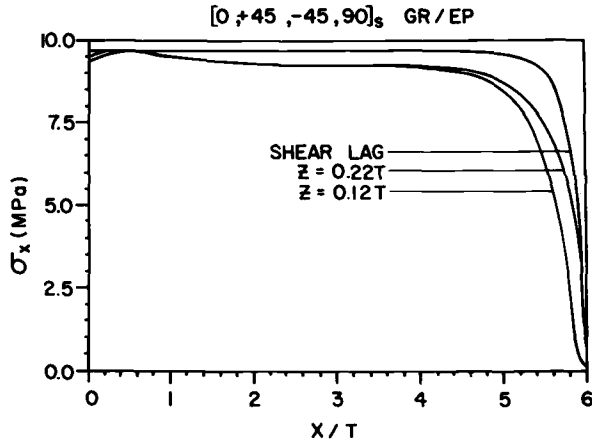


FIG. 2.—Normal stress distribution in cracked 90-deg ply of a  $[0, \pm 45, 90]_s$  graphite-epoxy laminate predicted by finite difference and shear lag models.

within a laminate yields a system of coupled, second order differential equations in displacements. This system is similar in nature to those obtained for coupled oscillator problems, and the solutions take the form of sums of characteristic solutions multiplied by arbitrary constants. The application of boundary conditions, including stress-free surfaces at transverse crack faces, applied displacements, and applied strains, determines the arbitrary constants.

In Fig. 2, a comparison is made between the normal stress distributions in the cracked 90-deg plies of a  $[0, \pm 45, 90]_s$  graphite-epoxy laminate predicted by the shear lag and finite difference models. For the finite difference model, an aspect ratio  $L/T = 6$ , where  $T$  is the laminate half-thickness, was used. The crack was placed at  $X/T = 6$  in both cases. Material properties are shown in Table 1. The finite difference results show that there is a normal stress gradient through the thickness, but near the center of the ply ( $Z < 0.12T$ ) that gradient is not very pronounced. This affirms the existence of a shear lag region. The shear lag model is stiffer than the finite difference model but the stresses are similar to those predicted by the finite difference model as  $Z$  approaches  $0.5T$ , the interface between the 0 and  $-45$ -deg plies. Both models indicate that the stress level becomes constant at approximately  $X/T = 4.5$ . Figure 3 shows that similar trends exist in a  $[0, 90, \pm 45]_s$  graphite-epoxy laminate with cracked 90-deg plies. Note that due to the different constraint on the 90-deg plies, a stable stress level is reached at  $X/T = 5.0$ , which

TABLE 1—Material properties for graphite-epoxy and glass-epoxy.

Material	$E_1$ , GPa	$E_2$ , GPa	$\nu_{12}$	$G_{12}$ , GPa	$G_{23}$ , GPa	$G$ , GPa	$a$ , mm	$b$ , mm
Graphite-Epoxy	142	9.85	0.30	4.48	3.37	1.38	0.127	0.013
Glass-Epoxy	41.7	13.0	0.300	3.4	...	1.38	0.203	0.041

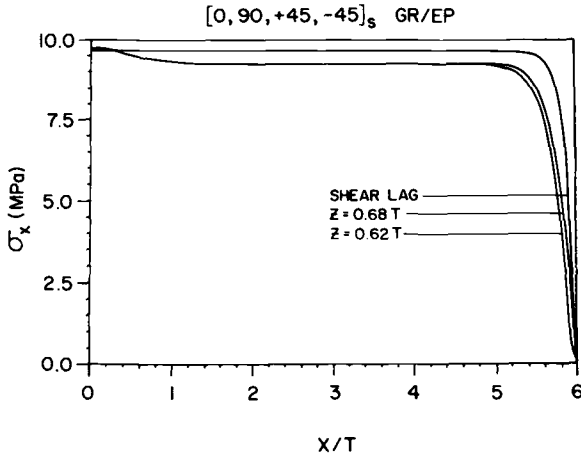


FIG. 3—Normal stress distribution in cracked 90-deg ply of a  $[0, 90, \pm 45]_s$  graphite-epoxy laminate predicted by finite difference and shear lag models.

is only two thirds of the distance from the crack which was determined in the previous case.

With the aid of stress distributions determined by these analyses, it is possible to develop a simpler model for laminate response after transverse cracking has occurred. In a given off-axis ply, transverse cracks generally run across the width parallel to the fiber of that ply. Therefore, no significant change is expected in the response of such a ply to a load in the fiber direction. However, both the finite difference solution and the shear lag solution indicate a change in the net load carried by that ply normal to the crack. The effect of this behavior on overall laminate response can be modelled by reducing the stiffness  $E_2$  in the cracked ply and using a laminate analysis to predict laminate stiffness values. In order to determine the degraded value of  $E_2$ , the shear lag model can be used to calculate the contribution to the overall load carried by the laminate of an off-axis ply damaged to a specified crack density. The appropriate reduction in  $E_2$  could then be made. However, we already have seen that the shear lag model is too stiff due to the assumption that other than the resin-rich shear transfer region, the material is rigid in shear. Instead,  $E_2$  can be assigned a zero value, which should be nearly true when damage is fully developed. The stiffness of a degraded laminate at the CDS will be underestimated, but the existence of small amounts of damage other than transverse cracking should decrease any discrepancy between predicted and observed values. The laminate analysis using reduced stiffnesses in cracked plies also will predict other laminate stiffness values. If the physics of the crack problem has been accurately simplified to producing a net decrease in stress normal to the crack face, these predictions of other stiffness also should be reliable.

## Procedure

Specimens of two geometries, 203 by 25.4 mm and 254 by 50.8 mm, were obtained from panels of  $[0,90_3]_s$ ,  $[90_3,0]_s$ ,  $[0,90]_s$ , and  $[0,\pm 45]_s$  type 1003 Scotchply reinforced plastic, which has a ply thickness of about 0.203 mm. Specimen edges were polished with 5  $\mu\text{m}$  and 3  $\mu\text{m}$  alumina to enhance the detail observed in edge replicas. Edge replicas are obtained by pressing acetone-softened acetate tape against the specimen edge. When the tape hardens it provides a permanent record of surface detail at the specimen edge [6].

Quasi-static tension tests and tension-tension fatigue tests in a load controlled testing mode were performed on the 25.4-mm-wide specimens. A stress ratio of  $R = 0.1$  was used for the fatigue tests. In both test types, at various stages of the load sequence, the specimen was unloaded, and a longitudinal stiffness was measured with the aid of a 50.8-mm gage length clip-on type extensometer. Edge replicas were made without removing the extensometer. Thus, a record of stiffness degradation at various stages of damage development was obtained.

Several stiffness components of the 50.8-mm-wide specimens were measured. Some specimens were instrumented with 0,45,90-deg stacked stress gage rosettes. For these, an initial shear modulus  $G_{xy}$  was obtained using a modified rail shear apparatus developed by O'Brien [7] by applying small compressive loads to the specimen-rig assembly. A bend test was then performed in which the specimen was supported along its length by two knife edges which were 47.63 mm apart, and line loaded along its center line in a constant crosshead rate test. Load versus deflection data could be used in conjunction with a Levy solution for a simply supported, infinitely long plate subjected to a line loading along its center line to determine the bending stiffness  $D_{yy}$ . Next, the initial longitudinal modulus  $E_x$  and Poisson's ratio  $\nu_{xy}$  were determined in a load controlled quasi-static test. After a specimen was damaged, the measurements described previously were repeated so that values of  $E_x$ ,  $\nu_{xy}$ ,  $G_{xy}$  and  $D_{yy}$  for a damaged specimen were obtained. The rail shear and bend tests give qualitative information about changes in  $G_{xy}$  and  $D_{yy}$ , but actual stiffness values may be suspect.

Considerable variations in the value of  $\nu_{xy}$  measured in the damaged laminates were observed, and were thought to be due to the local nature of the stress measurement of a strain gage. An alternative scheme was devised in which two clip-on type extensometers were used to measure strains in some of the 50.8-mm-wide specimens. A 50.8-mm gage length clip gage was mounted on one specimen face to measure longitudinal strain, and a 25.4-mm gage length clip gage was mounted on the other face to measure transverse strains. This configuration is illustrated in Fig. 4. The specimen then was loaded quasi-statically in a load-controlled test to determine  $E_x$  and  $\nu_{xy}$ . The

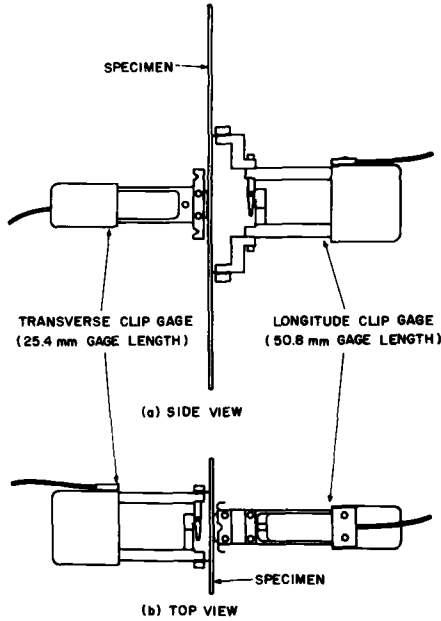


FIG. 4—Clip gage configuration for Poisson's ratio measurement.

two clip gage technique improved the consistency of the measured value of  $\nu_{xy}$ .

**Results and Discussion**

As mentioned above, the  $[0,90_3]_s$  and  $[90_3,0]_s$  laminates were expected to exhibit large stiffness changes after transverse cracking occurred. The shear

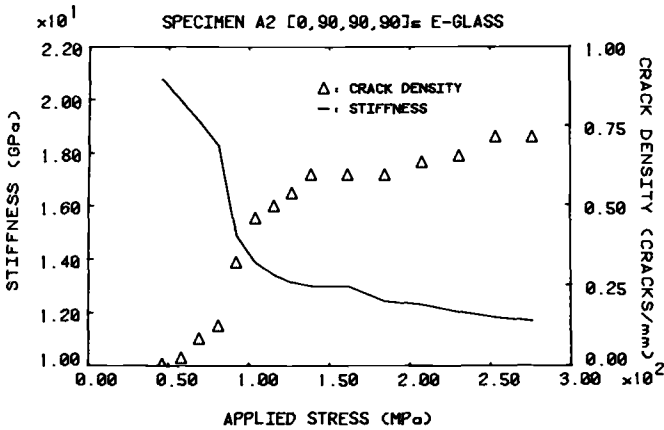


FIG. 5—Stiffness and crack density versus stress level for a  $[0,90_3]_s$  laminate.

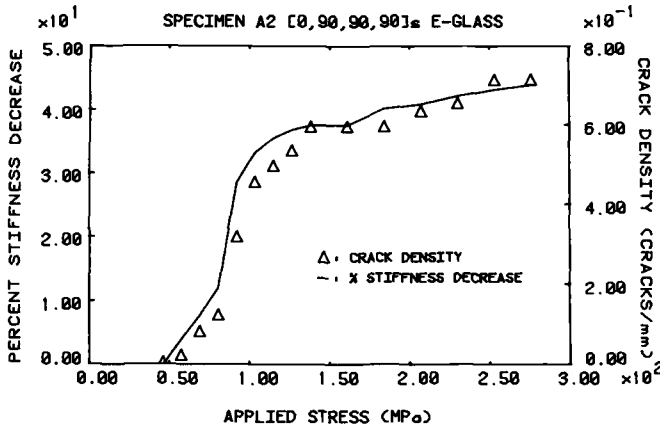


FIG. 6—Stiffness decrease and crack density versus stress level for a [0,90<sub>3</sub>]<sub>s</sub> laminate.

lag analyses of these two laminates are identical. Typical quasi-static test results for a [0,90<sub>3</sub>]<sub>s</sub> specimen, in this case Specimens A6, are shown in Fig. 5. The initial stiffness was approximately 21 GPa. The general trend indicated by the plot is that as the crack density increases, the stiffness decreases. At the higher load levels, both the stiffness and the crack density reach relatively stable values; the maximum crack density is about 0.75 cracks/mm, and the minimum stiffness is about 11 GPa. The stable crack density indicates that the CDS for this laminate has been attained. Figure 6 shows that large increases in crack density occur simultaneously with large decreases in stiffness; when smaller increases in crack density occur, the stiffness decrease is also smaller. Good correlation between stiffness and crack density is indicated, and the stiffness change which was expected to be large, was 45 percent. A typical damage pattern for [0,90<sub>3</sub>]<sub>s</sub> materials subjected to large loads is shown in Fig. 7. The spacing of the large cracks that extend through all six 90-deg plies is nearly uniform. Also, some crack branching—smaller cracks extending from larger ones—is seen.

Figure 8 illustrates typical quasi-static test results for a [90<sub>3</sub>,0]<sub>s</sub> specimen, in this case Specimen II-3. The results are similar to those for the [0,90<sub>3</sub>]<sub>s</sub> laminate in that the stiffness decrease is large (37 percent), and that when the crack density increases, the stiffness decreases. The crack density does not quite reach a stable value at high stress levels. The significant differences are

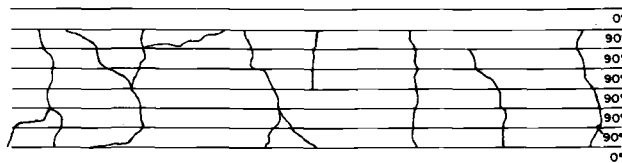


FIG. 7—Typical saturation crack patterns observed in [0,90<sub>3</sub>]<sub>s</sub> laminate.

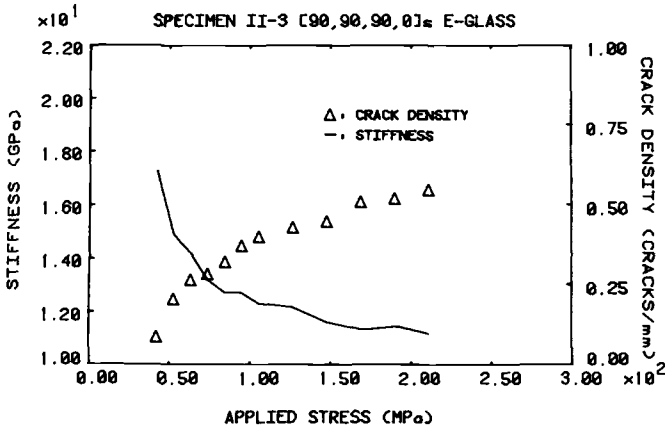


FIG. 8—Stiffness and crack density versus stress level for a  $[90_3,0]_s$  laminate.

that both the initial stiffness (19.3 GPa) and the final crack density (0.51 cracks/mm) are lower than the corresponding values for the  $[0,90_3]_s$  laminates. The damage pattern for  $[90_3,0]_s$  material shown in Fig. 9 indicates again a relatively uniform crack spacing in the 90-deg plies and some crack branching.

Fatigue results for  $[0,90]_s$  Specimen V-6 are shown in Fig. 10. The maximum stress applied during the fatigue cycle was 207 MPa. The initial stiffness is approximately 22.7 GPa, and decreases to 20.2 GPa within the first 10 000 fatigue cycles. The stiffness decreases more slowly over the next 90 000 cycles to a stable value of about 19.3 GPa. The stiffness decreases by about 15 percent. During the first 10 000 cycles, the crack density increases from a near zero value, to about 1.6 cracks/mm. During the final 90 000 cycles, the change in crack density is small; the crack density reaches a stable value of 1.9 cracks/mm. Again, a large increase in crack density is accompanied by a large decrease in stiffness. A damage pattern for  $[0,90]_s$  material near CDS, illustrated in Fig. 11, shows that cracks in the 90-deg plies are almost evenly spaced, and usually extend through both 90-deg plies. Little crack branching is observed.

Fatigue data for Specimen IV-6, a representative  $[0,\pm 45]_s$  laminate, are

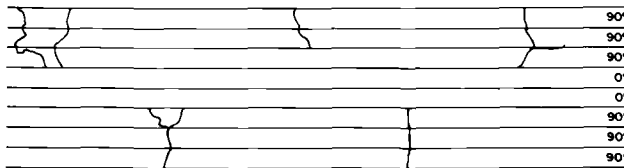


FIG. 9—Typical saturation crack patterns observed in  $[90_3,0]_s$  laminate.

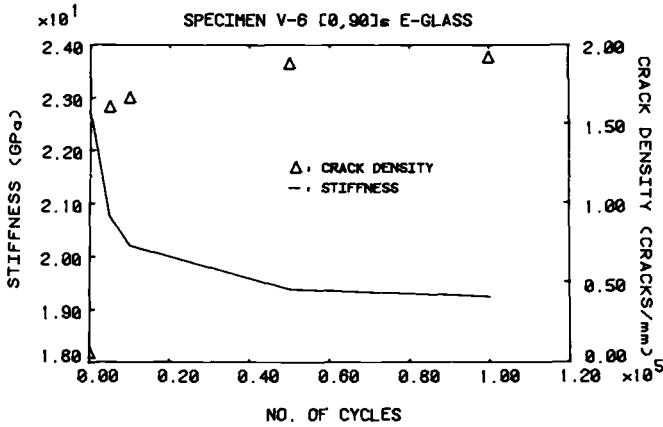


FIG. 10—Stiffness and crack density versus cycles of loading for a  $[0,90]_s$  laminate.

shown in Fig. 12. The maximum stress applied during the fatigue cycling was 172 MPa. Again, the decrease in stiffness over the first 10 000 cycles is large, and beyond 10 000 cycles the stiffness change is small. Also, during the first 10 000 fatigue cycles virtually all of the cracking occurs in both the +45 and -45-deg plies, and after 10 000 cycles both of those crack densities have reached stable values. The stable crack density in the +45-deg plies is about 1.8 cracks/mm, while the stable crack density in the -45-deg plies is about 1.2 cracks/mm. A representative saturation damage state is shown in Fig. 13. Note that local delamination frequently occurs between the tips of cracks in the +45 and -45-deg plies. The damage is obviously not limited to transverse cracking.

The results for all four cases could be summarized in general terms. As the loading is increased, either in stress level for a quasi-static test or in number of cycles for a fatigue test, the crack density increases until it reaches some stable value. During this process, the stiffness decreases and reaches a stable value when the crack density does. Further, the rate of increase of the crack density is related to the rate of decrease of the stiffness. Large stiffness changes occur when large crack density changes occur, and small stiffness changes occur when small crack density changes occur.

In Fig. 14 theoretical predictions and experimental observations for stiffness as a function of crack density are shown. The material properties used

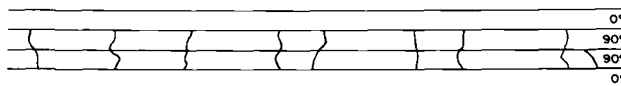


FIG. 11—Typical saturation crack patterns observed in  $[0,90]_s$  laminate.

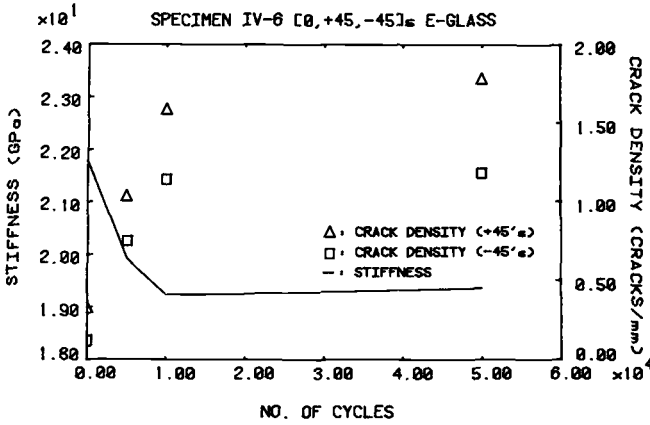


FIG. 12—Stiffness and crack density versus cycles of loading for a  $[0, \pm 45]_s$  laminate.

in the analysis are shown in Table 1. A comparison of the shear lag predictions with experimental results indicates that while the general shape of the predicted curve is correct, the stiffness is overestimated. Some of this discrepancy could be eliminated by reevaluating the value of the shear transfer layer thickness  $b$  used in the analysis based on the finite difference results. Some difference between theory and experiment is expected in any case, since damage is not restricted exclusively to transverse cracking. As shown, the shear lag analysis predicts a 29 percent stiffness reduction, while a reduction of 45 percent was observed. The dashed line indicates the axial stiffness predicted by a laminate analysis in which  $E_2$  of the 90-deg plies has been reduced to zero. Of importance is that this prediction and the shear lag prediction bound the observed results. Also, the laminate analysis provides a reasonable, and for design considerations conservative, estimate for the longitudinal stiffness when damage is fully developed.

A comparison of measured changes in the four stiffness components  $E_x$ ,  $\nu_{xy}$ ,  $G_{xy}$ , and  $D_{yy}$  with corresponding laminate analysis predictions for all four stacking sequences is given in Table 2. For the  $[0, 90_3]_s$ ,  $[90_3, 0]_s$ , and  $[0, 90]_s$  cases, the predicted values and measured values are in close agreement. Some longitudinal splitting, or cracking in fiber direction in the 0-deg plies, was observed and might account for the difference between the observed and predicted changes in  $D_{yy}$  in this case. The measured change in  $G_{xy}$

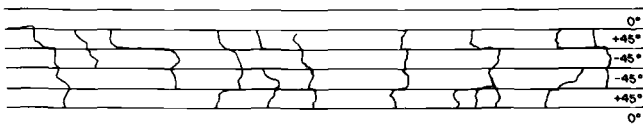


FIG. 13—Typical saturation crack patterns observed in  $[0, \pm 45]_s$  laminate.

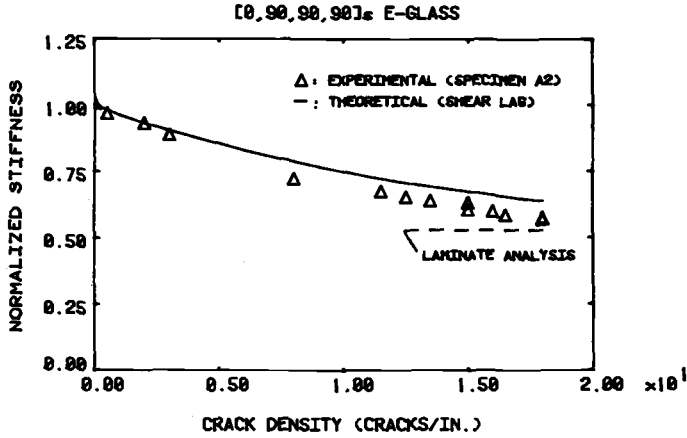


FIG. 14—Predictions and measurements of stiffness as a function of crack density for a [0,90]<sub>s</sub> laminate.

for the [0,90]<sub>s</sub> material is not unreasonable because of the local nature of the strain measurement of a strain gage. In the [0,90]<sub>3</sub><sub>s</sub>, [90<sub>3</sub>,0]<sub>s</sub>, and [0,90]<sub>s</sub> cases, the analysis is somewhat conservative; it overestimates the longitudinal stiffness change. Agreement between theory and experiment for the [0,±45]<sub>s</sub> case is not good, but in this laminate, other damage modes are observed. Fiber breakage in the 0-deg plies, longitudinal splitting, and local delamination are also evident in the [0,±45]<sub>s</sub> material, and thus also can be expected to contribute to the overall degradation of the mechanical response of the laminate. The simple analysis postulated does not account for these additional damage modes.

**Conclusions**

In general, the objective of the investigative program reported in the present paper was to isolate stiffness changes due to matrix cracking experimen-

TABLE 2—Predicted and observed stiffness decreases for glass-epoxy laminates.

Material		ΔE <sub>x</sub> , %	Δν <sub>xy</sub> , %	ΔG <sub>xy</sub> , %	ΔD <sub>yy</sub> , %
[0,90 <sub>3</sub> ] <sub>s</sub>	observed	42.0	...	0.0	0.6
	predicted	47.3	74.3	0.0	3.4
[90 <sub>3</sub> ,0] <sub>s</sub>	observed	38.8	71.0	0.0	0.0
	predicted	47.3	74.3	0.0	2.0
[0,90] <sub>s</sub>	observed	17.1	49.8	11.2	7.3
	predicted	22.6	48.9	0.0	1.0
[0,±45] <sub>s</sub>	observed	9.4	8.1	28.4	5.3
	predicted	4.3	20.6	11.8	11.0

tally and to model those changes analytically. The experiments were designed to promote matrix cracking in off-axis plies, the type of matrix cracking that was modelled. Some longitudinal cracking in the on-axis plies was caused by tensile transverse normal stresses in those plies for the cross ply laminates, and some matrix cracks which were not transverse to the load axis (and possibly some fiber fracture) occurred in the  $[0, \pm 45]$ , laminates. The limitations of the analysis also are identified easily. The best stress analysis available to us for the representation of internal matrix crack patterns is three dimensional and highly sophisticated, but approximate. And, most important, the philosophy which we have developed for representing the effect of matrix cracking on the tensor stiffness components of the individual laminae is still in a relatively adolescent stage.

What can be said, at this point, is that the correlation of tensor stiffness changes due to matrix cracking predicted by our analysis with those measured in the experiments strongly suggests that a solid analytical foundation has been laid, and that tensor stiffness changes due to matrix cracking can be predicted with what might be called engineering accuracy using very simple lamina stiffness reduction principles and standard laminate analysis. The practical implications of such a capability are obvious. The intricate relationships between such tensor stiffness changes and the corresponding internal stress redistributions which control the residual strength and life of such laminates are certainly less obvious, but these relationships may well hold the key to the development of successful mechanistic models for the prediction of the engineering materials response of composite laminates.

### *Acknowledgments*

The authors gratefully acknowledge the support of this investigation by the National Science Foundation under grant CME-7680213, monitored by C. J. Astill. We also express our appreciation to R. Davis for assistance in the fabrication of specimens.

### **References**

- [1] O'Brien, T. K. in *Mechanics of Nondestructive Testing*, W. W. Stinchcomb, Ed., Plenum, New York, 1980, pp. 101-121.
- [2] Reifsnider, K. L., Henneke, E. G., and Stinchcomb, W. W., "Defect-Property Relationships in Composite Materials," AFML-TR-76-81, Part IV, Air Force Materials Laboratory, June 1979.
- [3] Reifsnider, K. L., "Some Fundamental Aspects of the Fatigue and Fracture Response of Composite Materials," *Proceedings*, 14th Annual Society of Engineering Science Meeting, Lehigh University, Bethlehem, Pa., 14-16 Nov. 1977.
- [4] Talug, A., "Analysis of Stress Fields in Composite Laminates with Interior Cracks," Thesis, Doctor of Philosophy, College of Engineering, Virginia Polytechnic Institute and State University, Sept. 1978.

- [5] Zweben, C., *Journal of Mechanics and Physics of Solids*, Vol. 19, 1971, pp. 103-116.
- [6] Stalnaker, D. O. and Stinchcomb, W. W., *Composite Materials: Testing and Design (Fifth Conference)*, ASTM STP 674, American Society for Testing and Materials, 1979, 620-641.
- [7] O'Brien, T. K. and Reifsnider, K. L., *Experimental Mechanics*, Vol. 20, No. 5, May 1980, pp. 145-152.

# The Dependence of Transverse Cracking and Delamination on Ply Thickness in Graphite/Epoxy Laminates

---

**REFERENCE:** Crossman, F. W. and Wang, A. S. D., "The Dependence of Transverse Cracking and Delamination on Ply Thickness in Graphite/Epoxy Laminates," *Damage in Composite Materials, ASTM STP 775*, K. L. Reifsnider, Ed., American Society for Testing and Materials, 1982, pp. 118-139.

**ABSTRACT:** (25/-25/90<sub>n</sub>),  $n = 1/2, 1, 2, 3, 4, 6, 8$ , and (25<sub>2</sub>/-25<sub>2</sub>/90<sub>2</sub>), T300/934 graphite/epoxy laminate coupons were tested in tension and examined periodically by di-iodobutane (DIB) enhanced X-radiography following progressively larger increments of applied load. The tensile strain required to initiate transverse cracking in the 90-deg ply was found to depend on the thickness of the 90-deg layer. For  $n \leq 3$  delamination was initiated at the edge of the coupon. The onset of delamination occurred before or after transverse cracking, depending on the laminate construction. For  $n \geq 4$  delamination at the 25/90 interface was initiated across the entire width of the coupon by the formation of a transverse crack in the 90-deg ply. In some laminate constructions the location of specimen separation during final fracture was associated with the growth and coalescence of edge delaminations under either incrementally increasing or constant strain cyclic loading. Comparisons of experiments to the fracture sequence predictions by stress and energy analysis are made to assess our ability to account for the ply thickness dependence of fracture in these laminates.

**KEY WORDS:** composite laminates, graphite-epoxy, fracture, delamination, transverse cracking, X-radiography, tension testing, composite materials

The process of composite laminate fracture under static or fatigue loading is known to involve a sequential accumulation of damage, in the form of matrix dominated cracking, prior to final fracture by fiber breakage in the primary load carrying plies. One type of damage consists of multiple transverse cracks running parallel to fibers in plies which are oriented transverse to the applied load. A second type of matrix dominated damage consists of interply delamination cracks which are frequently found near the free edge

<sup>1</sup> Staff scientist, Lockheed Palo Alto Research Laboratory, Palo Alto, Calif. 94304.

<sup>2</sup> Professor, Department of Mechanical Engineering and Mechanics, Drexel University, Philadelphia, Pa. 19104.

of a laminate. The density of transverse cracks has been observed to increase to a peak level characteristic of the laminate construction and loading conditions, while the degree of delamination damage is frequently observed to increase steadily until failure occurs by fiber fracture in the primary load carrying plies [1].<sup>3</sup> Both matrix dominated damage modes can be detrimental to the structural reliability and durability of composite laminates since they result in a redistribution of lamina stresses which can influence the onset of final fracture involving fiber breakage in the primary load carrying plies.

The sequence of damage accumulation in composite laminates is found to depend strongly on the laminate construction and stacking sequence. In a (0,±45,90) quasi-isotropic symmetric laminate series, certain stacking sequences are found to delaminate more easily than others. For example, the ultimate tensile strength of a delamination prone (±45/0/90)<sub>s</sub> T300/934 laminate is found to be 30 percent less than the strength of a (90/±45/0)<sub>s</sub> construction which does not delaminate prior to failure [2]. The out-of-plane normal and shear stresses which exist near laminate free edges are known to influence the initiation and growth of delaminations. For this reason many studies have been conducted in recent years to determine the gradient of the free edge stresses due to mechanical, thermal, and hygroscopic loading. The location of the observed delamination is usually successfully predicted by finite element or more approximate numerical methods [3]; however, in other cases, especially those involving hygrothermal loading, delamination is not observed in locations where the calculated free edge normal stress  $\sigma_z$  is several times larger than the transverse tensile strength of the composite [4].

More recent studies of transverse cracking [5] and delamination [6] have shown that varying the thickness of the plies used to construct the laminate alters the applied strain (load) needed to initiate these damage modes. For example, the tensile strain at onset of delamination of (±45<sub>n</sub>/0<sub>n</sub>/90<sub>n</sub>)<sub>s</sub>,  $n = 1, 2, 3$  graphite epoxy laminates was found to vary inversely with the square root of the laminate thickness [6]. The observed ply thickness effect on fracture initiation cannot be predicted from stress analysis alone. Two approaches based on Weibull statistics [7] and fracture mechanics [8] have been taken to account for these results. Wang and Crossman [9] have employed a finite element energy analysis procedure to predict the onset of both transverse cracks and edge delamination in (±25/90<sub>n</sub>)<sub>s</sub>,  $n = 1, 2, 3, 4$  T300/934 laminates. They assume that the values of critical strain energy release rate (fracture toughness) associated with transverse fracture and interply delamination are the same. The energy analysis successfully predicted the observed dependence of onset strain for transverse cracking and delamination upon the thickness of the 90-deg plies and the alteration of delamination mode from the midplane to the 25/90 interface [9,10].

In this paper we examine the tensile fracture sequence of (25/−25/90<sub>n</sub>)<sub>s</sub>,

<sup>3</sup> The italic numbers in brackets refer to the list of references appended to this paper.

$n = \frac{1}{2}, 1, 2, 3, 4, 6, 8$  and  $(25_2/-25_2/90_2)_s$  T300/934 laminates. In addition to providing documentation of fracture predictions described in previous references [9,10], the paper summarizes our observations of the interdependencies of transverse cracking and delamination fracture processes and their influence upon final fracture involving 25-deg ply failure. Our goal is to delineate the degree of structural modeling necessary to predict fracture successfully in composite laminates.

The  $(\pm 25/90)_s$  laminate series was chosen for these experiments because of its well documented propensity for delamination under tensile loading [3]. Pagano and Pipes even suggested it as alternative method of measuring the interlaminar tensile strength [11]. As described by Harris and Orringer, the through-thickness free edge stress distribution is complex [3].  $\tau_{xz}$  peaks at the  $(25/-25)$  interface, is small at the  $25/90$  interface, and vanishes midplane.  $\tau_{yz}$  is greatest at the  $25/90$  interface and of the same order of magnitude as  $\sigma_z$  which is high throughout the 90-deg layer. All three components reduce to zero far from the edge. The influence of stacking sequence on the prevailing delamination mode was first noted by Harris and Orringer [3]. They observed  $25/90$  delamination during tensile loading of  $(25/-25/-25/25/90)_s$  coupons but a zig-zag delamination within the 90-deg ply of  $(25/-25/25/-25/90)_s$  coupons. These results indicate that contributions from both  $\tau_{yx}$  and  $\sigma_z$  influence the particular delamination mode.

### Experimental Procedure

Laminates were fabricated from Fiberite T300/934 prepreg tape and autoclave cured at 450 K according to the manufacturer's recommended cure procedure. Nominal fiber volume was  $66 \pm 2$  percent. The 30 by 30 cm panels were cut by diamond saw to a coupon length of 22.5 cm and width of 2.5 cm. Fiberglass tabs of length 3.75 cm were bonded to each end of the coupon. Coupons were stored and tested under ambient conditions ( $22 \pm 3^\circ\text{C}$ ,  $60 \pm 5$  percent Relative Humidity) 3 to 6 months after fabrication. All tests were conducted on an Instron Universal Test Machine at a controlled displacement rate of 0.25 mm/min. The experimental procedure for documenting damage sequence was as follows:

1. An average ultimate tensile strength (UTS) for each type of laminate construction was determined by ramp tension testing of two replicas. Specimens were strain gaged ( $\frac{1}{4}$  in. strain gagers; EA-13-125TM-120 type) at the centroid of specimen gage length and width to determine the initial axial stiffness of each laminate type.
2. Three to five replicas of each laminate type were step loaded without strain gaging under axial tension; the loading increment was approximately 10 percent UTS until damage in the form of transverse cracks or delamination was detected. The loading increment subsequently was reduced to approximately 5 percent increments until ultimate failure.

3. After each step-loading, the specimen was removed from the tester, swabbed on the edges with di-iodobutane (DIB) solution to penetrate cracks, wiped off to remove excess DIB after 30 s, placed immediately into a Faxitron 804 point source X-radiographic chamber atop a Polaroid film (Type 55 positive/negative ASA 50) cassette, and exposed to X-rays for 1.25 min at 30 kV.

4.  $\times 2$  positives were prepared by enlarging the Polaroid negatives onto high contrast Kodak paper. The onset and density of transverse cracks and the onset and growth of delaminations visible on the positive prints were measured and recorded.

5. Following fracture, the edges of each specimen were optically examined under a  $\times 30$  microscope to document the location of delamination and details of the fracture process.

### Experimental Results and Observations

Table 1 summarizes the results of incremental tension testing and radiographic examination of the  $(\pm 25/90_n)_s$ ,  $n = \frac{1}{2}, 1, 2, 3, 4, 6, 8$  laminates as well as  $[(25/-25)_2]_s$ ,  $(25_2/-25_2/90_2)_s$ , and  $(90_8)_s$  laminates (designated as  $n = 0$ ,  $n = 2^*$ , and  $n = 8^{**}$ , respectively, in subsequent discussions). The average stresses at which the onset of transverse cracking and delamination were observed are tabulated with the range given in parentheses. The measured stress-strain response of these laminates was essentially linear to failure. The onset strain for each fracture event was estimated by dividing the measured stress by the laminate initial modulus.<sup>4</sup> Figure 1 plots the applied strain for

TABLE 1—Summary of tension tests on T300/934  $(25/-25/90_n)_s$  laminates.

$n$	Youngs Modulus, GPa	Stress at Onset of 90-deg Ply Transverse Cracking, MPa	Stress at Onset of Delamination, MPa	Ultimate Tensile Strength, MPa	Number of Specimens Tested
0	76.8	...	...	514 (480 to 538)	3
1/2	72.3	...	438 (425 to 457)	471 (455 to 492)	3
1	68.9	...	409 (393 to 413)	459 (453 to 464)	4
2 <sup>a</sup>	65.5	282 (272 to 291)	302 (296 to 308)	324 (310 to 341)	5
2	54.6	227 (207 to 243)	324 (311 to 332)	356 (342 to 378)	4
3	45.5	165 (147 to 167)	270 (258 to 287)	292 (282 to 302)	4
4	39.3	127 (127 to 127)	211 (200 to 216)	211 (200 to 216)	3
6	32.7	108 (98 to 120)	128 (125 to 135)	140 (133 to 147)	3
8	26.3	90.9 (85.4 to 97.8)	94.4 (92.3 to 97.8)	101 (97.1 to 104)	4
8 <sup>**b</sup>	11.3	...	...	44.1 (41.3 to 48.2)	5

<sup>a</sup>  $(25_2/-25_2/90_2)_s$  laminate.

<sup>b</sup>  $(90_8)_s$ , transverse unidirectional composite.

<sup>4</sup> The stress-strain response of these laminates was essentially linear to the point of delamination onset. Thereafter some small reduction in stiffness as measured by strain gage at the specimen centroid was noted, although the reduction in tangent modulus even at failure never exceeded 15 percent. The reader may verify that in the worse case of constant modulus to 0.60 percent strain, followed by a 15 percent modulus reduction to 0.75 percent failure strain, the error in estimating failure strain from ultimate stress divided by initial modulus is less than 3 percent.

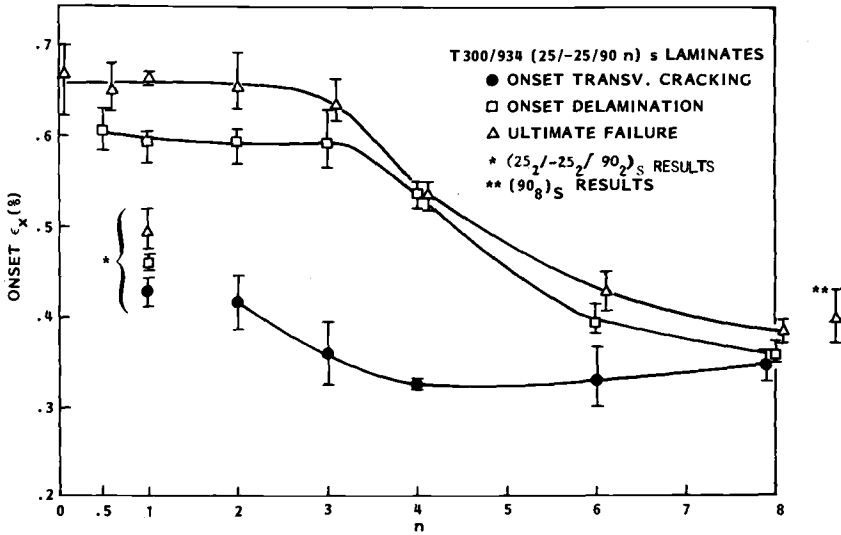


FIG. 1—Observed tensile strain  $\epsilon_x$  for transverse cracking, delamination, and ultimate failure versus the number of 90-deg plies in T300/923 laminates.

onset of transverse cracking, onset of delamination, and final fracture showing the average value and range as the thickness of the 90-deg ply varies from  $n = 0$  to  $n = 8$ . The strain to failure for  $n = 0, 1, 2, 3$  laminates is found to be constant. For  $n = 4, 6, 8$  laminates the strain to failure  $\epsilon_x^F$  shows a significant reduction as  $n$  increases. Delamination is observed to initiate at strains  $\epsilon_x \geq 0.90 \epsilon_x^F$  for each laminate; although for  $n = 4$  delamination is not observed prior to final fracture. The onset strain for transverse cracking shows a strong dependence upon  $n$ . Transverse cracks are not observed prior to delamination in  $n = \frac{1}{2}$  or  $n = 1$  laminates. The strains for onset of transverse cracking, delamination, and final failure in  $(25_2/-25_2/90_2)_S$  laminates are well below the values obtained in  $(25/-25/90)_S$  laminates with equivalent elastic stiffnesses.

Figure 2 provides a schematic view of the sequence of fracture in these laminates. Referring to Fig. 1 for the appropriate tensile strain, Column a shows the degree of transverse 90-deg cracking just prior to the initiation of delamination as viewed on radiographs of the specimen width. Column b shows specimen width and edge views (dotted lines are the 25/90 interfaces viewed on edge) immediately after edge delamination is observed. Column c shows the area occupied by delamination and the type of delamination immediately prior to final failure. Transverse cracks are displayed only in the edge views when they are associated with the initiation of a local 25/90 delamination at the transverse crack tip. Before describing the fracture sequence of each laminate in more detail the following general observations are made:

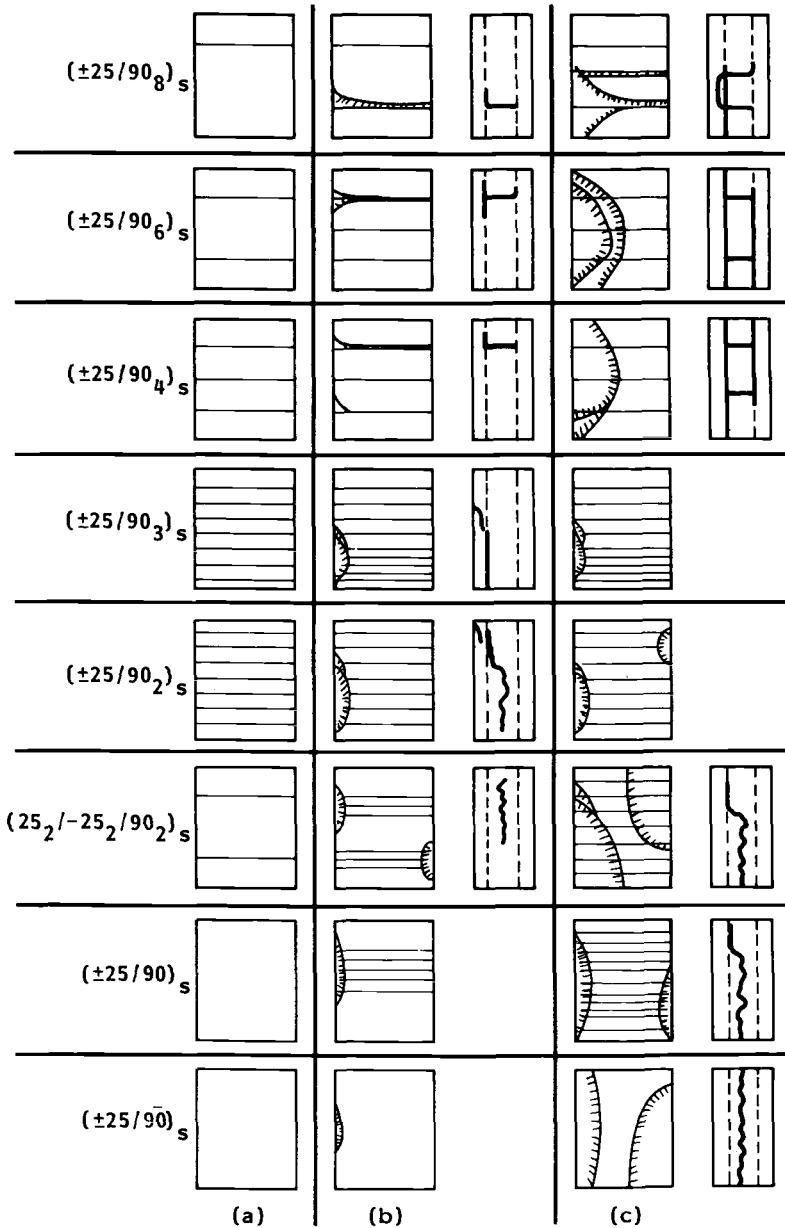


FIG. 2—Schematic of the fracture sequence in  $(25/-25/90_n)_s$  laminates: (a) just prior to delamination; (b) subsequent to delamination; and (c) just prior to final failure.

1. Prior to delamination, a well-developed set of transverse cracks exists only in  $n = 2, 3, 4$  laminates.

2. In  $n = 1, 2, 3$  and  $2^*$  laminates, a locally higher density of transverse cracks is observed in regions of edge delaminations subsequent to delamination.

3. In  $n = \frac{1}{2}, 1, 2,$  and  $2^*$ , an edge delamination which wanders through the 90-deg layer is predominant.<sup>5</sup>

4. In  $n = 3$  an edge delamination at the 25/90 interface is predominant.<sup>5</sup>

5. In  $n = 4, 6, 8$  laminates, 25/90 delamination initiates simultaneously with the creation of a new transverse crack when the applied stress is high. The delamination zone is larger at the edge but extends across the entire width of the specimen.

6. Transverse cracks across the entire width of  $n = \frac{1}{2}$  laminates are not observed even after extensive edge delamination.

7. The extent of midplane delamination prior to failure is greater in  $n = 2^*$  than in the comparable  $n = 1$  laminate with equivalent elastic properties.

8. The character of fracture sequence, density of transverse cracking, and the location and extent of delamination are seen to change consistently as  $n$  varies from  $\frac{1}{2}$  to 8.

#### $(\pm 25/90_8)_s$ Fracture

Figure 3 shows radiographs of portions of the gage section of two  $(\pm 25/90_8)_s$  laminates tensile loaded to 95 percent of UTS. The dark section at the base of each specimen is the image of the fiber glass tab area. Five transverse cracks are seen in Specimen 8-1. The top two transverse cracks which formed first during incremental loading show upon closer examination a narrow 25/90 delamination at the tip of the transverse crack in the 90-deg ply. The dark zone in Specimen 8-1, a delamination associated with the fourth crack from the top of the specimen, develops entirely within the last incremental loading. Cracks at 25-deg indicate that transverse splitting of the 25-deg plies parallel to the fiber axes also has taken place. The delamination and 25-deg ply splitting is developed more fully in Specimen 8-2. While delamination is found across the entire width of the specimen, the 25-deg cracking is concentrated at the specimen edge.

#### $(\pm 25/90_6)_s$ Fracture

25/90 delamination at the tip of 90-deg transverse cracks does not occur at the onset strain for transverse cracking, as evidenced by the radiographic image of several cracks in the lower portion of Specimen 6-7 in Fig. 4. At

<sup>5</sup> We distinguish here between a "90/90 delamination," which wanders back and forth within the 90-deg ply and in some instances runs a short distance along a 25/90 interface, and a "25/90 delamination," which runs predominantly along the ply interface. The schematic edge view accentuates these differences for clarity.

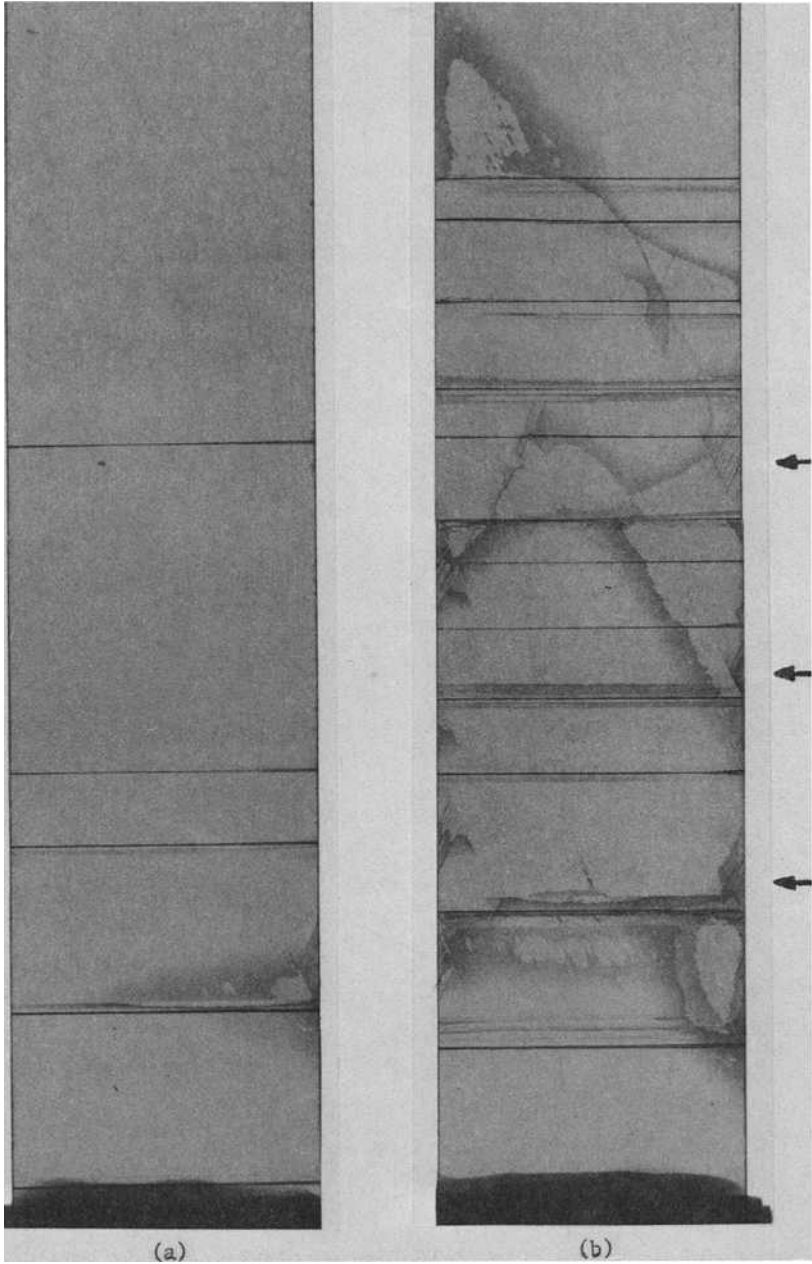


FIG. 3—DIB X-radiographs of  $(25/-25/90)_k$  Specimens A 8-1 and B 8-2 after tensile straining to 0.38 percent. Specimen width is 2.5 cm in all radiographs.

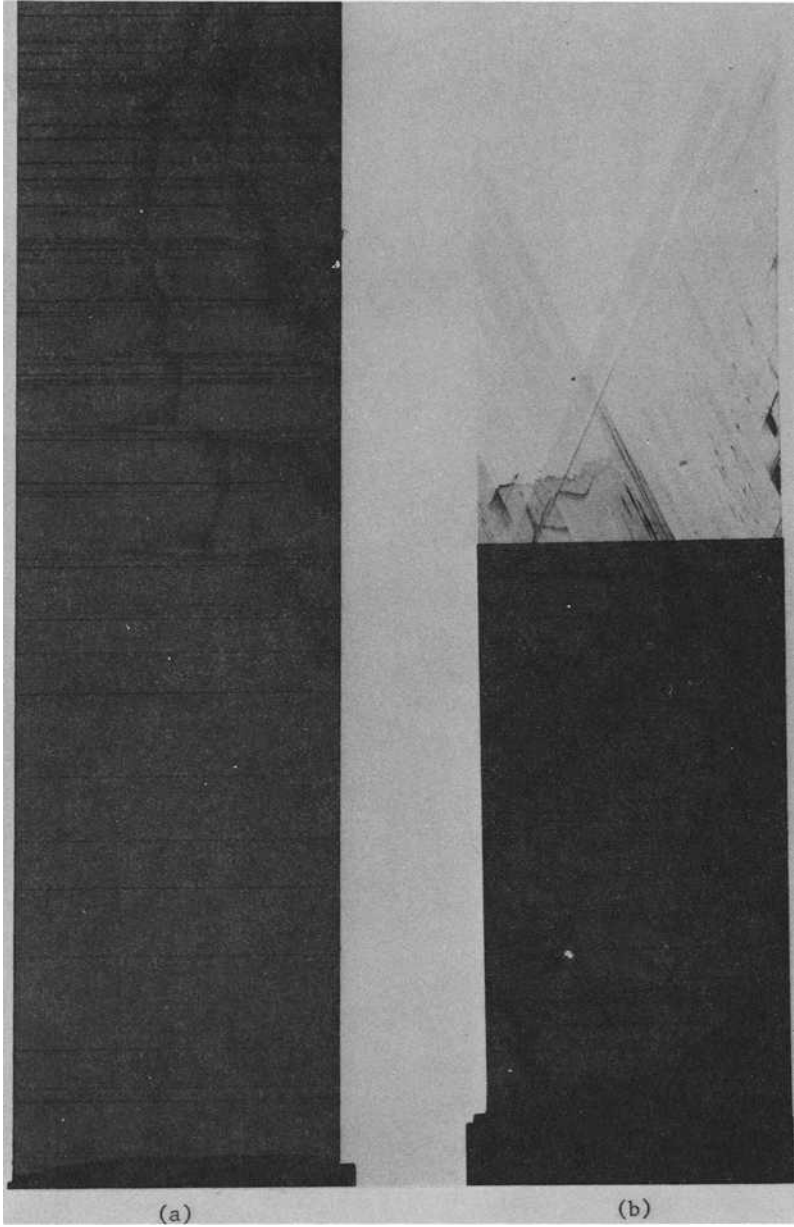


FIG. 4—DIB X-radiograph of  $(25/-25/90)_6$ , Specimens A 6-7 and B 6-9 after tensile straining to 0.41 percent and 0.45 percent, respectively.

slightly higher loads, edge 25/90 delamination develops rapidly but asymmetrically with respect to specimen width. The tendency for delamination to be associated with the transverse cracks is evident from the spiked appearance of the dark zones which delineate the tip of the delaminations where the DIB penetrant has concentrated by capillary action. The entire region to the right of each 25/90 delamination front is delaminated.  $n = 6$  and  $n = 4$  laminates showed similar fracture patterns involving separation along both 25/90 interfaces, and delamination extending across 50 percent of the specimen width prior to failure. 25-deg ply splitting parallel to the fibers is found along the right-hand edge of both specimens in Fig. 4. A radiograph of failed Specimen 6-9 demonstrates the mixed fracture of the 25-deg plies involving both inplane shear out and fiber fracture. The regions of fiber fracture (left side of Specimen 6-9) invariably exhibit a fracture line which is parallel to transverse cracks in the 90-deg ply. While one is tempted to associate this 25-deg fiber fracture crack with the stress concentration at the tip of a specific transverse 90-deg crack, the failure of  $(\pm 25_2)_s$  specimens exhibited essentially the same mixed failure mode and orientation of the fiber fracture regions.

#### $(\pm 25/90_3)_s$ and $(\pm 25/90_4)_s$ Fracture

These two laminates represent a transition from delamination associated with specific transverse cracks and delamination associated with free edge stresses. Both laminates develop a high density of transverse cracks prior to delamination initiation. In the  $n = 4$  laminate, 25/90 delamination initiates at the edge but in association with transverse cracks. In the  $n = 3$  laminate, edge delamination initiates at the 25/90 interface, and causes a simultaneous increase in the local density of transverse cracks in the delaminated region (see Fig. 5). Isolated areas of 25-deg ply splitting also are observed in association with the 25/90 delamination. The scallop-like edge delamination regions shown in Fig. 5 are typical of the  $n \leq 3$  laminates loaded in tension.

#### $(\pm 25/90_2)_s$ Fracture

$n = 2$  laminates exhibit the highest density of transverse cracks prior to delamination, as shown in Fig. 5. Edge delaminations of 90/90 and 25/90 types are seen in these specimens. The maximum extent of delamination in  $n = 3$  and  $n = 2$  laminates prior to ultimate failure is only 10 to 20 percent of the specimen width. Furthermore, the ultimate strain to failure is essentially that of  $(\pm 25_2)_s$  laminates.

#### $(\pm 25/90)_s$ Fracture

Although it is difficult to observe in the radiograph reproduced in Fig. 5, transverse cracking in the  $n = 1$  laminate is found only after the initiation of 90-deg ply delamination and only in those delaminated regions. Delamina-

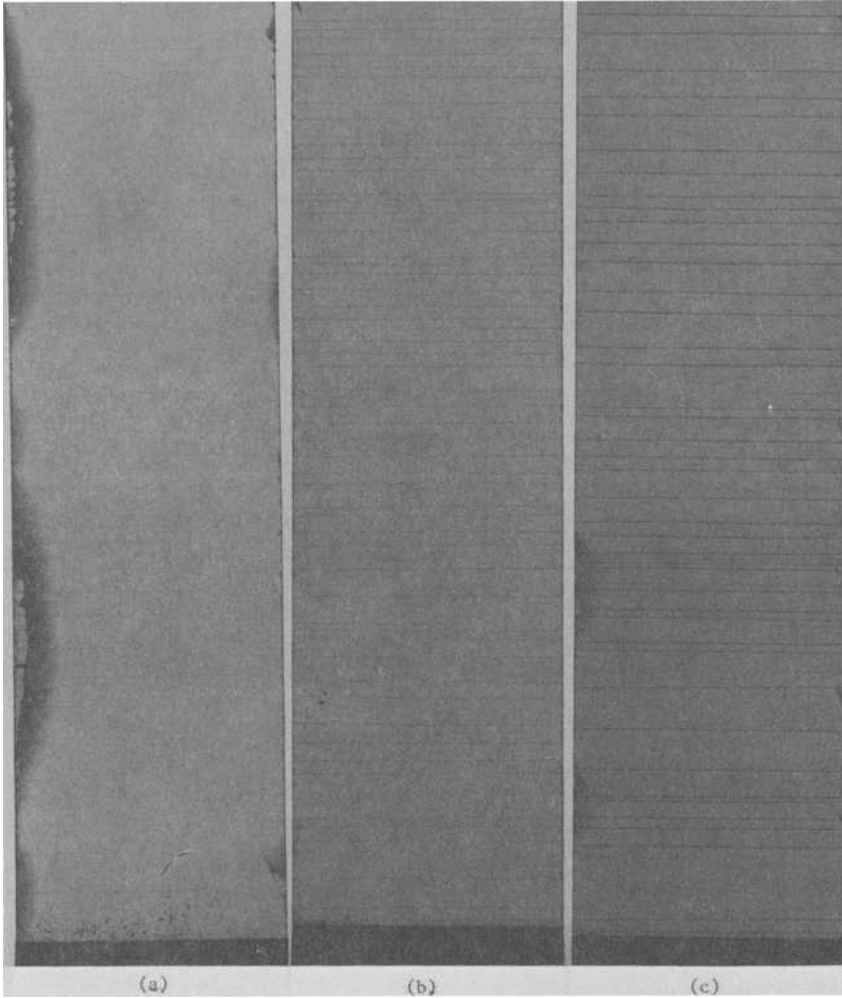


FIG. 5—DIB X-radiograph of (a)  $(25/-25/90)_s$  Specimen 5-4 after  $\epsilon_x = 0.67$  percent, (b)  $(25/-25/90_2)_s$  Specimen 7-4 after  $\epsilon_x = 0.61$  percent, and (c)  $25/-25/90_3)_s$  Specimen 8-4 after  $\epsilon_x = 0.59$  percent.

tions seem to alternate along both edges of the specimen but do not coalesce to cover the entire edge before ultimate failure. Figure 6 shows the maximum extent of delamination in an  $n = 1$  laminate at 96 percent of UTS. Some 25-deg ply splits seen within the right hand delamination region in Fig. 6a appear to identify the final failure surface in Fig. 6b. Fiber fracture and inplane shear out of the 25-deg plies are both observed at the fracture surface. This figure illustrates a trend observed in many specimens examined—the final fracture surface is found most commonly in the region of greatest delamination extension. However, a prediction of this location necessitates interrupting a tensile loading only a few percent below the UTS of the specimen.

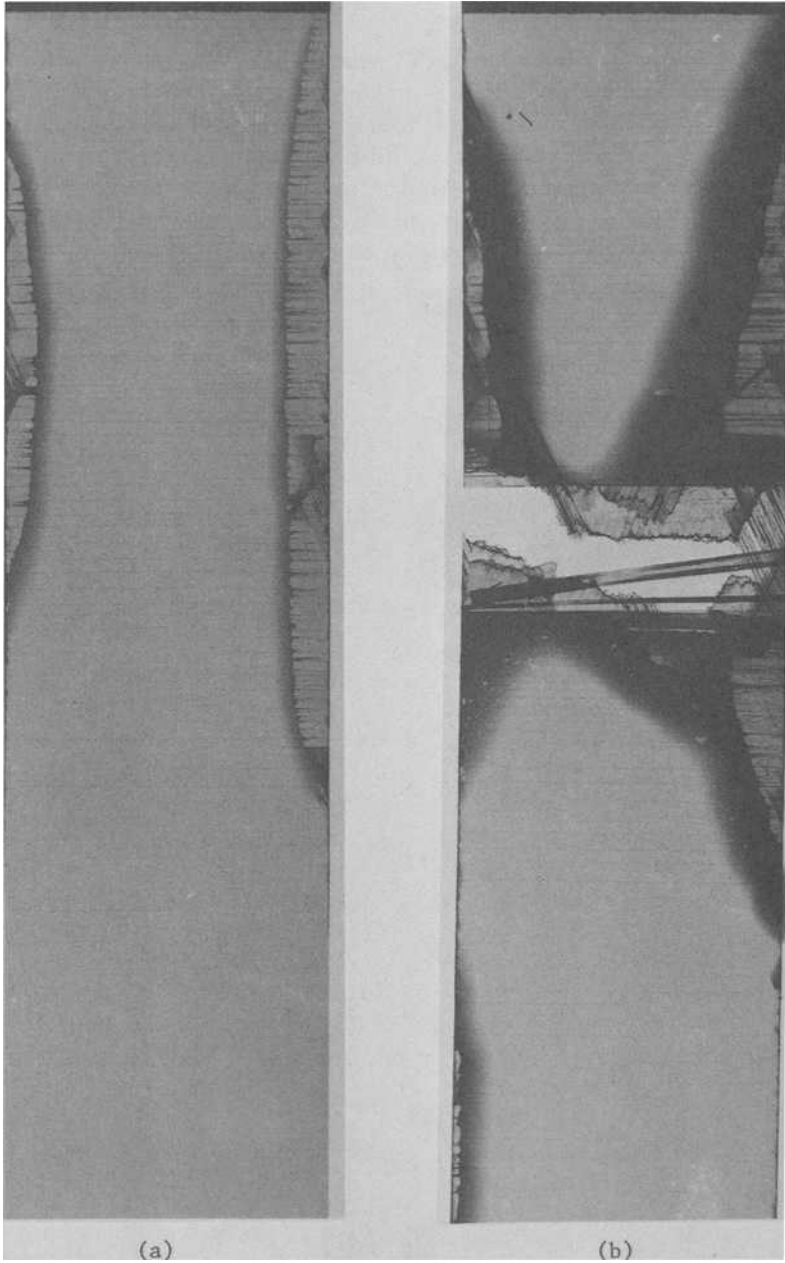


FIG. 6—DIB X-radiograph of  $(25/-25/90)_8$  specimen after (a)  $\epsilon_x = 0.64$  percent and (b)  $\epsilon_x = 0.67$  percent.

$(\pm 25/\overline{90})_n$  Fracture

Figure 7 shows the morphology of damage in  $n = \frac{1}{2}$  laminates at or close to tensile failure. Delamination is predominantly in the 90-deg plies. Some evidence of 25-deg ply splitting is found near the specimen edges, but the final fracture surface shows a mix of fiber fracture and inplane shear out of the 25-deg plies. Transverse cracking of the 90-deg plies is not observed prior to initiation of delamination. Subsequently, the transverse lines in the delaminated zone suggest 90-deg ply cracks which run only partially in from the



FIG. 7—DIB X-radiograph of  $(25/-25/\overline{90})_n$ . Specimens 11-2, 11-3, and 11-4 (left to right) after  $\epsilon_x = 0.63$  percent. Oblique cut made for microscopic examination of delamination Regions a and b is shown.

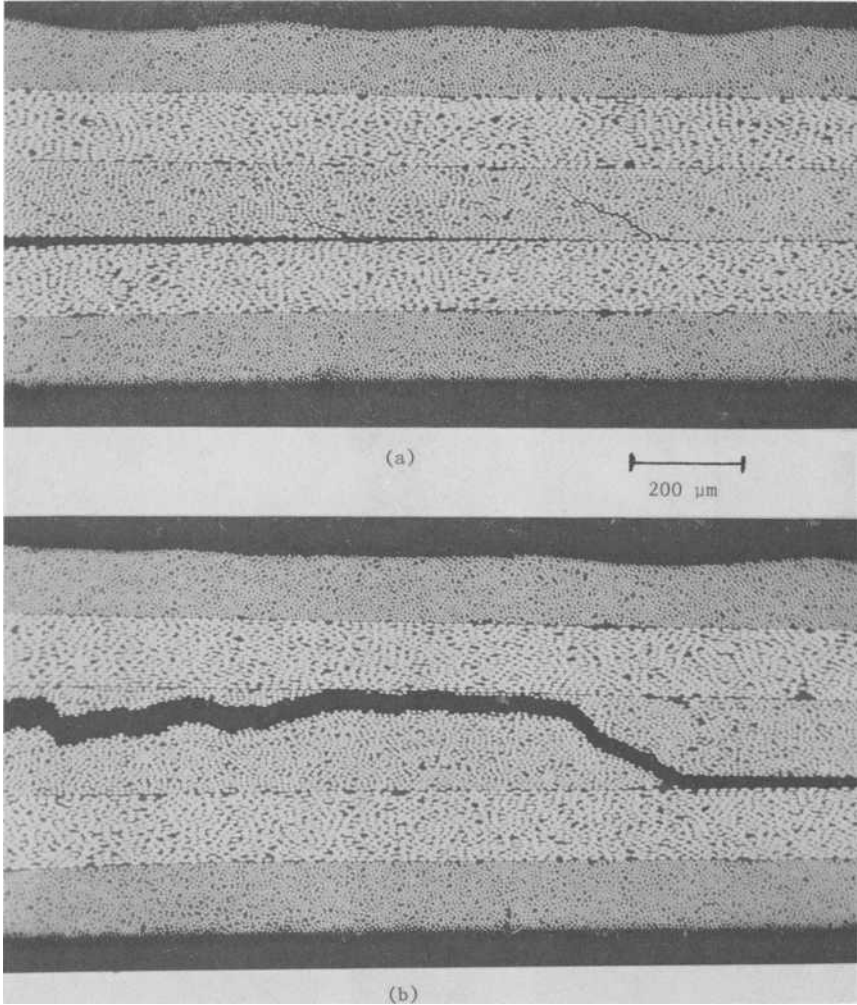


FIG. 8—Microscopic oblique section examination of  $(25/-25/90)_n$ , Specimen 11-4 in delamination Regions a and b. (See Fig. 7.) Original magnification  $\times 100$ .

edge. However, a microsectioning along an oblique cut in Specimen 11-4 (see Fig. 7) through the delamination region provides a different interpretation. In Fig. 8 the microscopic section shows the transverse line pattern at location *b* in Fig. 7 to be caused by the irregular delamination surface in the 90-deg ply. No transverse cracks are found in this region. At location *a* close to the tip of the delamination, we find that the delamination runs to the 25/90 interface and several oblique cracks, barely discernible in the radiographs, are found in the 90-deg ply. The orientation of these cracks strongly suggests that they initiate due to the locally complex shear and normal stress state in the vicinity of the 25/90 interface delamination.

$(25_2/-25_2/90_2)_8$  Fracture

Figure 9 illustrates the 90/90 delamination mode associated with  $n = 2^*$  laminate specimens. Although elastically equivalent to the  $(\pm 25/90)_8$  laminate,  $n = 2^*$  specimens exhibit transverse cracking prior to delamination, enhanced transverse crack densities in the delaminated regions, and clear evidence of local 25-deg and  $-25$ -deg ply splitting near the specimen edge, subsequent to delamination extension inward from the edge. Nearly 80 percent of the width of the specimen is found to delaminate prior to ultimate failure. The final fracture occurs at a much lower stress (strain) than that obtained for equivalent  $n = 1$  specimens. Indeed, the failure mode of the 25-deg plies is quite distinctively due to inplane shear out. Thus a doubling of the 25-deg ply thickness alters the predominant failure mode and lowers the strength of

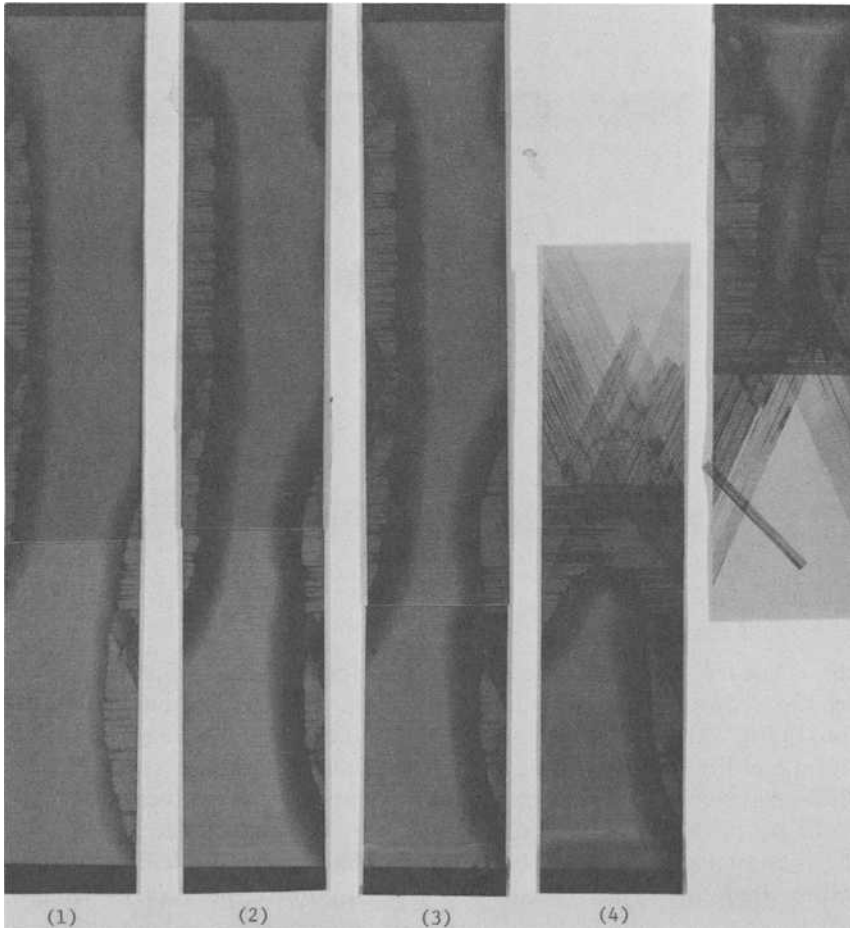


FIG. 9—DIB X-radiographs of  $(25_2/-25_2/90_2)_8$  Specimen D6-6 tensile strained to progressively increasing levels in 13 steps and then cycled 4 times at  $\epsilon_x = 0.49$  percent.

the laminate. Figure 9 shows the effect of four tensile loading cycles at constant peak load ( $R = 0$ ) on delamination area. Growth of delamination is found to be a function not only of the previous peak load increment, but also of the number of cycles at a constant high stress (strain) level. This observation demonstrates the difficulty of associating a given delamination extension with a particular static load level. The incremental nature of the experimental procedure also can include crack extension by a mechanical fatigue mechanism.

### Discussion of Results

Given the widely varying sequence of damage accumulation and failure in these  $(\pm 25/90)_n$  laminates, this discussion will describe briefly several analytical models which seek to predict certain aspects of the laminate failure process. A detailed exposition of these models is not appropriate here, but references providing these details are cited.

#### Transverse Cracking

Transverse cracking of the 90-deg plies is the first damage mode in  $n = 2, 3, 4, 6,$  and  $8$  laminates. Although free edge effects might influence the tensile strain at which transverse cracking is initiated, the contribution of the free edge to the transverse normal stress  $\sigma_x$  in the 90-deg plies is typically only 10 percent above the value calculated by laminated plate theory [12]. In Table 2 the transverse normal stress in the  $(\pm 25, 90)_n$  laminates is calculated by laminated plate theory using the LPARL\*ADVLAM code [13]. The elastic constants used in the analysis:  $E_L = 163.4$  GPa,  $E_T = 11.9$  GPa,  $G_{LT} = 6.5$  GPa, and  $\nu_{LT} = 0.30$ , were based on previous experiment [2]. Table 2 shows the individual contributions to transverse normal stress due to thermal and mechanical (tensile) loading. The combined thermal and mechanical stress which exists at the tensile strain  $\epsilon_x$  equal to the onset strain for transverse cracking  $\epsilon_x^{TC}$  is given in Column 4 of the table. The calculated stress is not found to be constant as  $n$  varies. Furthermore, all the calculated stresses are significantly higher than the transverse tensile strength of  $(90_8)_s$  specimens

TABLE 2—Calculated transverse normal stress  $\sigma_x$  in 90-deg plies of  $(25/-25/90)_n$  laminates.

$n$	Thermal Residual Stress $\Delta T = -1^{\circ}\text{F} = -0.56^{\circ}\text{C}$ , kPa	Mechanical Stress $\epsilon_x = 1 \times 10^{-4}$ kPa	Total Stress at Transverse Cracking Onset $\Delta T = -125^{\circ}\text{C}$ ; $\epsilon_x = \epsilon_x^{TC}$ , MPa	$\epsilon_x^{TC}$ , %
1/2	173	10.4	106	0.650** <sup>b</sup>
1	170	11.0	111	0.665** <sup>b</sup>
2**	170	11.0	85.6	0.430
2	163	11.4	83.9	0.415
3	156	11.5	76.5	0.360
4	149	11.6	71.2	0.325
6	137	11.7	69.4	0.330
8	128	11.7	69.2	0.345

\* \*  $(25_2/-25_2/90_2)_s$  laminates.

<sup>b</sup> \*\*Ultimate failure strain.

listed in Table 1. It is clear that a maximum stress or strain failure theory does not predict the strong dependence of transverse cracking upon the thickness of the 90-deg ply.

In Figure 10 the density of transverse cracks—as determined by radiographic observations over the gage length of each specimen—is plotted versus applied tensile stress. Individual data points for  $n = 2$  and  $n = 3$  laminates have been reported earlier [9] and only the limits of the experimentally observed range are shown. The accumulation of transverse cracks with additional tensile load can be attributed to two causes: a statistically distributed variation in transverse strength from point to point; or the result of 90-deg ply stress relaxation in the vicinity of each transverse crack which effectively reduces the average stiffness of the 90-deg ply.

The latter mechanism implies that a slightly higher applied tensile load will be required to initiate a second transverse crack even in the absence of a statistical variation in strength of that layer. Finite element modeling [8] of each cracked state can be used to predict crack density as a function of applied load, but the procedure is tedious. Furthermore, the finite element analysis demonstrates that the stress redistribution around each transverse crack is closely approximated by a simplified shear lag theory [9]. Parvizi and Bailey have used the shear lag analysis to predict successfully the average spacing of

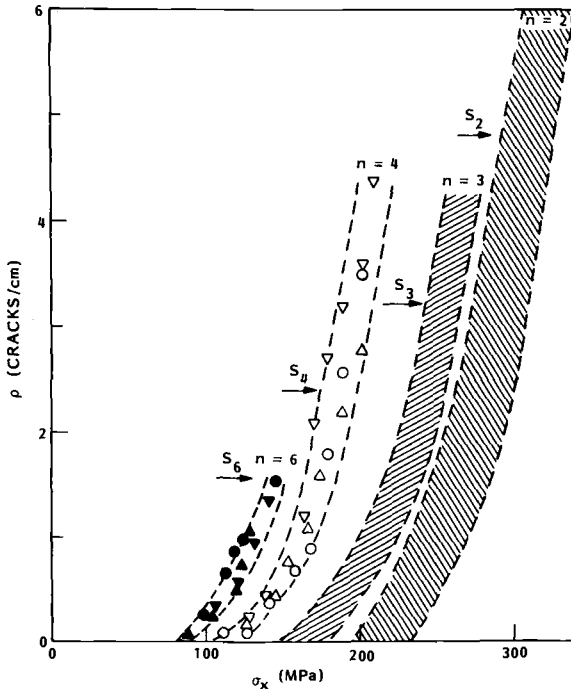


FIG. 10—Density of transverse cracks versus applied tensile stress in  $(\pm 25/90)_n$  laminates for  $n = 2, 3, 4, 6$ . Theoretical transverse crack saturation densities  $S_n$  are shown.

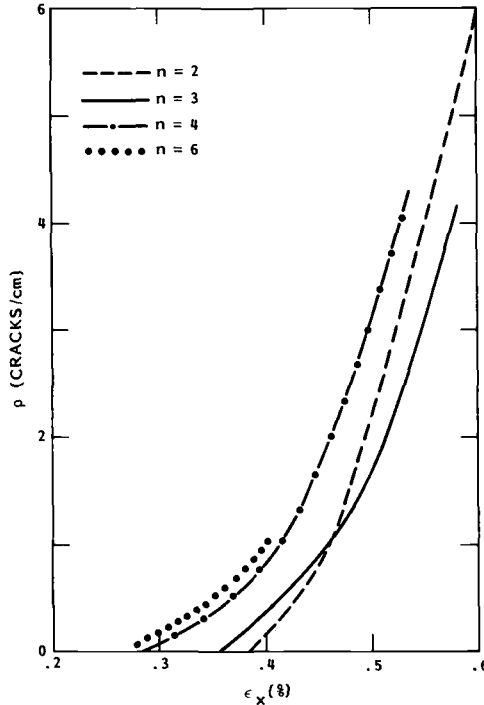


FIG. 11—Density of transverse cracks versus applied tensile strain in  $(\pm 25/90)_n$  laminates for  $n = 2, 3, 4, 6$ .

cracks as a function of applied load in crossplied glass-epoxy laminates [14]. By plotting the density of transverse cracks versus applied strain in Fig. 11, we find that, once initiation of cracks begins, the average crack density versus  $\Delta\epsilon_x$  above the threshold  $\epsilon_x^{TC}$  is strikingly similar in  $n = 2, 3, 4$ , and 6 laminates. Thus the density of cracks above the onset threshold is predicted readily by a laminate stress analysis.

Assuming a position-invariant ultimate strength for the 90-deg layer, one can use the shear lag theory [1] or energy analysis [8] to predict the ultimate saturation spacing of transverse cracks. Both procedures give a saturation spacing  $S_n \approx 8nt$  where  $n$  is the number of 90-deg plies above the symmetry plane and  $t$  is the thickness of an individual ply. For a ply thickness of 0.013 cm in T300/934 composites, the calculated saturation crack spacings  $S_n$  for  $n = 2, 3, 4$ , and 6 laminates, and the equivalent crack densities were determined. The densities are shown as arrows in Fig. 10. The transverse crack densities in this figure were measured only at loads below the onset of delamination. As noted earlier, many more transverse cracks initiate subsequently in the delamination regions; thus, the shear lag model, while successful in predicting the trend of density increase versus tensile load [14], underestimates the peak densities which can develop locally in delaminated re-

gions. Perhaps a shear lag model which takes into account statistical strength variation of the 90-deg ply would prove more successful; however, the significantly greater transverse crack density under delaminations (Figs. 5 to 6) would not be predicted by analysis based simply on the average tensile strain applied to the coupon.

### *Initiation of Transverse Cracking and Delamination*

We have noted the inadequacy of laminated plate stress analysis to predict the thickness dependence of the onset of the transverse cracking. Recently Wang et al have calculated the elastic strain energy release rate associated with the transverse cracking and edge delamination cracking by a generalized plane strain finite element analysis [8-10]. The energy release rate for a crack (transverse or delamination) of Size  $a$  can be expressed as

$$G(a) = \phi_1(a) \sigma_x^2 + \phi_2(a) \sigma_x \Delta T + \phi_3(a) \Delta T^2$$

where  $\sigma_x$  is the applied tensile stress,  $\Delta T$  is the difference between the test temperature and the stress-free temperature, and functions  $\phi_1$ ,  $\phi_2$ , and  $\phi_3$  are determined by the finite element analysis. The thermomechanical coupling term  $\phi_2$  is extremely important in  $(\pm 25/90)_n$  laminates and accounts for 30 to 60 percent of the energy released when transverse cracks are formed [15]. The values of the  $\phi_i$  functions are directly proportional to the thickness of the laminate plies. More energy is released from thicker plies when a geometrically similar crack initiates or propagates. For example, in laminates of  $(\pm 45_n/0_n/90_n)_s$ ,  $n = 1, 2, 3$  the delamination onset stress varies as in  $1/\sqrt{n}$  [6]. In Fig. 1 the onset strain for delamination in  $(\pm 25_n/90_n)_s$ ,  $n = 1, 2$  laminates also varies as  $1/\sqrt{n}$ , as predicted by the energy analysis. Figure 12 compares experimental data with the predicted onset for transverse cracking and edge delamination [15]. Predictions were based upon this energy analysis and a single value of critical strain energy release rate (appropriate for cracks which do not cut fibers) for both the transverse cracking and delamination processes. The effect of 90-deg ply thickness on transverse cracking is predicted quite well by the analysis. Edge delamination predictions are reasonably accurate for  $n \leq 3$ , but clearly do not account for the 25/90 delaminations associated with particular transverse cracks prevalent in the  $n \geq 4$  laminates. Prediction of this latter delamination mode involves further detailed energy analysis of transverse crack/delamination crack interaction, described elsewhere [15].

### *25-deg Ply Failure*

Radiographic examination of  $(\pm 25/90)_n$  laminates just prior to ultimate failure typically shows small triangular regions of 25-deg ply splitting near the edge of the tensile coupons (Figs. 3 to 5). In  $(25_2/-25_2/90_2)_s$  laminate coupons (Fig. 9) these triangular regions extended over as much as 20 per-

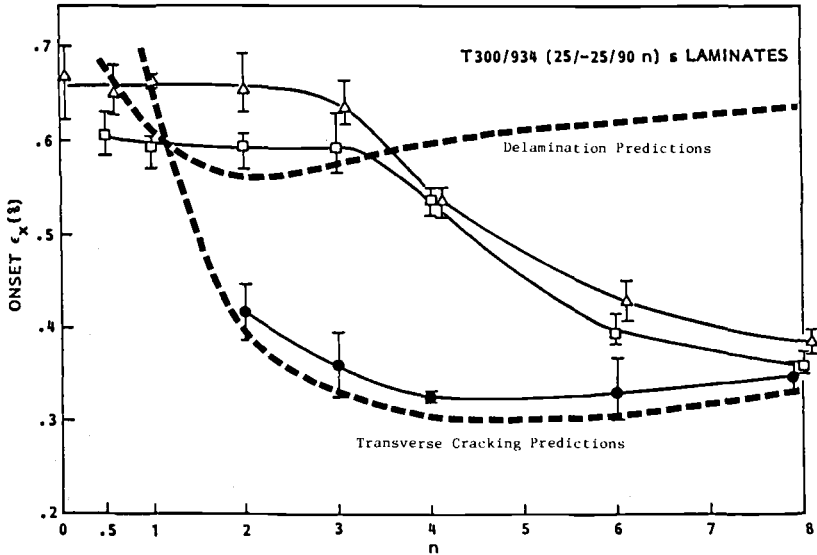


FIG. 12—Comparison of predicted [15] onset strains for transverse cracking and edge delamination to experimental results (see legend in Fig. 1) obtained on  $(\pm 25/90)_n$  T300/934 laminates.

cent of the specimen width before failure at a stress significantly lower than that in the elastically equivalent  $(\pm 25/90)_s$  laminate. The experimental observations suggest that failure analysis must take into account the local edge damage in the 25-deg plies and the effects of 25/90 delamination or 90-deg transverse cracking on the redistribution of stress within the 25-deg ply. The rapid drop in ultimate strain for  $n \geq 4$  laminates points to some kind of stress concentration effect in the 25-deg plies resulting from the transverse cracking and delamination which is more effective in thicker laminates, but detailed modeling of such processes have not been attempted to date.

One may examine the ability of laminated plate theory to predict ultimate failure by some inplane stress (or strain) criterion for failure. Table 3 displays the inplane stresses in the 25-deg ply of each laminate under unit thermal and tensile loads and the combined thermomechanical stresses which are calculated at the tensile ultimate strain  $\epsilon_x^F$ . These calculations were based on laminated plate analysis and properties described earlier in this section. The reader is free to employ any of the common strength theories to this stress state to develop a consistent prediction of failure. We have been notably unsuccessful in our attempts. Surprisingly, the 25-deg ply stresses developed in a  $(\pm 25_2)_s$  laminate ( $n = 0$ ) at ultimate failure are significantly less than those in  $n = \frac{1}{2}, 1, 2,$  and 3 laminates. Detailed modeling of the effects of transverse cracking and delamination would be expected to locally raise the 25-deg ply stresses in the latter series even higher than those values based on laminated plate analysis.

TABLE 3—Calculated stresses in 25-deg ply of  $(25/-25/90)_n$  laminates.

<i>n</i>	Thermal Residual Stress $\Delta T = -1^\circ\text{F} = -0.56^\circ\text{C}$ , kPa			Mechanical Stress $\epsilon_x = 1 \times 10^{-6}$ , kPa			Total Stress at Failure $\Delta T = -125^\circ\text{C}$ , $\epsilon_x = \epsilon_x^F$ MPa			
	$\sigma_x$	$\sigma_y$	$\tau_{xy}$	$\sigma_x$	$\sigma_y$	$\tau_{xy}$	$\sigma_x$	$\sigma_y$	$\tau_{xy}$	$\epsilon_x^F$
0	0	0	-102	82.8	0	31.2	538	0	180	0.660
1/2	-43.2	102	-105	106	16.7	41.8	677	132	248	0.650
1	-84.9	109	-120	110	19.8	43.8	710	156	264	0.665
2 <sup>a</sup>	-84.9	109	-120	110	19.8	43.8	524	123	190	0.495
2	-163	102	-150	112	21.8	45.0	699	165	261	0.655
3	-233	90.1	-178	113	22.5	45.5	668	163	249	0.635
4	-298	78.1	-204	114	22.9	45.7	539	140	197	0.532
6	-413	55.9	-250	114	23.4	46.0	396	112	140	0.427
8	-510	36.2	-289	115	23.6	46.2	323	98.1	111	0.382

<sup>a</sup> $(25_2/-25_2/90_2)_s$  laminate.

## Conclusions

Incremental tensile loading and DIB enhanced radiographic examination of T300/934  $(\pm 25/90)_n$ ,  $n = \frac{1}{2}, 1, 2, 3, 4, 6, 8$  and  $(25_2/-25_2/90_2)_s$  laminates were employed to document the dependence of damage type and development sequence on ply thickness. Comparison of experimental results was made to predictions based on analytical methods in current use to delineate the degree of structural modeling necessary to predict successfully the details of damage initiation and growth in composite laminates. While stress and energy methods prove useful in predicting the onset of transverse cracking, the density of transverse cracking, and the onset of delamination at the laminate free edges, more detailed analysis is shown to be necessary for prediction of the saturation density of transverse cracks, delamination growth under fatigue loading, and the ultimate strength of the primary load carrying plies.

## Acknowledgments

This study was supported in part by a research contract from the Air Force Office of Scientific Research (AFOSR) and in part by the Lockheed Independent Research Program. We wish to acknowledge the contributions of W. J. Warren (Lockheed) and G. E. Law (Drexel University), who performed the tensile loading and radiographic examination of the composites specimens.

## References

- [1] Reifsnider, K. L., Henneke, E. G., and Stinchcomb, W. W., "Defect Property Relationships in Composite Materials," AFML-TR-76-81, Part IV, Air Force Materials Laboratory, June 1979.

- [2] Bjeletich, J. G., Crossman, F. W., and Warren, W. J. in *Failure Modes in Composites IV*, J. R. Cornie and F. W. Crossman, Eds., American Institute of Mining, Metallurgical, and Petroleum Engineers, New York, 1979, p. 118.
- [3] Harris, A. and Orringer, O., *Journal of Composite Materials*, Vol. 12, 1979, p. 285.
- [4] Crossman, F. W., Mauri, R. E., and Warren, W. J., "Hygrothermal Damage Mechanisms in Graphite-Epoxy Composites," NASA-CR-3189, National Aeronautics and Space Administration, Dec. 1979.
- [5] Bader, M. G., Bailey, J. E., Curtis, P. T., and Parvizi, A., *Proceedings of the 3rd International Symposium on Mechanical Behavior of Materials*, Cambridge, England, 1979, p. 227.
- [6] Rodini, B. T. and Eisenmann, J. R., "An Analytical and Experimental Investigation of Edge Delamination in Composite Laminates," *Proceedings of the 4th Conference on Fibrous Composites*, San Diego, Calif., Nov. 1978.
- [7] Parvizi, A., Garrett, K. W., and Bailey, J. E., *Journal of Materials Science*, Vol. 13, 1978, p. 195.
- [8] Wang, A. S. D. and Crossman, F. W., *Journal of Composite Materials*, Supplementary Vol. 14, 1980, p. 71.
- [9] Crossman, F. W., Warren, W. J., Wang, A. S. D., and Law, G. E., *Journal of Composite Materials*, Supplementary Vol. 14, 1980, p. 88.
- [10] Wang, A. S. D., *Third International Conference on Composite Materials (ICCM3) Proceedings*, Paris, France, Aug. 1980, p. 170.
- [11] Pagano, N. J. and Pipes, R. B., *International Journal of Mechanical Sciences*, Vol. 15, 1973, p. 679.
- [12] Wang, A. S. D. and Crossman, F. W., *Journal of Composite Materials*, Vol. 11, 1977, p. 92.
- [13] Flaggs, D. L. and Crossman, F. W., *Composites Technology Review*, Vol. 1, 1979, p. 8.
- [14] Parvizi, A. and Bailey, J. E., *Journal of Materials Science*, Vol. 13, 1978, p. 2131.
- [15] Law, G. E., Ph.D. dissertation, Drexel University, Philadelphia, Pa., June 1981.

# Characterization of Delamination Onset and Growth in a Composite Laminate

---

**REFERENCE:** O'Brien, T. K., "Characterization of Delamination Onset and Growth in a Composite Laminate," *Damage in Composite Materials, ASTM STP 775*, K. L. Reifsnider, Ed., American Society for Testing and Materials, 1982, pp. 140-167.

**ABSTRACT:** The onset and growth of delaminations in unnotched  $[\pm 30/\pm 30/90/\overline{90}]_s$  graphite-epoxy laminates is described quantitatively. These laminates, designed to delaminate at the edges under tensile loads, were tested and analyzed. Delamination growth and stiffness loss were monitored nondestructively. Laminate stiffness decreased linearly with delamination size. The strain energy release rate,  $G$ , associated with delamination growth, was calculated from two analyses. A critical  $G$  for delamination onset was determined, and then was used to predict the onset of delaminations in  $[+45_n/-45_n/0_n/90_n]_s$  ( $n = 1, 2, 3$ ) laminates. A delamination resistance curve ( $R$ -curve) was developed to characterize the observed stable delamination growth under quasi-static loading. A power law correlation between  $G$  and delamination growth rates in fatigue was established.

**KEY WORDS:** graphite-epoxy, delamination, ply-cracking, rule of mixtures, stiffness loss, strain energy release rate,  $R$ -curve, fatigue, growth law, composite materials

## Nomenclature

- [ $A$ ] Extensional stiffness matrix
- $A$  Delaminated area
- $A^*$  Area of interface containing a delamination
- $a$  Strip delamination size
- $\Delta a$  Incremental strip delamination size
- $da/dN$  Delamination growth rate in fatigue
- [ $B$ ] Coupling stiffness matrix
- $b$  Half width of laminate cross section
- $C, \beta$  Empirically determined coefficients
- [ $D$ ] Bending stiffness matrix
- $E$  Axial stiffness of a partially delaminated laminate

<sup>1</sup> Research engineer, Structures Laboratory, U. S. Army Research and Technology Laboratories (AVRADCOM), National Aeronautics and Space Administration-Langley Research Center, Hampton, Va. 23665.

$E_{LAM}$	Axial laminate stiffness calculated from laminated plate theory
$E^*$	Axial stiffness of a laminate completely delaminated along one or more interfaces
$E_i$	Axial stiffness of the $i^{th}$ sublaminde formed by a delamination
$E_o$	Initial tangent modulus of an undamaged laminate
$E_{11}, E_{22}, E_{33}$	Lamina moduli
$dE/dA$	Rate of stiffness change with delamination area
$dE/dN$	Rate of stiffness change with fatigue cycles
$G_{11}, G_{12}, G_{13}$	Lamina shear moduli
$G$	Strain energy release rate associated with delamination growth
$G_I, G_{II}, G_{III}$	Strain energy release rate components due to opening, in-plane shear, and out-of-plane shear fracture modes
$G_{FEM}$	Values of $G_I, G_{II}, G_{III}$ calculated from finite element analysis
$G_c$	Critical strain energy release rate for delamination onset
$G_R$	Delamination resistance
$G_{max}$	Maximum strain energy release rate in constant strain amplitude fatigue test
$h$	Ply thickness
$K$	Saturation spacing of cracks in 90-deg plies
$l$	Gage length used to measure axial displacements
$N$	Number of fatigue cycles
$n$	Number of plies in a laminate
$t$	Laminate thickness
$t_i$	Thickness of $i^{th}$ sublaminde formed by delamination
$u, v, w$	Displacements in $x, y, z$ directions
$U, V, W$	Displacement functions in $x, y, z$ directions
$\mathcal{V}$	Material volume
$d\mathcal{U}/dA$	Rate of strain energy released as flaw extends
$d\mathcal{W}/dA$	Rate of work done by applied load as flaw extends
$x, y, z$	Cartesian coordinates
$X, Y, Z$	Nodal forces in $x, y, z$ directions
$X_{11}$	First element of the inverse extensional stiffness matrix ( $A_{ij}^{-1}$ ) ( $i, j = 1, 2, 3$ )
$\epsilon$	Nominal axial strain
$\epsilon_o$	Uniform axial strain assumed in finite element analysis
$\epsilon_c$	Nominal axial strain at onset of delamination
$\epsilon_{max}$	Maximum cyclic strain level in fatigue
$\nu_{12}, \nu_{13}, \nu_{23}$	Lamina Poisson's ratio
$\sigma_x$	Axial stress in a ply
$\sigma_c$	Remote axial stress applied at onset of delamination
$\sigma_z$	Interlaminar normal stress between plies

A commonly observed failure mode in laminated composite materials is delamination between the composite layers. Delaminations may develop during manufacture due to incomplete curing or the introduction of a foreign particle; they may result from impact damage; or they may result from the interlaminar stresses that develop at stress-free edges or discontinuities. Furthermore, delaminations may grow under cyclic loading. Delamination growth redistributes the stresses in the plies of a laminate, and may influence residual stiffness, residual strength, and fatigue life. Hence, a fatigue analysis for composite materials should take into account the presence and growth of delaminations.

A bibliography of experimental and analytical work on delamination is contained in Ref 1.<sup>2</sup> One of the most promising techniques for characterizing delamination growth is based on the rate of strain energy released,  $G$ , with delamination growth [1]. Previous work has shown that the cyclic growth rate of debonds between the metal and composite components of reinforced panels could be correlated with  $G$  [2]. Measured critical  $G$  values have been used in sophisticated analyses [3,4] to predict the onset of edge delaminations in unnotched composite laminates.

In the present study, a simple technique was developed, employing strain energy release rates to characterize the onset and growth of delaminations in a composite laminate. First, the damage that developed in unnotched  $[\pm 30/\pm 30/90/90]_s$  graphite-epoxy laminates under static tension loading and tension-tension fatigue loading was determined. Next, stress distributions generated from a finite element analysis were correlated with the observed damage. Then, during quasi-static test loads, delamination growth and stiffness loss were monitored nondestructively to relate laminate stiffness and delamination size. The resulting test data and analysis were used to derive a closed-form equation for the strain energy release rate,  $G$ , associated with delamination growth. Next, a critical value of  $G$  for delamination onset was determined. It then was used to predict the onset of delamination in  $[+45_n/-45_n/0_n/90_n]_s$  ( $n = 1,2,3$ ) laminates. A delamination resistance curve ( $R$ -curve) was developed to characterize the observed stable delamination growth during quasi-static loading. Finally, a power law correlation between  $G$  and delamination growth rates in fatigue was established.

### Specimens and Apparatus

Unnotched  $[\pm 30/\pm 30/90/90]_s$ , T300-5208 graphite-epoxy laminates were tested in tension. This laminate was designed to have relatively high tensile interlaminar normal stresses at the edges resulting in the formation of a delamination [5]. Figure 1a shows the delamination that developed along the edge.

<sup>2</sup>The italic numbers in brackets refer to the list of references appended to this paper.

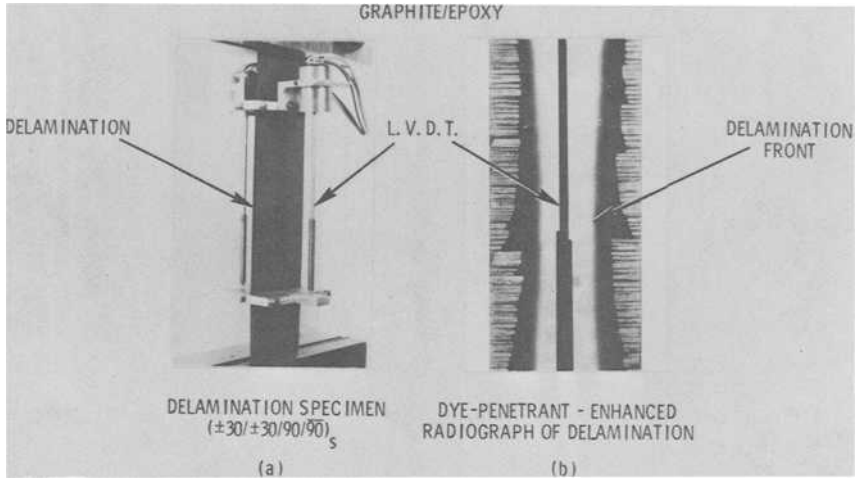


FIG. 1—Typical instrumented test specimen and dye-penetrant enhanced radiograph.

The specimens were 254 mm (10 in.) long by 38 mm (1.5 in.) wide. These eleven-ply laminates had an average ply thickness of 0.14 mm (0.0054 in.). Specimens were tested in a closed-loop hydraulic testing machine. The specimen length between the grips was 180 mm (7.0 in.).

Also shown in Fig. 1a is a pair of linear variable differential transducers (LVDT's) that were mounted on the specimen to measure displacements over a 102-mm (4.0-in.) gage length. To prevent slippage, a fast drying glue was applied to the central 5.6 mm (0.22 in.) portion of the LVDT mounts where they touched the specimen. During "strain-controlled" loading, these LVDT's were used as the feedback device in the closed loop.

Dye-penetrant enhanced radiography was used to monitor delamination growth through the specimen width. Diiodobutane (DIB), a dye penetrant opaque to X-rays, was injected along the delaminated edge. The film was placed immediately behind the specimen. While still mounted in the test machine, specimens were exposed to X-rays generated for 5 s at 18 kV from a portable point-source unit positioned 386 mm (15.5 in.) away from the specimen. The radiographs showed the location of the delamination front (Fig. 1b). The dark outline in the center of the picture is the "shadow" (X-ray image) of the LVDT rods used to measure displacements.

### Damage Development

The same type of damage developed during both quasi-static tension and constant-amplitude, tension-tension fatigue. First, a few isolated cracks formed in the 90-deg plies. These were followed almost immediately by the formation of small delaminations along the edge, as seen in Fig. 2a. When the delaminations formed, the number of 90-deg-ply cracks increased signifi-

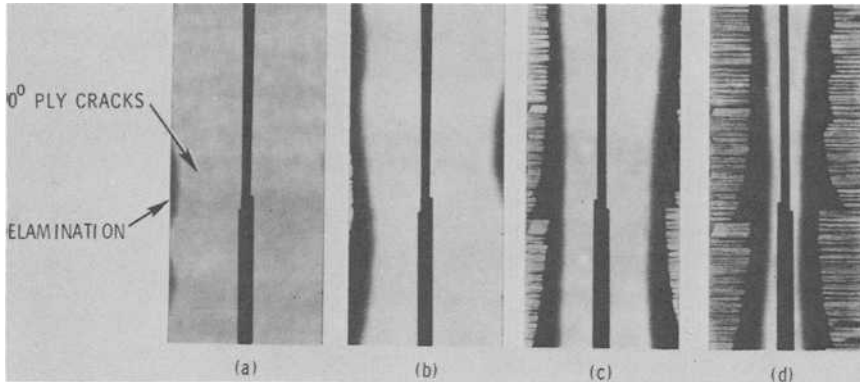


FIG. 2—Radiographs showing damage growth through the width of  $[\pm 30/\pm 30/90/90]$  laminates.

cantly along the delaminated length of the specimen. Most of the 90-deg-ply cracks, which appear as horizontal lines on the radiographs in Fig. 2, extended beyond the delamination front outlined in the X-ray photograph. Many of the ply-cracks immediately extended halfway across the specimen width. As loading continued, additional delaminations formed and joined with original delaminations. Delaminations grew much more rapidly along the length of the specimen than across the width (Fig. 2b). Eventually, two delaminations, one on each side of the specimen, extended along the entire specimen length between the grips (Fig. 2c), after which the delaminations continued to grow across the width. Loading was terminated when the delamination front reached the shadow of the LVDT rods (Fig. 2d).

To illustrate the location of damage through the thickness, a few acetate tape replicas of a delaminated edge were made [6]. Figure 3 shows photographs of two replicas and a portion of the delaminated edge. As shown in Fig. 3a, ply cracks extended through the thickness of all three interior 90-deg plies. As shown in Fig. 3b, delaminations formed and grew in  $-30/90$  interfaces, typically shifting from one interface, through 90-deg ply cracks, to its symmetric  $-30/90$  counterpart. However, delaminations did not shift interfaces at every 90-deg ply crack encountered. As shown in a photograph of the delaminated edge, Fig. 3c, interface shifting did not occur in a regular pattern.

Besides formation of delaminations at the  $-30/90$  interfaces and cracks in the 90-deg plies, an occasional angular crack formed in the innermost  $-30$ -deg ply. The replica of the edge in Fig. 4a shows two angular cracks in the innermost  $-30$ -deg plies originating at a 90-deg ply crack tip and creating delaminations in the  $+30/-30$  interfaces. As shown in the radiograph in Fig. 4b, the delaminations in the  $+30/-30$  interfaces were small and triangular in shape. These  $+30/-30$  delaminations often temporarily arrested initial  $-30/90$  interface delamination growth along the length of the edge. However,

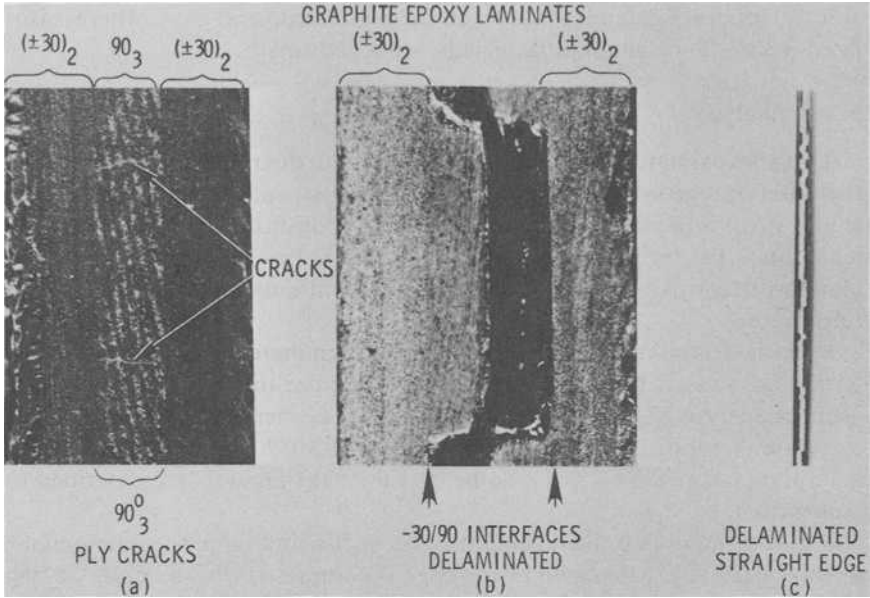


FIG. 3—Damage location through the thickness of  $[\pm 30/\pm 30/90/\bar{90}]_n$  laminates.

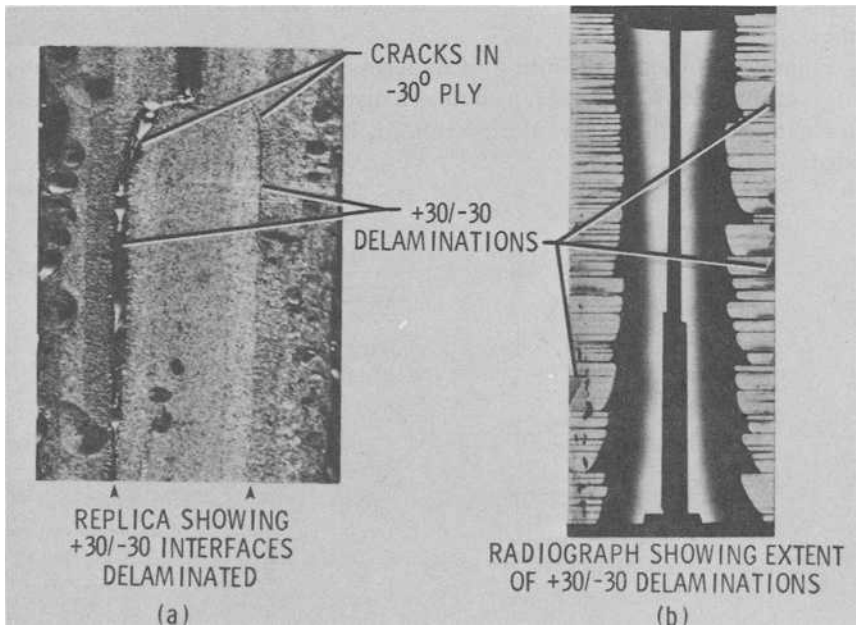


FIG. 4—Delaminations in +30/-30 interfaces.

-30/90 interface delaminations eventually joined up and grew, whereas isolated +30/-30 delaminations usually remained small.

### Stress Analysis

Two approximate analyses were used to obtain quantitative predictions of the onset and growth of delaminations. The first was a quasi-three-dimensional stress analysis that yielded stress distributions and strain energy release rates. The second was a simple rule of mixtures analysis that was used along with laminated plate theory to calculate stiffness loss and strain energy release rates.

Because delaminations form in unnotched laminates as a result of the interlaminar stresses that develop at the edge, a quasi-three-dimensional finite element analysis [7] was performed. The finite element analysis was used to calculate stress distributions in the  $[\pm 30/\pm 30/90/90]_s$  laminate for a unit axial nominal strain ( $\epsilon_0 = 1$ ). Some details of the analysis are described in Appendix I.

Figure 5 shows that the through-thickness distribution of the interlaminar normal stress,  $\sigma_z$ , calculated at the edge is compressive in the outer 30-deg plies but reaches a relatively high tensile value at the -30/90 interface and throughout the 90-deg plies. Also shown in Fig. 5 is the approximate  $\sigma_z$  distribution through the thickness calculated from laminated plate theory and an assumed stress distribution across the width [8]. This plot also shows the highest tensile  $\sigma_z$  stresses to be at the -30/90 interface and within the 90-deg plies.

Figure 6 shows a distribution of  $\sigma_z$  across the specimen width, near the edge, at the -30/90 interface, as well as a distribution of the axial stress,  $\sigma_x$ , in the adjacent 90-deg ply. Both  $\sigma_z$  and  $\sigma_x$  have high tensile values at the edge.

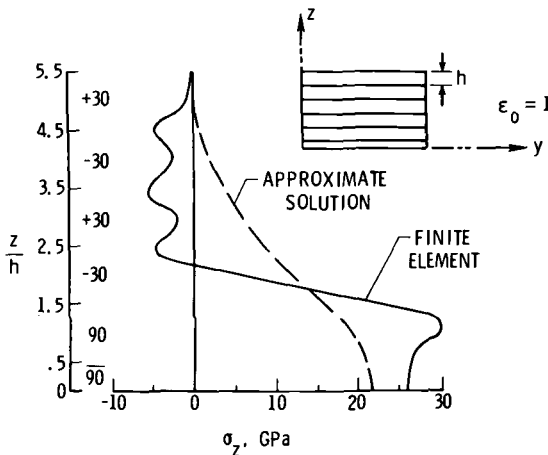


FIG. 5—Through-thickness  $\sigma_z$  distribution at edge of  $[\pm 30/\pm 30/90/90]_s$  laminate.

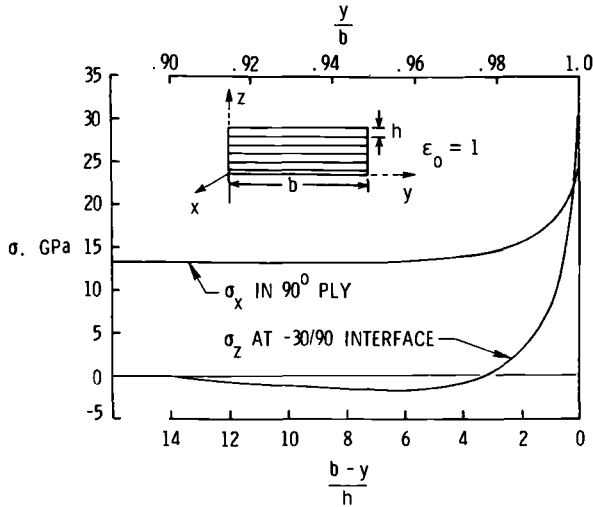


FIG. 6—Through-width distributions of  $\sigma_x$  and  $\sigma_z$  near the edge.

These stress distributions showed reasonable correlation with the observed damage that developed. Indeed, examining  $\sigma_z$  and interlaminar shear stress distributions are helpful in identifying likely delamination sites. However, interlaminar stress distributions calculated from finite element analyses were not useful for modeling damage growth quantitatively because the magnitude of calculated peak stresses at the edge varied with mesh size. Furthermore, linear elastic analysis suggests that the interlaminar stresses at ply interfaces can become singular at the edge [7]. This singular behavior would preclude the use of a failure criterion based on maximum interlaminar stress values. Therefore, an alternate approach, based upon strain energy release rates, was adopted to quantitatively describe the onset and growth of delaminations.

### Stiffness Loss

In many composite laminates, stiffness loss may reflect delamination growth. Furthermore, the rate of stiffness loss with delamination growth can be related directly to strain energy release rates. Therefore, analysis and experiments were performed to correlate laminate stiffness and delamination size.

### Rule of Mixtures Analysis

To analyze stiffness loss due to delamination, a simple rule of mixtures analysis, along with laminated plate theory, was used. First, the stiffness (tangent modulus) of a balanced, symmetric composite laminate (Fig. 7a) was calculated from laminate theory [9,10] as

$$E_{LAM} = \frac{1}{X_{11}t} \tag{1}$$

where  $X_{11}$  is the first element of the inverse extensional stiffness matrix,  $A_{ij}^{-1}$  ( $i, j = 1, 2, 3$ ), and  $t$  is the laminate thickness. Next, assuming a complete delamination in one or more interfaces, and using the rule of mixtures assumption that the sublaminates formed undergo the same axial strain (but no longer have the same transverse strains), results in

$$E^* = \frac{\sum_{i=1}^m E_i t_i}{t} \tag{2}$$

where

- $m$  = number of sublaminates formed by the delamination,
- $E^*$  = stiffness of a laminate completely delaminated along one or more interfaces,
- $E_i$  = the laminate stiffness of the  $i^{th}$  sublaminate formed by the delamination, and
- $t_i$  = the thickness of the  $i^{th}$  sublaminate.

Although Eq 2 represents a two-dimensional formulation,  $E^*$  will depend upon which interfaces delaminate. This, in turn, determines the stiffness,  $E_i$ , and thickness,  $t_i$ , of each new sublaminate. Hence, Eq 2 is sensitive to the through-thickness location of the delamination. For the  $[\pm 30/\pm 30/90/90]_s$  laminate, assuming a delamination in both  $-30/90$  interfaces (Fig. 7b) Eq 2 becomes

$$E^* = \frac{8E_{(\pm 30)} + 3E_{(90)}}{11} \tag{3}$$

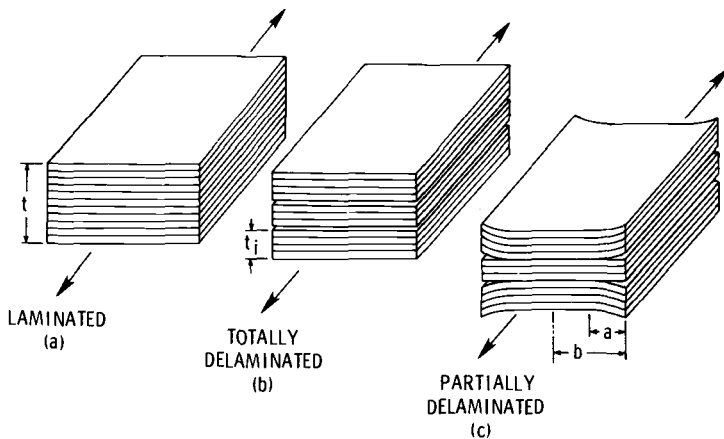


FIG. 7—Rule of mixtures analysis of stiffness loss.

Finally an equation for the stiffness,  $E$ , of a partially delaminated specimen was developed using the rule of mixtures. Equal-sized delaminated strips were assumed to exist at both edges of the laminate (Fig. 7c). Then, by assuming the laminated and delaminated portions of the specimen act as independent components loaded in parallel, the rule of mixtures yields

$$E = (E^* - E_{LAM}) \frac{a}{b} + E_{LAM} \quad (4)$$

A more general form of Eq 4 may be developed by assuming that the relationship between laminate stiffness loss and delamination size can be represented by

$$\frac{E - E_{LAM}}{E^* - E_{LAM}} = \frac{A}{A^*} \quad (5)$$

where

$A$  = delaminated area and  
 $A^*$  = total interfacial area.

Rearranging Eq 5 yields

$$E = (E^* - E_{LAM}) \frac{A}{A^*} + E_{LAM} \quad (6)$$

Equation 4 is a special case of Eq 6 where  $a/b = A/A^*$ .

### Experiments

To verify the linear relationship between stiffness and delamination size implied by Eqs 4 and 6, four quasi-static tension tests were conducted. The specimens were loaded in a strain controlled mode until a delamination formed. Then, the specimens were unloaded to ten percent of the peak nominal strain, DIB was placed on the specimen edges, and an X-ray photograph was taken. Next, the specimens were reloaded in strain increments of 0.00025 above the previous maximum strain level. This procedure was repeated until the specimen was almost totally delaminated.

During each loading, output signals of the two LVDT's were averaged, and load deflection curves were plotted on an X-Y plotter. The initial linear portion of each plot was used to calculate laminate stiffness corresponding to the damage recorded in the previous X-ray photograph (Fig. 8). Delaminated areas recorded on the photographs within the 102-mm (4-in.) gage length were measured with a planimeter. To minimize data reduction error, each delamination was traced three times and measured areas were averaged. Then, a strip delamination size,  $a$ , having equal area over the LVDT gage length as the measured delamination, was calculated (Fig. 9).

Figure 10 shows a plot of normalized stiffness,  $E/E_o$ , as a function of normalized delamination size  $a/b$ . A least-squares regression line for the

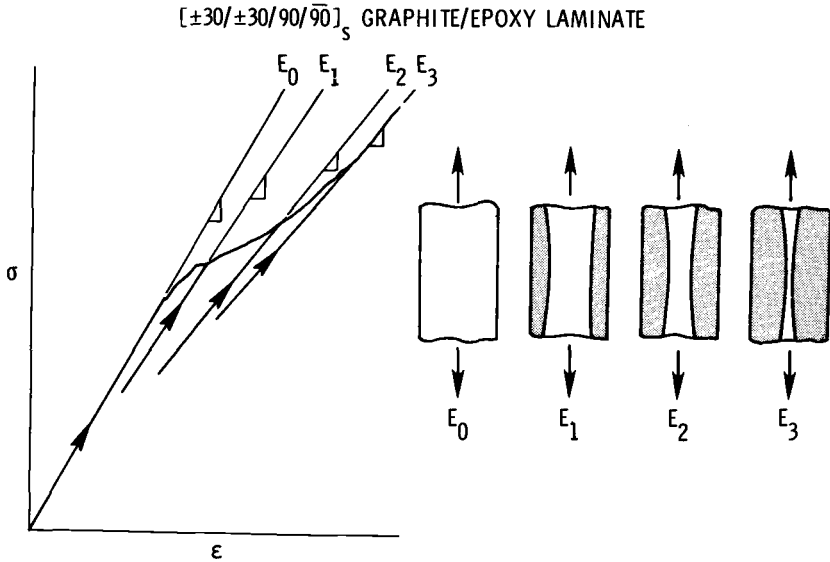


FIG. 8—Delamination size and stiffness data accumulation during quasi-static loading.

data indicated that  $E^* = 0.742E_o$ , where  $E_o$  is the initial tangent modulus measured. Hence, a total delamination in the  $[\pm 30/\pm 30/90/\overline{90}]_s$  laminate would result in a 25.8 percent reduction in laminate stiffness. The data agreed with the linear rule of mixtures Eq 4, normalized by  $E_{LAM}$ , where  $E^*$  was calculated from Eq 3 and sublaminates stiffnesses were calculated using Eq 1 (see Appendix II) with material properties from Ref 11.

Finally, Eqs 2 and 4 were used iteratively to calculate laminate stiffness for specimens having  $-30/90$  interface delaminations and concurrent, although small,  $+30/-30$  interface delaminations (see Appendix III). The contribution of  $90$ -deg ply cracks to laminate stiffness loss also was considered (see Appendix III). However, the net effect of both secondary mechanisms ( $+30/-30$  delaminations and ply cracks) on stiffness loss was negligible for the  $[\pm 30/\pm 30/90/\overline{90}]_s$  laminate.

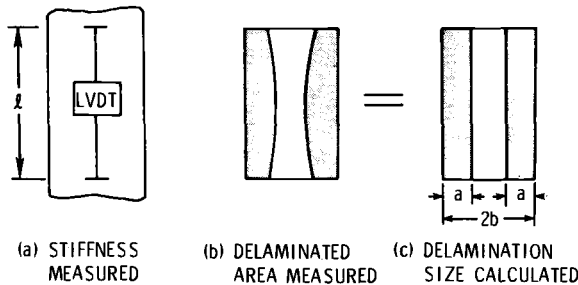


FIG. 9—Illustration of strip delamination approximation.

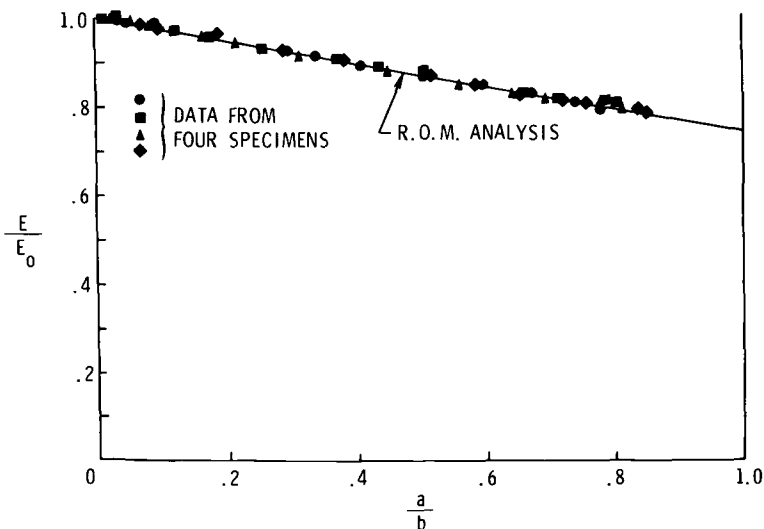


FIG. 10—Stiffness as a function of delamination size.

### Strain Energy Release Rate

For an elastic body containing a planar flaw of area  $A$ , the strain energy release rate,  $G$ , is the difference between the rate of work done,  $d\mathcal{W}/dA$ , and the rate at which elastic strain energy is stored,  $d\mathcal{U}/dA$ , as the flaw area increases [12], that is

$$G = \frac{d\mathcal{W}}{dA} - \frac{d\mathcal{U}}{dA} \quad (7)$$

Assuming that a nominal strain,  $\epsilon$ , is sufficient to extend the flaw, the work term vanishes. Then, if  $\mathcal{U}$  is expressed as a product of the strain-energy density and volume of the body,  $\mathcal{V}$ , substituting Hooke's law into Eq 7 yields

$$G = -\mathcal{V} \frac{\epsilon^2}{2} \frac{dE}{dA} \quad (8)$$

where  $dE/dA$  is the rate of stiffness change as the flaw extends.

In this study, the body was a tensile-loaded, unnotched composite laminate, containing edge delaminations. The strain energy release rate associated with the growth of edge delaminations can be calculated by assuming two strip delaminations (Fig. 9) where

$$\begin{aligned} \mathcal{V} &= 2b l t \\ A^* &= 2b l \\ A &= 2 l a \\ dA &= 2 l da \end{aligned} \quad (9)$$

Then, substituting Eqs 9 into Eq 8 and differentiating Eq 4 yields

$$G = \frac{\epsilon^2 t}{2} (E_{LAM} - E^*) \tag{10}$$

Equation 10 also may be derived for an arbitrary-shaped delamination by substituting Eq 6 into Eq 8, differentiating, and noting that  $\mathcal{V} = A^*t$ . Hence, as indicated in Eq 10, the strain energy release rate associated with delamination growth is independent of the delamination size. The magnitude of  $G$  depends only on the laminate layup and location of the delaminated interface(s) (which determine  $E_{LAM}$  and  $E^*$ ), the nominal strain,  $\epsilon$ , and the laminate thickness,  $t$ .

Furthermore, the strain energy release rate (Eq 10) may have contributions from any of the three components  $G_I$ ,  $G_{II}$ , or  $G_{III}$ , corresponding to the opening, in-plane shear, and out-of-plane shear fracture modes. In addition, near the edge,  $G$  may deviate from the value predicted by Eq 10, which was developed using laminated plate theory and the rule of mixtures. Therefore, a virtual crack extension technique was used with the quasi-three-dimensional finite element analysis to calculate  $G_I$ ,  $G_{II}$ , and  $G_{III}$  as a function of delamination size (see Appendix I). As shown in Fig. 11, the finite element analysis indicated that the total  $G$ , represented by  $G_I + G_{II}$  ( $G_{III}$  was negligible), reached the value predicted from Eq 10 once the delamination had grown a very small distance in from the edge.

Because  $G$  increased rapidly with “ $a$ ” near the edge, a small delamination that formed (for whatever reason) at the edge would be expected to undergo rapid initial growth. This behavior was observed in the quasi-static tension tests used to generate stiffness data. As soon as a delamination was detected,

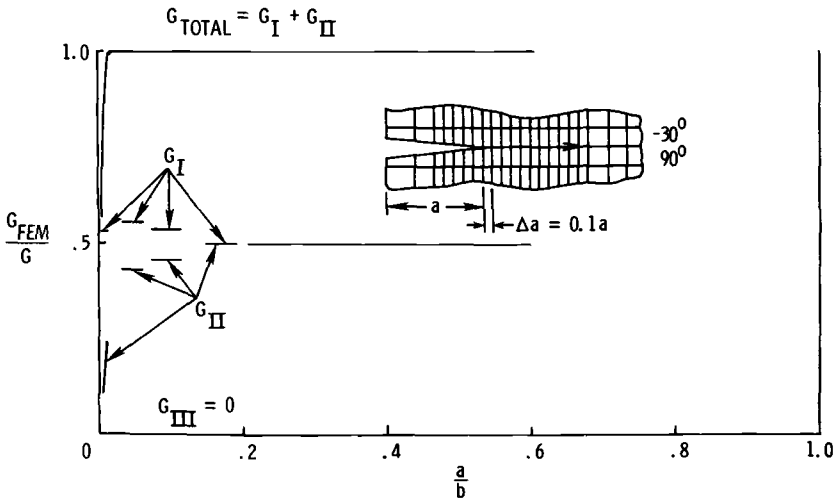


FIG. 11—Strain energy release rate components from finite element analysis as a function of delamination size.

the loading was stopped. The formation and growth of the delamination to some finite size appeared to be nearly instantaneous. Therefore,  $G$  calculated from Eq 10 at the nominal strain where delamination first was detected was considered to be the critical value,  $G_c$ , required to form the delamination. This  $G_c$  then was used to predict the onset of delamination in other laminates.

### Delamination Onset

To predict the onset of delamination in other laminates, several things were done. First, tension tests of  $[\pm 30/\pm 30/90/90]_s$  laminates were run to determine the nominal strain level,  $\epsilon_c$ , at which delamination begins. Next,  $\epsilon_c$  was used in Eq 10 to predict a critical  $G_c$  for the onset of delamination. Then,  $G_c$  was used to predict the nominal strain at the onset of delamination in other laminates. A more detailed description of the procedure follows.

#### Critical $G_c$ Determination

First, eighteen  $[\pm 30/\pm 30/90/\overline{90}]_s$  graphite-epoxy laminates were loaded monotonically in tension at a rate of 44.5 N/s (10 lb/s) until a delamination was detected. The load level corresponding to delamination onset was recorded and the corresponding applied stress,  $\sigma_c$ , was calculated. Then, to determine the nominal strain at the onset of delamination,  $\epsilon_c$ ,  $\sigma_c$  was divided by  $E_{LAM}$ , calculated from laminated plate theory using the following elastic properties from Ref 11

$$E_{11} = 138 \text{ GPa (20.0 Msi)}$$

$$E_{22} = 15 \text{ GPa (2.1 Msi)}$$

$$G_{12} = 5.9 \text{ GPa (0.85 Msi)}$$

$$\nu_{12} = 0.21$$

The average  $\epsilon_c$  value was 0.00347. In addition,  $\epsilon_c$  was determined from LVDT measurements on the four tests conducted to generate stiffness data. In each of these four tests, the load deflection plot was linear until the delamination formed. The average value of  $\epsilon_c$  where the load-deflection curve deviated from linear for these four tests was also 0.00347.

Next,  $\epsilon_c$  was substituted into Eq 10 to determine  $G_c$ . Stiffness  $E_{LAM}$  and  $E^*$  were calculated from Eqs 1 and 3, respectively, using elastic properties from Ref 11. The average laminate thickness, measured with micrometers, was 1.51 mm (0.0594 in.). A value of 137 J/m<sup>2</sup> (0.78 in · lb/in.<sup>2</sup>) was calculated for the critical strain energy release rate.

#### Delamination Onset Prediction

To predict the onset of delamination in other laminates, Eq 10 was inverted to yield

$$\epsilon_c = \sqrt{\frac{2G_c}{t(E_{LAM} - E^*)}} \tag{11}$$

The critical  $G_c$  determined from  $[\pm 30/\pm 30/90/90]_s$  laminate data was used in Eq 11 to predict the nominal strain at the onset of delamination in  $[+45_n/-45_n/0_n/90_n]_s$  ( $n = 1, 2, 3$ ) T300-5208 graphite-epoxy laminates having the same stacking sequence but different thicknesses. To evaluate  $E^*$ , delaminations were modeled along both 0/90 interfaces where high tensile  $\sigma_z$  stresses were anticipated [3] on the basis of the approximate analysis of Ref 8. Delaminations have been observed in the 0/90 interface of a  $[\pm 45/0/90]_s$  laminate in Ref 13. Then, stiffness  $E_{LAM}$  and  $E^*$  were calculated from Eqs 1 and 2, respectively, using elastic properties from Ref 11.

A ply thickness of 0.15 mm (0.0057 in.) was determined in Ref 3 for the 8-ply ( $n = 1$ ), 16-ply ( $n = 2$ ), and 24-ply ( $n = 3$ ) laminates. In Fig. 12, predictions of  $\epsilon_c$  were compared to  $\epsilon_c$  values calculated by dividing measured  $\sigma_c$  values from Ref 3 by  $E_{LAM}$ . Because the data from Ref 3 represent the average of only two or three tests for each stacking sequence, only preliminary conclusions can be drawn. Nevertheless, the good comparison indicates that  $G_c$  may be independent of the ply orientations that make up the delaminating interface. For example,  $G_c$  may be the same for delamination onset in the  $-30/90$  interfaces of  $[\pm 30/\pm 30/90/90]_s$  laminates and for delamination onset in the 0/90 interfaces of the  $[+45_n/-45_n/0_n/90_n]_s$  ( $n = 1, 2, 3$ ) laminates. In fact, Eq 11 indicates that the dependence of  $\epsilon_c$  on stacking sequence and the ply orientations that make up the delaminating interface is accounted for in the  $(E_{LAM} - E^*)$  term.

In addition, both Eq 11 and the data indicate that delaminations will form at a lower nominal strain in thicker laminates of identical stacking se-

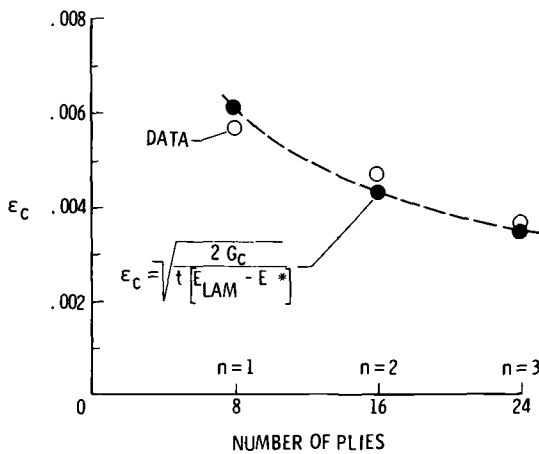


FIG. 12—Edge delamination onset prediction compared with  $[+45_n/-45_n/0_n/90_n]_s$  ( $n = 1, 2, 3$ ) data.

quences. According to Ref 4, interlaminar stress distributions calculated from elastic analysis will be identical for all  $[+45_n/-45_n/0_n/90_n]_s$  laminates subjected to the same applied stress. Therefore, the authors concluded that a failure criterion, if based on critical interlaminar stresses, would not predict the thickness dependence of delamination onset. Hence, the strain energy release rate appears to be the most useful parameter for quantitatively predicting the onset of delamination after the delamination-prone interface(s) have been identified from a stress analysis.

## Delamination Growth

### *Quasi-Static Tension*

Edge delamination has been observed to be a stable fracture process in laminates subjected to tension loading [1,5,14]. Hence, the applied load must be increased to force the delamination to grow. Tension tests on the  $[\pm 30/\pm 30/90/90]_s$  laminates confirmed this observation. Unstable growth of the delamination through the width did not occur before the laminate failed (fractured into two pieces). In the four quasi-static tests conducted to generate stiffness data, delaminations did not grow after the mean applied load exceeded 13 350 N (3000 lb). The four laminates eventually failed at a mean load of 20 000 N (4500 lb). Therefore, the  $[\pm 30/\pm 30/90/90]_s$  laminate is well suited to studying stable delamination growth.

The stable growth of flaws can be characterized using the crack growth resistance curve (*R*-curve) concept of fracture mechanics [15]. Therefore, a delamination resistance curve was constructed. Strain energy release rates,  $G$ , were calculated from Eq 10. Because  $G$  does not depend on delamination size, it appears as a horizontal line in Fig. 13. The three horizontal lines shown are  $G$  values calculated for a single specimen at three successive nominal strain levels. In addition, the delamination resistance,  $G_R$ , was calculated using the maximum nominal strain in Eq 10. However,  $G_R$  was plotted as a point corresponding to the size (see Fig. 9) of the delamination created by the nominal strain. As shown in Fig. 13, the curve formed by all such points, generated during the four  $[\pm 30/\pm 30/90/90]_s$  quasi-static tension tests, constitutes the delamination growth resistance curve (*R*-curve) for the graphite-epoxy specimens tested. The critical  $G_c$  used in the previous section to predict the onset of delamination represents the first value of  $G_R$ , that is, the first point on the *R*-curve. Hence, the *R*-curve characterizes the laminates' resistance to delamination growth under tensile loading.

If the *R*-curve is independent of the ply orientations that make up the delaminated interface, as  $G_c$  appears to be (see previous section), then Eq 10 and the *R*-curve can be used to predict the growth of delaminations under quasi-static tension in other laminates. As the loading is increased,  $G$  can be calculated from Eq 10 and compared with the *R*-curve to predict delamina-

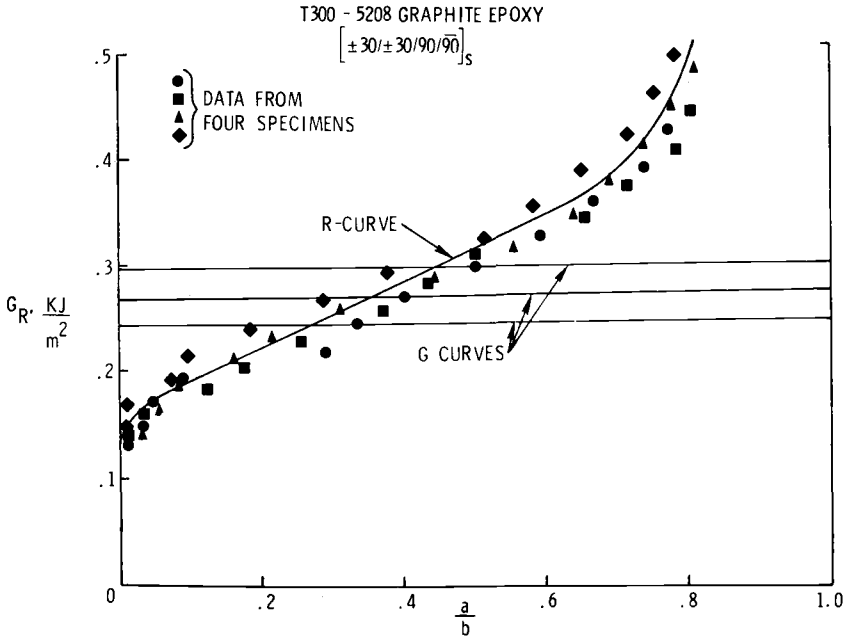


FIG. 13—Delamination resistance curve (R-curve) for  $[\pm 30/\pm 30/90/90]_S$ , T300-5208 graphite-epoxy laminates.

tion size. Hence, delamination size as a function of applied load could be predicted for other laminates.

### Fatigue

**Experiments**—Constant amplitude, tension-tension, strain-controlled fatigue tests of  $[\pm 30/\pm 30/90/90]_S$  graphite-epoxy specimens were conducted at a frequency of 10 Hz and a strain ratio of 0.2. Specimens were loaded slowly in tension until a small delamination appeared. Laminate stiffness was measured during this initial loading. Then, the specimen was unloaded and delamination size was recorded using DIB-enhanced X-ray photography. Next, the specimen was reloaded to the mean strain and the stiffness of the delaminated specimen was recorded. Then, constant-strain-amplitude cyclic loading was applied. The cyclic loading was interrupted at specified intervals to measure delamination size and static stiffness. Hence, a photographic record of delamination size and a record of static stiffness as a function of load cycles were accumulated. Cyclic loading was terminated when the delamination had grown across most of the specimen width and the front was obscured by the X-ray image of the LVDT rods (Fig. 2d).

**Delamination Growth Rate Measurements**—Figure 14 shows a typical plot of delamination size as a function of load cycles. A strip delamination size,

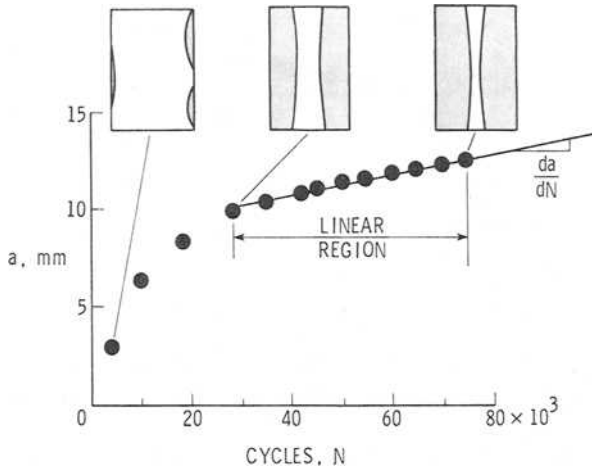


FIG. 14—Typical plot of delamination size as a function of load cycles.

$a$ , was calculated from the delaminated area (Fig. 9) measured from X-ray photographs using a planimeter. Three separate planimeter tracings of each delaminated area were performed to minimize data reduction error. As indicated in Fig. 14, once the delamination had grown over the entire length of the specimen edge, a constant growth rate,  $da/dN$ , eventually was achieved. Table 1 lists the growth rates,  $da/dN$ , determined from least squares linear regression analysis of the data for each fatigue test.

TABLE 1—Fatigue growth rate measurements.

$\epsilon_{max}$ , $\mu\text{m/m}$	$G_{max}$ , $\text{J/m}^2$	Specimen Number	$da/dN$ , mm per cycle		$dE/dN$ , Pa per cycle	Cycle range of linear fit, cycles $\times 10^3$
			Area Measure	Stiffness Measure		
3000	102	C20	26.0	22.3	-17.7	45 to 120
3000	102	F18	19.5	29.0	-22.9	40 to 120
3000	102	F24	24.5	27.0	-21.3	25 to 80
3000	102	C10	28.3	30.2	-23.8	40 to 115
3000	102	mean	24.6	27.1	...	...
3250	119	A7	41.8	...	...	40 to 80
3250	119	F3	63.9	64.2	-50.7	14 to 50
3250	119	E4	23.3	51.2	-40.3	40 to 70
3250	119	C16	23.6	25.4	-20.1	40 to 120
3250	119	mean	38.2	46.9	...	...
3500	138	D2	52.6	106.2	-83.8	30 to 60
3500	138	B13	87.1	119.7	-94.5	16 to 40
3500	138	D22	64.6	39.7	-31.3	20 to 60
3500	138	B21	47.9	46.6	-36.7	28 to 75
3500	138	mean	63.0	78.0	...	...

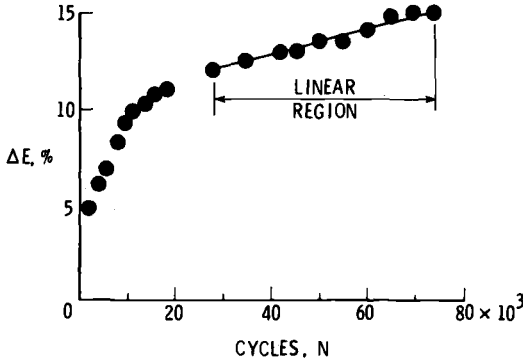


FIG. 15—Typical plot of static stiffness loss as a function of load cycles.

Figure 15 shows a typical plot of static stiffness loss as a function of load cycles. This plot also became fairly linear once the delamination had grown away from the edge. Stiffness degradation rates,  $dE/dN$ , were calculated from least squares linear regression analysis of the data over the same cyclic range used to fit  $da/dN$  data. Because stiffness was found to be linearly related to delamination size, differentiating both sides of Eq 4 with respect to number of cycles ( $N$ ) allowed an alternate determination of delamination growth rates,  $da/dN$ , from measured stiffness degradation rates,  $dE/dN$ , that is

$$\frac{da}{dN} = \left( \frac{b}{E^* - E_{LAM}} \right) \frac{dE}{dN} \tag{12}$$

Therefore, delamination growth rates for the edge delamination specimens

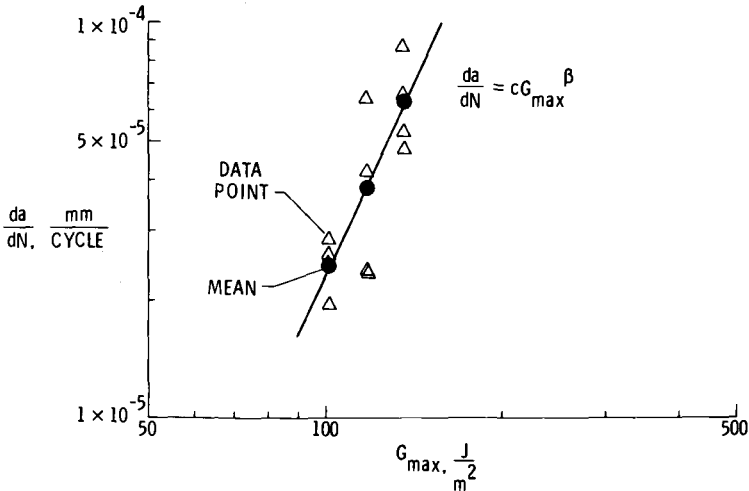


FIG. 16—Power law curve fit for  $da/dN$  as a function of  $G_{max}$ .

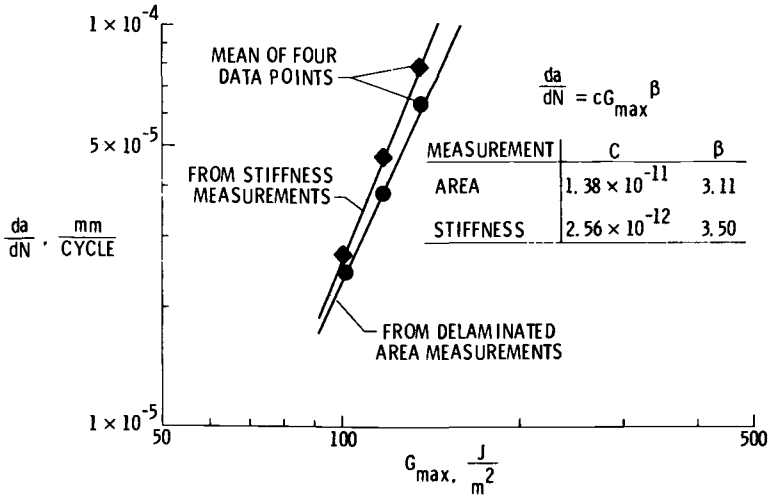


FIG. 17—Effect of delamination measurement method on power law curve fit.

could be estimated without measuring the delamination size directly (Table 1). Hence, the  $[\pm 30/\pm 30/90/90]_s$  specimens used in this investigation should be useful for generating baseline delamination growth data.

**Data Correlation with Analysis**—Four fatigue tests were conducted at each of three maximum cyclic strain levels. The maximum cyclic strain levels,  $\epsilon_{max}$ , chosen were 0.003, 0.00325, and 0.0035. The maximum strain energy release rate,  $G_{max}$ , was calculated from Eq 10 using  $\epsilon_{max}$ . Therefore, a constant  $\epsilon_{max}$  test was also a constant  $G_{max}$  test. The mean of the four delamination growth rates,  $da/dN$ , was determined for each of the three  $G_{max}$  levels. A power curve of the form  $da/dN = cG_{max}^\beta$  was fit to the three mean values of  $da/dN$  and the three values of  $G_{max}$  using a least squares routine. An excellent correlation was achieved for both delamination growth rate measurement techniques.

Figure 16 shows  $da/dN$  as a function of  $G_{max}$  for growth rates estimated directly from measured delaminated areas. The growth rates for all four tests at each  $G_{max}$  level are shown along with the mean growth rate. Figure 17 compares the least-squares power law fits using direct area measurements and indirect stiffness estimates of delamination growth rates. Because both  $da/dN$  and  $G$  can be calculated without direct measurement of delamination size, the stiffness technique presents a relatively simple means of generating data to determine the dependence of empirical parameters  $c$  and  $\beta$  on differences in load history, frequency, temperature, etc.

With the parameters  $c$  and  $\beta$  determined, the power law might be applied to other laminates. The calculated strain energy release rates could be used with  $c$  and  $\beta$  measured from edge-delamination baseline tests to determine delamination growth rates.

## Concluding Remarks

### *Methodology Summary*

A methodology for analyzing the onset and growth of delaminations in composite materials was formulated based on findings in the current work and in the literature. The methodology is as follows.

First, a stress analysis of the particular material, configuration, and loading must be performed. The analysis should establish where delaminations will be located. For unnotched laminates, the approximate analyses discussed in this paper [8, 16] might be adequate. After the location is established, the delamination onset and growth can be characterized quantitatively using strain energy release rates. Such a characterization incorporates the influence of material volume. Furthermore, determination of the singular stress field at the delamination front is not required.

The current work indicates that a total strain energy release rate may be sufficient to characterize the onset and growth of edge delaminations in tensile-loaded coupons. More work is required to determine if this is true for other configurations and loadings. However, if strain energy release rates must be separated into  $G_I$ ,  $G_{II}$ , and  $G_{III}$  components using a numerical analysis, then the dependence of these calculated components on grid size should be checked carefully and documented.

### *Immediate Results*

A simple rule of mixtures analysis, using laminated plate theory, indicated that laminate stiffness was a linear function of delamination size. The analysis accurately predicted stiffness loss due to edge delaminations in  $[\pm 30/\pm 30/90/90]_n$  graphite-epoxy laminates. The linear stiffness relationship was used to derive a closed-form equation for the strain energy release rate,  $G$ , associated with delamination growth in unnotched laminates. The simple  $G$  equation was used to predict delamination onset in  $[+45_n/-45_n/0_n/90_n]_n$  ( $n = 1, 2, 3$ ) laminates using a critical  $G_c$  determined from  $[\pm 30/\pm 30/90/90]_n$  laminates. Stable delamination growth in the  $[\pm 30/\pm 30/90/90]_n$  laminates was characterized by developing a delamination resistance curve ( $R$ -curve). Delamination growth in  $[\pm 30/\pm 30/90/90]_n$  laminates in fatigue was characterized by developing a power law correlation between  $G$  and delamination growth rates.

### *Potential Applications*

Preliminary predictions of delamination onset in  $[+45_n/-45_n/0_n/90_n]_n$  laminates using a critical  $G_c$  determined from tests on  $[\pm 30/\pm 30/90/90]_n$  laminates indicated that  $G_c$  may be independent of the ply orientations that make up the delaminating interface. If this is true for stable delamination growth with increased tensile load and delamination growth in fatigue, then

the delamination resistance curve (*R*-curve) and power law developed on  $[\pm 30/\pm 30/90/90]_s$  laminates can be used to predict delamination growth in other laminates.

## APPENDIX I

### Finite Element Analysis

#### Formulation

The quasi-three-dimensional finite element analysis was developed in Ref 7. A displacement field of the form

$$\begin{aligned} u &= \epsilon_0 x + U(y, z) \\ v &= V(y, z) \\ w &= W(y, z) \end{aligned} \quad (13)$$

was assumed, where  $\epsilon_0$  was a prescribed uniform axial strain. Eight-noded quadrilateral, isoparametric elements with 3 deg of freedom per node were used to model a cross section along the specimen length (Fig. 18). Only one quarter of the cross section was modeled due to symmetry conditions. Each ply was modeled with one element through its thickness except for the central 90-deg ply, which was modeled with one element through its half-thickness. The graphite-epoxy unidirectional properties [11] used in the analysis were

$$\begin{aligned} E_{11} &= 138 \text{ GPa (20.0 Msi)} \\ E_{22} &= E_{33} = 15 \text{ GPa (2.1 Msi)} \\ G_{12} &= G_{13} = G_{23} = 5.9 \text{ GPa (0.85 Msi)} \\ \nu_{12} &= \nu_{13} = \nu_{23} = 0.21 \end{aligned} \quad (14)$$

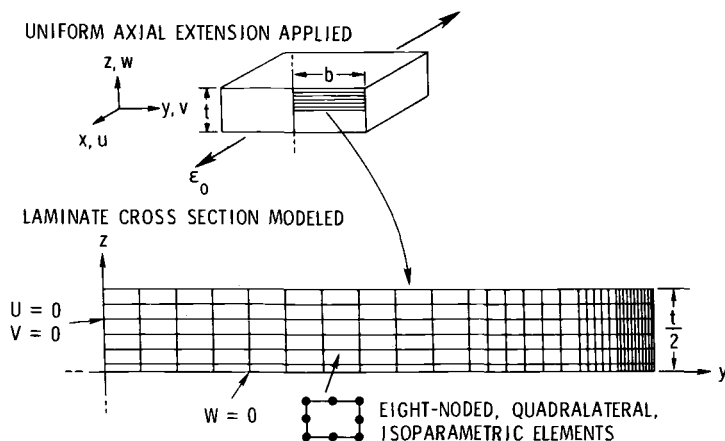


FIG. 18—Finite element discretization of specimen cross section.

*Virtual Crack Extension Technique*

Previously, a virtual crack extension technique has been applied to finite element analysis of delaminations [1,4]. In this technique, the work required to close the delamination, expressed in terms of nodal forces and displacements is assumed to be equivalent to the strain energy released as the delamination extends due to a constant nominal strain. This technique greatly simplifies the computation of  $G_I$ ,  $G_{II}$ , and  $G_{III}$  because knowledge of the singular stress field near the crack tip is not required.

Figure 19 illustrates the technique as it was used with the quasi-three-dimensional finite element analysis. First, the nodal forces were calculated for an initial delamination of size  $a$ . Then, the delamination was extended an amount  $\Delta a$  and the resulting nodal displacements at the same location were calculated. The expressions for  $G_I$ ,  $G_{II}$ , and  $G_{III}$  in terms of nodal forces and displacements were

$$\begin{aligned} G_I &= \frac{1}{2\Delta a} [(Z_b^1 + Z_b^2)(W_b - W_c) + Z_d^2(W_d - W_e)] \\ G_{II} &= \frac{1}{2\Delta a} [(Y_b^1 + Y_b^2)(V_b - V_c) + Y_d^2(V_d - V_e)] \\ G_{III} &= \frac{1}{2\Delta a} [(X_b^1 + X_b^2)(U_b - U_c) + X_d^2(U_d - U_e)] \end{aligned} \quad (15)$$

where, for example,  $Z_b^1$  represents the force in the  $z$  direction at node  $b$  calculated from Element 1.

Figure 11 shows  $G_I$  and  $G_{II}$  as functions of delamination size.  $G_{III}$  was negligible for this case. Strain energy release rates,  $G_{FEM}$ , calculated using Eqs 15, were normalized by the constant value predicted from Eq 10. The total  $G$ , represented by  $G_I + G_{II}$ , reached the value<sup>3</sup> predicted by Eq 10 once the delamination had grown a very small distance in from the edge. Furthermore, the total  $G$  calculated was not sensitive to mesh refinement. However, the values of  $G_I$  and  $G_{II}$  calculated were sensitive to mesh refinement.

Figure 11 shows the nodal discretization used in the finite element analysis. Four different initial delamination sizes,  $a$ , were modeled. For each  $a$ , the delamination was grown in ten increments,  $\Delta a$ , equal to one tenth of the initial delamination size. As  $a$  was increased, the mesh refinement changed accordingly. For the smallest delamination size,  $G_{II}$  continually increased as the delamination grew, but  $G_I$  was constant for all ten increments of growth. The ten values of  $G_I$  for the smallest  $a$  are represented by a horizontal line segment. For the next three delamination sizes, both  $G_I$

<sup>3</sup> Because the finite element analysis models only one quarter of the laminate cross section due to symmetry, the analysis assumes four delaminations grow simultaneously, two on each side, located in the  $-30/90$  interfaces. However, in the derivation of Eq 10, only a single delamination was considered on either edge to be consistent with the physically observed behavior shown in Fig. 3c and illustrated in Fig. 20a. Making the same assumptions as the finite element analysis would have yielded

$$\begin{aligned} \mathcal{V} &= 2bt \\ A^* &= 4bl \\ A &= 4la \\ dA &= 4l da \end{aligned}$$

which would result in  $G = (\epsilon^2/4)(E_{LAM} - E^*)$ . Hence, the values calculated from the finite element analysis using Eq 15 were doubled to be consistent with Eq 10 and the observed physical behavior.

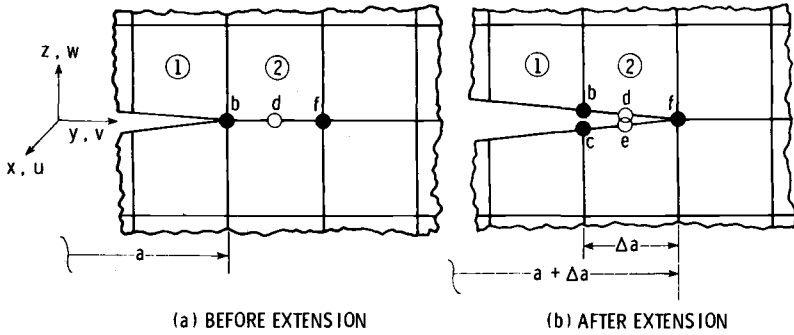


FIG. 19—Virtual crack extension technique used to calculate strain energy release rates.

and  $G_{II}$  were constant for all ten increments of growth, but the ratios  $G_I/G_{II}$  changed. For the largest delamination size modeled,  $G_I$  and  $G_{II}$  were identical, both equal to one-half the total  $G$ . Hence, calculations of  $G_I$  and  $G_{II}$  varied with mesh size.

## APPENDIX II

### Effect of Coupling on Stiffness Loss

The stiffness of an arbitrary composite laminate may be calculated from laminate theory [9,10] as

$$E_{LAM} = \frac{1}{[A_{11}]t} \tag{16}$$

where

$$[A'] = [A]^{-1} + [A]^{-1}[B][D^*]^{-1}[B][A]^{-1},$$

$$[D^*] = [D] - [B][A]^{-1}[B],$$

and  $[A]$ ,  $[B]$ ,  $[D]$  are the extensional, coupling, and bending stiffness matrixes, respectively, defined in Ref 9. If the laminate is symmetric, the  $[B]$  matrix vanishes, and Eq 16 reduces to Eq 1.

For an arbitrary laminate containing delaminations in one or more interfaces, Eq 16 may be used in Eq 2 to calculate the stiffness,  $E_i$ , of the sublaminates that are formed. For the  $[\pm 30/\pm 30/90/90]_s$  laminate, with delaminations modeled in both  $-30/90$  interfaces, Eq 2 becomes Eq 3

$$E^* = \frac{8E_{(\pm 30)_2} + 3E_{(90)_2}}{11}$$

If the  $(\pm 30)_2$  sublaminate stiffnesses are calculated using Eq 16 and material properties from Ref 11, then  $E^* = 0.69 E_{LAM}$ , which exceeds the value of  $E^*$  extrapolated from a least-squares regression line for the stiffness data. However, both  $-30/90$  interfaces did not delaminate completely (Fig. 3). As shown in Fig. 20a, delaminations shifted from one  $-30/90$  interface to another through various  $90$ -deg ply cracks. Delaminations were believed to grow in this manner to reduce the effect of bending-extension coupling that would have been present had only one interface been cleanly

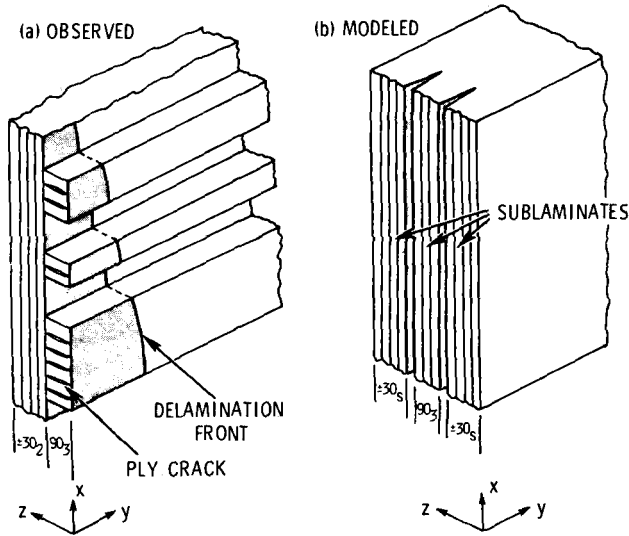


FIG. 20—Approximate model of observed damage.

delaminated or had both interfaces delaminated at the same time. Therefore, delaminations were modeled over both  $-30/90$  interfaces (Fig. 20b) but the bending-extension coupling in the  $(\pm 30)_2$  sublaminates was neglected. Hence, the stiffness of each sublaminate was evaluated using Eq 1. This resulted in  $E^* = 0.743 E_{LAM}$  which agreed with the value of  $E^*$  extrapolated from a least-squares regression line for the stiffness data (Fig. 10).

In addition, stiffness loss for delaminations of various sizes was calculated from the finite element analysis. Concurrent strip delaminations were assumed in both  $-30/90$  interfaces. Uniform axial extension also was assumed and, hence, bending-

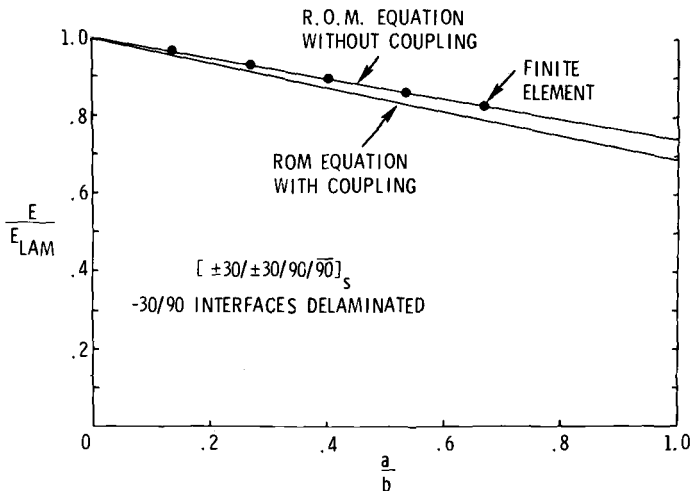


FIG. 21—Effect of coupling on stiffness loss prediction.

extension coupling was ignored. The stiffness corresponding to a particular delamination size was calculated using the technique outlined in Ref 16. Figure 21 shows the stiffness loss predicted by the linear rule of mixtures (ROM) equation without coupling ( $E_i$  calculated from Eq 1) and with coupling ( $E_i$  calculated from Eq 16). The finite element predictions agreed with the rule of mixtures equation that neglected bending-extension coupling. Hence, the finite element results also agreed with the data plotted in Fig. 10.

## APPENDIX III

### Stiffness Change from Secondary Mechanisms

#### Ninety Degree Ply Cracks

The spacings of 90-deg ply cracks in the laminated portion of partially delaminated  $[\pm 30/\pm 30/90/90]_s$  laminates were measured directly from enlarged X-ray photographs. The mean spacing is plotted in Fig. 22 as a function of delamination size (see Fig. 9) for three quasi-static test specimens. As the delaminations grew, the crack spacings decreased to within values predicted by a simple one-dimensional model [6].

Near the 90-deg ply cracks, load was assumed to be transferred to the neighboring plies and then back into the 90-deg plies to form the next crack. The model predicted that 90-deg ply cracks would reach a characteristic saturation spacing,  $K$ , determined by the laminate stacking sequence, ply thickness, and ply stiffness, but independent of load history.

For the  $[\pm 30/\pm 30/90/90]_s$  laminate, the model predicted a saturation spacing of 0.838 mm (0.033 in.). For a  $[\pm 30/\pm 30/90_3]_s$  sublaminates, representative of the delam-

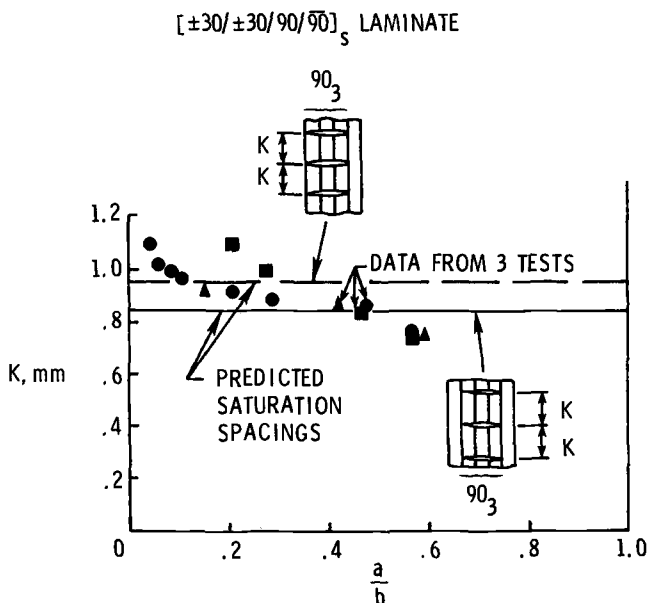


FIG. 22—Ninety degree ply crack spacing as a function of delamination size.

$[\pm 30/\pm 30/90/\overline{90}]_s$  LAMINATE

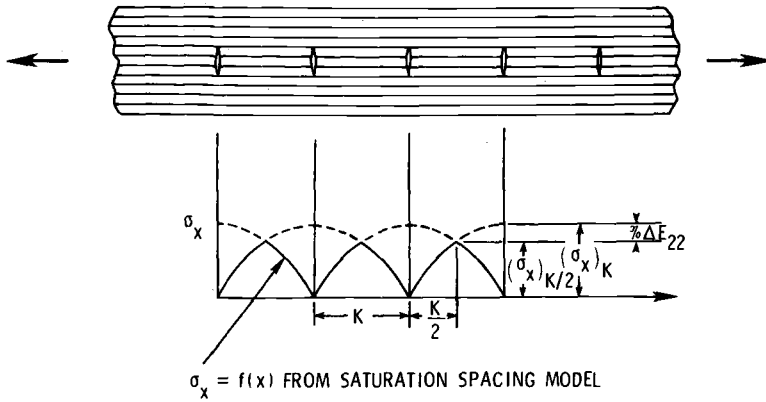


FIG. 23—Estimate of stiffness loss from 90-deg ply cracks.

inated portion of the  $[\pm 30/\pm 30/90/\overline{90}]_s$  laminate, the model predicted a saturation spacing of 0.955 mm (0.0367 in.).

Stiffness change due to 90-deg ply cracking in the partially delaminated specimen was estimated by reducing the maximum axial stress in the 90-deg plies based on the density of cracks present. As shown in Fig. 23, the transverse stiffness of the 90-deg plies,  $E_{22}$ , was reduced by the percentage difference in the maximum axial stress, calculated from the one dimensional model, at the predicted crack spacing  $K$  and at one half the spacing  $K/2$ . This difference represents the reduction in load carried by the 90-deg ply once the saturation crack pattern has formed.

For the  $[\pm 30/\pm 30/90/\overline{90}]_s$  laminate, a 12 percent reduction in the axial stress in the 90-deg plies was predicted. Reducing the transverse stiffness,  $E_{22}$ , of the 90-deg plies by 12 percent resulted in a 0.7 percent reduction in  $[\pm 30/\pm 30/90/\overline{90}]_s$  laminate stiffness. Similarly, for the  $[\pm 30/\pm 30/90]_s$  sublaminates, a 14 percent reduction in the axial stress in the 90-deg plies was predicted. Reducing the transverse stiffness,  $E_{22}$ , of the 90-deg plies by 14 percent resulted in a 2.2 percent reduction in the  $[\pm 30/\pm 30/90]_s$  sublaminates stiffness.

Because the estimated contributions of 90-deg ply cracks to stiffness reduction in the  $[\pm 30/\pm 30/90/\overline{90}]_s$  delamination specimen were so small, they were neglected in calculating  $E^*$ . However, for other laminates and materials, ply cracking may have a greater effect on axial stiffness and other stiffness parameters [17,18].

**+30/-30 Delaminations**

The largest +30/-30 interface delaminations,  $\bar{a}$ , recorded during the four quasi-static tension tests were measured and tabulated in Table 2. Only Specimen E20 had a +30/-30 delamination of significant size. Also shown in Table 2 are predicted stiffness values for the  $[\pm 30/\pm 30/90/\overline{90}]_s$  laminate, containing both -30/90 and +30/-30 interface delaminations. The stiffness was predicted using Eqs 2 and 4 first for the +30/-30 delamination, and then for the -30/90 delamination. The stiffness predicted for Specimen E20 was three percent less than the stiffness predicted assuming only -30/90 delamination. However, the data agreed best with the prediction that omitted the +30/-30 delamination. Hence, the effect of +30/-30 interface de-

TABLE 2—Effect of +30/−30 delamination on stiffness prediction.

Specimen Number	−30/90	+30/−30	$E/E_{LAM}$ Prediction		$E/E_0$ Measured
	a/b	$\bar{a}/b$	With $\bar{a}$	Without $\bar{a}$	
F9	0.848	0.009	0.778	0.780	0.782
E20	0.803	0.109	0.768	0.792	0.806
C18	0.812	0.004	0.790	0.790	0.798
D6	0.773	0.004	0.800	0.800	0.787

laminations on measured  $[\pm 30/\pm 30/90/\overline{90}]_s$ , stiffness loss was neglected in calculating  $E^*$ .

## References

- [1] Rybicki, E. F., Schmueser, D. W., and Fox, J., *Journal of Composite Materials*, Vol. 2, 1977, p. 470.
- [2] Roderick, G. L., Everett, R. A., and Crews, J. H., Jr. in *Fatigue of Composite Materials, ASTM STP 569*, American Society for Testing and Materials, 1975, pp. 295–306.
- [3] Rodini, B. T., Jr. and Eisenmann, J. R. in *Fibrous Composites in Structural Design*, Plenum, New York, 1980, pp. 441–457.
- [4] Wang, A. S. D. and Crossman, F. W., "Initiation and Growth of Transverse Cracks and Edge Delamination in Composite Laminates," Parts 1 and 2, *Journal of Composite Materials*, Supplemental Volume, 1980, pp. 71–106.
- [5] Lackman, L. M. and Pagano, N. J., "On the Prevention of Delamination in Composite Laminates," Paper No. 74–355, American Institute of Aeronautics and Astronautics/American Society of Mechanical Engineers and Society of Automotive Engineers 15th Structures, Structural Dynamics and Materials Conference, 1974.
- [6] Reifsnider, K. L., Henneke, E. G., and Stinchcomb, W. W., "Defect Property Relationships in Composite Materials," AFML-TR-76-81, Final Report, Air Force Materials Laboratory, Wright-Patterson Air Force Base, Ohio, June 1979.
- [7] Raju, I. S. and Crews, J. H., *Journal of Computers and Structures*, Vol. 14, No. 1–2, 1981, pp. 21–28.
- [8] Pagano, N. J. and Pipes, R. B., *International Journal of Mechanical Science*, Vol. 15, 1973, pp. 679–688.
- [9] Jones, R. M., *Mechanics of Composite Materials*, Scripta, South Orange, N. J., 1975.
- [10] O'Brien, T. K. and Reifsnider, K. L., *Journal of Testing and Evaluation*, Vol. 5, No. 5, 1977, pp. 384–393.
- [11] Wang, A. S. D. and Crossman, F. W., *Journal of Composite Materials*, Vol. 2, 1977, p. 92.
- [12] Irwin, G. R., "Fracture," *Handbuch der Physik*, Vol. 6, 1958, p. 551.
- [13] Bjeletich, J. G., Crossman, F. W., and Warren, W. T., "The Influence of Stacking Sequence on Failure Modes in Quasi-Isotropic Graphite Epoxy Laminates," *Failure Modes in Composites—IV*, American Institute of Mining, Metallurgical, and Petroleum Engineers, 1979.
- [14] Reifsnider, K. L., Henneke, E. G., II, and Stinchcomb, W. W. in *Composite Materials: Testing and Design (Fourth Conference)*, ASTM STP 617, American Society for Testing and Materials, 1977, pp. 93–105.
- [15] *Fracture Toughness Evaluation by R-Curve Methods*, ASTM STP 527, American Society for Testing and Materials, 1973.
- [16] O'Brien, T. K., "An Approximate Stress Analysis for Delamination Growth in Unnotched Composite Laminates," *Proceedings of the Sixth Annual Mechanics of Composites Review*, Dayton, Ohio, Oct. 1980.
- [17] Highsmith, A. L. and Reifsnider, K. L., "The Effect of Tensile Fatigue Damage on Tensile, Compressive, and Bending Stiffness of Composite Laminates," *Composites Technology Review*, Vol. 2, No. 1, Winter 1980.
- [18] Johnson, W. S. and Dvorak, G. J., "Mechanisms of Fatigue Damage in Boron/Aluminum Composites," in this publication.

D. J. Wilkins, J. R. Eisenmann, R. A. Camin, W. S. Margolis,  
and R. A. Benson<sup>1</sup>

## Characterizing Delamination Growth in Graphite-Epoxy

---

**REFERENCE:** Wilkins, D. J., Eisenmann, J. R., Camin, R. A., Margolis, W. S., and Benson, R. A., "Characterizing Delamination Growth in Graphite-Epoxy," *Damage in Composite Materials, ASTM STP 775*, K. L. Reifsnider, Ed., American Society for Testing and Materials, 1982, pp. 168-183.

**ABSTRACT:** As part of an overall effort to develop durability and damage tolerance methodology for graphite-epoxy composites, coupon specimens have been developed to measure the fundamental static fracture and subcritical growth behavior of delaminations. Two basic designs, one for the tensile opening mode (Mode I) and one for the forward shear mode (Mode II), are described. These specimens were used to characterize the behavior of two types of interfaces (0/0 and 0/90) for static fracture, constant amplitude fatigue, and spectrum fatigue. Fracture mechanics technology was applied through the principles of strain-energy release rate. Three-dimensional finite-element analyses were employed to interpret the experimental results. A simple growth law was shown to correlate the constant-amplitude and spectrum-growth data. It was found that the applied cyclic load must be nearly equal to the critical static load to obtain observable growth in the tensile opening mode. On the other hand, the graphite-epoxy delamination growth rate in the forward shear mode is comparable to the aluminum growth rate in tension, which suggests that shear is the chief subcritical growth mode for graphite-epoxy.

**KEY WORDS:** composite materials, composite structures, crack propagation, defects (materials), epoxy resin, fatigue (mechanics), fiber-reinforced composites, fracture (mechanics), graphite, laminates, life expectancy, mechanical properties, reliability assurance, spectra, test methods, tolerance, toughness

Delamination growth is the fundamental issue in the evaluation of laminated composite structures for durability and damage tolerance. When primary composite structures are evaluated originally with respect to durability (fatigue) and damage tolerance (safety), they are judged against the design service usage, and tests are performed to demonstrate their structural integrity. However, after the parts enter service, they are exposed to a variety of operational usages so that techniques are needed to estimate the behavior of defects as a function of time under changing service conditions.

<sup>1</sup> Engineering specialist senior, engineering specialist, senior engineer, senior engineer, and engineer, respectively, General Dynamics, Fort Worth Division, Fort Worth, Tex. 76101.

The experience of General Dynamics and other contractors has been that only rarely does a composite part fail in a realistic fatigue test. But when test conditions are extended to explore failure mechanisms, delamination is observed to be the most prevalent life-limiting growth mode [1-7].<sup>2</sup> An examination of the fracture toughness of glass-, boron-, and graphite-epoxy shows that interlaminar forces (through the thickness) are operating against an inherent weakness of the resin [8-23]. An additional observation is that common design features in laminated composites give rise to interlaminar shear and normal forces that depend on local details.

These facts suggested a fracture mechanics approach to delamination growth based on the concept of strain-energy release rate [11,12,22-31]. A technique known as virtual crack closure, using finite-element deformation analysis, proved to be a straightforward method of performing the calculations [31,32]. Subsequently, a program was organized to develop the data base and modeling procedures to implement the approach. Coupon tests were designed to provide one-dimensional fracture and growth information in both the peel (Mode I) and shear (Mode II) failure modes.

### Specimen Design

Delaminations in composite laminates generally are constrained to grow between layers because of the presence of the continuous fibers above and below each interface. In this sense the composite delamination process is analogous to debonding of metal-to-metal adhesive joints. As a result, the delamination specimen designs developed here for composites are based on those developed for investigations of adhesive fracture mechanics [31,32]. In contrast to metallic fracture mechanics, where the process is dominated by the tensile opening mode (Mode I), debonding of metal-to-metal adhesive joints and delamination of composite laminates generally involve other modes of fracture. The forward shear mode (Mode II) and the parallel shear mode (Mode III) are often present in addition to Mode I. Ideally, a separate specimen would be designed to individually characterize each of the three possible modes of delamination. With the exception of Mode I, such attempts have been largely unsuccessful.

Various versions of the double cantilever beam (DCB) specimen have been quite successful for characterizing the Mode I behavior of adhesive bonds [31,32] and of composite laminates [13,22,23,33,34].<sup>3</sup> The Mode I specimen design, shown in Fig. 1, is a DCB specimen consisting of a 2.5 by 22.9-cm (1 by 9-in.) coupon with secondarily bonded metal tabs attached at one end for load introduction. At the same end, a folded layer of 12.7- $\mu$ m (0.0005-in.)-thick Kapton film is included at the desired interface to initiate a delamination. When two plies of the same orientation are adjacent to each

<sup>2</sup>The italic numbers in brackets refer to the list of references appended to this paper.

<sup>3</sup>Private communication, K. T. Kedward, Convair Division of General Dynamics, 1978.

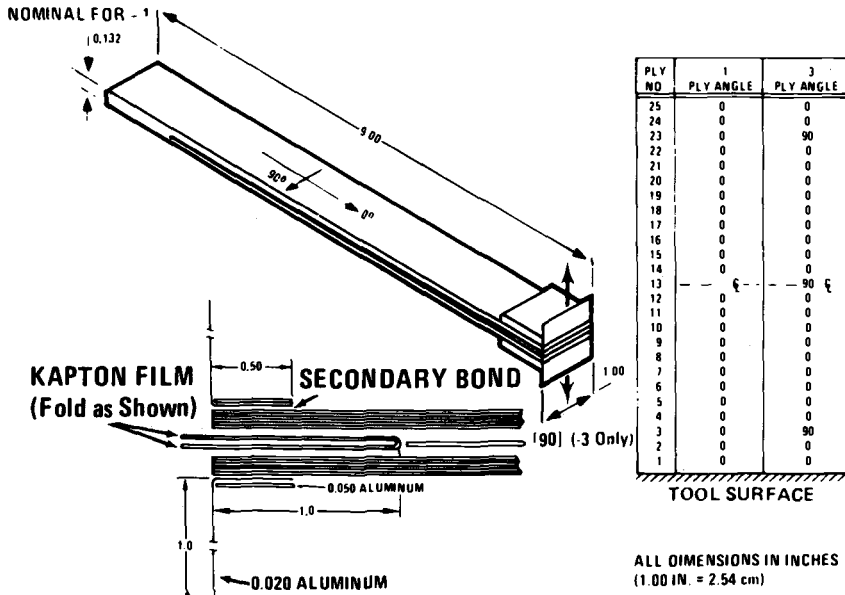


FIG. 1—Mode I coupon.

other in the laminate, cure pressure forces the plies to merge together, and removes the characteristic thin layer of resin that normally separates two plies of different orientation. This “nesting” of fibers between layers is maximized at a 0/0 interface and minimized at a 0/90 interface, so the two limiting cases were investigated. The -1 specimen consists of 24 plies of 0-deg material with Kapton film at the laminate midplane so that delamination between two 0-deg plies can be characterized. The -3 specimen has an additional 90-deg ply at the midplane so that delamination between a 0 and a 90-deg ply can be characterized. The -3 specimen also has the third ply from the outer surface replaced with a 90-deg ply to inhibit interlaminar normal tensile stresses induced during cure. The annealed-aluminum end tabs are sized to act as plastic hinges without inducing significant end moments during loading.

The mixed-mode specimen shown in Fig. 2, was patterned after the cracked lap shear (CLS) specimen used for bonded joints [31,32]. The specimen is a 2.5 by 25.4-cm (1 by 10-in.) coupon with a step change in thickness from 14 plies to 10 plies at the implanted delamination. The delamination initiator is again a folded layer of 12.7- $\mu$ m (0.0005-in.)-thick Kapton film placed between plies 10 and 11 during layup. The coupon is loaded via friction grips over a 3.81-cm (1.5-in.) length at each end. Holes are provided at both ends for alignment purposes only. The upper four plies have an average axial modulus of 106 GPa (15.4 Msi) compared to 44.3 GPa (6.4 Msi) for the lower 10-ply portion of the laminate. The ply stacking sequence for the -1

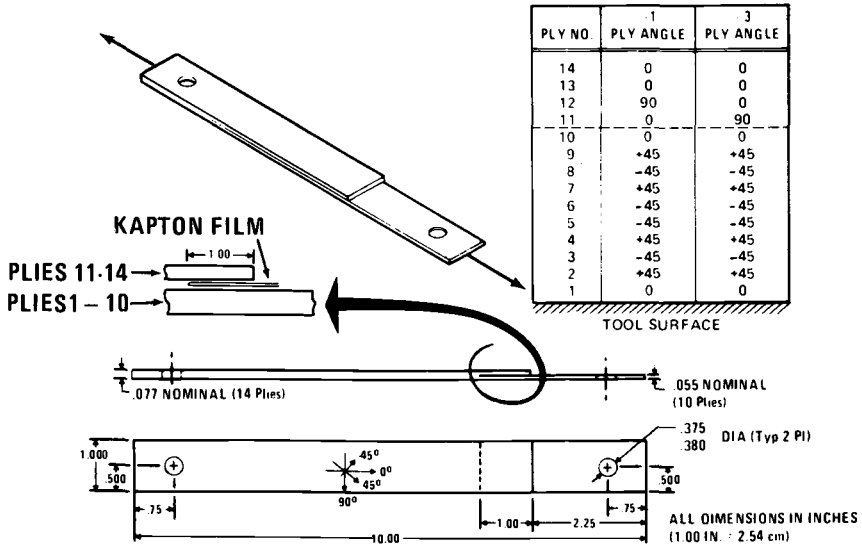


FIG. 2—Mixed-mode coupon.

specimen creates a delamination between two 0-deg plies, whereas the stacking sequence for the -3 specimen creates a delamination between a 0 and a 90-deg ply.

A coupon for Mode III behavior was not included in the characterization because it was not clear how to design such a specimen. In an investigation to characterize all three cracking modes for polymethylmethacrylate adhesives bonded with a urethane adhesive [31], Mode III behavior was obtained with a 90-deg-cone torsion test, which is essentially a butt joint between two cylinders. Critical strain-energy release rates for Modes I, II, and III were found to be 0.03, 0.07, and 0.10 kJ/m<sup>2</sup> (0.17, 0.40, and 0.58 in. · lb/in.<sup>2</sup>), respectively. Although the values for graphite-epoxy are expected to be different, the relative ranking should be maintained. Intuitively, the two shear modes, which should be similar, will give higher values than the peel mode. In any case, Mode II values can be used to conservatively estimate the criticality of Mode III behavior.

**Specimen Fabrication**

Both the Mode I and mixed-mode specimens were fabricated from Union Carbide’s Thornel 300 graphite fiber (3000 ends/tow) impregnated with Narmco Material’s 5208 epoxy resin. This graphite-epoxy system with an incoming resin content of 32 percent was procured to General Dynamics specification FMS-2023. The 7.62-cm (3.00-in.)-wide unidirectional tape form of the material was used to lay up one panel for each of the four specimen types. Each panel was sized to yield 12 individual specimens. During layup,

the folded Kapton film was placed between the appropriate plies to initiate a delamination under subsequent loading. The cure was conducted in accordance with the specification at 177°C (350°F), resulting in a cured resin content of 27 percent and a cured ply thickness of 0.14 mm (0.0055 in.).

After cure, all laminates were ultrasonically inspected by a reflector-plate technique with a 2.25-MHz pulse-echo transducer to verify that the cured material was free of voids. At this point, the metal tabs were prefit along one edge of the Mode I laminate with Reliabond 398 adhesive and cured under 310 kPa (45 psi) pressure at 177°C (350°F) for 1 h. Sawing of both types of specimens to the final 2.54-cm (1.00-in.) width was performed on a Micro-matic wafering saw to prevent machining damage along the specimen edges.

### Test Procedures

A critical issue was the evaluation of efficient, reliable procedures for performing the tests. The aim of all the tests was to either measure the critical strain-energy release rate,  $G_c$ , or measure the subcritical growth associated with a particular value of  $G$ . For linear, elastic material behavior [35], and the specimen geometries used here

$$G = P^2(dC/da)/2w \quad (1)$$

where  $P$  is the applied load,  $C$  is the compliance,  $a$  is the crack length, and  $w$  is the specimen width. Variations in the specific behavior of the two types of specimens caused test equipment and procedures to be slightly different for each.

### Mode I Coupon Static Test Procedures

Critical  $G$  values for the Mode I coupon were obtained in a standard displacement-controlled (Instron) test machine. After some development, thin metal-foil connectors were used between the specimen and test fixture. The specimen weight was supported by a low-stiffness spring and a bar. The edges of the specimens were painted with a white coating (typewriter correction fluid) marked at 1.27-cm (0.5-in.) increments to aid in crack observation.

The first load application was made to break the Kapton film and create a natural crack for the first set of measurements. Several tests were performed on each specimen. The displacement was applied to initiate crack growth and was increased until the crack propagated slowly to the next mark on the specimen edge. The displacement was then returned to zero, and the process repeated. Initial crosshead speeds were 0.008 cm/min (0.02 in./min) for the short cracks, and were increased to a maximum of about 0.08 cm/min (0.2 in./min) near the end of the specimen. Visual observations were made with an  $\times 20$  microscope. Load was plotted as a function of crosshead displacement (Fig. 3).

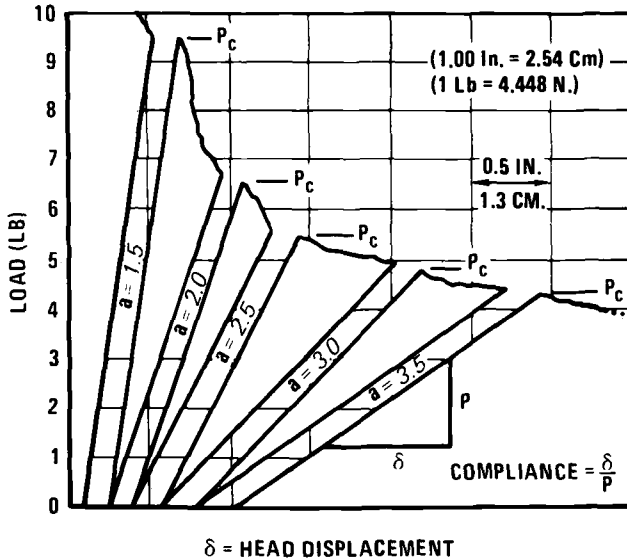


FIG. 3—Mode I static coupon load-deflection curve.

#### *Mode I Coupon Fatigue Test Procedures*

Constant-amplitude ( $R = 0.1$ ) fatigue tests were performed in custom displacement-controlled test frames at 0.5 Hz. The applied load was measured by a spring-displacement device and was servo-controlled by position feedback.

A Hewlett–Parkard 3050B Data Acquisition System was programmed to automatically perform compliance measurements, compare them to the compliance/crack-length relationship developed in static tests, and calculate the instantaneous crack length, as further described later in the Section on Data Reduction. A procedure was developed to begin cycling at  $G$  values near the critical value to obtain cracking rates in the range of  $2.5 \times 10^{-3}$  to  $2.5 \times 10^{-2}$  mm/cycle ( $10^{-4}$  to  $10^{-3}$  in./cycle). As the crack extended, the  $G$  corresponding to the fixed displacement diminished, allowing slower cracking rates to be obtained. Cycle counts were selected to give accurately measurable crack growth increments of about 0.5 to 1.3 mm (0.02 to 0.05 in.).

#### *Mixed-Mode Coupon Test Procedures*

Both static and fatigue tests of the mixed-mode coupon were performed in custom load-controlled fixtures commanded by a Varian computer and teletype interface. The specimens were carefully positioned and tightly clamped between serrated grips to prevent spurious results because of bearing damage in the alignment hole.

In the static tests, curves of axial load versus axial displacement were ob-

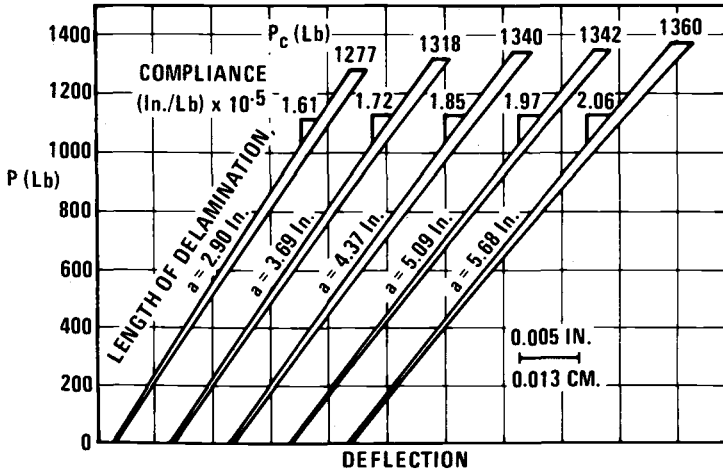


FIG. 4—Mixed-mode static coupon load-deflection curve.

tained on an  $x$ - $y$  plotter as a function of crack length (Fig. 4). Load was measured from a load-cell strain-gage bridge; displacement was measured from a parallel-mounted impedance gage (Kaman Model 2S); and crack length was visually measured from adjacent scales and  $\times 20$  microscopes.

Procedures similar to those for the Mode I coupons were used for the mixed-mode constant-amplitude ( $R = 0.1$ ) fatigue tests, except that visual crack measurements were used throughout. The compliance of the mixed-mode specimen did not vary enough with crack length to use automatic measurements.

Mixed-mode coupons were spectrum fatigue tested with two representations of the tension-only part of a stress spectrum for a typical fighter aircraft horizontal tail. One spectrum was a highly truncated version of the other.

### Data Reduction

As with the test procedures, the data reduction for the two coupons was somewhat different. In all cases, the relationship between load, compliance, and crack length represented by Eq 1 was employed.

#### Mode I Coupon Static Data Reduction

The measured values of critical load, deflection, and crack length were processed through the equations of linear beam theory to arrive at an automated, repeatable, scatter-averaging data reduction system. With the aid of a Hewlett-Packard 9830 desktop computer, plots such as shown in Fig. 5 were obtained.

For a pair of linear, elastic cantilever beams, joined at their fixed ends, the load-deflection relation is

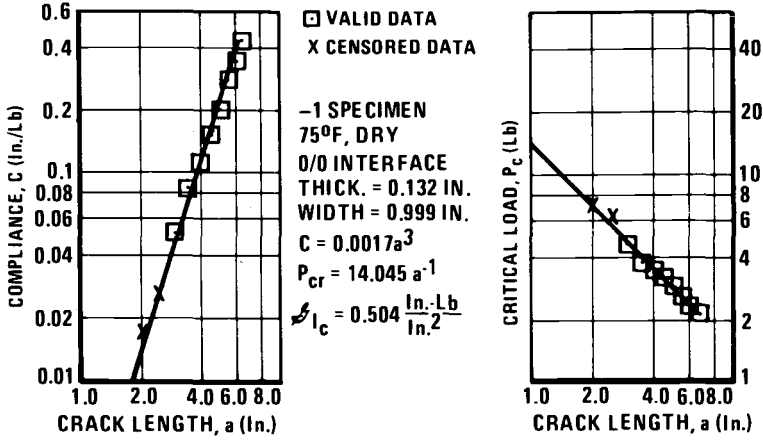


FIG. 5—Mode I static data reduction plot.

$$\delta = 2Pa^3/(3EI) \tag{2}$$

where  $\delta$  is the total opening displacement,  $P$  is the applied transverse load,  $a$  is the beam length (crack length),  $E$  is Young's modulus, and  $I$  is the moment of inertia of each of the two beams. The compliance relation is

$$C = \delta/P = 2a^3/(3EI) = A_1a^3 \tag{3}$$

Because the specimens were designed to be stiff enough to act as linear cantilever beams, the compliance was forced to be linearly related to the cube of the crack length. The plot of compliance as a function of crack length on the left side of Fig. 5 must then have a slope of 3. A least-squares-fit routine was used to calculate the intercept that gave the best fit of the data with a slope of 3. Also, the beam-theory relationship between compliance and crack length, when coupled with Eq 1, requires the critical load,  $P_c$ , to be inversely proportional to the crack length,  $a$ .

$$P_c = (G_c wEI)^{1/2}/a = A_2/a \tag{4}$$

This relationship is shown on the right side of Fig. 5, where a least-squares-fit routine was used to calculate the intercept that gave the best fit of the data with a slope of -1. The points indicated by "X" were censored from the fit. The use of the best-fit relationships for critical load and compliance, as shown in the center of Fig. 5, resulted in an "averaged" value of  $G_c$  for each specimen.

$$G_c = 3A_1A_2^2/(2w) \tag{5}$$

*Mode I Coupon Fatigue Data Reduction*

The Hewlett-Packard data system used to control the fatigue tests also was employed to organize the data for presentation. After a prescribed number

of cycles at a given maximum displacement, the incremental growth was divided by the cycle increment to give  $da/dN$ . These data, as well as absolute crack length, maximum load, and total cycle count, were stored on tape cassettes for subsequent plotting.

*Mixed-Mode Coupon Data Reduction*

Mixed-mode coupon data cannot be interpreted through simple beam theory, and the compliance varies slowly as a function of crack length, as shown in Fig. 4. An average compliance-curve slope was used to reduce all the data. The static and fatigue data were manipulated and reduced by hand, producing  $da/dN$  plots as a function of  $G$  in the constant-amplitude-loading case and producing crack-length plots as a function of spectrum repetitions (or blocks) in the spectrum-loading case.

*Mixed-Mode Coupon Fracture Analysis*

In applying Eq 1 to the reduction of the mixed-mode data, it is understood that the experimental  $G$  calculated from measured axial load and specimen compliance is the sum of all the components of  $G$  for Modes I, II, and III. To decompose this total  $G$  into these three modes, the crack-closure method [32] was used. As shown in Fig. 6, each strain-energy release-rate component can be calculated from the work required to close a debond over an area  $w\Delta a$ , where  $w$  is the width. The work becomes one half the force required to close the debond multiplied by the displacement through which the force moves in closing the debond. In practice the force is obtained from one finite-element model, and the distance through which the force travels is ob-

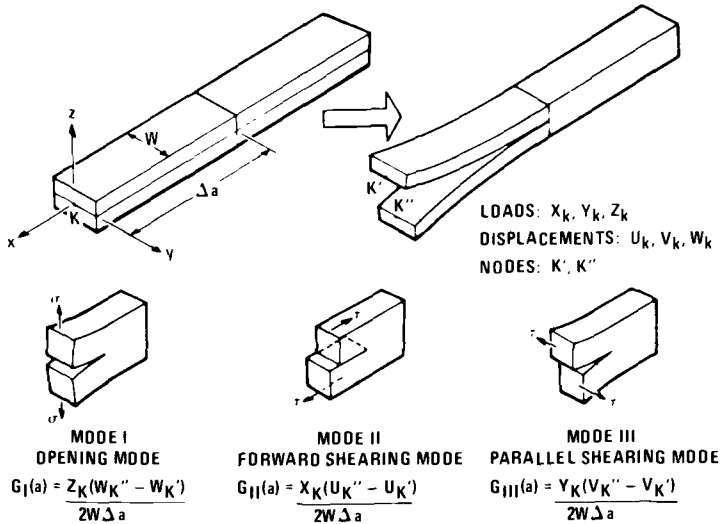


FIG. 6—Schematic of virtual crack closure method.

tained from a second finite-element model in which the debond is extended an incremental amount. As described in Fig. 6, each component of the strain-energy release rate can be calculated in this manner.

The mixed-mode coupon was analyzed with a 2174-deg-of-freedom three-dimensional anisotropic brick model. All elements used were isoparametric and can be found in the NASA Structural Analysis (NASTRAN) element library. The model used here can provide only an estimate of the  $G$  components, because it did not include geometrically nonlinear beam-column effects. Experimental values of critical load were observed to correspond with crack advancement along the centerline of the specimen, where Mode III effects disappear. At that point, the model estimates the Mode II component to be 75 percent of the total strain-energy release rate, and estimates the Mode I contribution to be the remaining 25 percent.

The computed model values of  $G$  were used to interpret the coupon results. The Mode I component of  $G$  at the critical load was found to be lower than the  $G_{IC}$  value obtained with the DCB coupons. In the absence of a firm theoretical criterion for mixed-mode fracture [8,9,21,25-31], it was assumed that each mode acted independently. This assumption allowed Mode II  $G$  values to be calculated as 75 percent of the total  $G$  measured.

**Test Results**

The static critical strain-energy release-rate data are plotted in Fig. 7. The 0/0 interface is critical in the Mode I case. In fact, the 0/90 interface test is invalid because of crack branching through the 90-deg ply. For Mode II, it is seen that the two interfaces give equivalent results.

A summary of the constant-amplitude fatigue data is shown in Fig. 8. The Mode I slopes are so much higher than the Mode II slopes that the contribu-

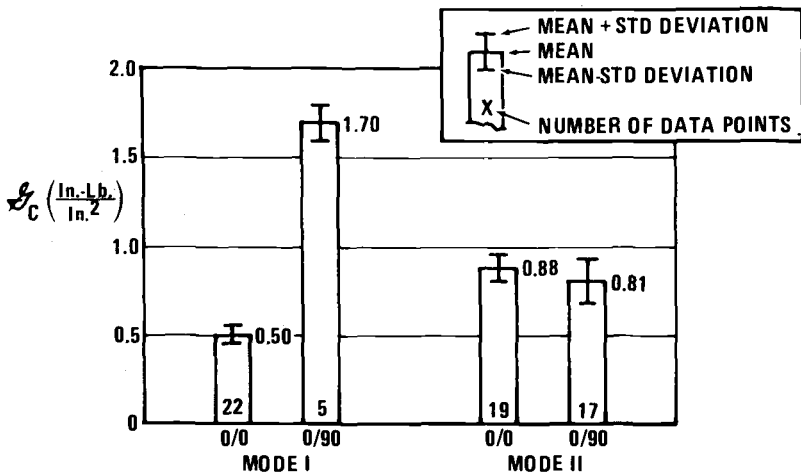


FIG. 7—Critical strain-energy release rates.

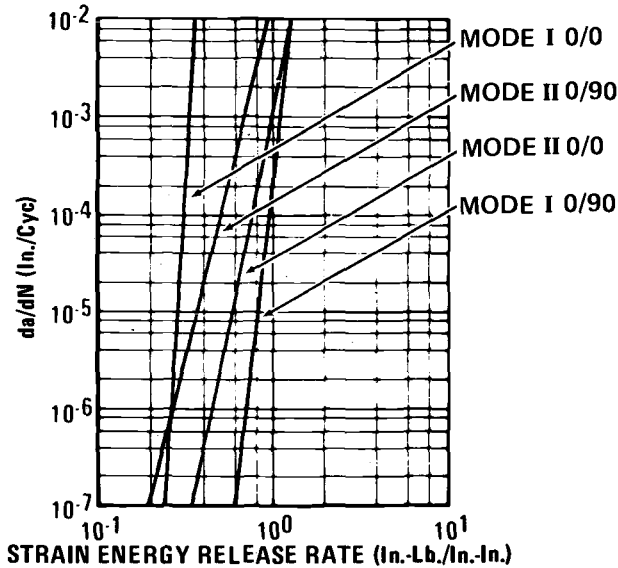


FIG. 8—Delamination growth rates.

tion to delamination from Mode I is insignificant in the mixed-mode coupon. Note that the delamination growth rates are plotted against  $G_{max}$  rather than  $\Delta G$ . An  $R$  value of 0.1 on load ( $min/max$ ) corresponds to a  $G$ -ratio ( $min/max$ ) of 0.01, so  $G_{max}$  and  $\Delta G$  are nearly equal. As a result, plotting  $da/dN$  versus either  $G_{max}$  or  $\Delta G$  gives equivalent results. Similar  $da/dN$  data have been correlated with  $\Delta K$  (change in stress intensity factor) [6,21], and it is intuitive that, for the Mode II case, different results should be obtained by testing at  $R = -1$  because of the doubling of the shear-stress range. Tests are now underway to investigate other load ratios. The spectrum results are given later following a description of a technique for predicting spectrum growth from a constant-amplitude data base.

#### Growth Correlation

Simple exponential fits obtained for the constant-amplitude data, of the form

$$da/dN = BG^n \quad (6)$$

where  $B$  and  $n$  are constants, were used to predict spectrum growth by summing up the growth contributions of each cycle.

No retardation effects were assumed, so that the incremental crack growth relationships defined by Eq 6 could be integrated easily to obtain

$$a = a_o + \sum_{i=1}^N BG_i^n \quad (7)$$

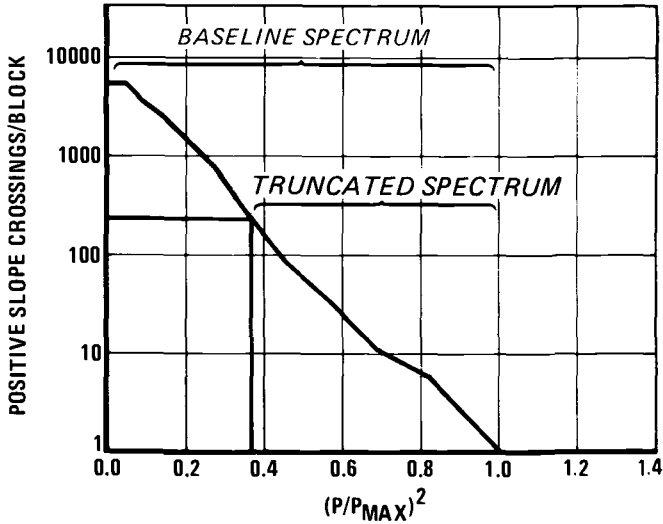


FIG. 9—Load spectra.

where  $a_0$  is the initial crack length. Equation 7 was employed to determine viable load truncation levels for the baseline spectrum. Experimental values of  $B$  and  $n$  were used to calculate crack-growth increments for several assumed load truncation levels. Based on these calculations, it was determined that truncating from 5200 positive slope crossings per block (16 blocks = 1 lifetime) to 244 positive slope crossings per block would result in essentially equivalent growth. The spectra are plotted in Fig. 9.

Predictions from the constant amplitude data and Eq 7 are compared to the baseline and truncated spectrum results in Fig. 10. The correlation is

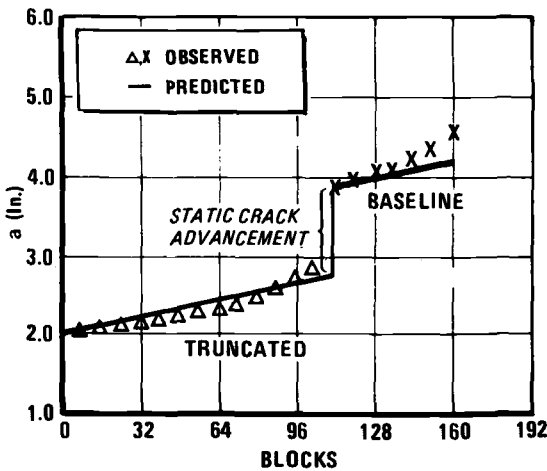


FIG. 10—Spectrum crack growth.

quite encouraging in view of the simplicity of the calculation scheme and the economic advantage to be gained by spectrum truncation. This exercise also tends to verify the assumptions involved in Eq 6.

### Conclusions

A quantitative measure of the effects of defects in composite structures is a key issue in material selection, manufacturing procedures, quality assurance plans, structural design, structural integrity predictions, maintenance planning, and repair decisions. Experience suggests that the inherent lack of interlaminar toughness is the root cause of such problems as poor in-plane compression properties, edge (and internal) delaminations, and low impact resistance.

Characterization of the behavior of delaminations has been approached by adapting and developing techniques for coupon design, static and fatigue testing, data analysis, fracture analysis for separation of modes, spectrum life prediction, and spectrum truncation. Critical strain-energy release-rate values have been obtained for Mode I and Mode II delamination. Interfaces between 0-deg plies and 0 and 90-deg plies have been investigated. Corresponding delamination growth rates have been measured.

Some significant observations have been made.  $G_{IC}$  for the 0/0 graphite-epoxy interface is at least ten times lower than that of structural adhesives [29-31].  $G_{IIC}$  is about twice  $G_{IC}$  and is about the same for either the 0/0 or 0/90 interface. The growth-rate exponent for Mode I delamination is high. Delaminations operating at high percentages of  $G_{IC}$  will grow rapidly to failure, but delaminations operating below about 50 percent of  $G_{IC}$  (70 percent of the critical load) will grow very slowly. For this reason, Mode I delamination can be thought of as a static design issue rather than a potential fatigue problem. On the other hand, the growth-rate exponent for Mode II delamination in graphite-epoxy is analogous to the growth-rate exponent for Mode I cracking in aluminum and must be considered as a fatigue design issue. A simplified analysis procedure, based on constant-amplitude crack-growth data, and ignoring sequence or retardation effects, is shown to predict spectrum crack growth. A possible explanation for this encouraging result is that the mechanism of plastic zone formation, so important in crack growth of metals, is minimized in the epoxy resin because of the small dimensions between fiber layers and the constraining effects of the graphite fibers themselves. A beneficial by-product is that extensive truncation may be employed to reduce the length of test load spectra.

### Recommendations

A key factor in the understanding of mixed-mode fracture is a series of tests of coupons designed to exhibit failures caused by various ratios of  $G_I$ ,

$G_{II}$ , and  $G_{III}$ . A combined-mode failure criterion, validated by test, will be needed to predict the behavior of the most general case.

Tests of coupons designed to accept reversed loadings are recommended to determine stress range effects. Such tests also could be used to guide the analysis of the case where the crack faces are subjected to normal compression, and frictional effects become important.

These test methods are applicable to other fiber-reinforced composite materials, and a data base needs to be built to compare various materials on an interlaminar toughness basis. Such comparisons have already begun [13], but much more work is required.

Delamination testing of graphite-epoxy interrogates the matrix failure mechanism, which always exhibits the highest statistical variability. Useful information regarding average behavior was obtained, but a more thorough statistical test program is needed.

The resin is the environmentally sensitive link in the system. Test programs should cover the useful temperature and moisture ranges of the material. By analogy to the performance of structural adhesives, the brittle response at cold, dry conditions is expected to be the most critical because increases in both temperature and moisture should increase  $G_c$ .

These tests are more likely to be influenced by processing variables than the usual mechanical tests used for quality control and process development. Such variables as prepreg viscosity, cure advancement, layup technique, cure-cycle parameters, cured resin content, number of fiber ends per tow, fiber-sizing effects, and many others could significantly affect interlaminar toughness. A careful test program could help sort out some of the manufacturing unknowns to arrive at quantitative relationships among manufacturing cost, inspectability, and structural integrity.

In a similar way, structural design detail concepts should be analyzed with the available techniques to develop relationships among the in-plane strain field, the geometry of the concepts, and the interlaminar strain-energy release rates. Free edges, open holes, ply terminations, bonded joints, and bolted joints all produce interlaminar normal and shear stress states that vary with geometry, stacking sequence, and ply properties. These design details can be analyzed for producibility, inspectability, and delamination resistance to aid in the selection of structural concepts and meaningful accept/reject criteria.

Finally, the analysis must be generalized to treat two-dimensional delamination growth in three-dimensional solid bodies. Then, the coupon data base may be employed in the solution of delamination problems in hardware. At that point, a durability and damage-tolerance methodology will be available that allows us to compare all types of structural materials on a common crack-growth basis so that engineers can select the best combination of materials for a particular application.

### Acknowledgments

This research was performed for the U. S. Air Force under contract F33657-75-C-0310, CCP 5065. F-16 System Program Office engineers responsible for the program were N. P. McManus, D. O. Tipps, and B. K. Archer, with the philosophical leadership of J. C. Halpin from the Technical Operations Branch of the Aeronautical Systems Division.

At General Dynamics, this work was truly a team effort. The contributions of M. E. Waddoups, W. D. Buntin, J. W. Morrow, R. O. Nay, J. M. Franks, K. W. Seaver, B. T. Rodini, and E. G. Conrad are gratefully acknowledged.

### References

- [1] Wolff, R. V. and Wilkins, D. J. in *Third Conference on Fibrous Composites in Flight Vehicle Design*, NASA TMX-3377, National Aeronautics and Space Administration, Washington, D. C., 1976, pp. 779-802.
- [2] Wolff, R. V. and Wilkins, D. J. in *Fourth Conference on Fibrous Composites in Structural Design*, Plenum Press, 1980, pp. 761-770.
- [3] Wagoner, G. and Erbacher, H., "Damage Tolerance Program for the B-1 Composite Stabilizer," *Proceedings of the American Institute of Aeronautics and Astronautics (AIAA) Conference on Aircraft Composites: The Emerging Methodology for Structural Assurance*, San Diego, Calif., 24-25 March 1977.
- [4] Parker, D. E., "Development of Low-Cost Composite Vertical Stabilizer, Vol. 11, Proof-loading Methodology," Technical Report AFFDL-TR-78-5, Air Force Materials Laboratory, Dayton, Ohio, 9 June 1978.
- [5] Byers, B. A., McCarty, J. E., and Stoecklin, R. L., "Behavior of Damaged Graphite/Epoxy Laminates Under Compression Loading," *National Aeronautics and Space Administration (NASA) Special Review of Aircraft Energy Efficiency (ACEE) Composites Programs*, Pasadena, Calif., 20 March 1979.
- [6] Ratwani, M. M. and Kan, H. P., "Compression Fatigue Analysis of Fiber Composites," NADC-78049-60, Naval Air Development Center, Warminster, Pa., Sept. 1979.
- [7] Sendeckyj, G. P., Stalnaker, H. D., and Kleismit, R. A. in *Fatigue of Filamentary Composite Materials*, ASTM STP 636, 1977, pp. 123-140.
- [8] Wu, E. M., *Journal of Applied Mechanics*, Vol. 34, 1967, pp. 967-975.
- [9] Lauraitis, K., "Tensile Strength of Off-Axis Unidirectional Composites," Theoretical and Applied Mechanics Report 344, University of Illinois at Urbana, 1971.
- [10] Konish, H. J., Swedlow, J. L., and Cruse, T. A., *American Institute of Aeronautics and Astronautics Journal*, Vol. 11, 1973, p. 40.
- [11] Rybicki, E. F., Schmueser, D. W., and Fox, J., *Journal of Composite Materials*, Vol. 11, 1977, p. 470.
- [12] Ramkumar, R. L., Kulkarni, S. V., and Pipes, R. B., "Definition and Modeling of Critical Flaws in Graphite Fiber Reinforced Epoxy Resin Matrix Composite Materials," NADC-76228-30, Naval Air Development Center, Warminster, Pa., Jan. 1978.
- [13] Miller, A. G., Hertzberg, P. E., and Rantala, V. W., *Proceedings of the Twelfth National Society for the Advancement of Material and Process Engineering (SAMPE) Technical Conference*, Seattle, Wash., Oct. 1980, p. 279.
- [14] Reifsnider, K. L., Henneke, E. G., and Stinchcomb, W. W. in *Composite Materials: Testing and Design*, ASTM STP 617, 1977, pp. 93-105.
- [15] Im, J., Mandell, J. E., Wang, S. S., and McGarry, F. J., "Surface Crack Growth in Fiber Composites," NASA-CR-135094, Massachusetts Institute of Technology, Cambridge, Mass., 1976.
- [16] Wang, S. S. and Mandell, J. F., "Analysis of Delamination in Unidirectional and Cross-ply Fiber-Reinforced Composites Containing Surface Cracks," NASA-CR-135248, Massachusetts Institute of Technology, Cambridge, Mass., 1977.

- [17] Wang, S. S. and Wang, H. T., *American Society of Mechanical Engineers (ASME) Journal of Engineering Materials and Technology*, Vol. 101, 1979, pp. 34-41.
- [18] Wang, S. S., *Proceedings of the Second International Conference on Composite Materials, (ICCM-II) The Metallurgical Society-American Institute of Mining, Metallurgical, and Petroleum Engineers*, 1978, pp. 277-291.
- [19] Wang, S. S. in *Composite Materials: Testing and Design (Fifth Conference), ASTM STP 674*, 1979, pp. 642-663.
- [20] Wang, S. S., "Edge Delamination in Composite Laminate Under Uniform Axial Extension," to appear in ASTM STP.
- [21] Wang, S. S., "Edge Delamination in Angle-Ply Composite Laminates," *Proceedings of the 22nd Structures, Structural Dynamics, and Materials Conference*, American Institute of Aeronautics and Astronautics, Atlanta, Ga., 1981, pp. 473-484.
- [22] de Charentenay, F. X., Bethmont, M., Benzeggagh, M., and Chrétien, J. F., "Delamination of Glass Fiber Reinforced Polyester, An Acoustic Emission Study," *Proceedings of International Conference on Materials (ICM 3)*, Vol. 3, Pergamon Press, Cambridge, England, Aug. 1979.
- [23] de Charentenay, F. X. and Benzeggagh, M., "Fracture Mechanics of Mode I Delamination in Composite Materials," *Proceedings of the Third International Conference on Composite Materials (ICCM3)*, Paris, France, Aug. 1980.
- [24] Wang, A. S. D., "On Free-Edge Delamination in Laminated Composites," Drexel University, Philadelphia, Pa. 1978.
- [25] Wang, A. S. D. and Crossman, F. W., *Journal of Composite Materials Supplement*, Vol. 14, 1980, pp. 71-87.
- [26] Crossman, F. W., Warren, W. J., Wang, A. S. D., and Law, G. E., *Journal of Composite Materials Supplement*, Vol. 14, 1980, pp. 88-108.
- [27] Roderick, G. L., Everett, R. A., and Crews, J. H., Jr. in *Fatigue of Composite Materials, ASTM STP 569*, 1975, pp. 295-306.
- [28] Roderick, G. L., Everett, R. A., and Crews, J. H., Jr., "Cyclic Debonding of Unidirectional Composite Bonded to Aluminum Sheet for Constant-Amplitude Loading," NASA TN D-8126, National Aeronautics and Space Administration, Washington, D. C., 1976.
- [29] Brussat, T. R., Chiu, S. T., and Mostovoy, S., "Fracture Mechanics for Structural Adhesive Bonds," AFML-TR-77-163, Air Force Materials Laboratory, Wright-Patterson Air Force Base, Ohio, Oct. 1977.
- [30] Brussat, T. R., Chiu, S. T., and Mostovoy, S., "Fracture Mechanics for Structural Adhesive Bonds, Phase II Final Technical Report," AFML-TR-77-163, Part 11, Air Force Materials Laboratory, Wright-Patterson Air Force Base, Ohio, 1978.
- [31] Anderson, G. P., Bennett, S. J., and DeVries, K. L., *Analysis and Testing of Adhesive Bonds*, Academic Press, New York, 1977.
- [32] Rybicki, E. F. and Kanninen, M. F., *Engineering Fracture Mechanics*, Vol. 9, 1977, pp. 931-938.
- [33] Bascom, W. D., Bitner, J. L., Moulton, R. J., and Siebert, A. R., *Composites Journal*, 1980, pp. 9-18.
- [34] Devitt, D. F., "Delamination Fracture Toughness of a Unidirectional Composite," M. S. thesis, Texas A&M University, 1979.
- [35] Paris, P. C. and Sih, G. C. in *Fracture Toughness Testing, ASTM STP 381*, 1970, pp. 30-83.

# Compression Fatigue Behavior of Composites in the Presence of Delaminations

---

**REFERENCE:** Ramkumar, R. L., "Compression Fatigue Behavior of Composites in the Presence of Delaminations," *Damage in Composite Materials, ASTM STP 775*, K. L. Reifsnider, Ed., American Society for Testing and Materials, 1982, pp. 184-210.

**ABSTRACT:** This paper discusses an experimental program that investigated the effect of imbedded (idealized) delaminations on the compression fatigue behavior of quasi-isotropic T300/5208 graphite/epoxy laminates. Three different stacking sequences of a 64-ply layup were tested. No lateral constraints were imposed on the specimen test section during static and fatigue loading, to permit unencumbered precipitation and propagation of delaminations. Test specimen geometry was chosen to preclude gross (Euler) buckling between test grip fixtures. Post-failure examination of specimen cross-sections revealed the absence of any fiber microbuckling. Consequently, the predominant failure mode in the test specimens was the propagation of imbedded delaminations to the tab region. A 1-D delamination, located below the surface ply across the entire width, and a 2-D circular delamination, buried one or four plies below the surface, were considered. The out-of-plane deflection of the thin delaminated region was measured during static loading to estimate the extent of post-buckling that induces delamination growth. During fatigue, the growth of an imbedded delamination was monitored using diiodobutane (DIB)-enhanced radiography. A new procedure, involving laser-drilled minute holes, was used successfully in extending the application of enhanced radiography to buried delaminations. S-N, half-life residual strength, and ultimate strength data were obtained.

**KEY WORDS:** interlaminar delamination, composites, graphite/epoxy, compression fatigue, enhanced radiography

Fiber-reinforced composite materials are continuing to replace conventional metals in secondary and primary aerospace structures owing to their high strength-to-weight ratio. Their mechanical response, however, is rendered complex by the many planes of weakness where local failures can initiate and grow until structural failure occurs. The interface between adjacent layers in a laminate presents one such plane of weakness where an

<sup>1</sup>Engineering specialist, Structural Mechanics Research, Organization 3852/82, Northrop Corporation, Aircraft Division, Hawthorne, Calif. 90250.

interlaminar delamination can initiate and grow. There are many processing, handling, and operating conditions under which an interlaminar delamination can occur. In most of these cases the delamination is generally present within the laminate, invisible to the naked eye on inspection. A low velocity impact of a blunt body on a laminated structure, for example, causes such a damage at low impact energy levels [1,2].<sup>2</sup> If the structural component containing the delamination were to be an upper wing skin of an aircraft that is subjected to compressive loads during service, the residual strength and the service life of the component could be severely affected [3]. Recognition of potentially deleterious effects of delaminations instigated many studies [4-15] that attempted to quantify such effects. The limited success of these investigations called for additional efforts. This paper summarizes the results of an experimental program that studied the effect of imbedded delaminations on the compression fatigue behavior of laminated composites.

### Details of the Experimental Program

Three different stacking sequences of a quasi-isotropic, T300/5208 graphite/epoxy layup were tested in the program. The test laminates were 64-ply thick, and their configurations were identified as shown: Laminate A, [0/45/90/-45]<sub>8s</sub>; Laminate B, [45/90/-45/0]<sub>8s</sub>; and Laminate C, [90/45/0/-45]<sub>8s</sub>.

During the layup of test panels, delaminations were introduced by imbedding two 0.08-mm (0.003-in.)-thick Teflon sheets at a chosen interface. Two flaw locations were selected near a free surface, to simulate low velocity impact damage. One location was between Plies 1 and 2 (Location 1), and the other was between Plies 4 and 5 (Location 4).

Two types of delaminations were imbedded at a selected flaw location in the various test specimens. The first type of delamination (1-D) was 12.7 mm (0.5 in.) long, centered between tabs, and extended across the 38.1 mm (1.5 in.) width of the test specimen. The second type of delamination (2-D) was 12.7 mm (0.5 in.) in diameter, and was centered within the test section. The size of the delamination relative to test specimen dimensions is illustrated in Fig. 1.

Test specimens were 152.4 mm (6 in.) long and 38.1 mm (1.5 in.) wide (see Fig. 1). The 38.1 mm (1.5 in.) square test section was laterally unconstrained during testing. The free surfaces of the test section permitted uninhibited growth of delaminations imbedded near the surface ply. The test length was chosen to be small [38.1 mm (1.5 in.) between tabs] and the laminates were chosen to be thick [8.10 mm (0.32 in.)] to make the Euler buckling stress exceed the virgin compressive strength of the unflawed test specimen. Specimen ends were ground to be flat and parallel to ensure alignment of the ap-

<sup>2</sup>The italic numbers in brackets refer to the list of references appended to this paper.

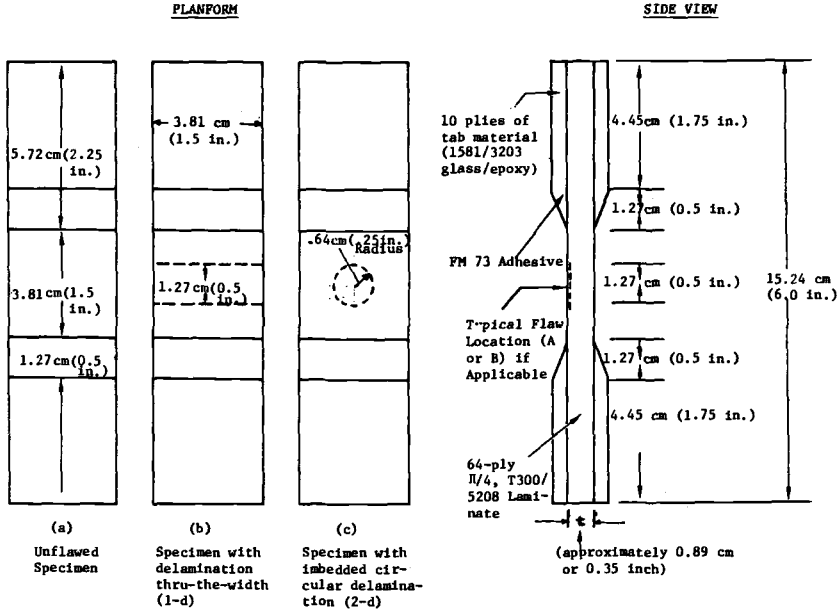


FIG. 1—Test specimen geometry, flaw size and location, and tab details.

plied load, most of which was introduced through direct bearing on the flat ends.

Table 1 defines the various tests conducted on Laminate A specimens, and Table 2 defines the tests conducted on Laminates B and C. A total of 50 specimens were tested in static compression, and 115 specimens were tested in constant amplitude compression fatigue at  $R = 10$  and  $\omega = 10$  Hz.  $R$  is the algebraic minimum-to-maximum fatigue load ratio, and  $\omega$  is the frequency of loading. The maximum compressive stress during fatigue was chosen to be a fraction,  $S$ , of the static compressive strength for each test case.

During static testing, strain gage and dial indicator readings were selectively obtained to monitor specimen Euler buckling and central out-of-plane ( $W$ ) deflection of the delaminated region. Readings corresponding to tests on virgin, unflawed specimens indicated the absence of any significant bending in the laterally unconstrained specimens. Data from tests on specimens with imbedded delaminations yielded strains and maximum  $W$  displacements at failure. In specimens with imbedded delaminations, failure was defined as the propagation of the delamination to the tab region.

During constant amplitude compression fatigue testing ( $R = 10$ ,  $\omega = 10$  Hz), growth in the imbedded delamination was monitored using enhanced radiography. Diiodobutane (DIB) was used as the radio-opaque dye penetrant. In specimens with 1-D delamination, DIB was injected into the delaminated region from the free edges. In specimens with buried (2-D) delaminations, introduction of DIB into the delaminated region presented a

TABLE 1—Tests conducted on Laminate A.<sup>a</sup>

Test Series	Delamination Type	Flaw Location	Compressive Load Type	S <sup>b</sup> (R = 10; ω = 10 Hz)	Number of Fatigue Cycles, N	Number of Specimens
1	none	. . .	static	1.0	1	5
2	1-D	1	static	1.0	1	5
3	1-D	1	fatigue	0.60	N <sub>f3</sub> <sup>c</sup>	5
4	1-D	1	fatigue	0.47	N <sub>f4</sub>	5
5	1-D	1	fatigue	0.45	N <sub>f5</sub>	5
6	2-D	1	static	1.0	1	5
7	2-D	1	fatigue	0.66	N <sub>f7</sub>	5
8	2-D	1	fatigue;RS <sup>d</sup>	0.66	N <sub>f7</sub> /2	5
9	2-D	1	fatigue	0.58	N <sub>f9</sub>	5
10	2-D	1	fatigue;RS	0.58	N <sub>f9</sub> /2	5
11	2-D	1	fatigue	0.55	N <sub>f11</sub>	5
12	2-D	1	fatigue;RS	0.55	N <sub>f11</sub> /2	5
13	2-D	4	static	1.0	1	5
14	2-D	4	fatigue	0.77	N <sub>f14</sub>	5
15	2-D	4	fatigue;RS	0.77	N <sub>f14</sub> /2	5
16	2-D	4	fatigue	0.72	N <sub>f16</sub>	5
17	2-D	4	fatigue;RS	0.72	N <sub>f16</sub> /2	5
18	2-D	4	fatigue	0.66	N <sub>f18</sub>	5
19	2-D	4	fatigue;RS	0.66	N <sub>f18</sub> /2	5
					Total	95

<sup>a</sup>[C/45/90/-45]<sub>8s</sub> layup.

<sup>b</sup>S = maximum cyclic compressive stress/static compressive strength.

<sup>c</sup>N<sub>f</sub> denotes the number of cycles for fatigue failure at S<sub>i</sub>.

<sup>d</sup>These are half-life residual strength (RS) tests under static compression.

TABLE 2—Tests conducted on Laminates B and C.<sup>a</sup>

Test Series Identification	Delamination Type	Flaw Location Identification	Compressive Load Type	S <sup>b</sup> (R = 10; ω = 10 Hz)	Number of Fatigue Cycles, N	Number of Specimens
1	none	. . .	static	1.0	1	5
6	2-D	1	static	1.0	1	5
7	2-D	1	fatigue	S <sub>7</sub> <sup>c</sup>	N <sub>f7</sub> <sup>d</sup>	5
8	2-D	1	fatigue	S <sub>8</sub>	N <sub>f8</sub>	5
13	2-D	4	static	1.0	1	5
14	2-D	4	fatigue	S <sub>14</sub>	N <sub>f14</sub>	5
15	2-D	4	fatigue	S <sub>15</sub>	N <sub>f15</sub>	5
					Total	35

<sup>a</sup>[45/90/-45/0]<sub>8s</sub> and [90/45/0/-45]<sub>8s</sub> layups, respectively.

<sup>b</sup>S = maximum cyclic compressive stress/static compressive strength.

<sup>c</sup>For Laminate B, S<sub>7</sub> = 0.61, S<sub>8</sub> = 0.54, S<sub>14</sub> = 0.66, and S<sub>15</sub> = 0.61.

For Laminate C, S<sub>7</sub> = 0.62, S<sub>8</sub> = 0.49, S<sub>14</sub> = 0.75, and S<sub>15</sub> = 0.67.

<sup>d</sup>N<sub>f</sub> denotes the number of cycles for fatigue failure at S<sub>i</sub>.

challenge. This was overcome by drilling small holes, approximately 0.10 mm (0.004 in.) in diameter, from the nearer surface to the delaminated interface, using a 6-W laser beam. A hypodermic needle was then used to inject DIB into the delaminated region. Based on the observations made by Tirosh [16], it was expected that the small laser-drilled holes would have negligible detrimental effects on delamination growth. A Magnaflux MX-10-50 microfocuss tube was mounted close to the specimen, between the vertical uprights of the test machine. The low kilovolt range required to operate this tube made it possible to meet radiation safety requirements simply by using lead-lined vinyl sheets around the test frame, as shown in Fig. 2. The microfocuss tube produced a small spot size [0.05 mm (0.002 in.)] that allowed the tube to be mounted near the film plane retaining an excellent degree of resolution. During the fatigue tests, cycling was stopped periodically, DIB injected into the delaminated region, a radiograph obtained on Polaroid film, and cycling resumed. Failure again was defined by the propagation of the imbedded delamination to the tab region.

Subsequent to the completion of fatigue life tests, a small number of half-life residual strength tests were conducted on Laminate A specimens with imbedded 2-D delaminations. For example, specimens corresponding to Test Series 8 were fatigued initially at  $S = 0.66$ ,  $R = 10$ , and  $\omega = 10$  Hz for approximately  $N_f/2$  cycles, where  $N_f$  is the average fatigue life for Test Series 7 (see Table 1). These specimens then were failed in static compression and the half-life residual strengths recorded. Half-life damage growth was

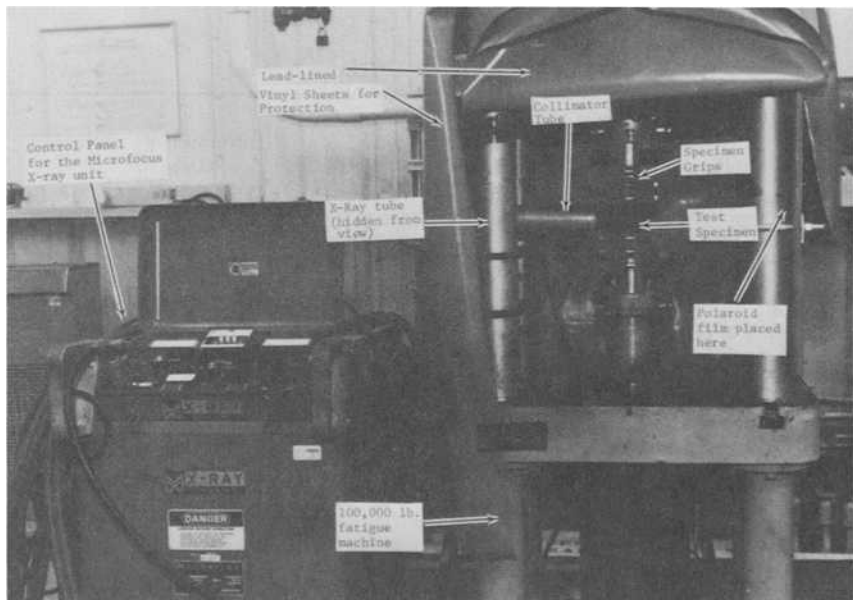


FIG. 2—Compression fatigue test arrangement.

recorded selectively prior to residual strength testing. At the completion of all the tests in Tables 1 and 2, the specimens were subjected to static compression to determine the ultimate failure load. These tests determined the load-carrying capacity of the specimens beyond delamination failure. The following section discusses the results from the various tests.

### Results from Static Compression Tests

A summary of all the static compression test results is presented in Table 3. The following conclusions are made based on these tests.

1. Static compression tests on unflawed virgin specimens indicated the absence of specimen gross (Euler) buckling between tabs, until failure.

2. Photomicrographs of selected failed specimens also indicated the absence of any fiber microbuckling. A specimen photomicrograph at  $\times 200$  magnification is shown in Fig. 3.

3. In all the unflawed specimens, failure was induced by the precipitation of interlaminar delaminations. This was accomplished by an unloading phenomenon and a loud "popping" sound.

4. Static compression tests on unflawed specimens yielded strengths that decreased as the outer ply fiber orientation was changed from 0 to 45 to 90-deg (Table 3), manifesting significant stacking sequence effects.

5. The virgin, unflawed strength of  $[0/45/90/-45]_{8s}$  (Laminate A) specimens is affected deleteriously by 1-D and 2-D delaminations. For a location below the surface ply, the 1-D delamination induces a larger strength loss. As the 2-D delamination location is moved toward the midplane of the laminate, failure occurs at a lower value of the applied stress with a smaller transverse deflection of the delaminated region.

6. When the delamination is located just below the surface (0-deg) ply in Laminate A specimens, the post-buckled, large transverse deflection of the delaminated ply induces matrix cracks between fibers. If the imbedded delamination has an initial circular geometry, matrix cracks occur along 0-deg lines that are tangential to the initial geometry, and the delamination propagates between these cracks toward the tab region, resulting in a rectangular delaminated area at failure.

7. The virgin, unflawed strength of  $[45/90/-45/0]_{8s}$  (Laminate B) and  $[90/45/0/-45]_{8s}$  (Laminate C) specimens is unaffected by locating a 2-D delamination between Plies 1 and 2. The low bending stiffness of the surface ply in the delaminated region is believed to be the reason for this observation. As seen in Laminate A specimens, locating the delamination closer to the midplane induces failure at a lower stress level, with a small deflection of the delaminated region.

8. Failure initiates and propagates in an unstable manner under static compressive loading. No stable delamination growth was observed.

TABLE 3—Summary of static compression test results.

Laminate Type	Delamination Type	Delamination Located Between Plies	Measurements at Delamination Failure		
			Average Stress, MPa	Average Strain, $\mu\text{mm}/\text{mm}$	Maximum Out-of-Plane Deflection, mm
A	none <sup>a</sup>	...	-519.4	-12.434	...
	1-D	1 and 2	-304.0	-6.923	0.059
	2-D	1 and 2	-358.0	-8.052	0.432
B	2-D	4 and 5	-341.0	-7.715	0.212
	none <sup>a</sup>	...	-498.3	-12.251	...
	2-D	1 and 2	-518.4	-12.768	0.492
C	2-D	4 and 5	-400.7	-9.991	0.038
	none <sup>a</sup>	...	-420.2	-10.243	...
	2-D	1 and 2	-498.2	-12.449	...
			-341.3	-7.781	0.076

<sup>a</sup>These are results from tests on unflawed, virgin specimens, and correspond to a different failure mode.

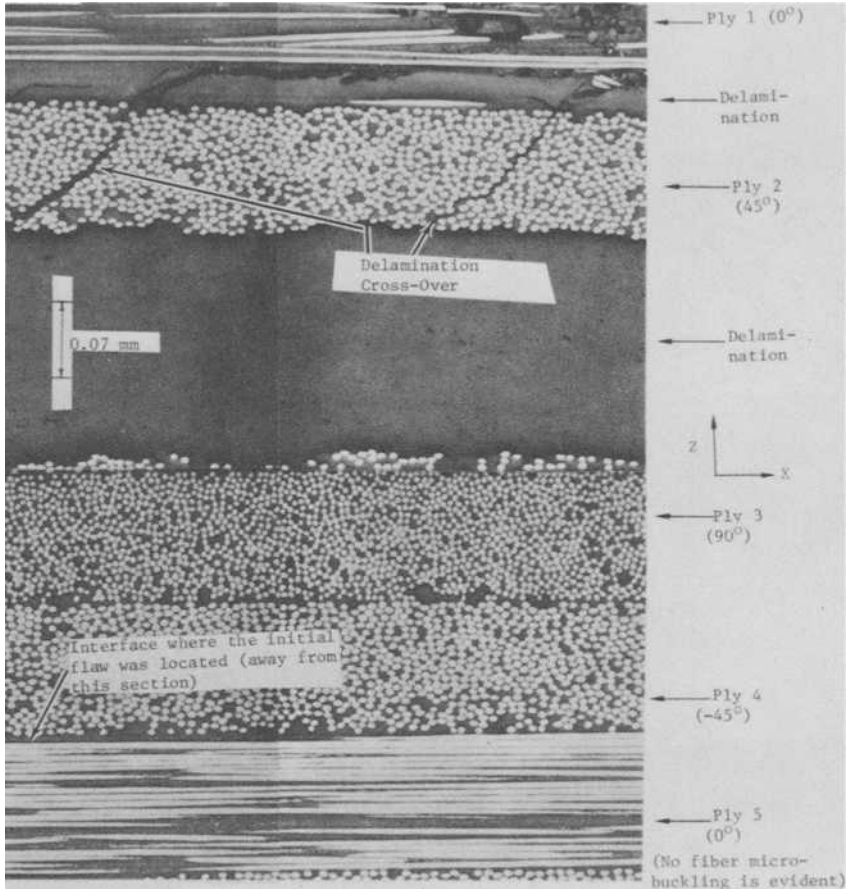


FIG. 3—Photomicrograph of an XZ cross-section of a failed Laminate A specimen (4284-70) from Test Series 14, showing the absence of fiber microbuckling.

### Results from Fatigue Life Tests

Subsequent to static tests, compression fatigue life tests were conducted as shown in Tables 1 and 2. The maximum compressive fatigue load was chosen to be a fraction ( $S$ ) of the corresponding static failure load. Different  $S$  values were chosen to precipitate delamination failure after the desired numbers of cycles ( $N$ ). When the imbedded delamination propagated to the tab region, fatigue life was assumed to have expired through the precipitation of a delamination failure. The generated S-N data were plotted for each test case, and a "best-fit" curve was drawn through each set of data (Figs. 4, 5, 6, and 7). During these tests, cycling was stopped periodically, and DIB-enhanced radiographs of the test specimens obtained. A few specimens are

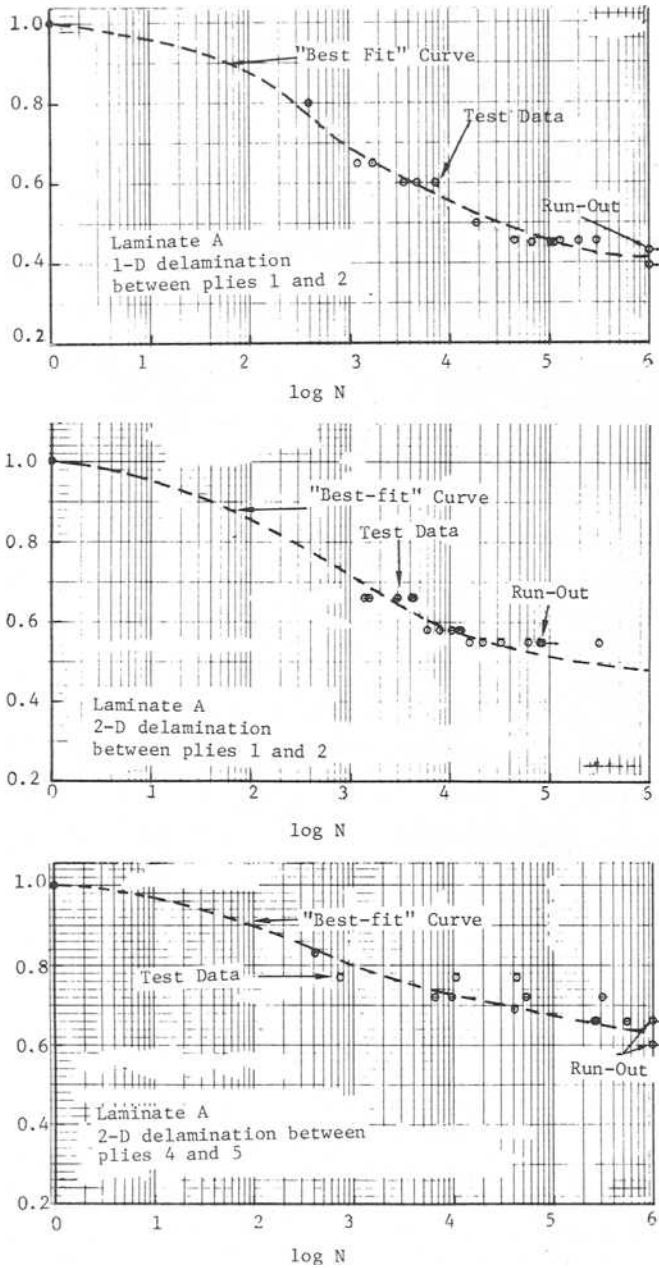


FIG. 4—S-N data for Laminate A.

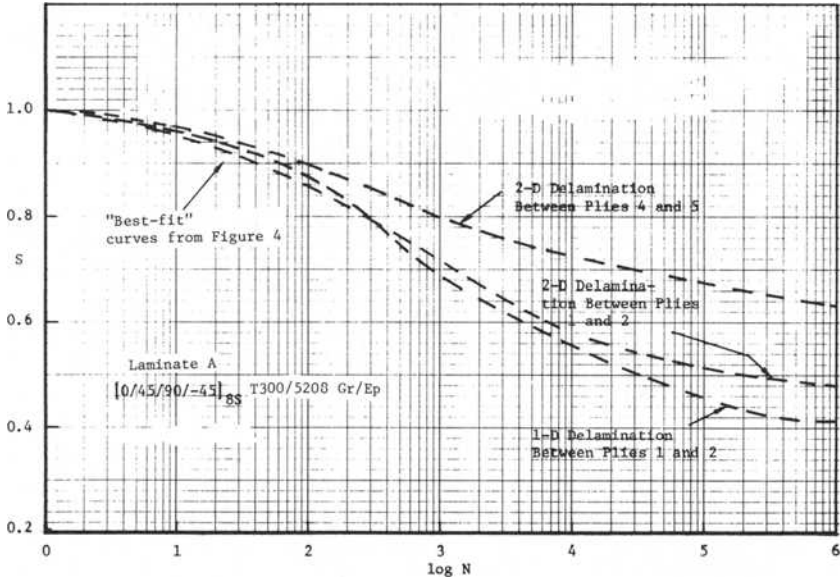


FIG. 5—Comparison of  $S$ - $N$  curves for Laminate A.

presented in Figs. 8–14. Only the 38.1 mm (1.5 in.) square test section and a small portion of the tab region are shown in the radiographs for brevity. From the fatigue life tests the following conclusions are drawn:

1. From the  $S$ - $N$  data for Laminate A it is seen that the “apparent” threshold value of the maximum compressive stress, at which failure is not expected to be precipitated for many millions of cycles, increases as the test case is changed from 1-D flaw at Location 1, to 2-D flaw at Location 1, to 2-D flaw at Location 4 (Fig. 5). The same effect was observed as a 2-D flaw was moved from Location 1 to Location 4 in Laminates B and C (Figs. 6, 7).

2. From the enhanced radiographs in Figs. 8–14, the growth in the imbedded delamination with fatigue cycles ( $N$ ) may be obtained. For a 1-D or a 2-D flaw between Plies 1 and 2 (Location 1) in laminates A and B, the imbedded delamination grew with  $N$  in a stable manner until failure. The large out-of-plane ( $W$ ) deflection of the delaminated region and its low transverse strength precipitated matrix cracks between fibers in the surface ply. This affected the manner in which the imbedded delaminations, especially the 2-D flaws, propagated to failure (see Figs. 8–14).

3. When a 2-D flaw was located below the surface 90-deg ply in Laminate C, fatigue failure was not induced by the growth of the imbedded delamination. The low transverse stiffness of the surface ply caused the delaminated region to exhibit no visible  $W$  deflection, with no consequent growth in the imbedded flaw. Failure was induced by other delaminations precipitated near the tab region.

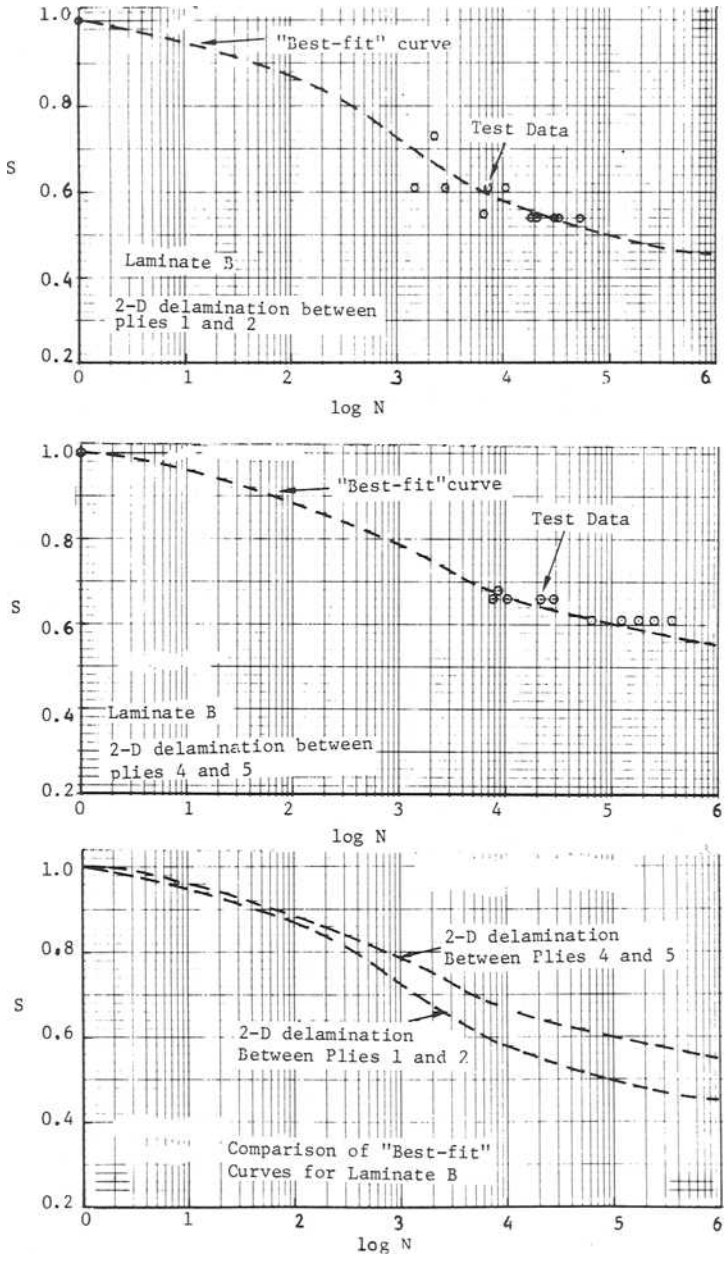


FIG. 6—S-N data for Laminate B.

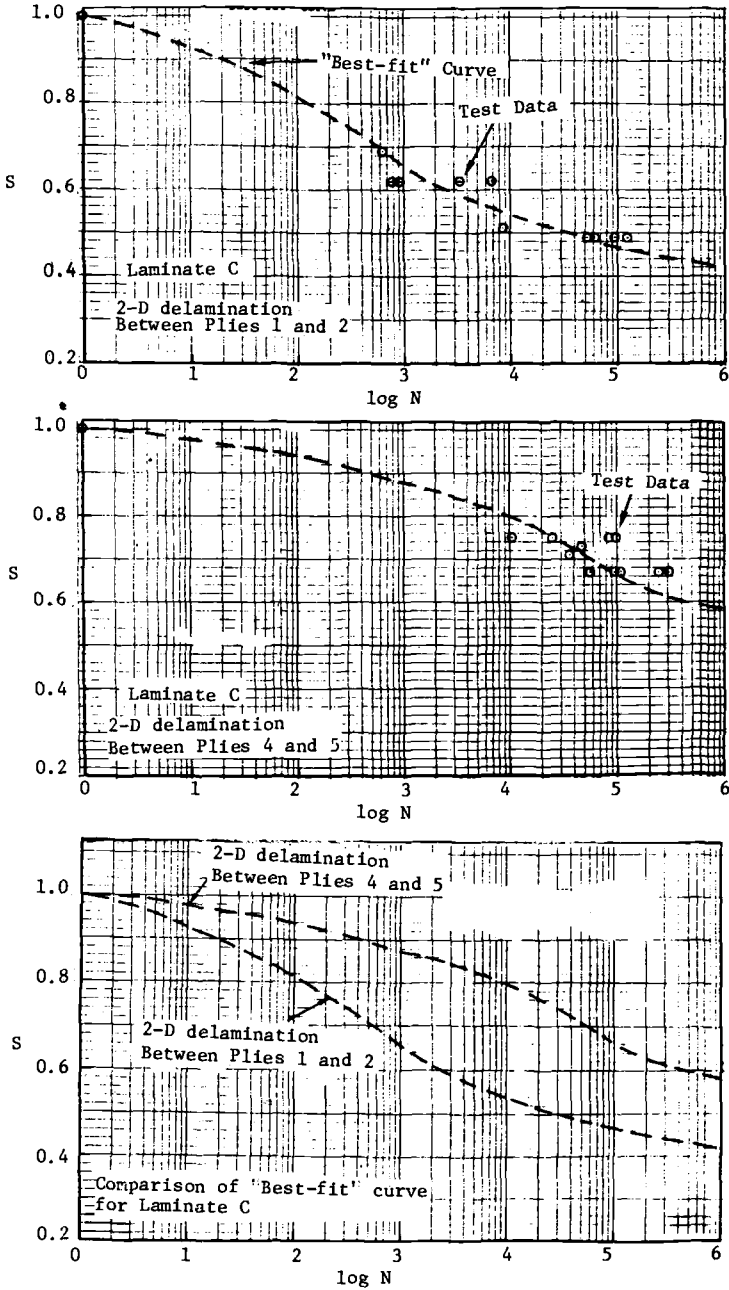


FIG. 7—S-N curves for Laminate C.

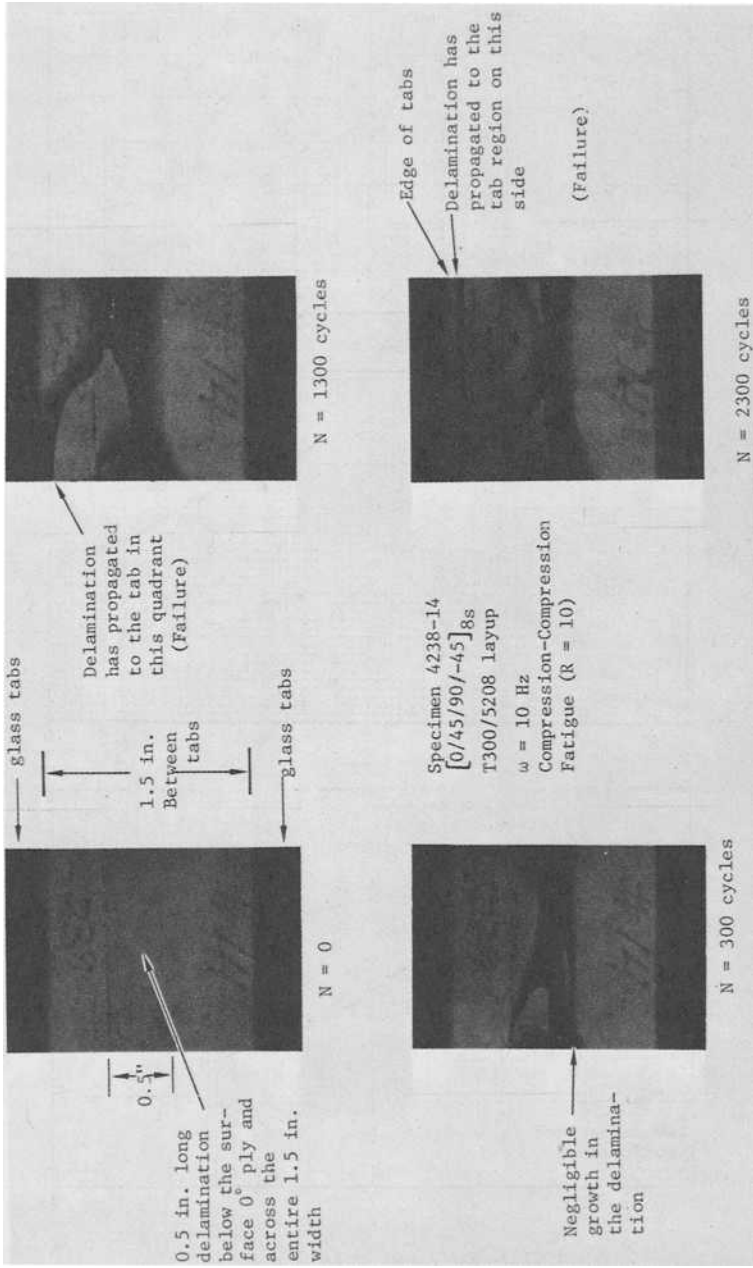


FIG. 8a—Delamination growth in Specimen 4238-14; Laminate A; Test Series 3; S = 0.65.

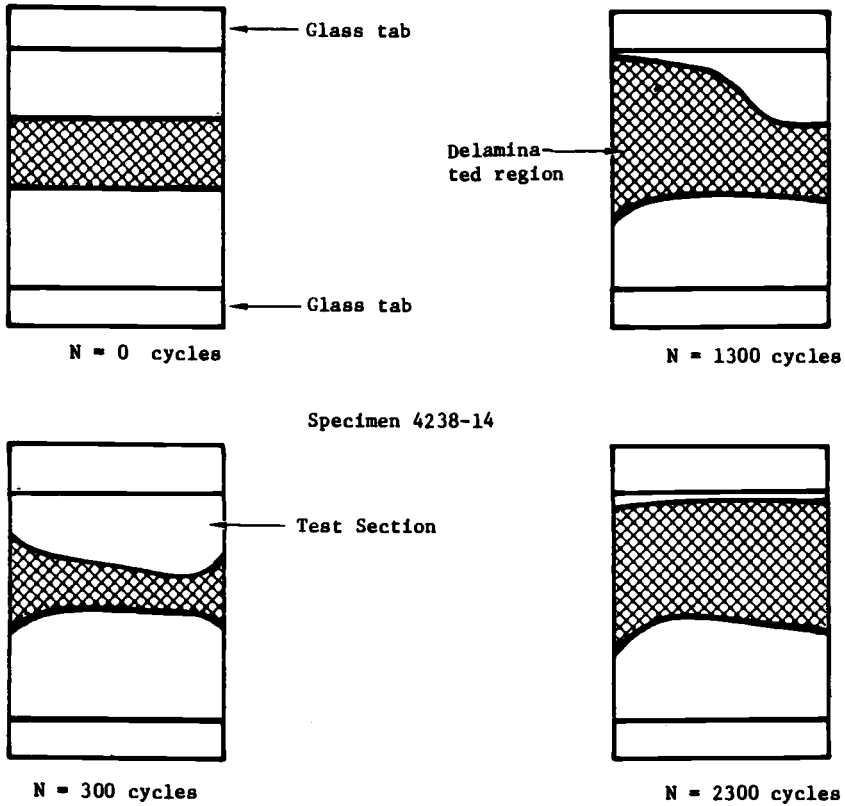


FIG. 8b—Outline of the delamination boundaries in the radiographs shown in Fig. 8a.

4. When the delamination was imbedded four plies below the surface ply, closer to the midplane, no significant flaw growth was observed in all three laminates until failure. At failure, an unstable propagation of the imbedded delamination to the tab region was observed, with accompanying matrix cracks between fibers in the delaminated region.

**Results from Half-Life Residual Strength Tests**

Only Laminate A specimens with 2-D delaminations were subjected to these tests (see Table 1). In conducting these tests, the specimens were initially subjected to compression fatigue loading ( $R = 10$ ;  $\omega = 10$  Hz) at the  $S$  value corresponding to the preceding fatigue life test series in Table 1. Cyclic loading was imposed for approximately half the average lifetime of the preceding fatigue life test series. At the completion of half-life cyclic loading, selected specimens were radiographed, using DIB for enhancement, to record the half-life growth of the imbedded delamination. A specimen is

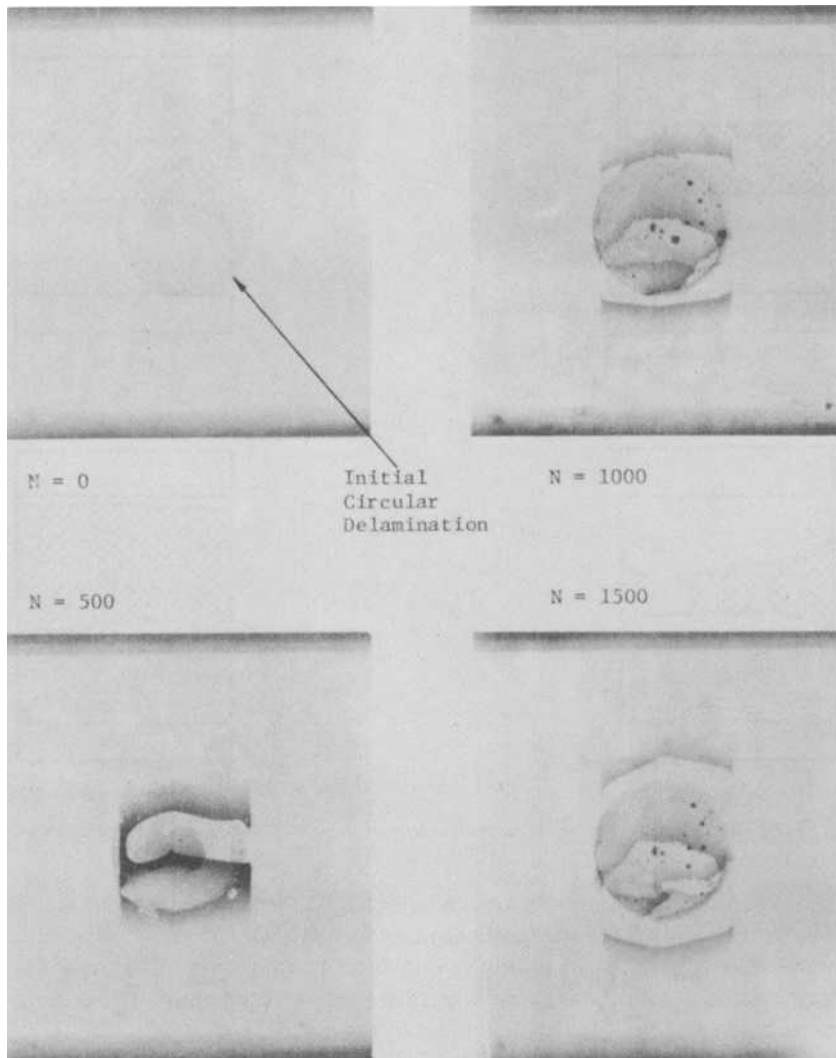


FIG. 9a—Delamination growth in Specimen 4284-55; Laminate A; Test Series 7;  $S = 0.66$ .

shown in Fig. 15. Subsequently, the specimens were failed in static compression to determine the half-life residual strength.

Table 4 presents half-life residual strength data for Laminate A specimens with 2-D delaminations below the surface (0-deg) ply. These data are superimposed over the S-N data in Fig. 16. It is noted that two specimens suffered fatigue failure (4284-53, 60) before they could be cycled to less than half the average lifetime of the preceding test series. Consequently, some specimens

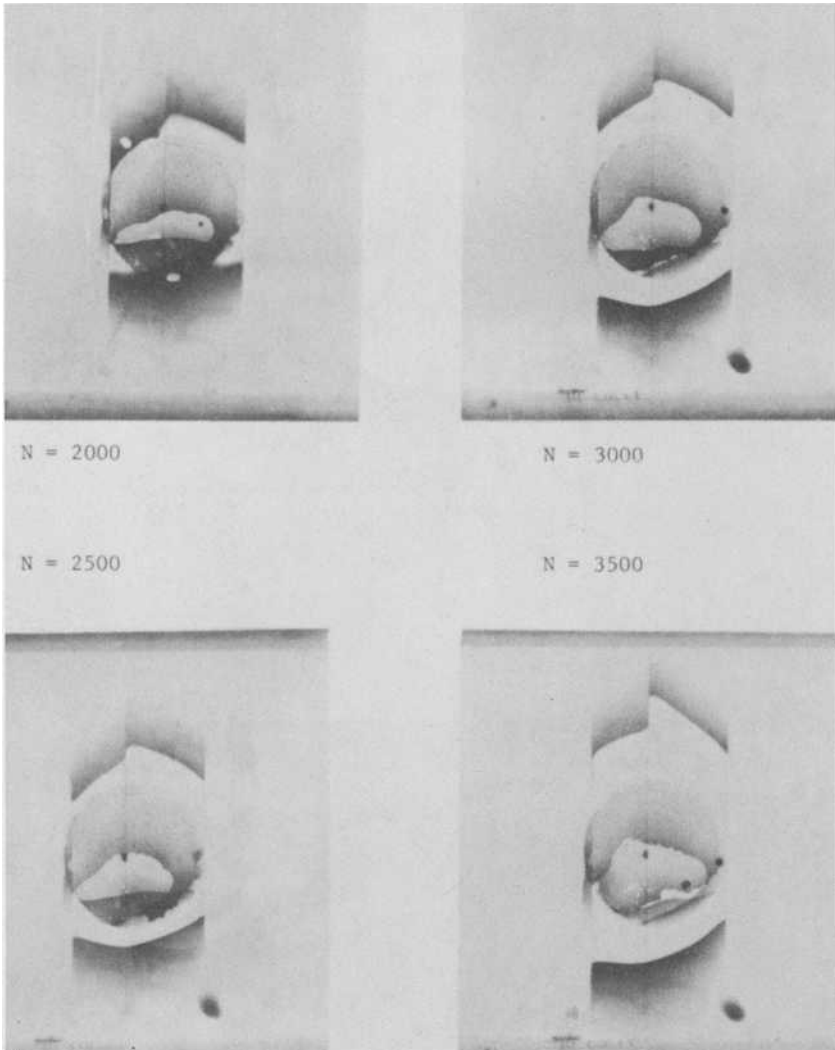


FIG. 9b—Delamination growth in Specimen 4284–55; Laminate A; Test Series 7;  $S = 0.66$ .

were cycled to a smaller number of cycles to avoid fatigue failure (see Table 4).

Table 5 presents half-life residual strength data for Laminate A specimens with 2-D delaminations between Plies 4 and 5. These data are superimposed over the corresponding S-N data in Fig. 17. It is believed that differing extents of delamination growth after the same number of fatigue cycles induce different percentage reductions in the static strength [17].

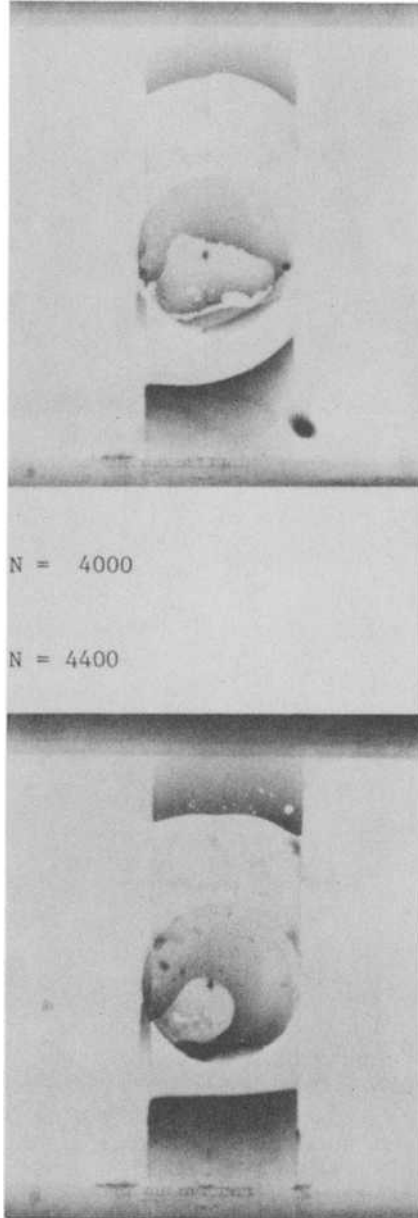


FIG. 9c—Delamination growth in Specimen 4284-55; Laminate A; Test Series 7;  $S = 0.66$ .

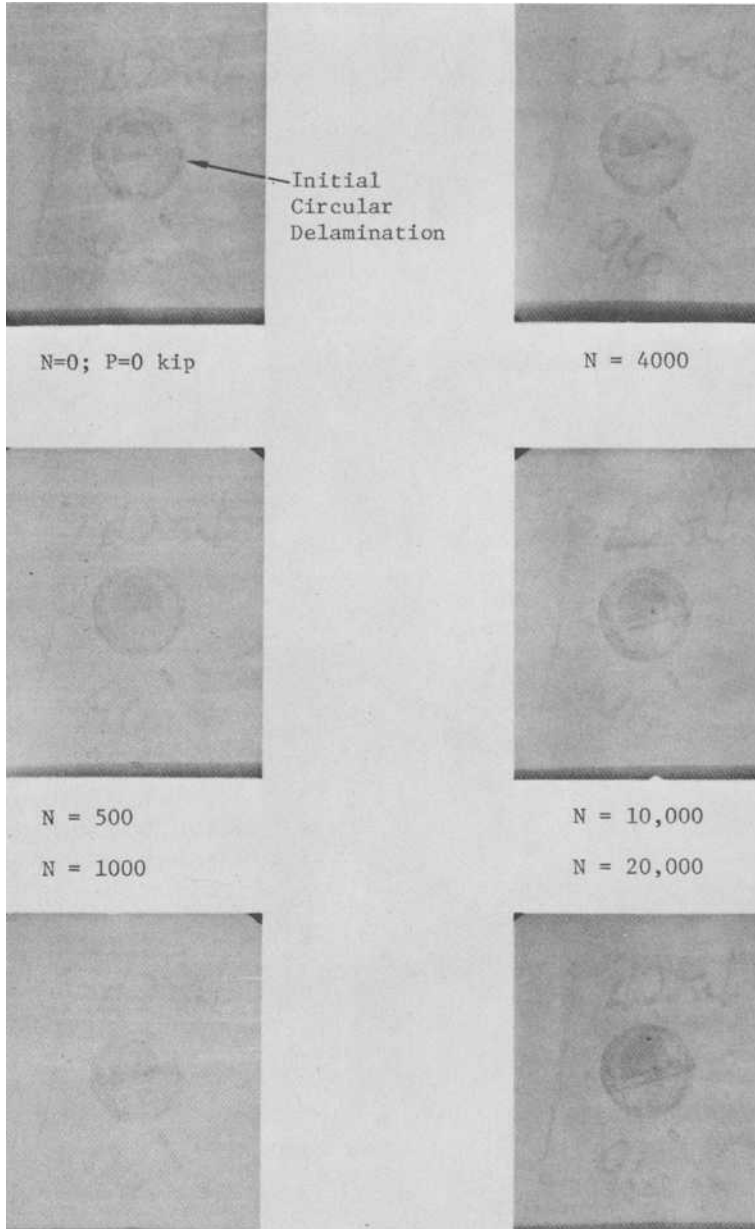
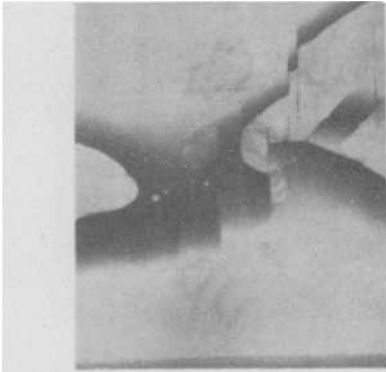
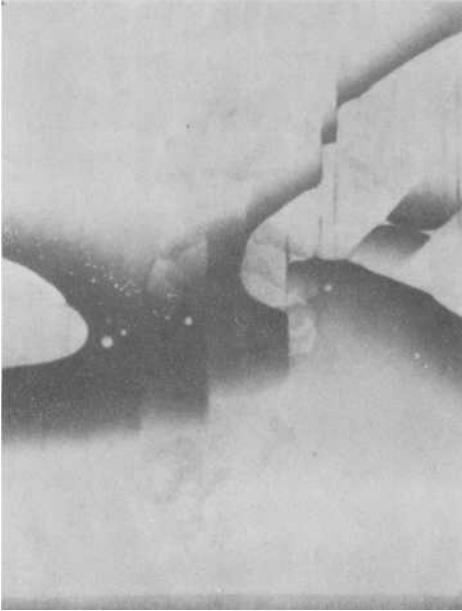


FIG. 10a—Delamination growth in Specimen 4284-96; Laminate A; Test Series 14;  $S = 0.77$ .



N = 43,880 (Failure)



Magnified View of the Failed Test Section (N = 43,880) obtained by placing the Polaroid film farther from the specimen

FIG. 10b—Delamination growth in Specimen 4284-96; Laminate A; Test Series 14; S = 0.77.

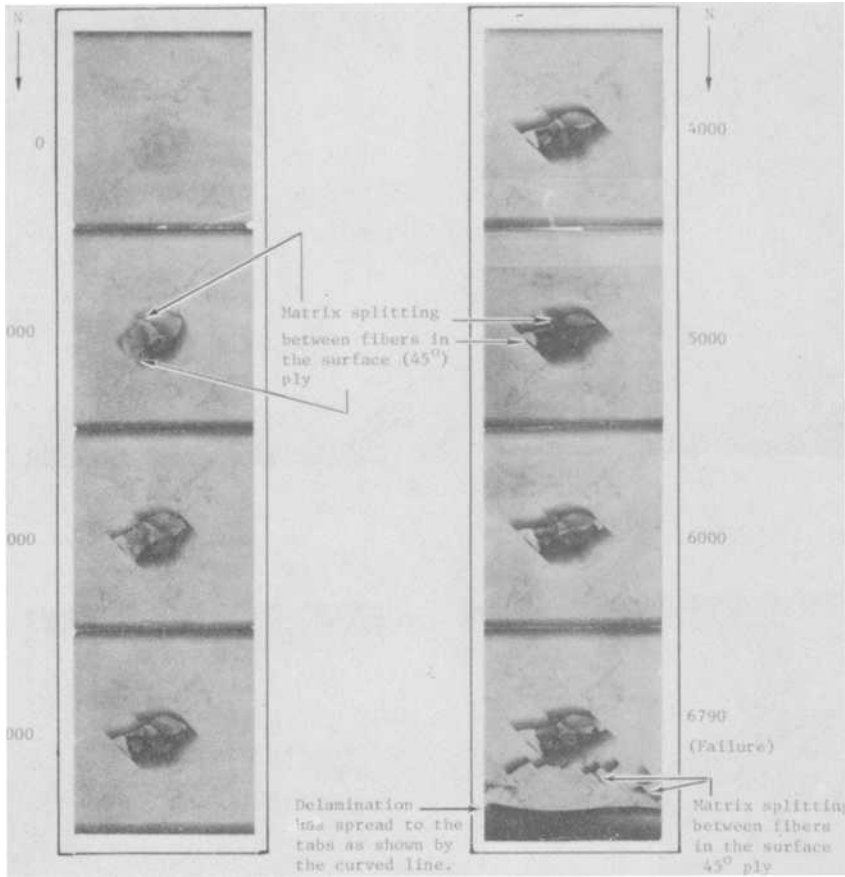


FIG. 11—Delamination growth in Specimen 4255-9; Laminate B; Test Series 7;  $S = 0.55$ .

### Ultimate Strength Tests

In the fatigue life tests and the half-life residual strength tests, failure was assumed to have occurred when an imbedded delamination propagated to the tab boundary. At this failure load level, the specimen need not necessarily lose all its load-carrying capacity. To determine the excess strength left in the specimens after this initial failure, ultimate static strength tests were conducted on fatigue life and half-life residual strength test specimens. The load was increased in a quasi-static manner, and two failure load levels were recorded. The lower value corresponded to an initial delamination failure, accompanied by a loud "popping" sound. The higher value corresponded to ultimate failure, beyond which no additional load can be sustained by the specimen. Tables 4 and 5 present ultimate strength data on half-life residual strength test specimens. It is seen that the ultimate strengths are considerably ( $>50$  percent) larger than the stresses corresponding to delamination fail-

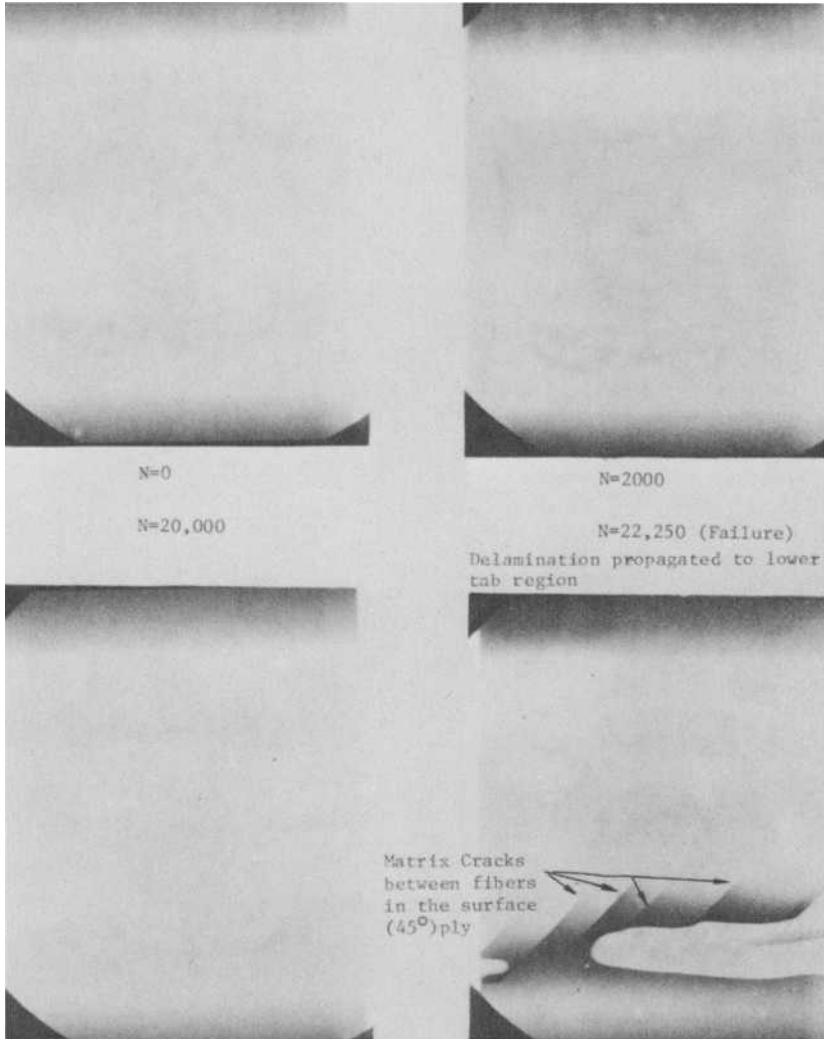


FIG. 12—Delamination growth in Specimen 4256-40; Laminate B; Test Series 14;  $S = 0.66$ ; radiographs taken with a 9.12 kN load.

ure. Similar results were obtained on all fatigue life test specimens, except for Laminate B specimens that seem to carry minimal additional load beyond delamination failure [17].

### Conclusions

The discussed experimental program provides a qualitative and a quantitative understanding of the effect of idealized interlaminar delaminations on

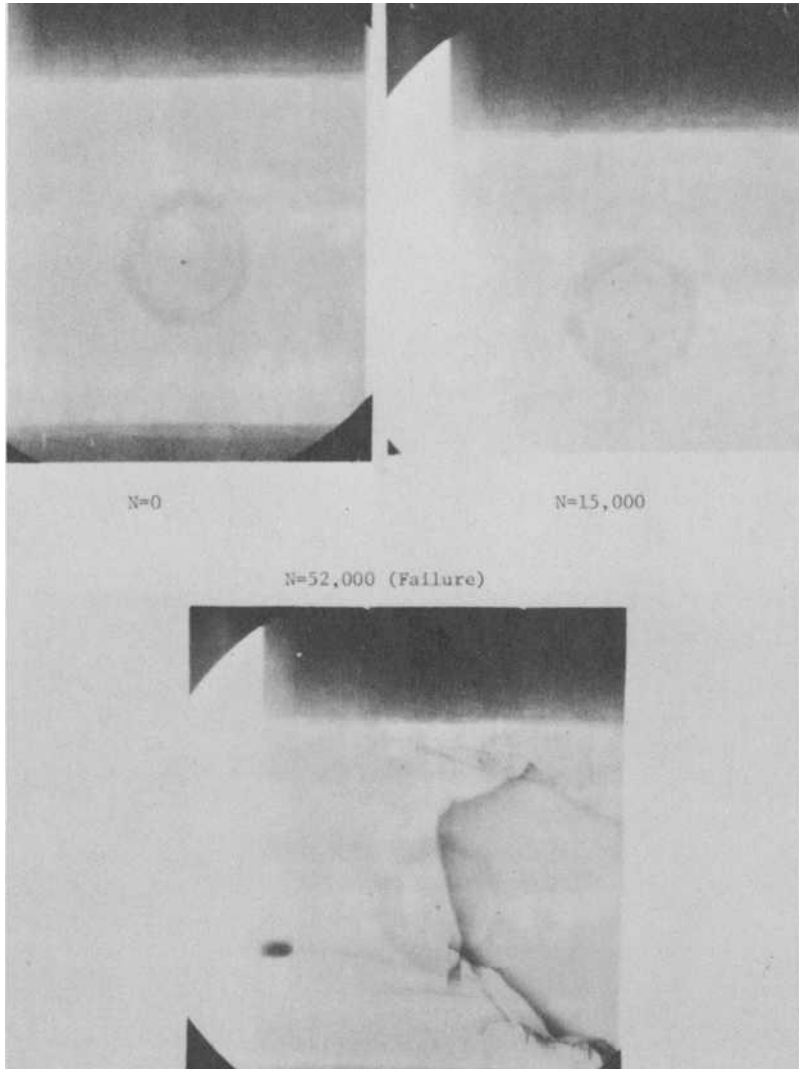


FIG. 13—Delamination growth in Specimen 4282-24; Laminate C; Test Series 8;  $S = 0.49$ .

the compression fatigue behavior of quasi-isotropic, T300/5208 graphite/epoxy laminates. Test specimens were designed to preclude gross (Euler) buckling between test grips, in the absence of lateral constraints. Fiber microbuckling was not observed in any of the failed specimens. Failures were induced predominantly by the propagation of imbedded delaminations to the tab region. Delamination growth was unstable under static loading. An

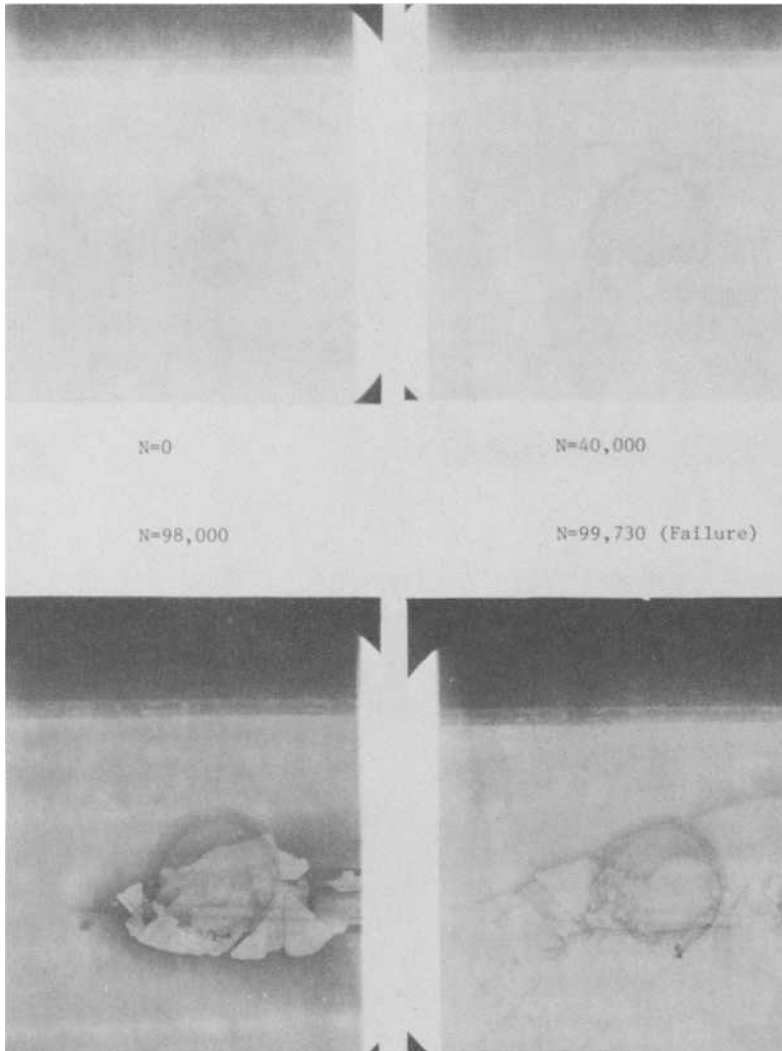


FIG. 14—Delamination growth in Specimen 4282-29; Laminate C; Test Series 14;  $S = 0.75$ .

imbedded flaw grew in a stable manner under compression fatigue, when the flaw was located below a stiff (0- or 45-deg) surface ply. This stable growth was accompanied by a large deflection of the delaminated region. When a 2-D delamination was located farther away from the surface (between Plies 4 and 5), the growth in the flaw was sudden and unstable, resembling a static failure mode.

S-N and half-life residual strength data were obtained for two flaw loca-

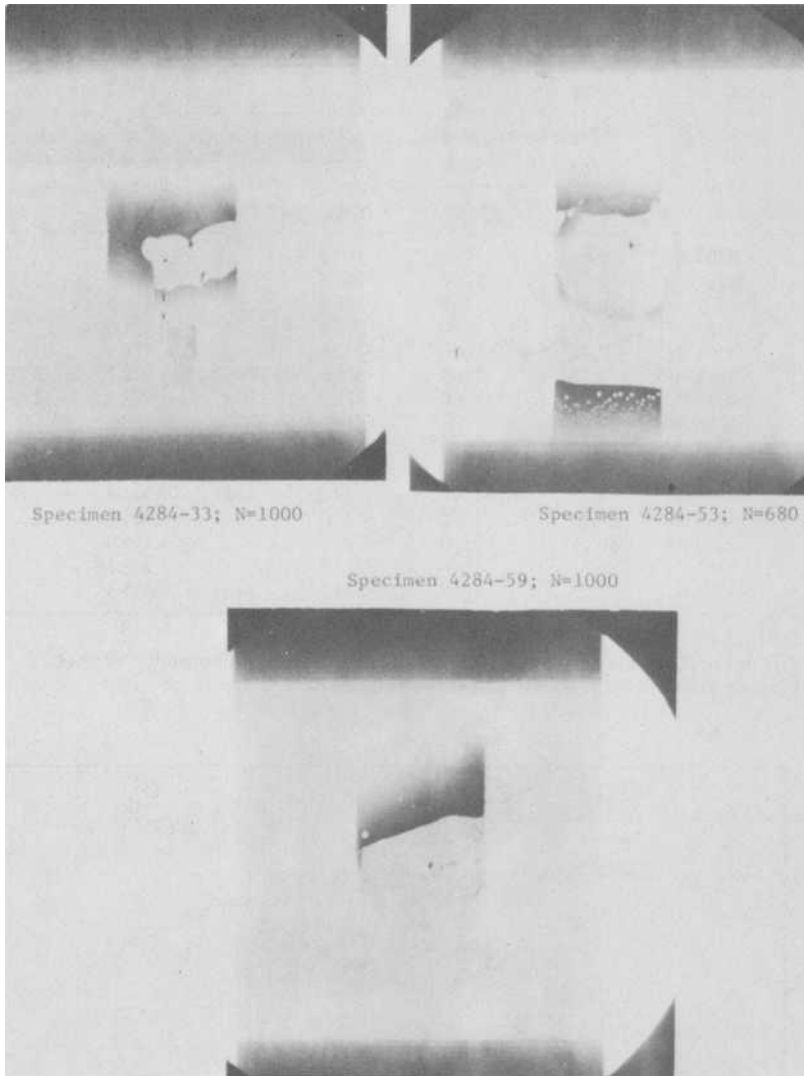


FIG. 15—Radiographs of residual strength test specimens after completing approximately half their lifetimes; Laminate A; Test Series 8;  $S = 0.66$ .

tions and two types of flaws. It was observed that, except for Laminate B specimens, other specimens could carry approximately 1.5 times the load corresponding to delamination failure before ultimate failure occurs.

A novel and efficient procedure, used in the program to monitor the growth of imbedded delaminations, can be extended to other test situations to obtain useful information regarding internal damage growth.

TABLE 4—Residual strength data from Laminate A specimens with 1.27 cm diameter delaminations between Plies 1 and 2.

Test Series	Specimen	Fatigue Loading ( $R = 10; \omega = 10$ Hz) Prior to Residual Strength Testing		Residual Strength Test Data at			
		S	N	Delamination Failure <sup>b</sup>		Ultimate Failure	
				Stress, MPa	Strain, $\mu\text{mm/mm}$	Stress, MPa	Strain, <sup>c</sup> $\mu\text{mm/mm}$
8	4284-33	0.66	1 000	-370.2	...	-481.2	...
	4284-36	0.66	1 000	-340.5	-9 471	-456.2	-12 551
	4284-53	0.66	680 <sup>d</sup>	-241.7	...	-456.6	...
	4282-59	0.66	500	-321.1	...	-474.6	...
	4361-11	0.66	1 000	-372.0	...	-578.6	...
10	4284-40	0.58	2 800	-302.6	-7 462	-498.3	-12 279
	4284-43	0.58	5 000	-326.9	-7 535	-518.4	-12 901
	4284-60	0.58	700 <sup>d</sup>	-216.5	...	-460.0	...
	4284-61	0.58	5 000	-290.3	...	-479.6	...
	4361-15	0.58	5 000	-313.2	...	-599.3	...
12	4284-41	0.55	10 000	-339.2	-9 465	-544.8	-11 587
	4284-42	0.55	8 000	-325.8	-7 948	-509.8	-12 372
	4284-68	0.55	10 000	-289.0	...	-465.0	...
	4361-14	0.55	3 000	-328.5	...	-590.1	...
	4361-17	0.55	6 000	-304.5	...	-523.8	...

<sup>a</sup>Delamination failure occurred prior to residual strength testing.

<sup>b</sup>The imbedded delamination propagated to the tab region in an unstable manner.

<sup>c</sup>Linearly extrapolated from values prior to delamination failure.

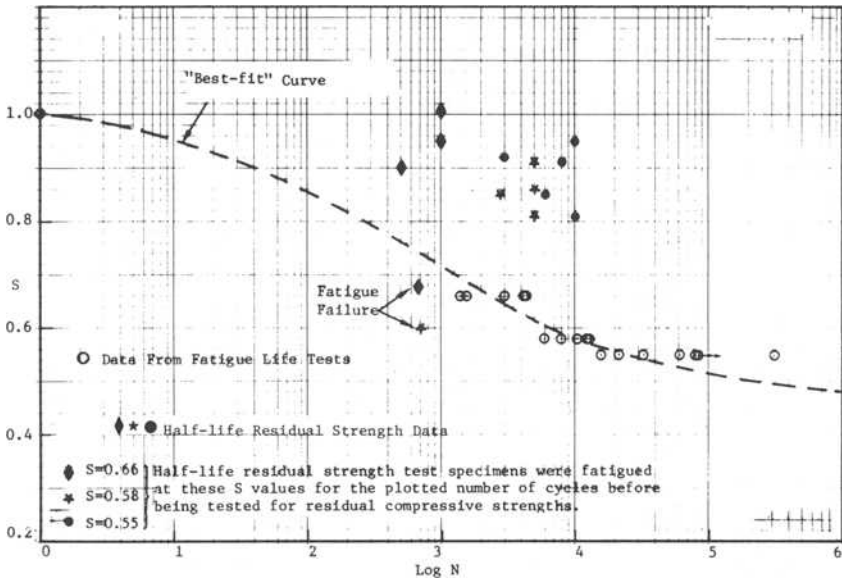


FIG. 16—S-N data and half-life residual strength data for Laminate A specimens with 1.27-cm (0.5-in.) diameter delamination (2-D) between Plies 1 and 2.

TABLE 5—Residual strength data from Laminate A specimens with 1.27 cm diameter delaminations between Plies 4 and 5.

Test Series	Specimen	Fatigue Loading ( $R = 10; \omega = 10 \text{ Hz}$ ) Prior to Residual Strength Testing		Residual Strength Test Data at			
		$S$	$N$	Delamination Failure <sup>b</sup>		Ultimate Failure	
				Stress, MPa	Strain, $\mu\text{mm/mm}$	Stress, MPa	Strain, <sup>c</sup> $\mu\text{mm/mm}$
15	4284-82	0.77	1 000	329.7	-9 620	-507.5	-14 444
	4284-83	0.77	1 000	323.1	-8 697	-525.7	-13 806
	4284-97	0.77	1 000	281.0	...	-427.6	...
	4284-98	0.77	550 <sup>a</sup>	263.9	...	-424.9	...
	4361-2	0.77	1 000	293.0	...	-535.1	...
17	4284-86	0.72	7 500	328.7	-8 996	-538.3	-13 900
	4284-87	0.72	7 500	309.4	...	-535.1	...
	4284-101	0.72	7 500	310.4	...	...	...
	4284-102	0.72	7 500	332.4	...	...	...
	4361-4	0.72	7 500	311.0	...	-520.0	...
19	4284-89	0.66	100 000	319.0	...	-535.9	...
	4284-90	0.66	100 000	297.1	-7 763	-501.5	-12 391
	4284-91	0.66	100 000	339.7	...	-534.0	...
	4284-105	0.66	100 000	307.1	...	-537.4	...
	4284-106	0.66	100 000	294.7	...	-448.4	...

<sup>a</sup>Delamination failure occurred prior to residual strength testing.

<sup>b</sup>The imbedded delamination propagated to the tab region in an unstable manner.

<sup>c</sup>Linearly extrapolated from values prior to delamination failure.

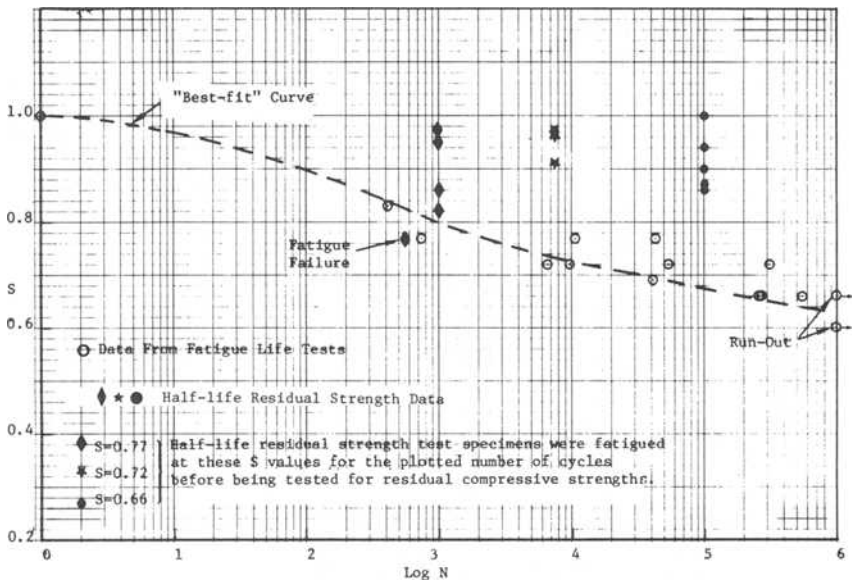


FIG. 17— $S$ - $N$  data for Laminate A specimens with 1.27-cm (0.5-in.)-diameter delamination (2-D) between Plies 4 and 5.

### Acknowledgments

The work reported in this paper was conducted at Northrop Corporation under Contract NAS1-15956 to the National Aeronautics and Space Administration (NASA), Langley Research Center.

The author would also like to acknowledge the help offered by W. R. Sturrock and S. Sandor, Jr. in aiding with NDI, J. Bock in conducting the tests, B. Parish in typing the manuscript, and R. Cordero in helping with the figures.

### References

- [1] Ramkumar, R. L., "Composite Impact Damage Susceptibility," Naval Air Development Center Contract N62269-79-C-0274, Northrop Corporation, Jan. 1981.
- [2] Bhatia, N. M. "Impact Damage Tolerance of Thick Graphite/Epoxy Laminates," Naval Air Development Center Report No. NADC-79038-60, Jan. 1979.
- [3] Ramkumar, R. L., "Environmental Effects on Composite Damage Criticality," Naval Air Development Center Contract N62269-79-C-0259, Northrop Corporation, June 1981.
- [4] Chatterjee, S. N., Hashin, Z., and Pipes, R. B., "Definition and Modeling of Critical Flaws in Graphite Fiber Reinforced Resin Matrix Composite Materials," Naval Air Development Center Report No. NADC-77278-30, Aug. 1979.
- [5] Ratwani, M. M. and Kan, H. P., "Compression Fatigue Analysis of Fiber Composites," Naval Air Development Center Report No. NADC-78049-60, Sept. 1979.
- [6] Byers, B. A., "Behavior of Damaged Graphite/Epoxy Laminates Under Compression Loading," NASA-CR-159293, National Aeronautics and Space Administration, Aug. 1980.
- [7] Brussat, T. R., Chiu, S. T., and Mostovoy, S., "Fracture Mechanics For Structural Adhesive Bonds, Phases I and II," Report AFML-TR-77-163, Parts I and II, Air Force Materials Laboratory, Wright-Patterson Air Force Base, Ohio, 1978.
- [8] Wilkins, D. J., Eisenmann, J. R., Camin, R. A., Margolis, W. S., and Benson, R. A., "Characterizing Delamination Growth in Graphite/Epoxy," this publication.
- [9] Saff, C. R., "Compression Fatigue Life Prediction Methodology for Composite Structures—Literature Survey," Naval Air Development Center Report No. NADC-78203-60, June 1980.
- [10] Wang, S. S. in *Composite Materials: Testing and Design (Fifth Conference)*, ASTM STP 674, American Society for Testing and Materials, 1979, pp. 642-663.
- [11] Reifsnider, K. L., Henneke, E. G., and Stinchcomb, W. W. in *Composite Materials: Testing and Design (Fourth Conference)*, ASTM STP 617, American Society for Testing and Materials, 1977, pp. 93-105.
- [12] Ramkumar, R. L., Kulkarni, S. V., and Pipes, R. B., "Definition and Modeling of Critical Flaws in Graphite Fiber Reinforced Epoxy Resin Matrix Composite Materials," Naval Air Development Center Report No. NADC-76228-30, Jan. 1978.
- [13] Chai, M., Babcock, C. D., and Knauss, W. G., "On the Failure of Laminated Plates by Delamination Buckling," Report No. 80-16, California Institute of Technology, July 1980.
- [14] Whitcomb, J. D., *Proceedings of the Mechanics of Composites Review*, Bergamo Center, Dayton, Ohio, Oct. 1980, pp. 87-91.
- [15] Pagano, N. J. and Pipes, R. B., "Some Observations on the Interlaminar Strength of Composite Laminates," *International Journal of Mechanical Sciences*, Vol. 15, 1973, pp. 679-688.
- [16] Tirosh, J., "On the Tensile and Compressive Strength of Solids Weakened (Strengthened) by an Inhomogeneity," *Journal of Applied Mechanics*, Sept. 1977, pp. 449-454.
- [17] Ramkumar, R. L., "Fatigue Degradation in Compressively Loaded Composites," NASA Contractor Report No. 165681, National Aeronautics and Space Administration, April 1981.

# Effect of Stacking Sequence on Damage Propagation and Failure Modes in Composite Laminates

---

**REFERENCE:** Ratwani, M. M. and Kan, H. P., "Effect of Stacking Sequence on Damage Propagation and Failure Modes in Composite Laminates," *Damage in Composite Materials*, ASTM STP 775, K. L. Reifsnider, Ed., American Society for Testing and Materials, 1982, pp. 211-228.

**ABSTRACT:** The effect of stacking sequence on damage growth and failure modes in composite laminates is discussed. Tests were conducted on AS/3501-6 graphite/epoxy coupons with four different stacking sequences. All laminates had the same percentage of 0, 90, and  $\pm 45$  degree plies. Constant amplitude fatigue tests were performed at  $R$  (minimum to maximum stress ratio) =  $-1.0$  and  $-\infty$ . The specimens were periodically taken out of the testing machine and subjected to nondestructive inspection using X-ray radiography with diiodobutane.

The results of nondestructive inspection indicate that the direction of damage propagation depends on the stacking sequence in the composite laminate. The damage may propagate predominantly along the loading direction or in a direction at some angle to the loading direction, depending on the stacking sequence. Interlaminar stress analysis of four laminates was performed to correlate the direction of damage propagation with the nature of interlaminar stresses.

**KEY WORDS:** composite materials, X-ray radiography, interlaminar stresses, delamination

Fatigue and fracture of composites has attracted considerable interest in the last decade due to the increasing use of these materials in aerospace structures. These materials exhibit extremely complex modes of failure both under static and fatigue loadings [1-12].<sup>2</sup> The failure is accompanied by one or more of the following phenomena: fiber splitting; delaminations around free edges or at stress concentrations; matrix crazing; and transverse cracking of the plies with fibers oriented in a direction perpendicular to the loading direction. These phenomena must be taken into consideration in predicting failure of the laminates.

<sup>1</sup> Manager, structural life assurance research and senior engineer, Northrop Corporation, Hawthorne, Calif. 90250.

<sup>2</sup> The italic numbers in brackets refer to the list of references appended to this paper.

Various investigators [13–15] have shown that the strength and failure modes of composites depend on the ply orientations and stacking sequence. Pagano and Pipes [13] have analytically investigated the influence of stacking sequence on laminate static strength. They have presented an approach for optimizing stacking sequence to reduce delaminations.

Daniel et al [14] have investigated experimentally the influence of stacking sequence on tensile strength and failure mode in composites. They showed that stacking sequences having interlaminar tensile stress or large shear stress showed 10 to 20 percent reduction in strength, compared to that of alternate stacking sequences. They observed that stacking sequence variations can alter the mode of failure from catastrophic to noncatastrophic. Whitney and Kim [15] have investigated experimentally the effect of stacking sequence on the notched strength of laminated composites. They investigated two different stacking sequences of quasi-isotropic graphite/epoxy laminates. One stacking sequence had large interlaminar tensile stresses, and another one had compressive stresses at the free edges of the tensile coupon. Their experimental data indicated that unnotched tensile strength is reduced by the presence of interlaminar tensile stresses at the free-edge, while the notched strength was not affected by the stacking sequence.

In the present investigations, the influence of stacking sequence on damage propagation and compression fatigue life of graphite/epoxy laminates is studied. The results, extracted from a broader study [16] designed to investigate compression fatigue behavior of composites, are discussed in this paper.

### Experimental Program

Sixteen-ply laminates with four different stacking sequences were selected for fatigue tests. All laminates have the same percentage of 0, 90, and  $\pm 45$  degree plies. The stacking sequences selected were: Laminate 1,  $(0/\pm 45/90/0_2/\pm 45)_s$ ; Laminate 2,  $(90/\pm 45/0_3/\pm 45)_s$ ; Laminate 3,  $(90/0/\pm 45/0_2/\pm 45)_s$ ; Laminate 4,  $(\pm 45/0/90/0_2/\pm 45)_s$ .

All specimens were fabricated from AS/3501–6 graphite/epoxy unidirectional tape of Type 1 prepreg (single-ply, with a nominal thickness of 0.132 mm (0.0052 in.)).

The specimen used in the test program is shown in Fig. 1. This type of specimen has been used by Rosenfeld and Huang [5] in compression fatigue tests. The test matrix is shown in Table 1.

All tests were conducted in MTS machines. The fatigue tests were conducted at frequency of 10 Hz. The specimens were gripped so as to avoid any out-of-plane bending. This was done by strain gaging initial specimens back to back (Fig. 1) to check out the test fixture and make sure that strain gage readings on back-to-back gages did not differ by more than 5 percent.

Some specimens were subjected to nondestructive inspection (NDI) at certain intervals of fatigue cycles. X-ray radiography with diiodobutane (DIB)

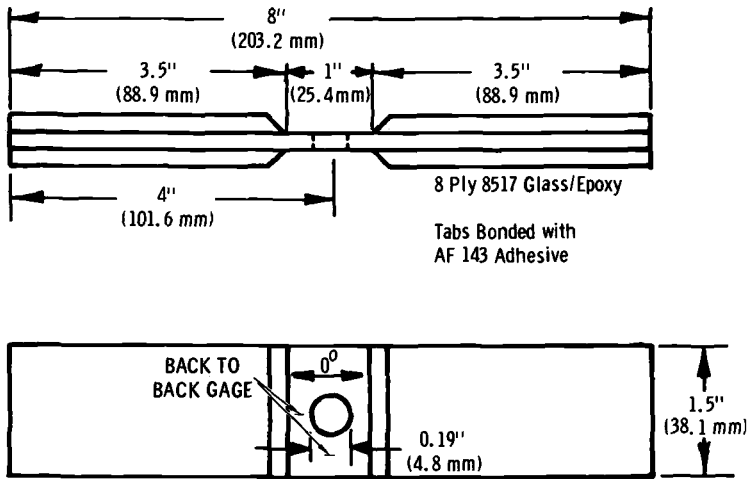


FIG. 1—Specimen configuration.

was the NDI technique used to determine the extent of damage. The specimens were taken out of the testing machine at regular intervals and subjected to X-ray radiography.

Diiodobutane was carefully applied to edges of interest, making sure that DIB did not splatter on the faces of the specimens. Within less than two hours of the application of DIB, the specimens were exposed in the HP804 X-ray cabinet. Kodak film type AA was used for X-ray.

**X-ray Radiography Results**

*Laminate 1*

X-ray radiography of Laminate 1 ( $0/\pm 45/90/0_2/\pm 45$ ), Specimen R1-17, tested at  $R = -1$  and  $\sigma_{min} = -427$  MPa ( $-62.0$  ksi), is shown in Fig. 2. The average notched compression static strength of this laminate is  $-461$  MPa ( $-66.9$  ksi). The X-ray radiography was taken after 300 and 800 cycles. The specimen failed after 840 cycles. It is seen that the delamination initiates around the hole at right angles to loading direction. The delamination sub-

TABLE 1—Test matrix.

Laminate	Number of Specimens Tested	R Ratio	Number of Specimens Subjected to X-ray Radiography
1	24	-1	13
1	13	$-\infty$	7
2	6	-1	3
3	6	-1	3
4	6	-1	5

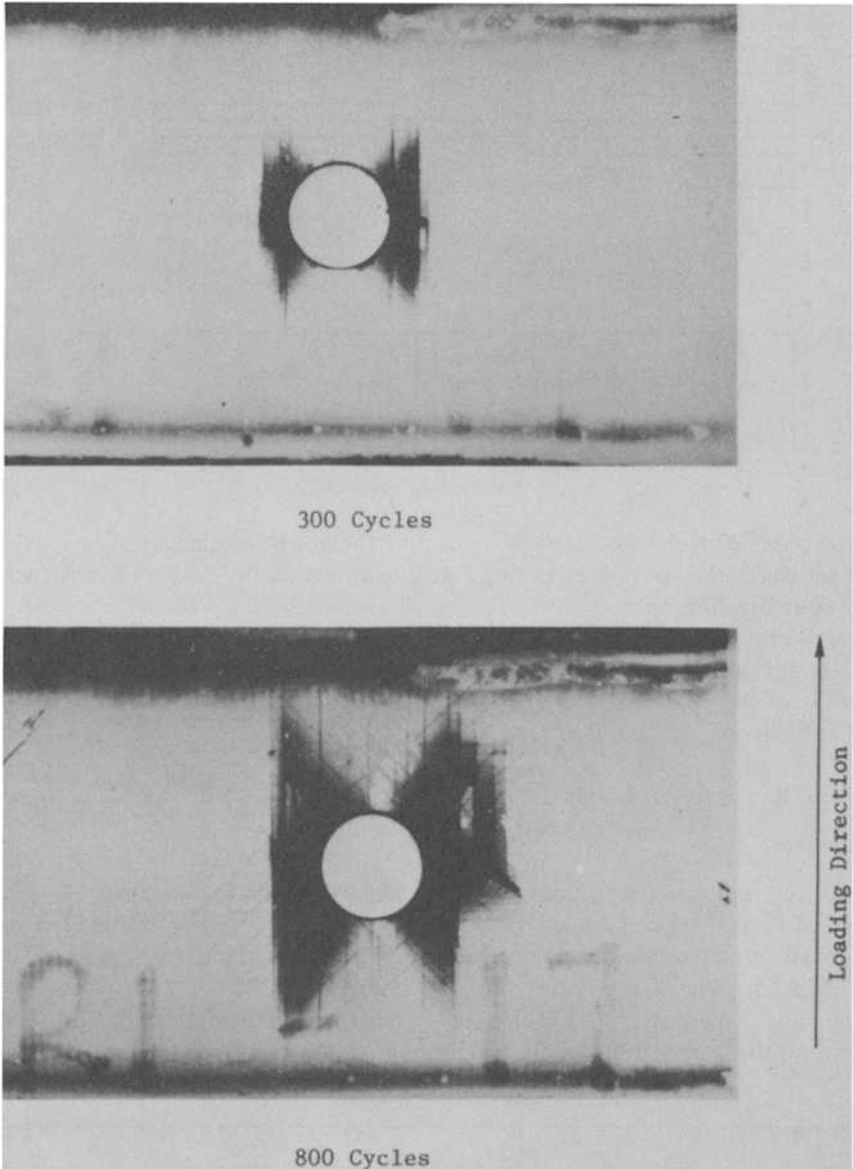


FIG. 2—X-ray radiography of Specimen R1-17 ( $0/\pm 45/90/0_2/\pm 45$ ), laminate, tested at  $R = -1$ ,  $\sigma_{\min} = -427 \text{ MPa}$  ( $-62 \text{ ksi}$ ). Specimen failed at 840 cycles.

sequently grows around the periphery of the hole and the loading direction. Major growth takes place along loading direction. Prior to failure, after 840 cycles, considerable cracking is observed in the laminate.

X-ray radiography of Laminate 1 Specimen R1-12, tested at  $R = -1$  and  $\sigma_{min} = -359$  MPa ( $-52$  ksi), is shown in Fig. 3 after 2500, 6000, 10000, and 40000 cycles. The specimen failed after 44480 cycles. The delamination growth in this specimen at 2500 cycles is identical to that in specimen R1-17 at 300 cycles. The delamination grows in the form of a triangle until it forms a strip with width slightly greater than the diameter of the hole. At 10000 cycles the entire length of the specimen appears to be delaminated in the form of a narrow strip on either side of the hole. At 40000 cycles the width of the delaminated strip on either side of the hole has increased. The entire length of the test area is delaminated. The delaminations are not able to grow any

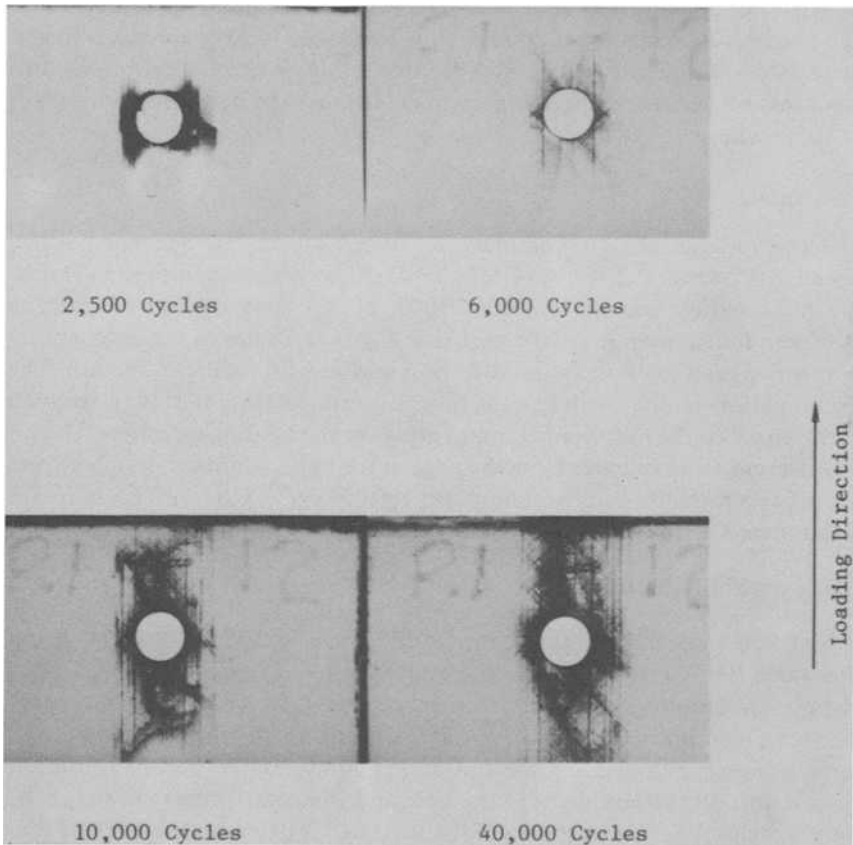


FIG. 3—X-ray radiography of Specimen R1-12 ( $0/\pm 45/90/0_2/\pm 45$ ), laminate, tested at  $R = -1$ ,  $\sigma_{min} = -359$  MPa ( $-52$  ksi). Specimen failed at 44480 cycles.

further along the loading direction because of the limited test length of the specimen and constraining effects of the tabs at the end of test area.

Figure 4 shows X-ray radiography of Laminate 1 Specimen R1-22, tested at  $R = -\infty$  and  $\sigma_{min} = -355$  MPa ( $-51.5$  ksi). The X-ray radiography pictures are shown after 150 000, 400 000, and 1 000 000 fatigue cycles. The specimen failed after 2 111 000 cycles. The delamination growth at  $R = -\infty$  is similar to that in specimens tested at  $R = -1.0$ . The delamination starts growing at the edge of the hole around its periphery and propagates along the loading direction. At 400 000 cycles the entire length of the test area is delaminated. However, the damage is confined to a narrow strip, extending on either side of the hole. The width of the damaged strip after 400 000 cycles and 1 000 000 cycles is almost the same.

In Specimen R1-12, tested at  $R = -1$  and  $\sigma_{min} = -359$  MPa ( $-52.0$  ksi), the entire length of the specimen is delaminated at 10 000 cycles, whereas in Specimen R1-22 [ $R = -\infty$  and  $\sigma_{min} = -355$  MPa ( $-51.5$  ksi)] the entire length is not delaminated even at 150 000 cycles. In the later specimen the entire length is damaged at 400 000 cycles. The X-ray radiography pictures of these two specimens indicate a very strong influence of  $R$  ratio (tension-compression versus compression-compression) on the delamination growth in composites.

### Laminate 2

X-ray radiography of Laminate 2 ( $90/\pm 45/0_3/\pm 45$ ), Specimen R2-9, tested at  $R = -1$ ,  $\sigma_{min} = -314$  MPa ( $-45.5$  ksi) is shown in Fig. 5. The X-ray radiography was taken after 20 000, 50 000, and 100 000 cycles. The specimen failed after 103 420 cycles. The figure indicates that the delamination propagates both in radial direction and axial (loading) direction. The delamination in the loading direction is confined to a narrow strip with width equal to the hole diameter and grows in the loading direction. The radial delamination initiates from the edge of the hole around its periphery and propagates radially. Prior to failure (at 100 000 cycles) the entire test area is delaminated as shown in the figure.

### Laminate 3

Figure 6 shows X-ray radiography of Laminate 3 ( $90/0/\pm 45/0_2/\pm 45$ ), Specimen R3-7, tested at  $R = -1.0$  and  $\sigma_{min} = -317$  MPa ( $-46.0$  ksi). The X-ray radiography pictures are shown after 8000, 18 000, and 30 000 cycles. The specimen failed at 50 790 cycles. The figure shows the delamination to initiate along  $\pm 45$ -deg angles, and at 18 000 cycles the delamination has spread around the periphery of the hole and is almost circular in shape. At 30 000 cycles the entire test area of the specimen is delaminated. Several contours in the figure indicate the presence of delaminations between several plies of the laminate. This was verified with stereo-radiography.

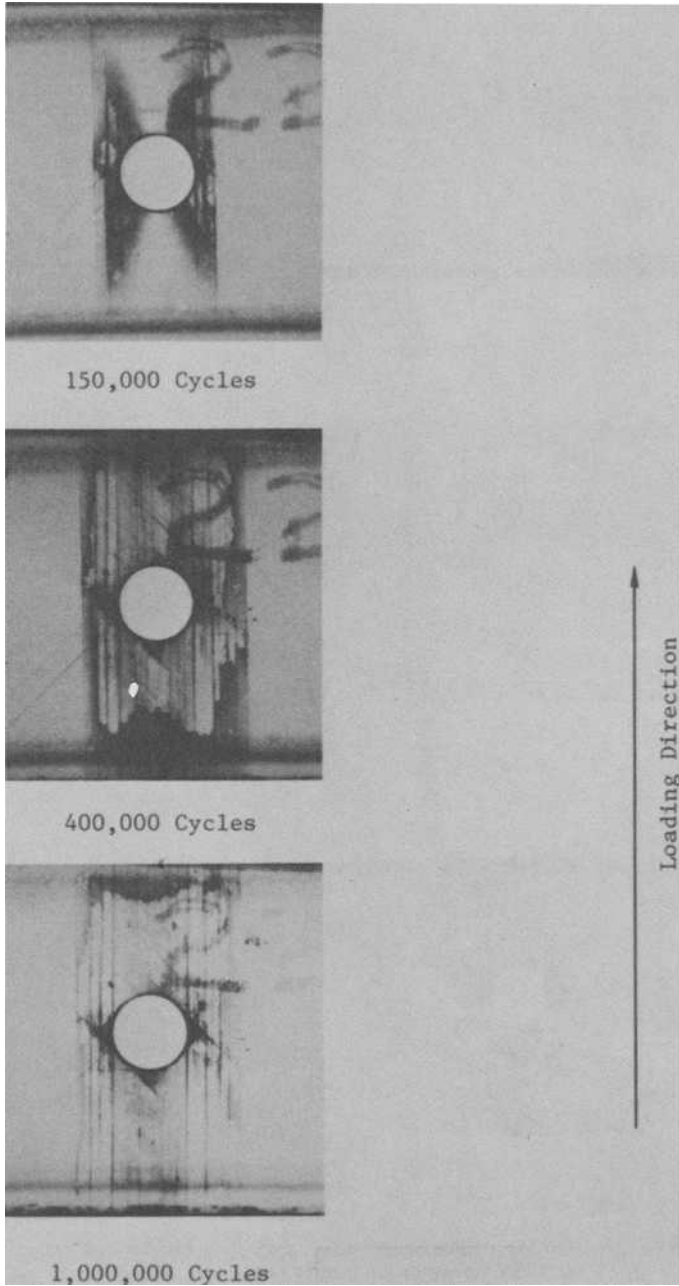


FIG. 4—X-ray radiography of Specimen R1-22 ( $0/\pm 45/90/0_2/\pm 45$ ), laminate, tested at  $R = -\infty$ ,  $\sigma_{\min} = -355$  MPa ( $-51.5$  ksi). Specimen failed at 2 111 000 cycles.

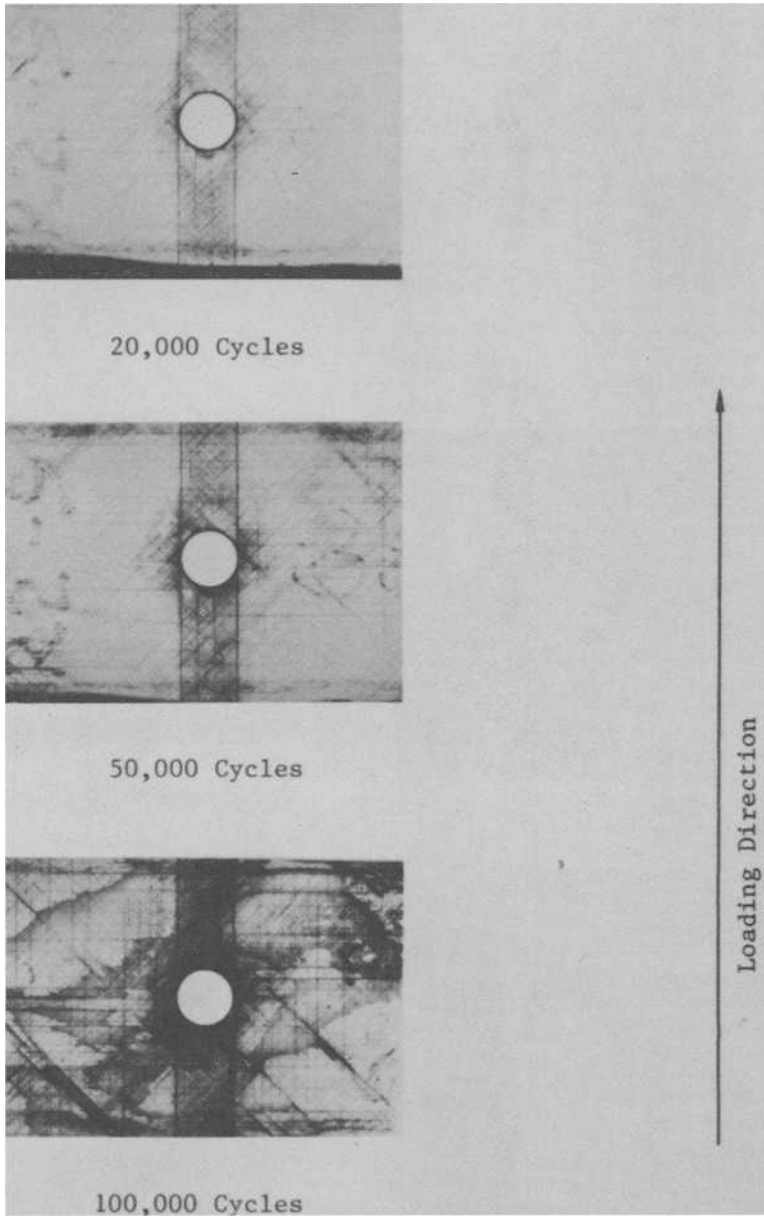


FIG. 5—X-ray radiography of Specimen R2-9 ( $90/\pm 45/0_3/\pm 45$ ), laminate, tested at  $R = -1$ ,  $\sigma_{\min} = -314 \text{ MPa}$  ( $-45.5 \text{ ksi}$ ). Specimen failed at 103 420 cycles.

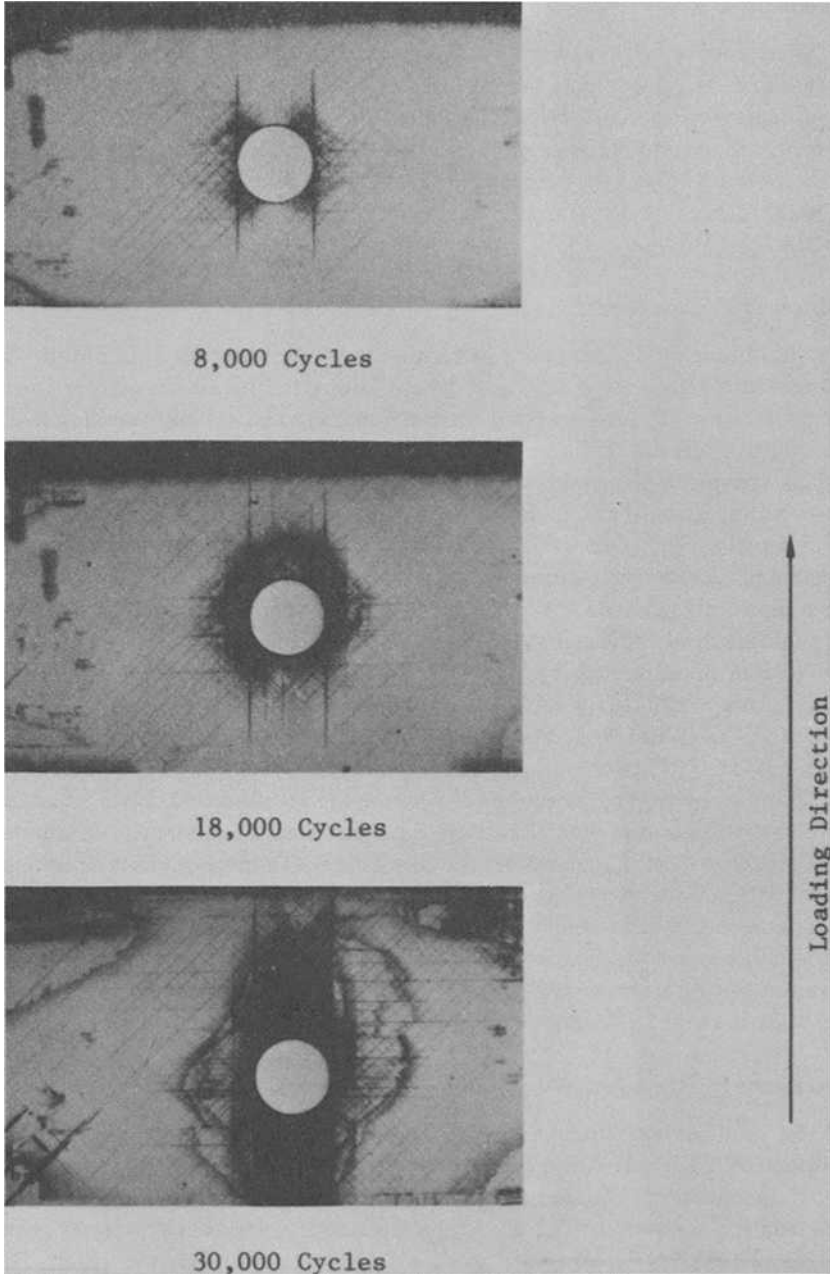


FIG. 6—X-ray radiography of Specimen R3-7 ( $90/0/\pm 45/0/\pm 45$ ), laminate, tested at  $R = -1$ ,  $\sigma_{\min} = -317$  MPa ( $-46$  ksi). Specimen failed at 50 790 cycles.

### Laminate 4

X-ray radiography of Laminate 4 ( $\pm 45/0/90/0_2/\pm 45$ ), Specimen R4-2, tested at  $R = -1$  and  $\sigma_{min} = -362$  MPa ( $-52.5$  ksi) is shown in Fig. 7. The figure shows dominant damage growing along the loading direction. However, there is some damage growth at right angles to the loading direction.

X-ray radiography of Specimen R4-4, tested at  $R = -1.0$  and  $\sigma_{min} = -362.0$  MPa ( $-52.5$  ksi) is shown in Fig. 8. The specimen failed after 8610 cycles.

### Observed Failure Modes

The failure modes observed in Laminate 1 under constant amplitude fatigue loading are shown in Fig. 9. These failure modes are shown for specimens tested under tension-compression and compression-compression loading. The failure mode under tension-compression loading differs from that under compression-compression loading. The specimen tested under tension-compression loading shows considerable delaminations between 0 and  $+45$  deg plies near outer surface, and between the  $+45$  and  $-45$ -deg plies. The specimen tested under compression-compression loading shows dominant delaminations between the  $+45$  and  $-45$  plies near the surface and also at the midplane of the laminate.

The failure modes observed in Laminate 2, tested under tension-compression loading, are shown in Fig. 10. The laminate shows delaminations between several plies. Near the surface of the specimen, the delamination occurs between  $+45$  and  $-45$ -deg plies.

Figure 11 shows the failure mode observed in Laminate 3 specimens tested under tension-compression loading. This laminate also exhibits delaminations between several plies. Near the surface, the laminate exhibits delaminations between 0 and  $+45$ -deg plies.

The failure modes observed in Laminate 4 specimens, tested under tension-compression loading, are shown in Fig. 12. This laminate also shows delaminations between several plies. Near the surface, the delaminations occur between  $+45$  and  $-45$ -deg plies.

### Interlaminar Stress Analysis

The interlaminar stress analysis of specimens with holes was performed with the NASTRAN finite element computer program [16], assuming uniform displacement at the end of the tabs in the specimen. A typical result of this analysis is shown in Fig. 13. In this figure, the interlaminar stresses in the ( $0/\pm 45/90/0_2/\pm 45$ ), laminate at the plane of symmetry are presented. The interlaminar stresses are normalized with respect to the gross applied stress,  $\sigma_0$ . It is seen that the interlaminar shear stress  $\tau_{\theta z}$  is the dominating component and has its maximum value at about 56 deg from the loading direction.

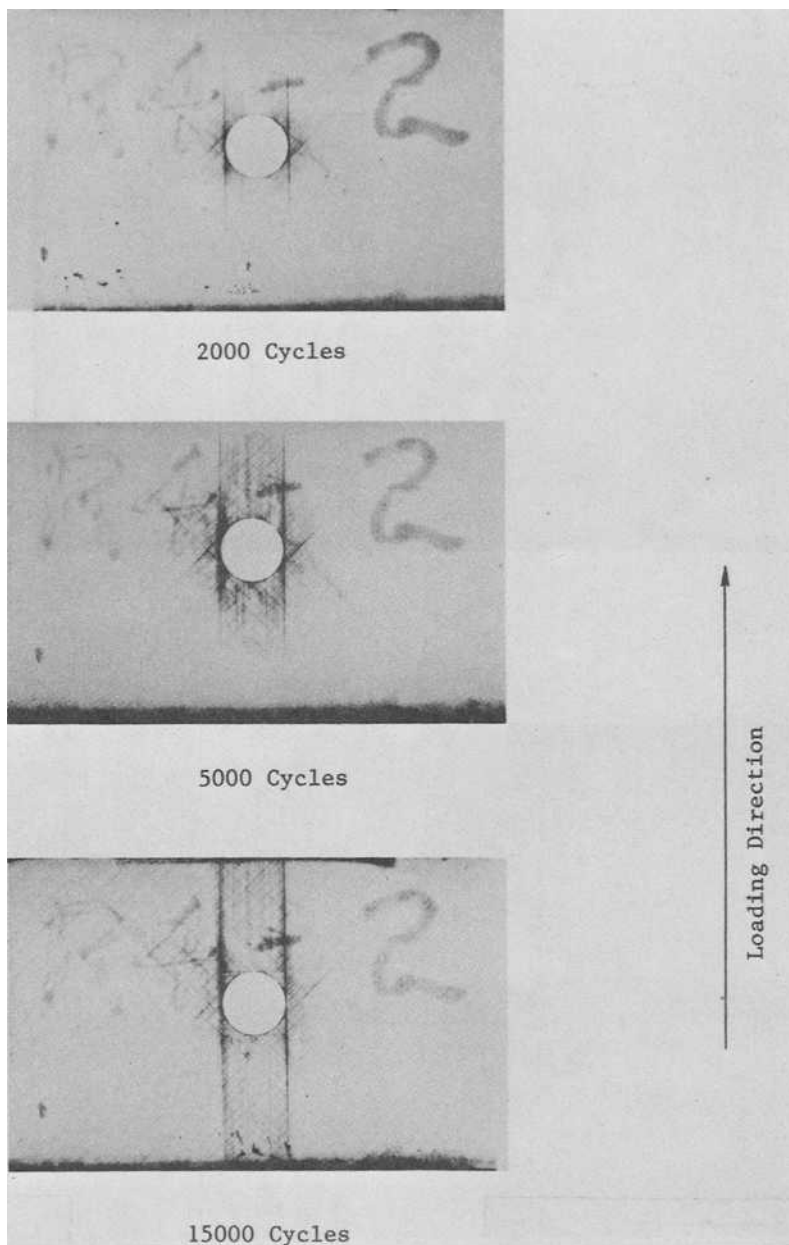


FIG. 7—X-ray radiography of Specimen R4-2 ( $\pm 45/0/90/0_2/\pm 45$ ), laminate, tested at  $R = -1$ ,  $\sigma_{\min} = -362$  MPa ( $-52.5$  ksi). Specimen failed at grips.

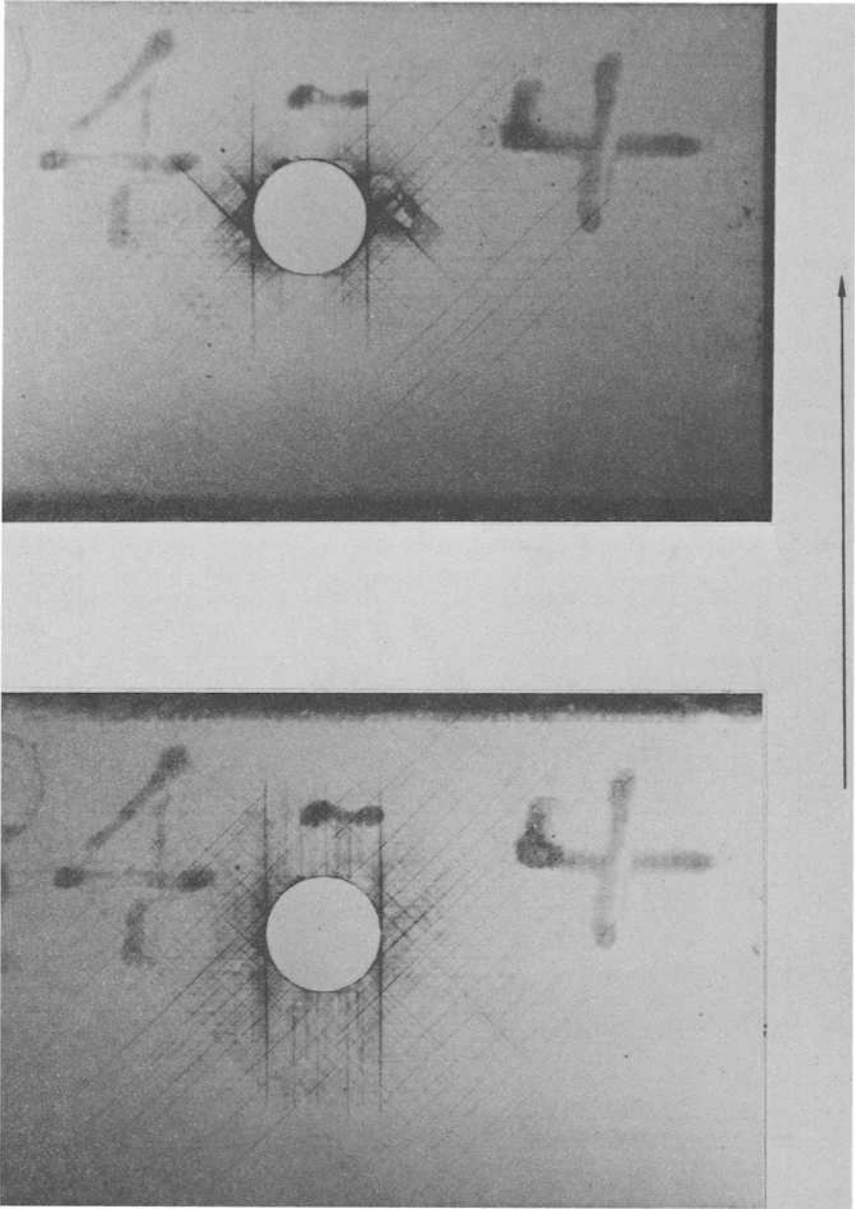


FIG. 8—X-ray radiography of Specimen R4-4 ( $\pm 45/0/90/0_2/\pm 45$ )<sub>s</sub> laminate, after 2000 and 5000 cycles tested at  $R = -1$ ,  $\sigma_{\min} = -362$  MPa ( $-52.5$  ksi). Specimen failed after 8610 cycles.

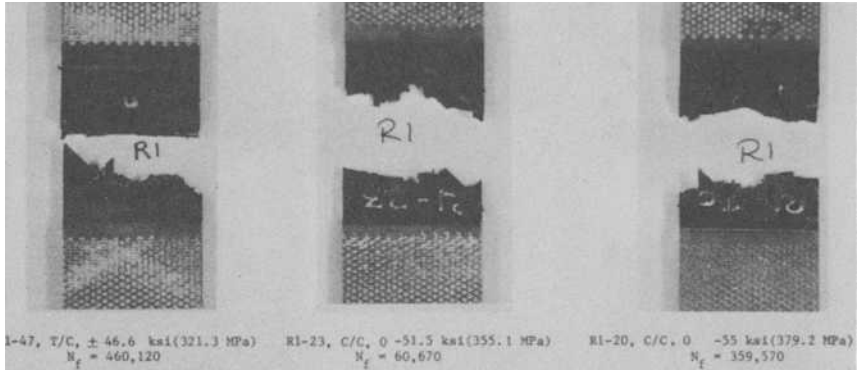


FIG. 9—Failure mode observed in Laminate 1 under constant amplitude fatigue loading.

The radial component of the shear stress,  $\tau_{rz}$ , has a high value at 90 deg from the loading, which is, however, very localized. The interlaminar stresses between various plies of the laminates were obtained from the finite element analysis. The maximum interlaminar stresses obtained for Laminate 1 ( $0/\pm 45/90/0_2/\pm 45$ ), are shown in Table 2. It is seen that interlaminar normal stress ( $\sigma_z$ ) is about 66 percent of the maximum shear stress ( $\tau_{rz}$ ) and occurs at a location different from that where shear stresses are high.

Similar analysis has been performed on all four laminates tested in the present research program. The maximum interlaminar stresses at various locations in Laminate 3 ( $90/0/\pm 45/0_2/\pm 45$ ), are shown in Table 3. Here, the

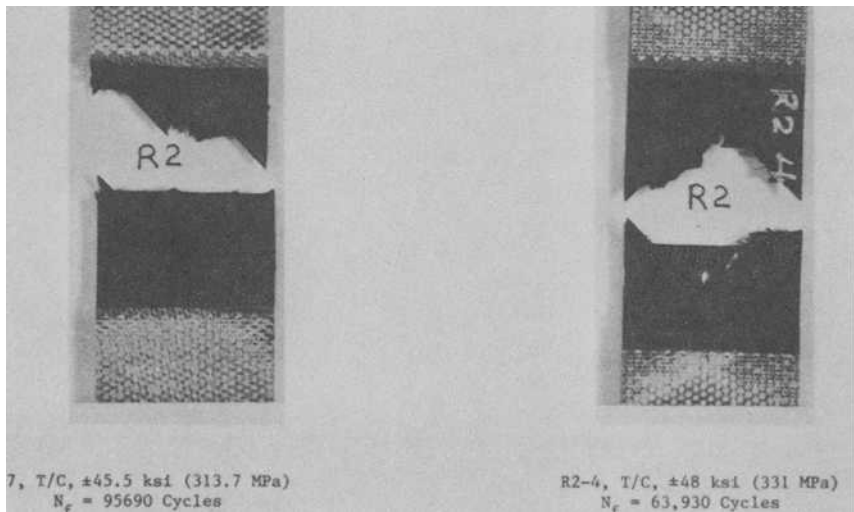


FIG. 10—Failure mode observed in Laminate 2 under constant amplitude fatigue loading.

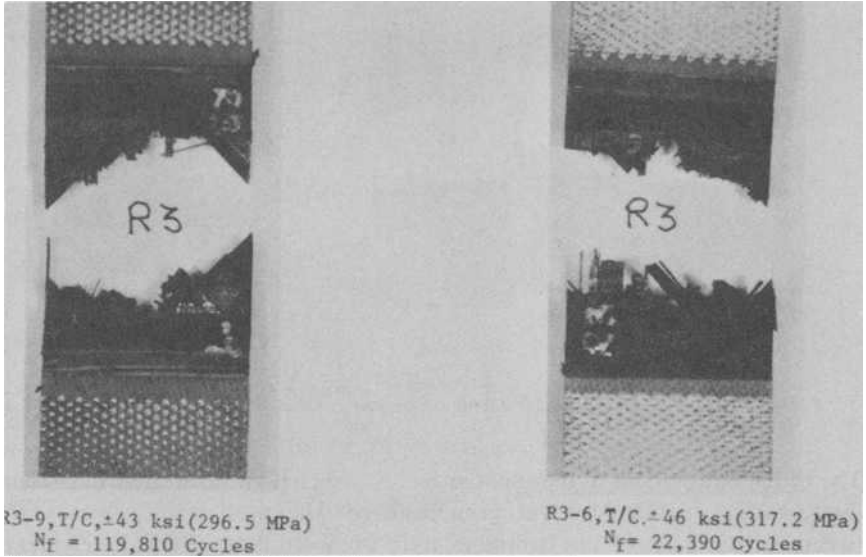


FIG. 11—Failure mode observed in Laminate 3 under constant amplitude fatigue loading.

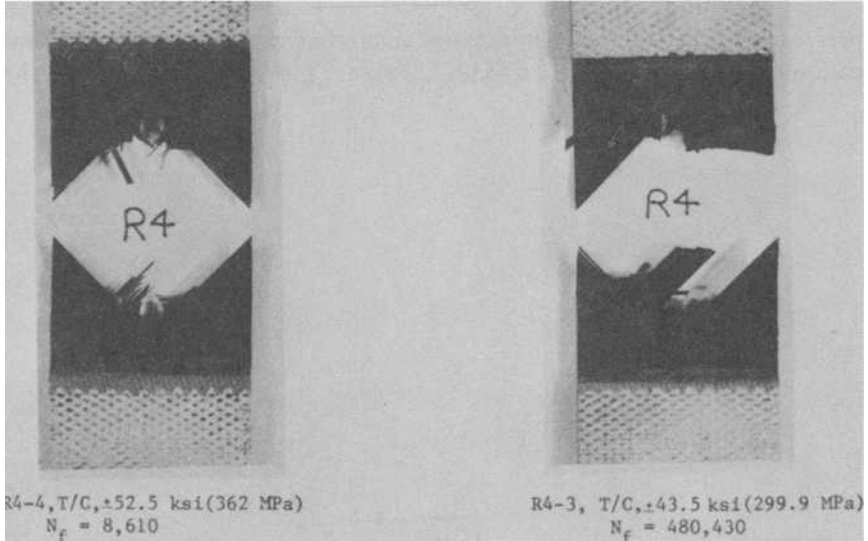


FIG. 12—Failure mode observed in Laminate 4 under constant amplitude fatigue loading.

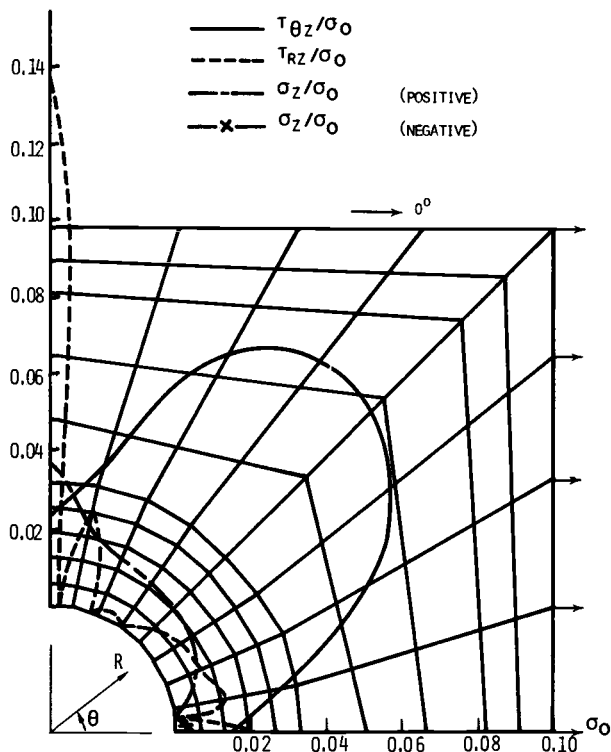


FIG. 13—Interlaminar stresses in the  $(0/\pm 45/90/0_2/\pm 45)_s$  laminate at midplane.

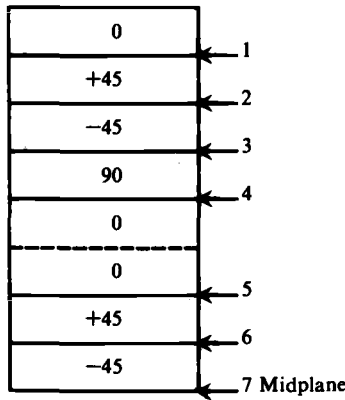
maximum interlaminar normal stresses are small compared to interlaminar shear stresses. Similar interlaminar stresses for Laminates 2 and 4 have been obtained and are reported in Ref 16.

### Discussion of Results

The maximum interlaminar stress in Laminate 1 is  $\tau_{rz}$  between the  $+45$  and  $-45$ -deg plies (interface 2) at  $\theta = 90$  deg, perpendicular to the loading direction; hence, the analysis suggests that the damage will initiate at right angles to the loading direction. Subsequent growth of the damage is influenced by the interlaminar stresses in the damaged specimens. The X-ray radiography pictures shown in Figs. 2 to 4 at  $R = -1$  and  $-\infty$  indicate that the damage initiates at a right angle to the loading direction and subsequently propagates along the loading direction. The interlaminar stress analysis of Laminates 2 and 3 indicates very small normal stresses. Interlaminar shear stresses are predominant, suggesting that the delamination in these laminates may be initiated by shear stresses. As seen in Table 3, the maximum interlaminar shear stresses ( $\tau_{\theta z}$ ) occur at  $45$  deg (ply interfaces 1 and 6); hence, the delaminations will most probably initiate along these directions. The distri-

TABLE 2—Location of maximum interlaminar stresses in Laminate 1 (0/±45/90/0<sub>2</sub>/±45)<sub>s</sub>.

Interface	$\tau_{\theta z}/\sigma_0$		$\tau_{rz}/\sigma_0$		$\sigma_z/\sigma_0$	
	Maximum Value	$\theta^0$ Location	Maximum Value	$\theta^0$ Location	Maximum Value	$\theta^0$ Location
1	-0.0911	56.25	0.0490	90	0.0286	56.25
2	-0.0548	56.75	0.1519	90	0.0553	90
3	0.0638	56.25	0.0633	90	0.1043	90
4	0.0377	67.50	-0.0695	90	0.0926	90
5	-0.1116	56.25	0.0377	22.50	0.0553	78.75
6	-0.1310	56.25	0.1024	90	0.0548	90
7 (midplane)	-0.0858	56.25	0.1359	90	0.0767	90



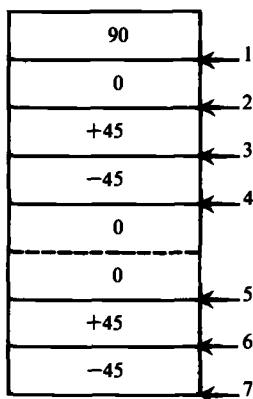
bution of interlaminar shear stress  $\tau_{\theta z}$ , shown in Fig. 13, indicates the shear stress distribution to have a semielliptical shape and a large value over a considerable distance around the periphery of the hole. Hence, the delaminations under interlaminar shear stress  $\tau_{\theta z}$  will tend to initiate over a large area around the hole. The observed initiation of delamination in Laminates 2 and 3 (Figs. 5 and 6) has a shape similar to the distribution of  $\tau_{\theta z}$  shown in Fig. 13, in the sense that delaminations spread around the periphery of the hole, contrary to Laminate 1, where the delaminations are confined to a small strip of a width slightly larger than the diameter of the hole. Figures 5 and 6 also indicate the entire width of the specimen to be delaminated in Laminates 2 and 3 prior to failure. In Laminate 1, only a small strip was delaminated prior to failure.

The interlaminar stress analysis of Laminate 4 shows interlaminar shear and normal stresses to be of the same order of magnitude. The damage in such a laminate will initiate under shear and normal stresses around the hole. Figure 7 indicates that the damage grows around the hole and along the loading direction.

The interlaminar stress analysis indicates the stresses to be significantly

TABLE 3—Location of maximum interlaminar stresses in Laminate 3 (90/0/±45/0<sub>2</sub>/±45)<sub>s</sub>.

Interface	$\tau_{\theta z}/\sigma_0$		$\tau_{rz}/\sigma_0$		$\sigma_z/\sigma_0$	
	Maximum Value	$\theta^0$ Location	Maximum Value	$\theta^0$ Location	Maximum Value	$\theta^0$ Location
1	-0.0496	45	-0.0518	90	-0.0084	90
2	-0.1174	45	-0.0347	67.50	-0.0161	90
3	-0.0866	45	0.1099	90	-0.0191	45
4	-0.0271	33.75	-0.0177	45	0.0333	90
5	-0.0855	45	-0.0359	22.50	-0.0220	45
6	-0.1183	56.25	0.1013	90	0.0224	90
7	-0.0779	56.25	0.1323	90	0.0447	90



large between several plies in all four laminates, and hence the delaminations should occur between several plies in the composite laminates. Experimental observations on the four laminates have shown similar behavior. The interlaminar stress analysis of Laminate 1 (Table 2) shows significant interlaminar shear stresses between the 0 and 45-deg plies near the surface; hence, the delaminations nearest to the surface will be between these plies, as shown by experimental results. Table 3 shows significant interlaminar shear stress  $\tau_{\theta z}$  between 0 and +45-deg plies near the surface of the specimen for Laminate 3. Hence, the delaminations nearest to the surface will be at these locations for this laminate. This was indicated by the postfailure examinations of the specimen. The location of delaminations near the surface in Laminates 2 and 4 as observed experimentally also was shown by interlaminar stress analysis.

The interlaminar stress analysis of laminates only suggests the initiation of damage. Subsequent propagation of damage depends on the type of loading (for example, static or fatigue; tension or compression) and the instantaneous configuration of the damage. In order to explain damage growth in composites analytically, it is necessary that the stress analysis method should incorporate these elements.

## Conclusions

1. Damage growth in composite laminates depends on the stacking sequence. The damage growth may completely change direction and location with change in stacking sequence.
2. The failure mode in composites changes with change in stacking sequence.
3. The location of delamination and matrix cracking for the different laminate stacking sequences investigated appeared to coincide with positions of highest interlaminar shear or normal stress predicted by a finite element approximate analysis.

## Acknowledgment

The work reported here was performed under contract from the Naval Air Development Center, Warminster, Pennsylvania. Special thanks to contract monitor L. Gause for useful discussions during the course of the investigations.

## References

- [1] Sendeckyj, G. P., "Some Observations on Fracture Behavior of Advanced Fiber-Reinforced Laminates," *Proceedings of 12th Annual Meeting of Society of Engineering Science*, M. Stern, Ed., University of Texas at Austin, Austin, Tex., 1975.
- [2] Kanninen, M. F., Rybicki, E. F., and Brinson, H. F., *Composites*, Jan. 1977, pp. 17-22.
- [3] Corten, H. T. in *Fracture Volume VII*, H. Liebowitz, Ed., Academic Press, New York, 1972, p. 676.
- [4] Zweben, C. in *Analysis of the Test Methods for High Modulus Fibers and Composites, ASTM STP 521*, American Society for Testing and Materials, 1973, pp. 65-97.
- [5] Rosenfeld, M. S. and Huang, S. L., "Failure Characteristics of Graphite/Epoxy Laminates under Compression Loading," presented at American Institute of Aeronautics and Astronautics/American Society of Mechanical Engineers 18th Structural Dynamics Conference, San Diego, Calif., 21-23 March 1977.
- [6] Ryder, J. T. and Walker, E. K., "Ascertainment of the Effect of Compression Loading on the Fatigue Lifetime of Graphite/Epoxy Laminates for Structural Applications," AFML-TR-76-241, Air Force Materials Laboratory, Dayton, Ohio, Dec. 1976.
- [7] Ramani, S. V. and Williams, D. P. in *Failure Modes in Composites III*, The Metallurgical Society of the American Institute of Mining Engineers, 1976, pp. 115-140.
- [8] Ramani, S. V. and Williams, D. P. in *Fatigue of Filamentary Composite Materials, ASTM STP 636*, 1977, pp. 27-46.
- [9] Roderick, G. L. and Whitcomb, J. D. in *Fatigue of Filamentary Composite Materials, ASTM STP 636*, 1977, pp. 73-88.
- [10] O'Brien, T. K. and Reifsnider, K. L., *Journal of Testing and Evaluation*, Vol. 5, No. 5, Sept. 1977, pp. 384-393.
- [11] Kulkarni, S. V., McLaughlin, P. V., Pipes, R. B., and Rosen, B. W. in *Composite Materials: Testing and Design (Fourth Conference), ASTM STP 617*, American Society for Testing and Materials, 1977, pp. 70-92.
- [12] Reifsnider, K. L. and Talug, A., *International Journal of Fatigue*, Jan. 1980, pp. 3-11.
- [13] Pagano, N. J. and Pipes, R. B., *Journal of Composite Materials*, Vol. 5, 1971, pp. 50-57.
- [14] Daniel, I. M., Rowlands, R. E., and Whiteside, J. B., *Experimental Mechanics*, Jan. 1974, pp. 1-9.
- [15] Whitney, J. M. and Kim, R. Y. in *Composite Materials: Testing and Design (Fourth Conference), ASTM STP 617*, American Society for Testing and Materials, 1977, pp. 229-242.
- [16] Ratwani, M. M. and Kan, H. P., "Compression Fatigue Analysis of Fiber Composites," Report No. NADC-78049-60, Naval Air Development Center, Warminster, Pa., Sept. 1979.

# Damage Mechanism and Life Prediction of Graphite/Epoxy Composites

---

**REFERENCE:** Badaliance, R. and Dill, H. D., "Damage Mechanism and Life Prediction of Graphite/Epoxy Composites," *Damage in Composite Materials, ASTM STP 775*, K. L. Reifsnider, Ed., American Society for Testing and Materials, 1982, pp. 229-242.

**ABSTRACT:** This paper describes observation of fatigue damage mechanism in composites subjected to compression dominated fatigue loading, formulation of a damage-indicating parameter based on the intralaminar microcracking of the resin, and its application in conjunction with a linear fatigue damage model to predict spectrum life of graphite/epoxy composite laminates.

**KEY WORDS:** damage mechanism, resin microcracks, graphite/epoxy laminates, damage-indicating parameter, linear residual strength reduction, constant amplitude fatigue, spectrum fatigue life prediction, composite materials

The use of composite materials in cyclic load carrying structural members has raised questions of their durability. Recent investigations into the fatigue behavior of composite materials have concentrated on the experimental determination of damage mechanisms and failure modes.<sup>2</sup>

In this work, enhanced X-ray radiography was used to facilitate observation of fatigue damage accumulation in graphite/epoxy laminates. Tetrabromoethane (TBE)-enhanced X-ray radiographs show that the damage progression sequence begins with matrix cracking at the fiber-matrix interface within a ply, followed by delamination in areas which have accumulated extensive matrix cracking. Delamination and interlaminar matrix cracking interact to produce eventual fatigue failure.

These observations led to the development of a damage correlation parameter based on strain energy density factor. In this approach to quantifying fatigue life degradation in composites, it is assumed that the matrix is the weak link of the system. The lamina is modeled as an isotropic layer of resin containing crack-like flaws sandwiched between semi-infinite orthotropic

<sup>1</sup> Technical specialist-Technology and branch chief-Technology, respectively, McDonnell Aircraft Co., McDonnell Douglas Corp., St. Louis, Mo. 63166.

<sup>2</sup> Saff, C. R., "Compression Fatigue Life Prediction Methodology for Composite Structures—Literature Survey," NADC-78203-60, Naval Air Development Center, June 1980.

plates representing combined fibers and matrix. A damage correlation parameter was developed by summing the strain energy density factors for each ply, normalized to laminate ultimate strength. This parameter is used in conjunction with linear fatigue damage and linear residual strength reduction models to predict spectrum fatigue life of center-hole specimens of AS/3501-6 graphite/epoxy laminates.

**Methodology Development Test Program**

The material was Hercules AS/3501-6 graphite/epoxy. Three panels of different layups—fiber dominated (48/48/4), matrix dominated (16/80/4), and intermediate (25/67/8)—were fabricated from 10.4 mil prepreg. The first number in the parenthesis is the percentage of 0-deg plies, the second number is the percentage of  $\pm 45$ -deg plies, and the third number is the percentage of 90-deg plies in the laminate. The stacking sequences of these three layups are:  $[(+45, -45, 0, 0)_3, 90, (0, 0, -45, +45)_3]$ ,  $[(+45, -45, 0, +45, -45)_2, (+45, -45, 90, -45, +45), (-45, +45, 0, -45, +45)_2]$ , and  $[(+45, 0, -45, 0, +45, 90, -45, 0, +45, -45, -45, +45)_5]$ . The test specimen geometry is shown in Fig. 1. This single-hole test specimen does not require tab ends, since the stress concentration created by the fastener hole is the fatigue critical area. The specimens were tested in an MTS closed loop system, with protruding-head close-tolerance bolts installed into the fastener hole. The nut was torqued finger-tight. Antibuckling guides were not used in compression testing, since the specimen's dimensions were configured to preclude buckling.

A total of 112 specimens were tested. Eighteen specimens were statically tested to determine ultimate strength, 78 were tested in constant-amplitude fatigue at different stress ratios ( $R = f_{min}/f_{max}$ ), and 16 were subjected to spectrum fatigue loads.

Ultimate strength test results are presented in Table 1. Results of constant-amplitude fatigue tests (Fig. 2) indicate that the life of graphite/epoxy com-

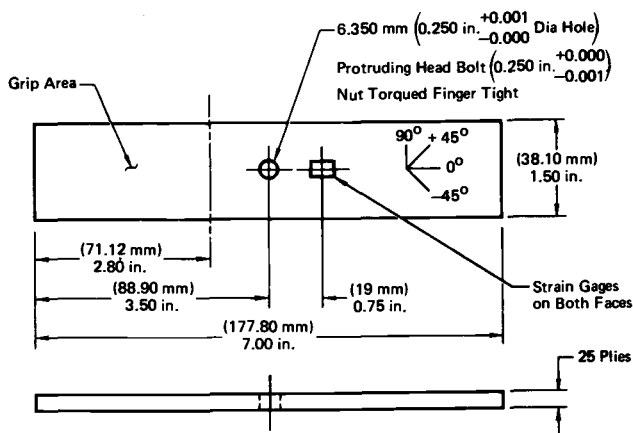


FIG. 1—Test specimen.

TABLE 1—Ultimate strength results.

Layup	48/48/4			25/67/8			16/80/4		
	Strain, $\mu\text{mm/mm}$	Stress, MPa	Stress, ksi	Strain, $\mu\text{mm/mm}$	Stress, MPa	Stress, ksi	Strain, $\mu\text{mm/mm}$	Stress, MPa	Stress, ksi
Compression	8 520	551.6	80.00	9 550	445.7	64.64	11 190	365.9	53.08
	7 770	558.7	81.03	9 565	445.7	64.64	9 440	325.3	47.18
	7 740	523.3	75.89	9 080	420.0	60.90	10 665	355.4	51.54
Average	8 010	544.7	79.00	9 398	437.1	63.39	10 432	348.9	50.60
Tension	5 835	449.1	65.13	5 435	268.9	39.00	7 350	261.7	37.95
	5 735	435.0	63.08	6 100	309.4	44.87	7 175	259.9	37.69
	5 345	396.0	57.44	6 010	309.4	44.87	7 355	265.2	38.46
Average	5 638	426.6	61.87	5 848	295.9	42.91	7 293	262.6	38.08

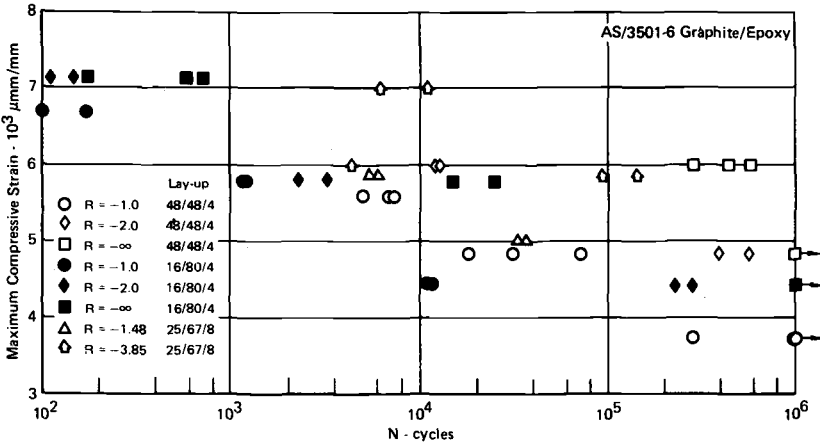


FIG. 2—Methodology development test program (constant amplitude results).

posite laminates is dependent upon the layup and the stress ratio. In order to reduce or eliminate stress-ratio testing for every layup that might be considered in design, a correlative methodology described in the following section was developed. X-ray radiography was used to aid the methodology development through observation of fatigue damage progression.

A number of specimens was examined nondestructively by X-ray photography to observe the type and location of damage during different stages of their fatigue life. Since the regular X-ray images of damaged specimens do not provide discernible contrast for examination, the test specimens were coated with a mixture of 25 percent TBE and 75 percent dye penetrant (ZL-2A). The fluid first was applied at the edges of the specimens for the purpose of detecting edge delaminations. The fluid then was applied at the fastener hole.

Figure 3 contains X-ray photographs of a fiber dominated (48/48/4) specimen where both the edges and fastener hole were coated with the TBE and ZL-2A fluid. The figure shows damage around the hole. The white lines in Fig. 3a indicate matrix cracks that are filled with the TBE and ZL-2A fluid. The distribution of matrix cracking through the thickness can be seen in Fig. 3b. Figure 4 contains TBE enhanced X-ray photographs of another fiber dominated specimen at two different stages of fatigue life. Figures 4a and b demonstrate the progression of matrix cracking from a quarter of the specimen's fatigue life to half life. Figure 5 contains X-ray photographs of two matrix dominated (16/80/4) specimens fatigued under similar conditions. The edges and fastener holes of both specimens were coated with TBE and ZL-2A fluid. The similarity of the two photographs indicates that the pattern of matrix cracking is a repeatable process. These figures indicate that the damage is concentrated at the hole.

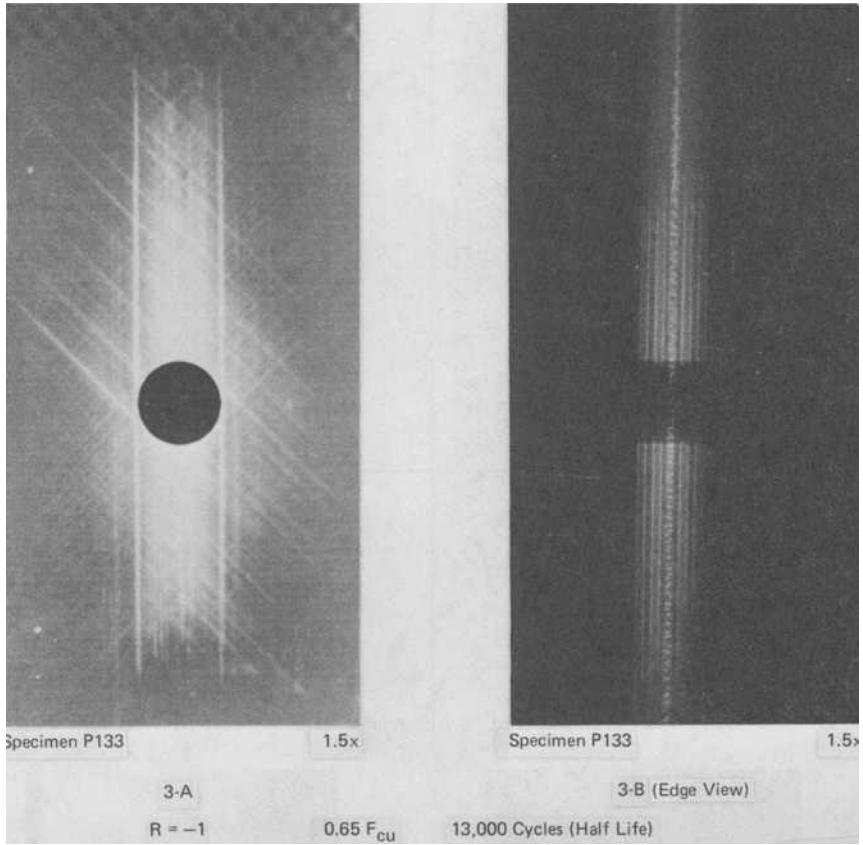


FIG. 3—X-ray photographs of fiber dominated layup with penetrant applied to specimen edges and hole.

**Life Prediction Methodology**

The data presented in Fig. 2 indicate that to predict the fatigue life of composite structures it is essential to account for layup and stress-ratio variations. A damage correlation parameter was developed based on the concept of strain energy density factor.<sup>3</sup> The strain energy stored in a volume element ( $dV = dx dy dz$ ) of an isotropic material is

$$\frac{dU}{dV} = \frac{1}{2E} (\sigma_x^2 + \sigma_y^2 + \sigma_z^2) - \frac{\nu}{E} (\sigma_x \sigma_y + \sigma_y \sigma_z + \sigma_z \sigma_x) + \frac{1}{2\mu} \times (\tau_{xy}^2 + \tau_{yz}^2 + \tau_{zx}^2) \quad (1)$$

<sup>3</sup> Sih, G. C., *International Journal of Fracture Mechanics*, Vol. 10, 1974, pp. 305-321.

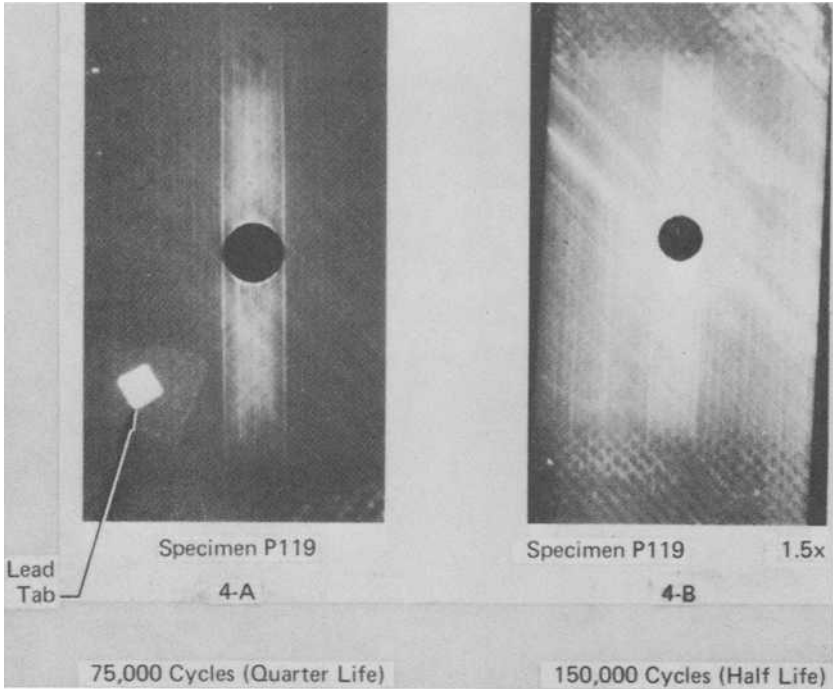
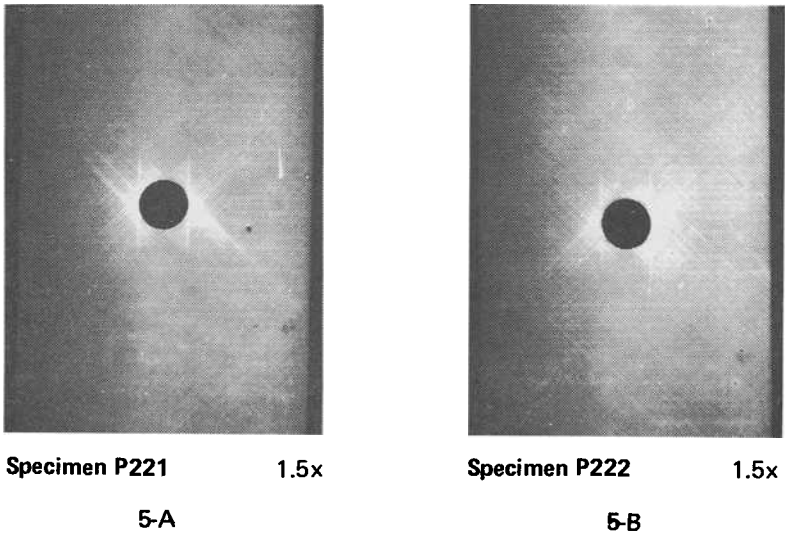


FIG. 4—X-ray photographs of fiber dominated layup at quarter and half life.



5,000 Cycles (Half Life)  
FIG. 5—X-ray photographs of matrix dominated layup for two specimens.

Substitution of stresses in terms of stress intensity factors results in the following simple relationship for strain energy density

$$\frac{dU}{dV} = \frac{S}{r} \quad (2)$$

where  $r$  is the distance from a crack tip, and  $S$  is a quadratic function in the form

$$S = a_{11}k_1^2 + 2a_{12}k_1k_2 + a_{22}k_2^2 + a_{33}k_3^2 \quad (3)$$

and is a measure of the intensity of the strain energy density field around the crack tip. The coefficients  $a_{ij}$  are

$$\begin{aligned} a_{11} &= \frac{1}{16\mu} \left[ (1 + \cos \theta) (\kappa - \cos \theta) \right] \frac{1}{\cos \omega} \\ a_{12} &= \frac{1}{16\mu} \left[ \sin \theta (2 \cos \theta - (\kappa - 1)) \right] \frac{1}{\cos \omega} \\ a_{22} &= \frac{1}{16\mu} \left[ (\kappa + 1) (1 - \cos \theta) + (1 + \cos \theta) (3 \cos \theta - 1) \right] \frac{1}{\cos \omega} \\ a_{33} &= \frac{1}{4\mu} \left( \frac{1}{\cos \omega} \right) \end{aligned} \quad (4)$$

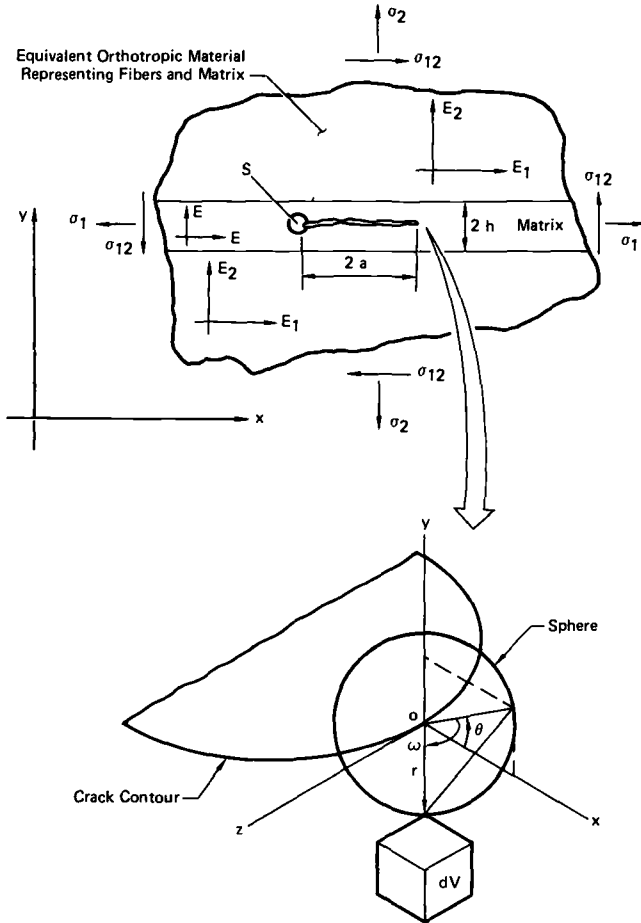
The elastic constant  $\kappa$  is equal to  $(3 - 4\nu)$  for plane strain and  $(3 - \nu)/(1 + \nu)$  for plane stress ( $\mu$  and  $\nu$  are shear modulus and Poisson's ratio, respectively). The angles  $\theta$  and  $\omega$  describe the crack trajectory and are defined in a special spherical coordinate system shown in Fig. 6.

An analytic model was developed with the assumption that the matrix is the weak link. This matrix is modeled as an isotropic layer of resin containing a through-the-thickness crack sandwiched between the edges of two semi-infinite orthotropic plates,<sup>4</sup> as shown in Fig. 6.  $E$  and  $\nu$  are the elastic constants of the resin, while  $E_1$ ,  $E_2$ ,  $\nu_{12}$ , and  $\mu_{12}$  are the elastic constants of the equivalent orthotropic material surrounding the resin strip of width  $2h$ . The subscripts 1 and 2 represent directions parallel and perpendicular to the ply fibers, respectively. The strip width  $2h$  is directly related to the fiber volume fraction. For low fiber volume fraction this width can be estimated to be

$$h = R \left( \frac{1}{2} \sqrt{\frac{\pi}{V_f}} - 1 \right) \quad (5)$$

where  $R$  is the fiber radius and  $V_f$  is the fiber volume fraction. However, for a graphite/epoxy composite system such as AS/3501-6 with high fiber volume

<sup>4</sup> Sih, G. C., Chen, E. P., Huang, S. L., and McQuillen, E. J., *Journal of Composite Materials*, Vol. 9, April 1975, pp. 167-186.



A Special Spherical Coordinate System

FIG. 6—Cracked lamina model.

fraction, the strip width  $2h$  is very small, hence the limiting value ( $h/a \rightarrow 0$ ) can be used.

The intensity of the crack tip stress field for this problem can be written as

$$\begin{aligned} k_1 &= \lambda_1 \sigma_2 \sqrt{a} \\ k_2 &= \lambda_2 \sigma_{12} \sqrt{a} \end{aligned} \tag{6}$$

where  $\sigma_2$  and  $\sigma_{12}$  are the normal and tangential stresses at the edge of the hole for a particular ply,  $a$  is half the crack length ( $a$  is assumed to be unity), and  $\lambda_1$  and  $\lambda_2$  are correction functions which depend on fiber spacing and elastic constants. Values of  $\lambda_1$  and  $\lambda_2$  for AS/3501-6 graphite/epoxy, calculated by the methodology of Sih, Chen, Huang, and McQuillen,<sup>4</sup> are

$$\lambda_1 = 0.2843$$

$$\lambda_2 = 0.0911 \tag{7}$$

Far field stresses  $\sigma_2$  and  $\sigma_{12}$  are obtained through lamination plate theory which assumes uniform strain distribution through the thickness of a laminate. This assumption reduces the three dimensional problem to a two dimensional one, which simplifies the formulation of the strain energy density factor  $S$ .

In the development of this preliminary model, for simplicity, it was assumed that the through-the-thickness crack grows parallel to adjacent fibers. This assumption permits omission of the interaction term  $2a_{12}k_1k_2$  from the strain energy density factor equation. The relationship for the simplified strain energy density factor is

$$S = a_{11}k_1^2 + a_{22}k_2^2 \tag{8}$$

Strain energy density factors for each ply are summed as a damage indicator parameter, and normalized with respect to ultimate compressive or tensile strength of the laminate to obtain the following relationship

$$\bar{S} = \left(\frac{f_i}{F_{u_i}}\right)^2 \sum_{n=1}^N (S_{\text{per ply}})_i + \delta_{ij} \left(\frac{f_j}{F_{u_j}}\right)^2 \sum_{n=1}^N (S_{\text{per ply}})_j \tag{9}$$

$i, j = \text{compression, tension}$

$$\delta_{ij} = \begin{cases} +1 & i \neq j \text{ (tension-compression)} \\ -1 & i = j \text{ (compression-compression)} \end{cases}$$

The parameter  $\bar{S}$  then was used to correlate constant-amplitude fatigue data for the three laminates. Results, shown in Fig. 7, indicate correlation of

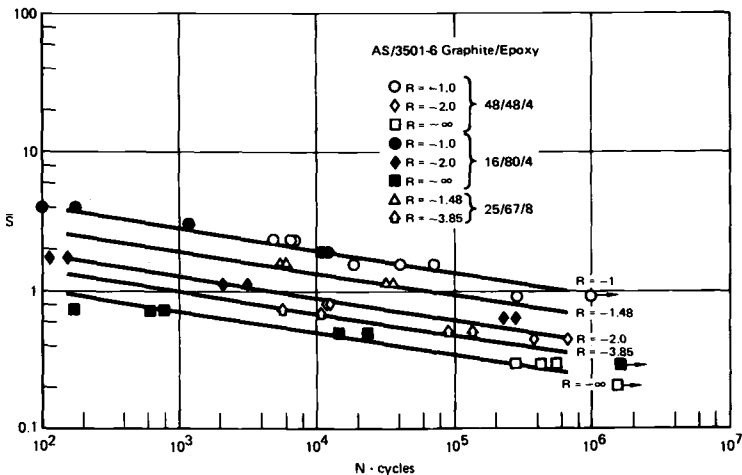


FIG. 7—Correlation of strain energy density with fatigue life.

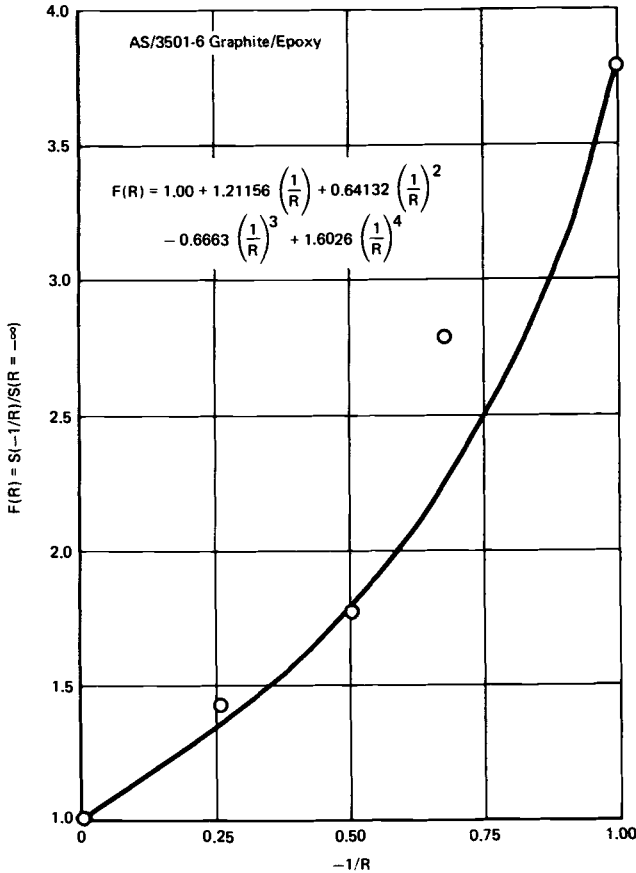


FIG. 8—Stress-ratio correction.

fatigue life for different layups for a given stress ratio  $-R$  and value of  $\bar{S}$ . Subsequently, an empirical relationship  $F(R)$  as shown in Fig. 8 was developed to account for  $R$ -ratio effect. This empirical relationship, when applied to the data presented in Fig. 7, resulted in a correlation of  $\bar{S}_{eq}$  and life that was independent of  $R$  ratio, as demonstrated in Fig. 9, where  $S_{eq} = S/F(R)$ . It is emphasized that  $\bar{S}_{eq}$  is used as a correlation parameter, not as a crack growth model.

This constant-amplitude predictive methodology then was used in conjunction with two linear fatigue damage models to predict spectrum fatigue life. The fatigue damage models used are linear strength reduction<sup>5</sup> and Miner's rule. The linear strength reduction model shown in Fig. 10 is a modi-

<sup>5</sup> Broutman, L. J. and Sahu, S. in *Composite Materials: Testing and Design (Second Conference)*, ASTM STP 497, 1972, pp. 170-188.

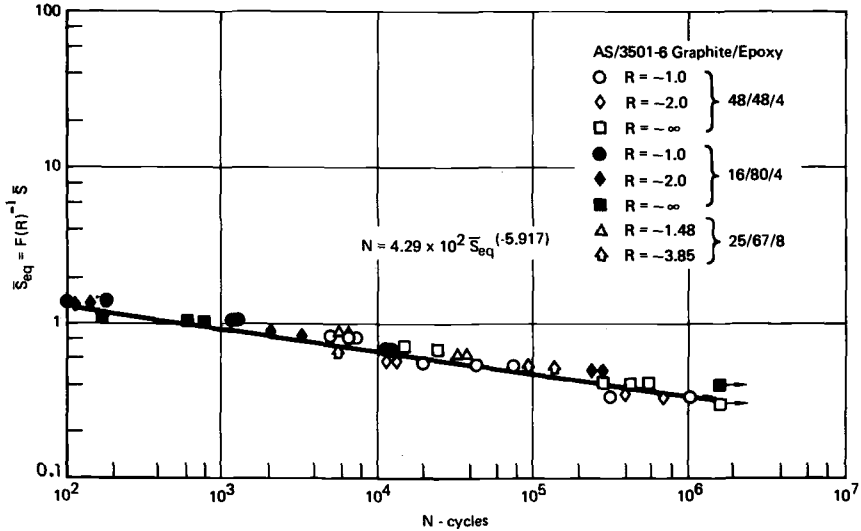


FIG. 9—Correlation of equivalent strain energy density with fatigue life.

fied version of Miner’s rule, with the assumption of a linear reduction in the residual compressive strength due to cyclic loading.

The linear strength reduction model in conjunction with the normalized strain energy density factor was used to predict fatigue lives of three different layups subjected to the spectrum loads represented in Fig. 11. The increased tension spectrum has a maximum tension load approximately two thirds of the maximum compression load. Correlations of test results and predictions

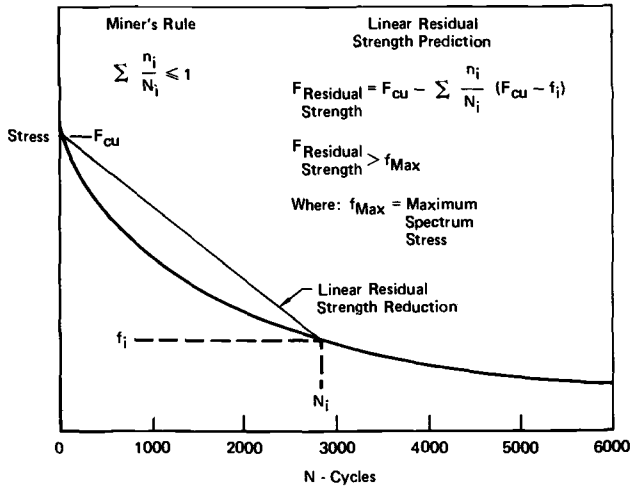


FIG. 10—Linear fatigue damage models.

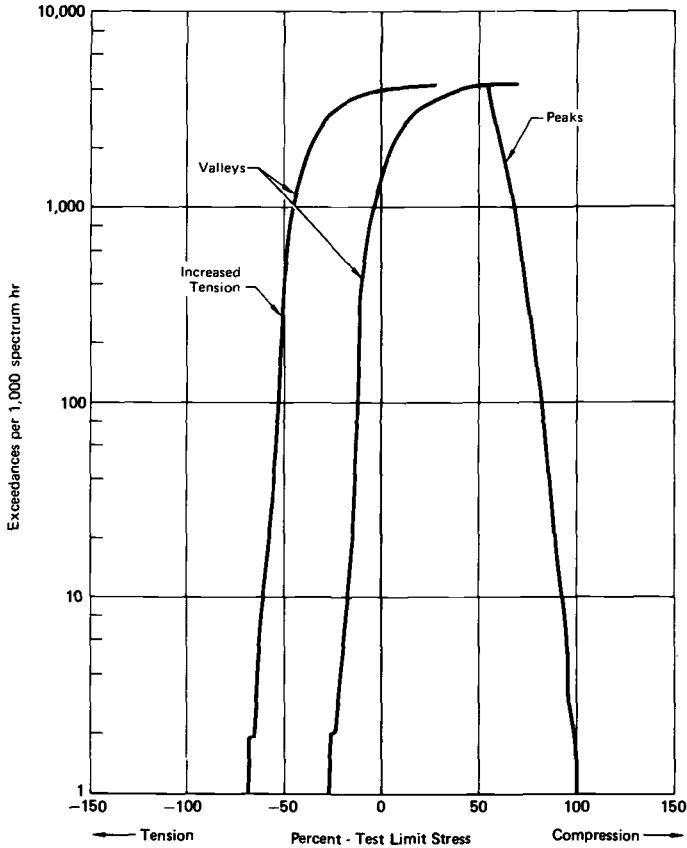


FIG. 11—Methodology development test spectra.

are shown in Fig. 12 along with the experimental data. The comparison between the linear strength reduction model and Miner's rule for the matrix dominated layup subjected to increased tension spectrum is shown in Fig. 13. This comparison shows Miner's rule to be substantially unconservative for higher values of test limit stress.

### Summary

Constant-amplitude fatigue data for AS/3501-6 graphite/epoxy was used to develop life prediction methodology. The correlation parameter  $\bar{S}_{eq}$  was developed to collapse constant-amplitude data for different laminates and stress ratios onto a single line, thus providing the means to account for the large range of stress ratios that exists in a fatigue load spectrum. In the development of  $\bar{S}_{eq}$  the dominant damage mechanism was assumed to be ma-

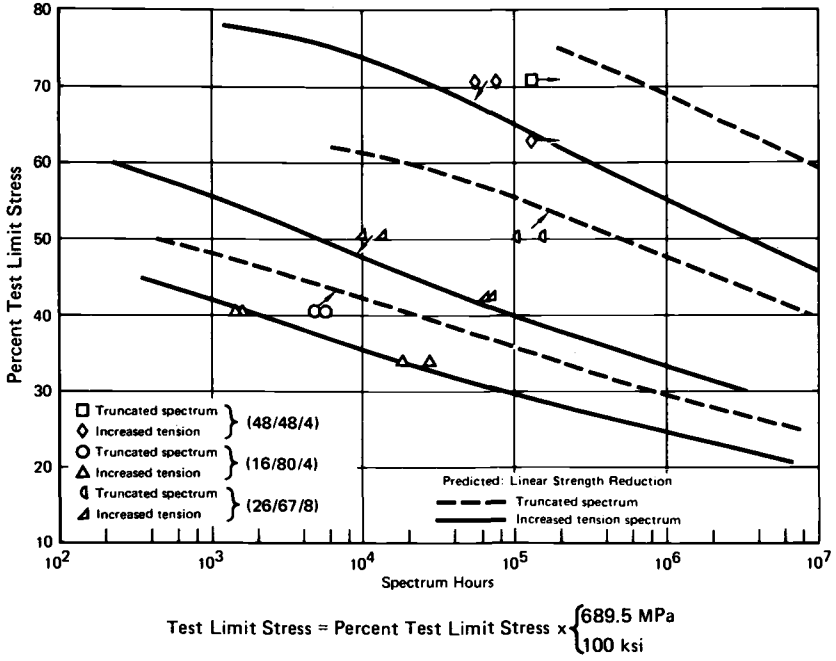


FIG. 12—Methodology development test program—results of spectrum fatigue tests.

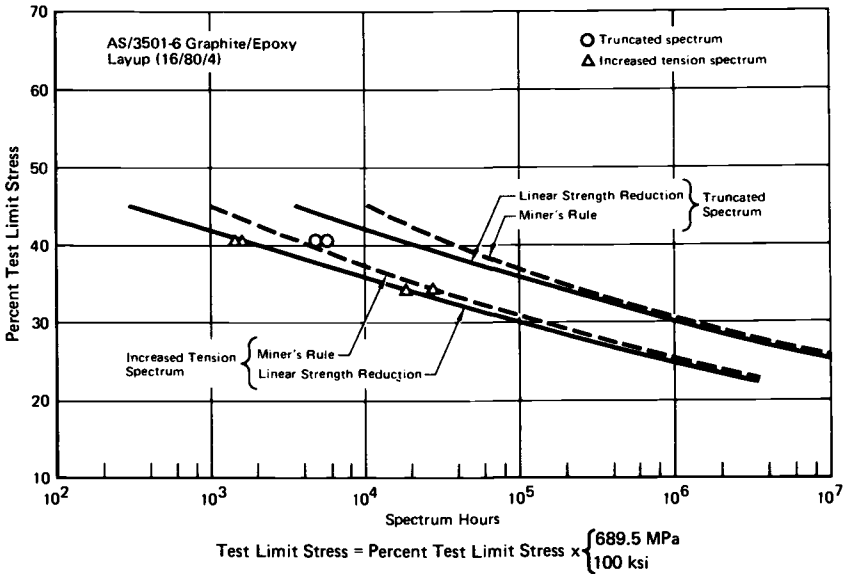


FIG. 13—Comparison of linear strength reduction and Miner's rule predictions.

trix cracking, based on the physical observation of fatigue damaged laminates. The life predictions methodology then was used to predict spectrum fatigue life of notched laminates, and results were compared with experimental data. Spectrum prediction accuracy is dependent on the validity of the linear residual strength reduction model.

# What Is Fatigue Damage?

---

**REFERENCE:** Fong, J. T., "What Is Fatigue Damage?", *Damage in Composite Materials*, ASTM STP 775, K. L. Reifsnider, Ed., American Society for Testing and Materials, 1982, pp. 243–266.

**ABSTRACT:** A conceptual definition of fatigue damage is proposed to assist in the selection of measurement techniques and parameters for correlating damage with fatigue life. To illustrate the concept, a critical review of some typical damage parameters for composite materials is given. A survey of some new techniques for damage monitoring, including the small angle neutron scattering (SANS) method, is presented and discussed. Pitfalls in damage modeling are illustrated with examples drawn from the literature. A summary of an ASTM E9.01 panel study on fatigue damage and research opportunities in the 1980's is presented.

**KEY WORDS:** composite materials, exo-electron emission, fatigue damage, materials science, mathematical modeling, microstructure, nondestructive evaluation, nonlinear modeling, optical holography, positron annihilation small angle neutron scattering, X-ray diffraction

## Fatigue, Fatigue Research, and Fatigue Damage

Fatigue is an interdisciplinary subject. The question, "What is fatigue damage?", has been under extensive study by researchers over the last two decades. Depending on who asks the question and in what context the question arises, a reasonable answer may take anywhere from a one-page essay to a lengthy report. Since research is still going on, no answer at this time may be considered complete or noncontroversial. Nevertheless, in my capacity both as a fatigue researcher and the immediate past chairman of the ASTM Subcommittee E9.01 on Fatigue Research, I gladly accept the invitation of the organizing committee to address the question and attempt an answer to stimulate discussion.

I would like to begin with a few words on fatigue and fatigue research. Most people learn from experience that nothing lasts forever and every structure or component we build possesses a finite service life. To avoid unexpected or premature failures which often carry economic or safety implications, it is imperative that a method exist to provide an estimate of that lifetime under a set of "normal" and "extreme" service conditions. Before 1960, when our techniques for probing the microstructures of a material

<sup>1</sup> Physicist (Applied Mathematics), National Bureau of Standards, Washington, D.C. 20234.

specimen were still primitive, the lifetime of a structure or component was estimated by subjecting specimens to repeated applications of a typical load cycle, counting the number of cycles to failure ( $N_f$ ), and interpreting the data for a variety of loads and specimen geometries with a simple mathematical model. This laboratory simulation of failure under cyclic loadings led naturally to the concept of "fatigue," and the word was incorporated officially into the ASTM vocabulary in 1946 when Committee E9, the parent committee of E9.01, was founded to promote the development of fatigue test methods. Fatigue damage, as defined in those days, was simply  $1/N_f$  per cycle for whatever context  $N_f$  was measured.

Beginning in the early 1960's, an explosion of new instrumentation and concepts took place that altered the course of fatigue research. The availability of electron microscopes and sophisticated nondestructive techniques of probing the microstructure made it possible to monitor fatigue damage by direct methods. The use of computers in closed-loop testing and in large-scale numerical simulation of fatigue crack growth improved dramatically the engineer's ability to predict  $N_f$ . By 1978, when ASTM, the National Bureau of Standards (NBS), and the National Science Foundation (NSF) co-sponsored an international symposium on fatigue mechanisms [1],<sup>2</sup> the technical community through the 200-plus symposium participants was able to predict that, under a favorable funding climate in the 1980's, a breakthrough in understanding damage mechanisms and predicting fatigue life from direct measurements would be imminent. Strong interest in accelerating fatigue research in this direction was expressed again at two subsequent workshops in 1979 [2,3] and two more in 1980 [4,5].

Consequently, in attempting to answer the question on fatigue damage, I would like to share some of the excitement surrounding the current state of fatigue research. This I intend to accomplish in two stages. The first stage is to provide the reader with a conceptual definition of damage which could be used to assess the relative merits of existing and new damage parameters based on direct measurements. This is done in A Conceptual Definition of Damage. The power of the definition is illustrated in subsequent sections up to and including Pitfalls of Fatigue Damage Modeling, with emphasis on applications to composites. The second stage is to sketch the main findings of a 5-year-long ASTM E9.01 panel study entitled "Fatigue Damage: Physical Measurement and Research Opportunities in the 1980's." This study was initiated in 1975 under the auspices of ASTM Subcommittee E9.01 on Fatigue Research, and was conducted by a broad segment of knowledgeable scientists and engineers whose views were respected in the fatigue community. The major findings of the panel report, given in the section summarizing the study, are intended to complement my answer because they cover not only the technical but also the manpower and the research support aspects of the fatigue damage problem.

<sup>2</sup> The italic numbers in brackets refer to the list of references appended to this paper.

### A Conceptual Definition of Damage

Whether we are interested in a global or local definition of damage, it is necessary that the concept of  $N_f$ , the number of cycles to failure, be retained as a fundamental parameter. A large amount of data on  $N_f$  as a function of material variables, load and temperature variables, specimen geometry variables, etc., are already available in the open literature. To formulate a conceptual definition of damage, we introduce a nondimensional variable  $x$  which is defined as the ratio of  $n$ , the cycle number, to  $N_f$ , that is,  $x = n/N_f$ . We also introduce, without specifying how one measures damage, a nondimensional, nonnegative scalar quantity  $\Delta$ , to be called the damage parameter, with values between 0 and 1, such that  $\Delta$  is a function of  $x$  satisfying the following simple criteria

$$\Delta = f(x); \quad f(0) = 0; \quad f(1) = 1 \quad (1)^3$$

For convenience, we have suggested in these criteria the existence of an initial state that is "damage-free." It can be shown that this assumption is not restrictive and the conceptual nature of the damage definition is preserved if Eq 1 is changed to read  $f(0) = \alpha$ ,  $f(1) = 1 + \alpha$ , and  $\alpha$  is some measurable quantity characterizing the initial damage state of the material. We have adopted the nondimensional quantity  $1 + \alpha$  as a measure of the final damage state because most of us are interested in the net amount of damage a material can sustain during service, and we denote that amount symbolically as 1.

Let us now introduce a physical concept that is at the heart of the damage definition. If  $\Delta$  is indeed a state variable which changes with  $x$ , then it stands to reason to assume that the rate of change of  $\Delta$ , that is,  $d\Delta/dx$ , should depend strongly on the state variable  $\Delta$ . Without knowing anything about either the quantity  $\Delta$  or the relation between  $d\Delta/dx$  and  $\Delta$ , it is natural to postulate, as a first approximation, that the damage rate varies linearly with  $\Delta$

$$\frac{d\Delta}{dx} = k\Delta + k' \quad (2)$$

where  $k$  and  $k'$  are two constants of which only one is available as a free parameter to fit the experimental data. The solution to Eq 2 with Eq 1 is

$$\text{For } k \neq 0, \quad \Delta = f(x) = \frac{e^{kx} - 1}{e^k - 1} \quad (3)$$

<sup>3</sup>This definition is clearly restrictive in the sense that we assume (a) a single measurement is adequate to describe the state of a local region or the entire specimen, (b) there exists a failure state such that the measurement made for that state can be used to normalize the data for all cycle ratios between 0 and 1, and (c) within the context of this formulation, no provision is made for any dependence on stress, temperature, frequency, etc. As will become clear later in this paper, the underlying goal of introducing this conceptual definition is to provide a powerful screening tool for assessing the relative merits of measurement techniques for fatigue research. For specific applications, this definition undoubtedly needs further refinement.

For  $k \rightarrow 0$ , this solution has a limit given by  $\Delta = f(x) = (kx + \dots) / (k + \dots)$  or  $\Delta = x$ . This is the solution that corresponds to the ad-hoc definition of damage mentioned in the previous section where the damage per cycle,  $\Delta/n$ , equals  $x/n$  or  $1/N_f$ . A plot of the relation given by Eq 3 for typical values of  $k$  ranging from  $-4$  to  $+4$  is given in Fig. 1.

Let us consider three regimes of cycle ratio  $x$  to assist in the interpretation of Eq 3:

- Regime 1:  $0 < x < x_1$ . Remark: damage incubation period.<sup>4</sup>
- Regime 2:  $x_1 < x < x_2$ . Remark: damage sharing period.<sup>4</sup>
- Regime 3:  $x_2 < x < 1$ . Remark: damage runaway period.<sup>5</sup>

Assuming a typical value of  $x_1 = 0.2$ , we see from Fig. 1 that the curve associated with  $k = -4$  would yield a more sensitive damage parameter for Regime 1 than those associated with  $k = 2$  and 4. Similarly, if we take  $x_2$  to be 0.8 and again look at Fig. 1, the curve given by  $k = 4$  should be preferred over all others in selecting a damage parameter for Regime 3. The common thread in this discussion is the need to calibrate the sensitivity of each damage parameter or the associated measurement technique such that a range of applicability can be established for specific purposes. The fact that Eq 3 can be used to bring out this crucial feature of damage measurement is interesting in the sense that a single parameter  $k$  may serve as a guide in distinguish-

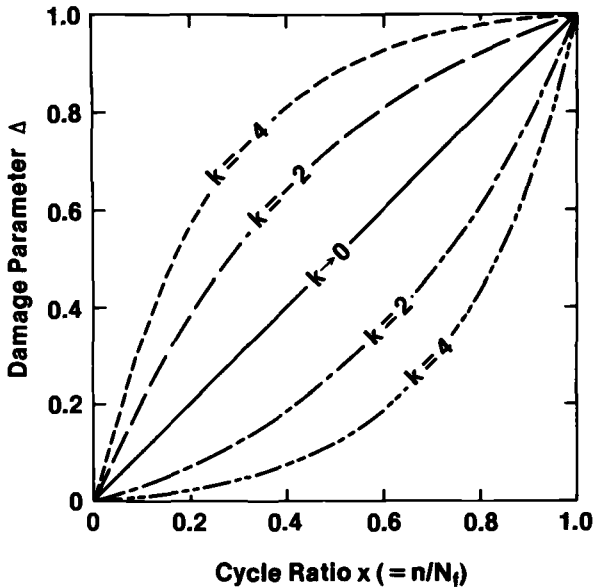


FIG. 1—A one-parameter family of damage versus cycle ratio relations.

<sup>4</sup> These two regimes, when combined, correspond to the so-called initiation stage.  
<sup>5</sup> This regime corresponds to the so-called propagation stage in the fatigue literature.

ing one damage parameter from another. In the next three sections, the conceptual definition of  $\Delta$  as displayed in graphical form in Fig. 1 will be employed to review critically the state of fatigue research and damage modeling.

### Damage Parameters for Composites: A Critical Review

In a review article by Stinchcomb and Reifsnider [6] presented at the 1978 ASTM-NBS-NSF symposium on fatigue mechanisms, the authors concluded that "fatigue behavior is one of the least understood areas of response, due, in part, to our incomplete knowledge of basic fatigue mechanisms in composite materials" [6, p. 786]. They based their conclusion on the observation that even though we have identified many failure mechanisms such as fiber fractures, fiber buckling, matrix cracking, matrix crazing, fiber debonding, ply delamination, etc., "a systematic investigation of the precise nature of damage development . . . has not been undertaken" [6, p. 777]. When asked by one of the symposium participants (H. Lamba of International Harvester, Hinsdale, Ill.) on fatigue mechanisms of a laminated composite, W. W. Stinchcomb gave a succinct explanation of the difficulties as shown in this excerpt from Ref 6, pp. 784-785:

*H. Lamba (discussion)*—Let us assume that we know the failure modes of polymers and the failure modes for fibers by themselves. Can we from mechanisms of polymers and from fibers quantify what effect the mechanisms will have when you put them together in the laminated composite?

*W. W. Stinchcomb*—We can get some idea of how the laminate is going to behave; however, when you have just properties of fibers or failure mechanisms of fibers and properties or failure mechanisms of matrix material, you have neither the fiber-matrix interface nor the properties of that interface. The way the interface interacts with the matrix and with the fibers is quite important in determining fatigue damage initiation in composite materials.

To illustrate the difficulties of characterizing the fiber-matrix interface, let us examine four typical damage parameters as reported in Refs 7, 8, and 9:

- $\Delta_1$  = normalized residual tensile strength;
- $\Delta_2$  = maximum damage length (over all damage lines recorded on X-ray films);
- $\Delta_3$  = number of debonded fibers (including fractions over a fixed region);
- and
- $\Delta_4$  = total resin crack length (over a fixed size of an optical micrograph).

In Fig. 2, we reproduce the data reported by Tanimoto and Amijima [7] who chose the ratio of the residual tensile strength  $\sigma$  to the ultimate strength  $\sigma_{ult}$  as a damage parameter ( $\Delta_1 = \sigma/\sigma_{ult}$ ,  $\sigma_{ult} = 222$  MPa) for a glass fiber reinforced plastic with 29.3 percent volume of glass content. Specimens were subjected to a uniaxial zero-tension fatigue loading with the maximum stress

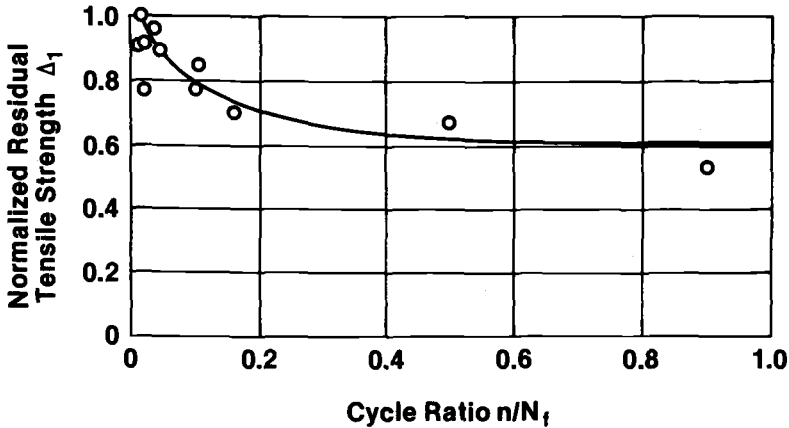


FIG. 2—Damage versus cycle ratio for a glass fiber reinforced plastic under zero-tension fatigue loading with  $\sigma_{\max}/\sigma_{ult} = 0.40$ ,  $\sigma_{ult} = 222$  MPa,  $N_f = 1.057 \times 10^6$ ,  $\Delta_1 = \sigma/\sigma_{ult}$ . After Ref 7.

amplitude equal to 40 percent of  $\sigma_{ult}$  at a frequency of 30 Hz. The measurement technique is destructive and macroscopic.

To assess whether  $\Delta_1$  as reported in Fig. 2 is a viable candidate of damage parameter for further fundamental research, let us make a simple transformation, that is

$$\Delta = \frac{1 - \Delta_1}{0.4} \quad (4)$$

This brings the curve in Fig. 2 to the type of curves exhibited in Fig. 1. The constant  $k$  characterizing the curve in Fig. 2 is estimated to be about  $-5$ . One may conclude at this point that  $\Delta_1$  satisfies the criterion of being a sensitive damage parameter for fatigue cycle Regime 1 (damage incubation period), but fails a consistency criterion owing to the large scatter of data in that regime.

In Fig. 3, we reproduce the data reported by Chang and his co-workers [8] who designed a graphite/epoxy laminate specimen with a center slit and monitored the development of damage lines near the slit by taking periodic X-ray pictures with the images enhanced through the introduction of an opaque additive. Of all the damage lines identified and measured on X-ray pictures, the maximum was taken as a measure of fatigue damage. The data in Fig. 3 were obtained for four laminates with ply orientation of  $(0/\pm 45)_{2S}$ , each of which was subjected to a zero-tension fatigue loading at 5 Hz with the maximum stress amplitude indicated in the figure. Even though the stress levels varied from 120 to 160 MPa (17.4 to 23.2 ksi), Chang et al [8] reported that their corresponding  $N_f$ 's stayed close to  $2 \times 10^6$  as shown in Fig. 3.

To evaluate  $\Delta_2$ , one can perform a transformation similar to Eq 4 for each of the four curves in Fig. 3, and the resulting values of  $k$  range from 0 to 1.5.

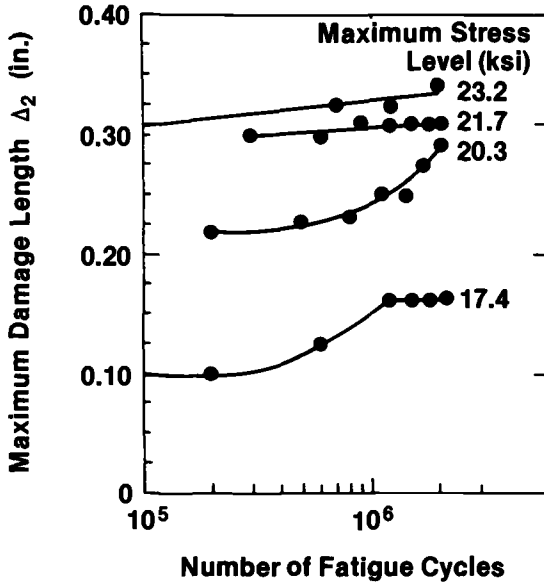


FIG. 3—Damage versus cycle for a series of graphite /epoxy laminate specimens under zero-tension fatigue loadings varying from 120 MPa (17.4 ksi) to 160 MPa (23.2 ksi). After Ref 8.

The parameter fails both the sensitivity criterion (because two of the four curves are too flat) and the consistency criterion if it is intended to apply over a range of stress levels of interest to the damage investigator. It is, however, important to recognize that the measurement technique is nondestructive and microscopic. A different choice of the damage parameter may yield a powerful tool that is both sensitive and consistent. In short, the technique is more promising than the parameter.

Using optical microscope and conventional photography, Owen and Howe [9] observed the development of damage at several sites of the polished edge of a glass chopped strand mat/polyester resin specimen during either fully reversed or zero-tension fatigue loadings at 1.7 Hz. For a fixed region at each site, the total number of debonded fibers including fractions estimated from the micrographs was recorded as damage parameter  $\Delta_3$ , and the total length of resin cracks, also over a fixed region, was measured as  $\Delta_4$ . We reproduce their data at six sites for two loadings in Fig. 4 and three loadings in Fig. 5 for a critical assessment. More details on the experiment [9] are omitted here for brevity.

Qualitatively speaking, the six curves in Fig. 4 suffer from a lack of adequate data in both Regime 1 (damage incubation period) and Regime 3 (damage runaway period) where the parameter  $\Delta_3$  appears to be sensitive enough to be useful. In addition, the measurement technique contains a judgmental component on the estimate of partial debonding, which could lead to a large variability due to human factors. The plotting of data from

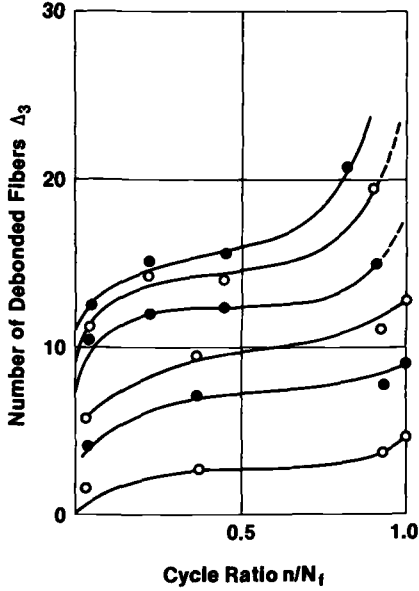


FIG. 4—Damage versus cycle ratio at three local sites for each of two glass/polyester resin specimens during different fatigue loadings. Black dot denotes fully reversed at 82.8 MPa and  $N_f = 2210$ . Open circle denotes zero-tension at 82.8 MPa maximum stress and  $N_f = 2700$ . After Ref 9.

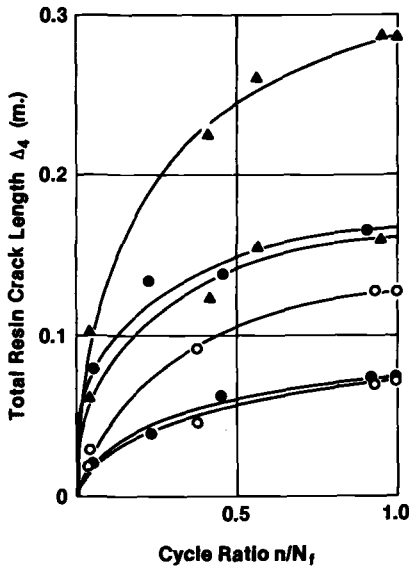


FIG. 5—Damage versus cycle ratio at two local sites for each of three glass/polyester resin specimens during different types of fatigue loadings. Black dot denotes fully reversed at 82.8 MPa and  $N_f = 2210$ . Open circle denotes zero-tension at 82.8 MPa maximum stress and  $N_f = 2700$ . Triangle denotes fully reversed at 55.2 MPa and  $N_f 2.6 \times 10^5$ . After Ref 9.

two different types of fatigue loading in Fig. 4 is more confusing than shedding any light on the curious conclusion by the authors that "the fatigue damage was substantially independent of stress conditions" [9, p. 1643]. Much more data would be needed to prove or disprove that assertion. For the data on hand, one cannot even assess whether  $\Delta_3$  is a viable candidate or not. What is obvious in Fig. 4 is the message that a composite may be locally homogeneous in microstructure geometry but is likely to be locally inhomogeneous in material properties and failure mechanisms.

The damage parameter  $\Delta_4$  as shown in Fig. 5 is the most promising of all examined so far. Using a transformation similar to Eq 4, we can interpret those six curves with a value of  $k$  close to  $-3$ . The parameter satisfies both the sensitivity and the consistency criteria and deserves recognition as a viable candidate for Regime 1 (damage incubation period).

### Direct Measurement of Damage: A Brief Survey

So far, we have examined four damage parameters for composite materials and found one, the total resin crack length, satisfying our sensitivity and consistency criteria. Buck and Alers [10] have put together an excellent review of new techniques for detection and monitoring of fatigue damage. These techniques have been applied to pure and not so pure materials including metal alloys, ceramics, and composites. In this brief survey, I have selected five surface and one volumetric measurement techniques, all nondestructive, to illustrate the concept developed in the Conceptual Definition of Damage section. The six techniques and the appropriate references describing them are given here:

1. Positron annihilation and lifetime measurement. See Ref 11.
2. Photo-stimulated exo-electron emission method. See Ref 12.
3. X-ray diffraction method. See Ref 13 and 14.
4. Optical correlation holographic method. See Ref 15.
5. Surface temperature measurement technique. See Ref 16.
6. Small angle neutron scattering (SANS) method. See Ref 17-21.

Eight additional damage parameters, denoted by  $\Delta_5$  through  $\Delta_{12}$ , are displayed in Figs. 6 through 16 to show the richness of the current advances in fatigue monitoring instrumentation. With the exception of the data on  $\Delta_5$  in Figs. 6 and 7, most of the information given in the plots is self-explanatory. The main thrust of this section is to discuss the typical output of each measurement technique and assess accordingly.

In Figs. 6 and 7, we reproduce the results reported by Tien and his co-workers [11] on measuring the positron lifetime in metals as a technique for studying surface defects. In Fig. 6, the first slope yields  $\tau_1$  (attributable to vacancies in the metal) and the second slope,  $\tau_2$  (associated with an increase in

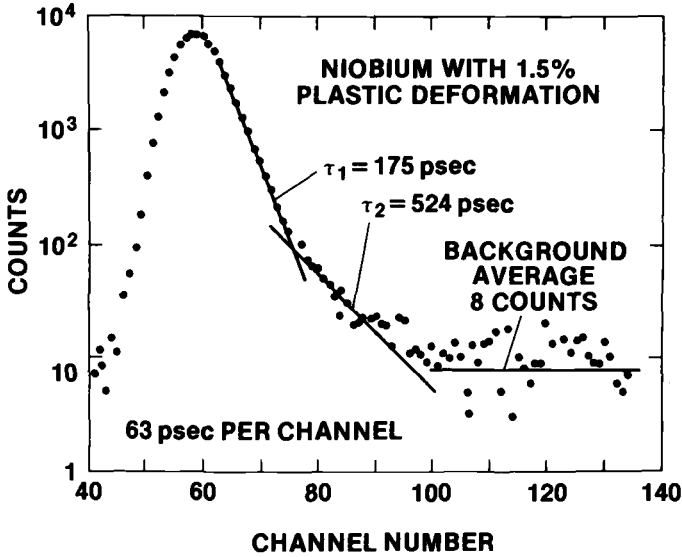


FIG. 6—Typical raw positron-lifetime data. The steep slope corresponds to  $\tau_1$  and the gentle one to  $\tau_2$ .  $\tau_2$  does not appear unless the specimen has been deformed. After Ref 11.

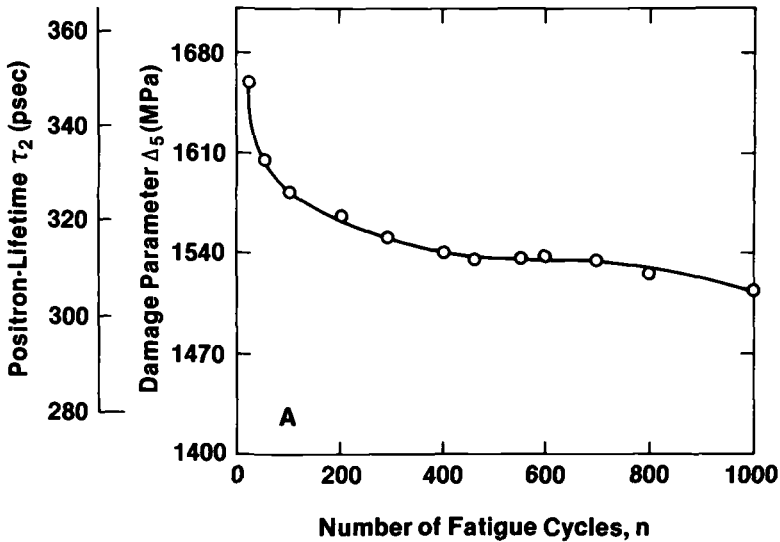


FIG. 7—Damage (stress range in a strain-controlled fatigue test) versus cycle of monocrystalline Mar-M-200 specimen at 2 percent total strain range, with a one to one correspondence between positron-lifetime and damage observed for different crystals. After Ref 11.

dislocation density). In Fig. 7, a one-to-one relationship between  $\tau_2$  and a proposed damage parameter  $\Delta_5$  equal to the total stress range from the hysteresis curve of a strain-controlled experiment for a monocrystalline material (Mar-M-200), was used to show that in effect the positron lifetime  $\tau_2$  could serve as a viable damage parameter. A transformation of the damage parameter similar to Eq 4 brings the curve in Fig. 7 to conform with one of those curves in Fig. 1 with  $k = -4$ . Positron lifetime is therefore a good damage parameter for fatigue Regime 1 (damage incubation period).

The other four surface measurement techniques and the damage parameters generated by them are: (a) Photo-stimulated exo-electron emission method as applied to commercially pure aluminum (Al 1100) in two different hardness conditions by Buck and his co-workers [12] with their data reproduced in Fig. 8; (b) X-ray diffraction method as applied to aluminum Al 2024-T3 by Weissmann et al [13] and Pangborn [14] with their data reproduced in Figs. 9 and 10; (c) Optical correlation holographic method as applied also to aluminum Al 2024-T3 by Haworth and his co-workers [15] with their data reproduced in Fig. 11; and (d) Surface temperature monitoring by thermocouples and temperature sensitive coatings and strips as applied to E-Glass/Epoxy laminate ( $\pm 45^\circ$ )<sub>S</sub> by Nevadunsky and his co-workers [16] with their data reproduced in Fig. 12. All curves in Figs. 8 through 12 can be interpreted using Eq 3 and a transformation similar to Eq 4. It suffices to say that the damage parameter  $\Delta_6$  in Fig. 8 is good for Regime 1,  $\Delta_7$  in Fig. 9 appears

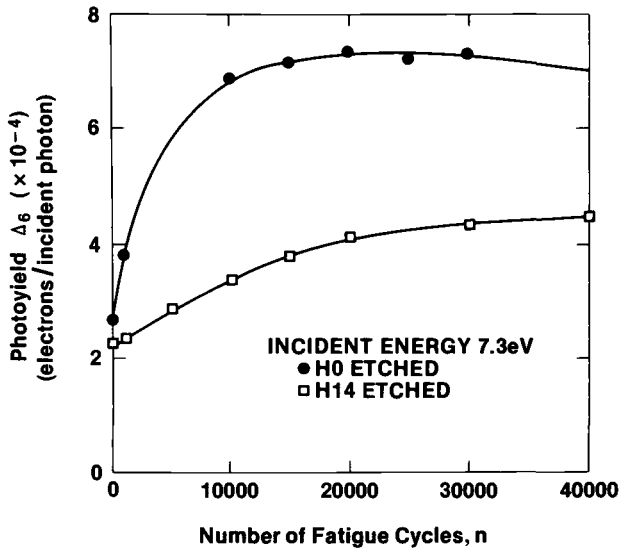


FIG. 8—Photoyield of commercially pure aluminum versus Cycle for two material states (H0, well-annealed; H14, work-hardened). Specimens were of cantilever beam type and flexurally fatigued to 0.3 percent  $\epsilon_{\max}$ . After Ref 12.

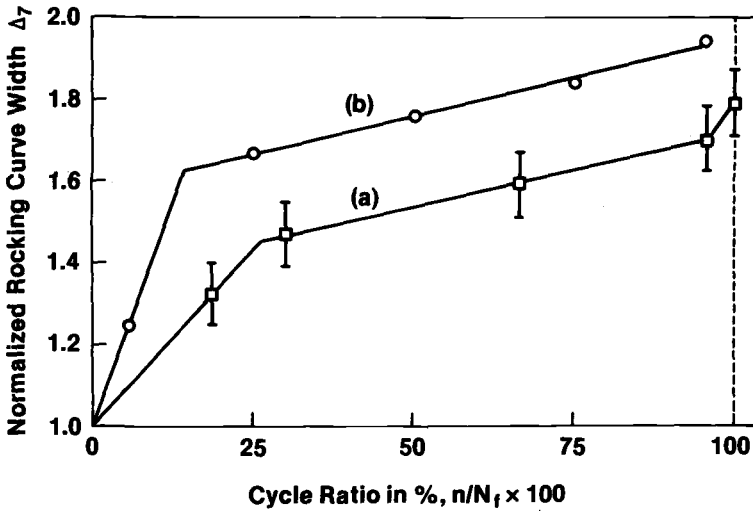


FIG. 9—Damage (excess dislocations) versus cycle ratio for Aluminum 2024-T3 with (a)  $50 \mu\text{m}$  grain size and (b)  $40 \mu\text{m}$  grain size, both at fully reversed fatigue loading of  $\pm 200.6 \text{ MPa}$  stress amplitude. After Ref 13.

viable also for Regime 1 even though we could use some more data,  $\Delta_8$  in Fig. 10 appears very good for Regime 2 (damage sharing period), and  $\Delta_9$  and  $\Delta_{10}$  in Figs. 11 and 12 look very promising for Regime 3 (damage runaway period). The validity of these observations rests, of course, on the specific material, specimen geometry, and loading for which the damage data were generated.

The last of the group, the SANS technique, which is nondestructive and volumetric, happens to be one of the most exciting developments in microstructure measurement in recent years. The use of a neutron beam instead of the X-ray is to replace, in terms of data analysis, the scattering length of an electron by the coherent scattering length of the atom. Hendricks, Schelten, and Schmatz [17] applied this technique to 99.9999 + percent — pure aluminum single crystals of dimensions 25 mm diameter by 38 mm long, which were irradiated to fluences between  $0.3$  and  $2.0 \times 10^{21} \text{ n cm}^{-2}$  at  $57^\circ\text{C}$  to produce an observable distribution of voids. A comparison of their data with those from transmission electron microscopy (TEM) which sampled only a very small portion of the crystal is given in Fig. 13. Page, Weertman, and Roth [18] reported the change of the void distribution curves due to fatigue of high purity (99.999 percent) copper specimens at elevated temperatures, using the same technique. Their data for  $405^\circ\text{C}$  are reproduced in Fig. 14, and their proposed damage parameters,  $\Delta_{11}$  and  $\Delta_{12}$ , corresponding to data for  $567^\circ\text{C}$  are displayed in log-log plots in Figs. 15 and 16. Based on all the information reported in Ref 18, it appears that both damage parameters are promising candidates not only for Regime 1, as one would expect for void

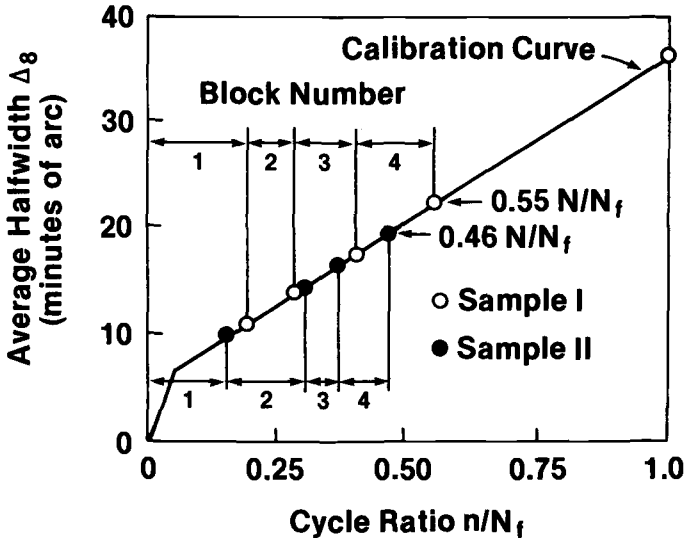


FIG. 10—Damage versus cycle ratio for two Aluminum 2024 specimens subjected to an identical sequence of cycling blocks conducted at successively higher amplitudes. Halfwidth measured by X-ray double-crystal diffractometry [13,14].

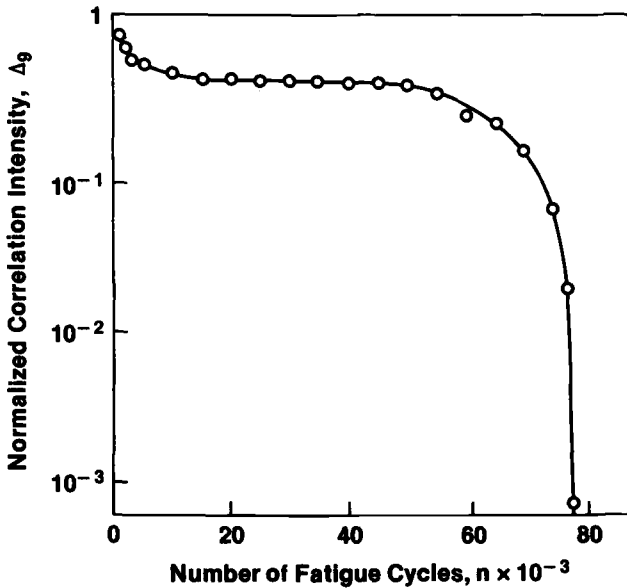


FIG. 11—Damage versus cycle for Aluminum 2024-T3 specimen subjected to tension-tension fatigue loading with mean stress equal to 325 MPa and total stress range equal to 210 MPa. Surface finish No. 600 grit silicon carbide. After Ref 15.

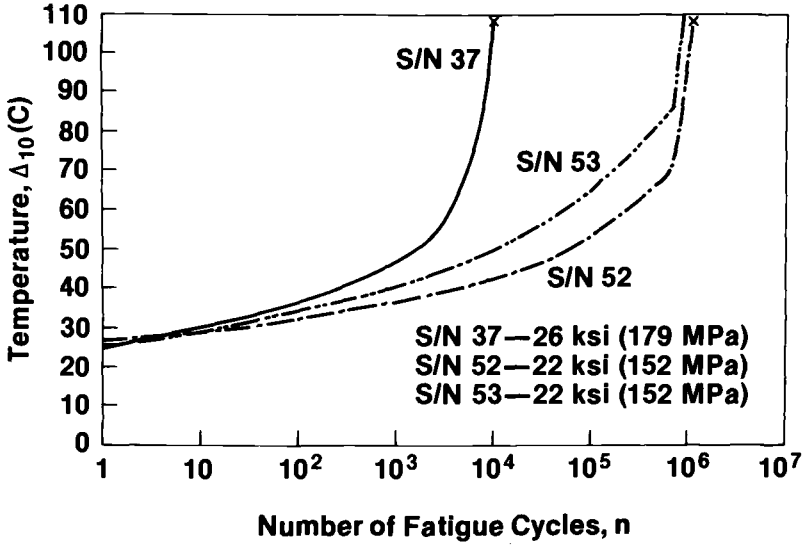


FIG. 12—Damage (temperature increase) versus cycle for  $(\pm 45^\circ)_s$  E-glass/epoxy specimens subjected to tension-tension fatigue loading of stress ratio equal to 0.1 (min/max) and the stress range given as shown. After Ref 16.

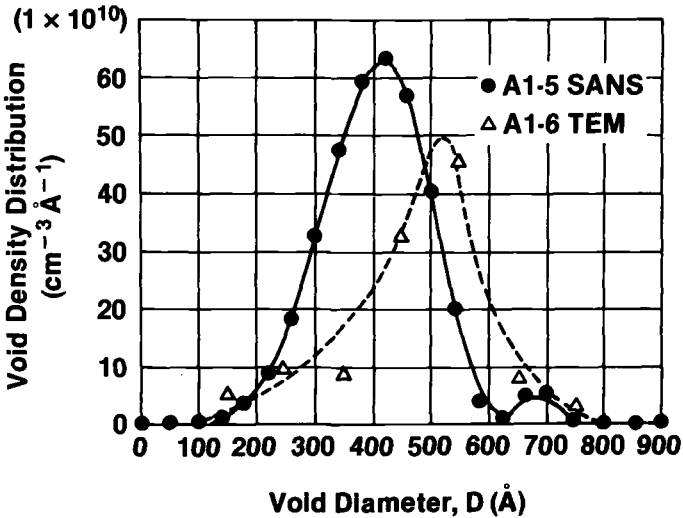


FIG. 13—Damage data by SANS technique versus TEM for two pure aluminum crystals Al-5 and Al-6 irradiated to produce observable voids. After Ref 17.

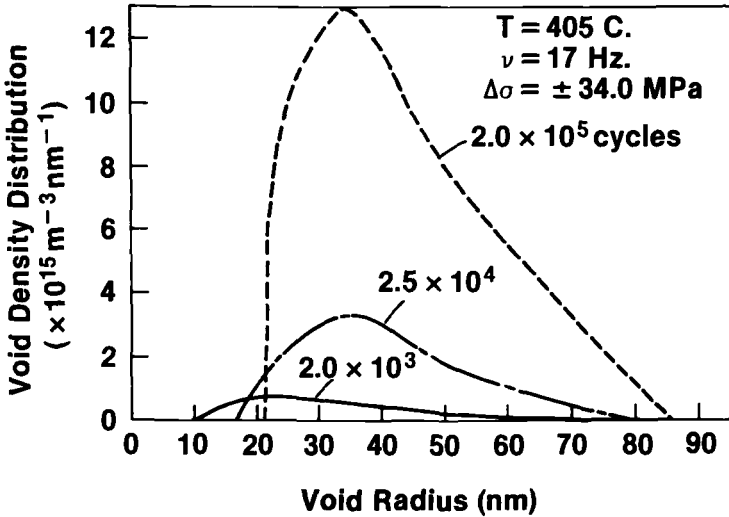


FIG. 14—Damage data in terms of void size distributions by SANS technique for pure copper specimens fatigued at elevated temperature and stress level as shown. Data corrected for grain growth. After Ref 18.

**TOTAL VOID VOLUME VS. TIME  
(NORMALIZED TO 60μm G.S.)**

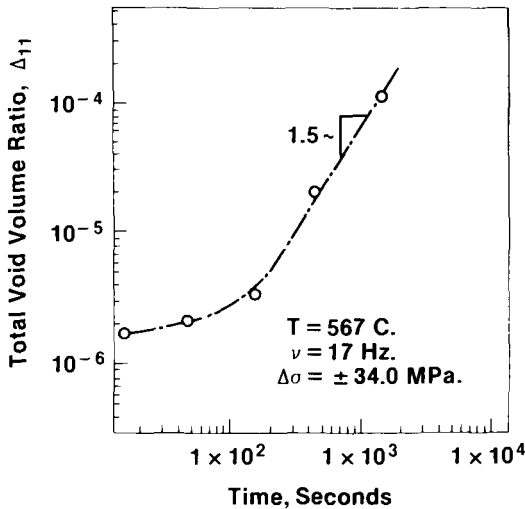


FIG. 15—Damage (total void volume ratio) versus fatigue time by SANS technique for pure copper specimens fatigued at elevated temperature and stress level as shown. Data corrected for grain growth. After Ref 18.

**TOTAL NUMBER OF VOIDS VS. TIME  
(NORMALIZED TO 60 $\mu$ m G.S.)**

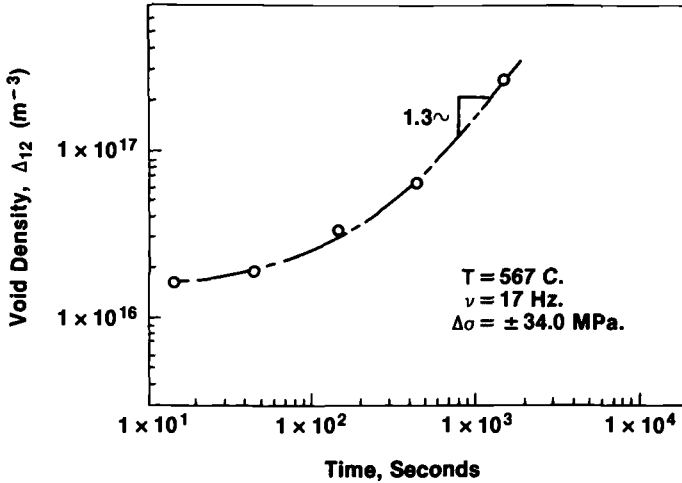


FIG. 16—Damage (void density) versus fatigue time by SANS technique for pure copper specimens fatigued at elevated temperature and stress level as shown. Data corrected for grain growth. After Ref 18.

nucleation during the damage incubation period, but also for Regimes 2 and 3 as well. As a nondestructive technique of monitoring certain features of a microstructure, the SANS method has been applied to Inconel 700 and Inconel X-750, as reported by Cortese et al [19], and it will not be long before we shall see more such results as more SANS facilities become available. For a review of the method and some recent applications, the reader may consult Ref 20 and 21.

### Pitfalls of Fatigue Damage Modeling

Having passed judgment on a total of twelve damage parameters based on a simple conceptual definition of damage and a three-regime allocation of the viability of those parameters, I am obliged to qualify my enthusiasm with a few words of caution. We are all aware that the ultimate goal of measuring fatigue damage is to be able to predict  $N_f$  with confidence. The natural questions to ask are: how close are we to that goal, and if not close, why?

For some limited class of materials in a very restricted range of applications, engineers have conducted a large amount of tests to ensure that we can indeed build some structures or components with confidence.<sup>6</sup> But that ap-

<sup>6</sup> In addressing the international symposium of fatigue mechanisms [1], I estimated that we spent worldwide close to one billion U. S. dollars a year on fatigue testing to provide the database for fatigue design. See p. 730 of Ref 1.

proach is both costly and time-consuming. Without a fundamental understanding of fatigue, the approach based on testing at a macroscopic level is inadequate to simulate real-time degradation or to predict residual life for a structure or component in service. A systematic study of microstructural changes due to fatigue, using the latest instrumentation for observation and measurement as mentioned in the last section, must be carried out to achieve that ultimate goal. Five discrete processes of this study have been identified by ASTM Subcommittee E9.01 in their panel study report, a summary of which will appear in this paper following this section. They are: (a) Measurement; (b) Data Analysis; (c) Nonlinear Modeling; (d) Physical Modeling of Fatigue as an evolutionary and thermodynamic process involving the onset of micro- and macro-stabilities; and (e) Codes and Standards Development for fatigue analysis and decision-making. The purpose of this section is to discuss fatigue damage modeling in general and some selected pitfalls in particular.

Fatigue damage modeling is difficult and expensive primarily for two technical reasons. The first is the enormous scale that separates the atomic level ( $10^{-10}$  to  $10^{-8}$  m) where understanding begins, through the subgrain, grain, and specimen levels, to the component and structure levels ( $10^{-2}$  to  $10^2$  m) for which the prediction of the model is intended. The second reason is the impossibility of producing "identical" specimens with well-characterized microstructural features for controlled experimentation. The two, when combined, provide the basis for answering the earlier question in the negative, that is, we are far from the goal of having a general method of predicting  $N_f$ . To focus a little more on this difficulty, we can think of  $N_f$  at several levels, namely,  $N_f^{(local)}$ ,  $N_f^{(specimen)}$ ,  $N_f^{(structure)}$ , etc. Since  $N_f$  is used often as a normalizing constant, a confusion about which level  $N_f$  fits in can be a source of modeling difficulty. In particular, let us examine Figs. 17 and 18 which correspond to the data reported by Owen and Howe [9] and reproduced in this paper as Figs. 4 and 5, respectively. The information summarized in Figs. 17 and 18 is misleading because the authors failed to recognize an important distinction between the concept of  $N_f^{(specimen)}$  as defined by macroscopic data and the concept of  $N_f^{(local)}$  at six sites along the edge of the specimen as defined by the damage data. By normalizing their damage data with respect to the individual values of damage at  $N_f^{(specimen)}$  rather than  $N_f^{(local)}$ , the latter being unmeasurable and therefore unknown, the authors introduced two erroneous assumptions in arriving at a scatter band for the normalized data: (a) The unknown  $N_f^{(local)}$  at each site equals  $N_f^{(specimen)}$ , and (b) the partially damaged states, as numerically quantified by the individually normalized damage parameters given in Figs. 17 and 18 are "additive" both temporally and spatially to yield a global measure of damage. In short, without submitting a reasonable analysis of the microstructural equilibrium of the composite during fatigue, the reduction of data from Figs. 4 and 5 to Figs. 17 and 18 is premature. This type of pitfall in damage modeling due to

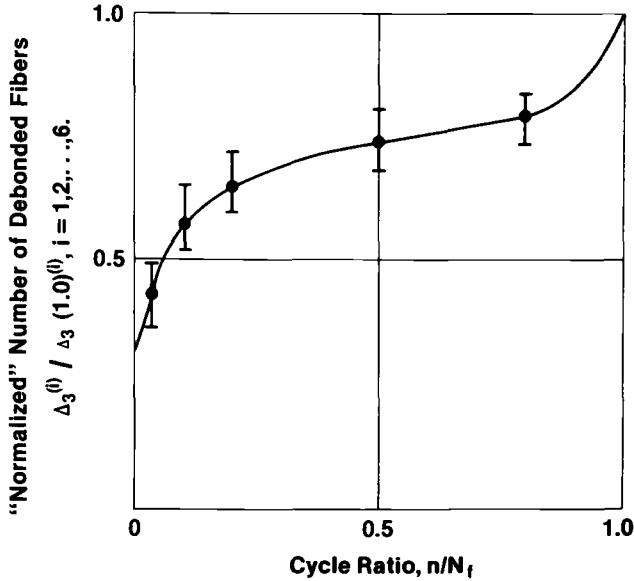


FIG. 17—Damage ("site-specific" normalized debonding between fiber and matrix) versus cycle ratio for two glass/polyester resin specimens during different types of fatigue loadings. Original data appear in Fig. 4. After Ref 9.

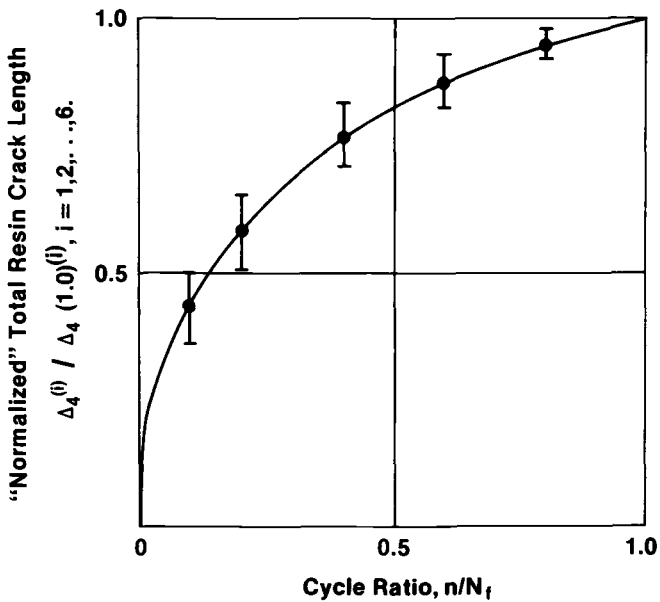


FIG. 18—Damage ("site-specific" normalized resin crack length) versus cycle ratio for three glass/polyester resin specimens during different types of fatigue loadings. Original data appear in Fig. 5. After Ref 9.

a confusion over scale is unfortunately rather common in the fatigue literature.

Another type of pitfall is in oversimplification. A case in point is given in Fig. 19, which is also due to Owen and Howe [9]. Based on the observation that the improperly normalized total resin crack length curve (labelled A in Fig. 19) and extrapolated but correctly normalized residual tensile strength curve (labelled B) are similar in form, Owen and Howe first proposed a non-linear model to fit A and B, and then argued on the ground of inevitable scatter in fatigue testing that "a linear representation (curve C) may be adequate." This oversimplification is both incorrect and unconservative because (a) our analysis in the Damage Parameters section shows that both damage parameters are appropriate for Regime 1 but not sensitive enough to support a full-range model, and (b) the linear model underestimates  $n/N_f$  in Regime 1 and thus overestimates  $N_f$  for a fixed  $n$  for which damage is measured.

Another difficulty in damage modeling is in knowing where to draw the line between two regimes of fatigue cycling. Manjoine [22] displays a generic curve as shown in Fig. 20 where the message is that for low total strain range, Regimes 1 and 2 occupy about 95 percent of  $N_f$  whereas for high total strain range, the two regimes last no more than 5 percent. In this notation, our Regime 3 (damage runaway period) corresponds to Manjoine's period of propagation. Is there a quantitative basis for this curve? Yes, but only for a few

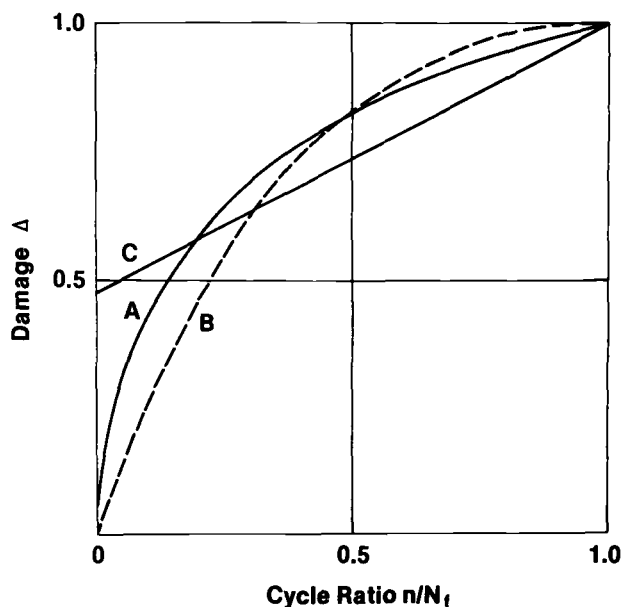


FIG. 19—Damage parameters versus cycle ratio for a class of glass/polyester resin specimens: A, resin crack accumulation (Fig. 18); B, reduction of residual strength; C, approximate linear damage rule. After Ref 9.

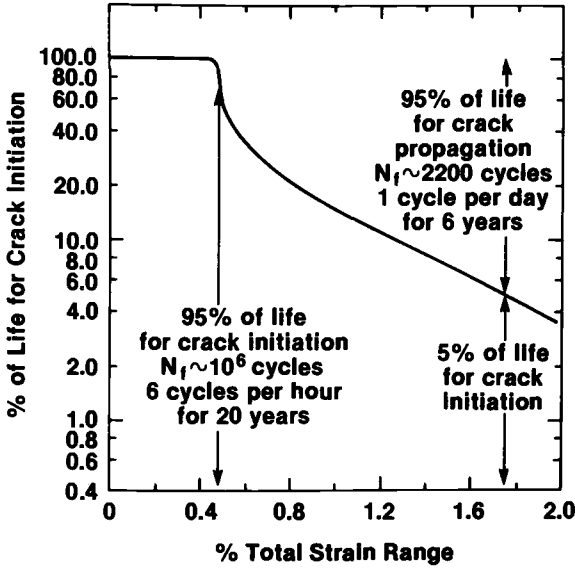


FIG. 20—Percent of life for crack initiation in cold-worked T-316 stainless steel specimen in ambient air. After Ref 22.

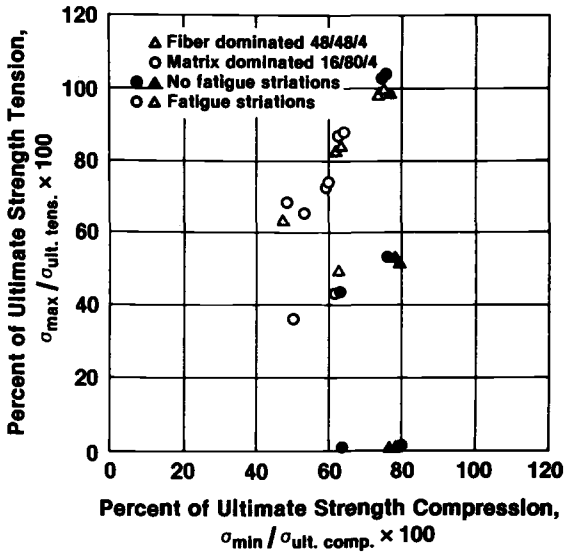


FIG. 21—Plot of combined fiber and matrix dominated fatigue test specimens with or without fatigue striations as reported by Morris and Hetter [23].

materials in a limited range of applications. The curve of Fig. 20 is not true in general and can be misleading in the hands of a policy maker in fatigue research funding. This is the pitfall of false generalization.

Elsewhere in this publication is a paper by Morris and Hetter [23] which discusses the fractographical technique of failure analysis and points up the importance of observing striations in both the fiber and the epoxy in damage studies. A typical output of that study is given in Fig. 21 from which they conclude that "this plot . . . indicates that the maximum compressive strengths that resulted in striation formation were somewhere between 65 and 80 percent of the ultimate compressive stress." The lack of a reasonable effort on data acquisition and data analysis in reaching a conclusion, no matter how tentative, is a pitfall common to many modeling activities reported in the literature.

### Summary of an ASTM E9.01 Panel Study on Fatigue Damage

In response to a natural desire of the public to avoid unexpected or premature failure of structures or components, engineers began in the 1960's to introduce fatigue design requirements with appropriate safety factors into codes and standards for all new aircrafts, pressure vessels, and nuclear components. Fatigue design of buildings, bridges, pipelines, and automobiles soon followed. It is expected that the trend will continue into the 1980's so that by the end of this decade, we shall expect all safety-related man-made structures and components, including ships and offshore oil-drilling platforms, to withstand fatigue failure.

During the middle of the 1970's, the public reacted to the world-wide crisis of energy and material shortages by investing less in the acquisition of new equipment and more on proper maintenance of existing equipment to prolong its service life. To accelerate the development of a credible methodology for fatigue damage estimate and life prediction, ASTM Subcommittee E9.01 began a concerted effort to identify in a three-part study the overall research needs and opportunities of the technical community on the question of fatigue damage. An ad-hoc panel consisting of officers of E9.01 and its parent committee E9 as well as numerous invited contributors from the broad national and international community of fatigue researchers was given a five-year time frame to (a) collect factual information and opinions on fatigue research through interviews and laboratory visits from 1975 to 1980, (b) organize an international symposium on fatigue mechanisms (Kansas City, 1978) and publish a complete proceedings including discussions and closures, and (c) report findings on research needs and opportunities in the 1980's for debate and dissemination at an ASTM conference (Bal Harbour, 1980). As chairman of that study panel and editor of the panel report [24], I am pleased to summarize the major findings of the consensus document as approved by the subcommittee in November 1981 at its St. Louis meeting:

*Technical Finding:* Current knowledge on damage measurement, data analysis, nonlinear modeling, micro-mechanics, surface science, and other disciplines related to fatigue research, is adequate to foster a favorable climate for major breakthroughs if both manpower and funding requirements are met.

*Manpower Finding:* Fatigue training at the doctoral and master levels in U. S. educational institutions appears to be less emphasized while continuing education courses in fatigue and on-the-job training in fatigue testing at industrial and governmental laboratories are popular as a result of an increase in fatigue design code requirements and testing facilities.

*Research Support Finding:* Government support by civilian agencies tends to decrease while that from the military will hold constant unless a case is made to bring fatigue research<sup>7</sup> into the forefront of materials science as a line item in a budget document. Industry support is difficult to forecast due to uncertainty in economy and regulatory decisions.

In addition, the panel recommended the pooling of experimental, analytical, computational, and managerial resources from academic, governmental, and industrial centers of fatigue research to contribute to a systematic study consisting of five discrete processes as mentioned previously in *Pitfalls of Fatigue Damage Modeling*. This recommendation stemmed from the panel's recognition that a fundamental study of the complete problem of fatigue damage is beyond the capability of any single group or individual.

### Concluding Remarks

Fatigue damage at three microscopic levels ( $10^{-10}$  to  $10^{-8}$  m;  $10^{-8}$  to  $10^{-6}$  m; and  $10^{-6}$  to  $10^{-4}$  m) in simple, composite, and multi-phase materials can be quantified by recently developed surface and volumetric measurement techniques. Of the twelve damage parameters examined in this paper, ten have been found sensitive and consistent enough to qualify for accelerated applications in fatigue damage research. A simple and nonlinear form of the damage  $\Delta$  versus cycle ratio  $x$  relation

$$\Delta = \frac{e^{kx} - 1}{e^k - 1}, \quad (k \neq 0; 0 \leq x \leq 1) \quad (5)$$

which corresponds to the physical notion that the rate of damage,  $d\Delta/dx$ , depends linearly on  $\Delta$  as a first approximation, has been found useful as a concept in assessing the relative merits of damage parameters and measurement techniques.

Five discrete processes of fatigue research leading to the ultimate goal of

<sup>7</sup> Fatigue research, as defined by ASTM E9.01, includes all activities aimed at achieving an understanding of the fatigue process. In this context, we exclude a large amount of testing activities which generate data primarily for engineering decision-making.

predicting fatigue life from direct or indirect measurements of damage, have been identified by an ASTM panel in a five-year-long study on fatigue damage. These processes are: (a) Measurement; (b) Data Analysis; (c) Nonlinear Modeling; (d) Evolutionary and Thermodynamic Theory; and (e) Codes and Standards Development. Only two of the five, namely (a) and (c), are discussed in this paper. Based on my own work in data analysis [1, pp. 729–758; 25], evolutionary and thermodynamic theory [26,27,28], and codes and standards development [29,30], and the major technical finding of the ASTM E9.01 study panel on fatigue damage [24], I strongly believe that a systematic study of the complete problem of fatigue damage is now technically feasible.

### Acknowledgment

I would like to thank J. Morrow of University of Illinois-Urbana for initiating a comprehensive discussion on measurable quantities of fatigue damage during his tenure as the chairman of the ASTM Subcommittee E9.01 (1973–78), numerous members of E9.01 and invited contributors who donated their time and effort to the E9.01 study panel report on fatigue damage on which part of this paper is based, and several colleagues at the National Bureau of Standards, namely, H. Berger, R. Fields, J. Filliben, C. Glinka, E. Kearsley, J. Lechner, J. Mandel, L. Mordfin, R. W. Penn, J. H. Smith, and L. J. Zapas, for their technical assistance over a number of years during the 1970's. The names of the contributors to the E9.01 study panel report, which appear in Ref 24, are not repeated here for brevity.

### References

- [1] *Fatigue Mechanisms, ASTM STP 675*, American Society for Testing and Materials, 1979.
- [2] Williams, M. L., Ed., *Mechanics-Structure Interactions with Implications for Material Fracture*, University of Pittsburgh, School of Engineering, SETEC-DO-80-012.1, 1980.
- [3] Beevers, C. J., Ed., *The Measurement of Crack Length and Shape During Fracture and Fatigue*, Engineering Materials Advisory Services Ltd., United Kingdom, 1980.
- [4] Stouffer, D. C. et al, Eds., *A Continuum Mechanics Approach to Damage and Life Prediction*, University of Cincinnati, Department of Engineering Science, 1980.
- [5] Buck, O. and Wolf, S. M., Eds., *Nondestructive Evaluation: Microstructural Characterization and Reliability Strategies*, The Metallurgical Society of the American Institute of Mining, Metallurgical, and Petroleum Engineers, 1980.
- [6] Stinchcomb, W. W. and Reifsnider, K. L. in *Fatigue Mechanisms, ASTM STP 675*, American Society for Testing and Materials, 1979, pp. 762–787.
- [7] Tanimoto, T. and Amijima, S., *Journal of Composite Materials*, Vol. 9, 1975, p. 380.
- [8] Chang, F. H. et al, *Journal of Composite Materials*, Vol. 10, 1976, p. 182.
- [9] Owen, M. J. and Howe, R. J., *Journal of Physics D: Applied Physics*, Vol. 5, 1972, p. 1637.
- [10] Buck, O. and Alers, G. A. in *Fatigue and Microstructure*, M. Meshii, Ed., American Society for Metals, 1979, pp. 101–147.
- [11] Tien, J. K. et al in *Electron and Positron Spectroscopies in Materials Science and Engineering*, O. Buck et al, Eds., Academic Press, New York, 1979, p. 73.
- [12] Buck, O. et al, *Applied Physics*, Vol. 12, 1977, p. 301.
- [13] Weissmann, S., Pangborn, R., and Kramer, I. in *Fatigue Mechanisms, ASTM STP 675*, American Society for Testing and Materials, 1979, pp. 163–167.

- [14] Pangborn, R. N., "X-ray Diffraction Techniques for Damage Measurement and Some Open Questions," in *Fatigue Damage*, ASTM E9.01 Subcommittee Document, J. T. Fong, Ed., American Society for Testing and Materials, to be published.
- [15] Haworth, W. L., Hieber, A. F., and Mueller, R. K., *Metallurgical Transactions Annual*, Vol. 8A, 1977, p. 1597.
- [16] Navadunsky, J. J., Lucas, J. J., and Salkind, M. J., *Journal of Composite Materials*, Vol. 9, 1975, p. 394.
- [17] Hendricks, R. W., Schelten, J., and Schmatz, W., *Philosophical Magazine*, Vol. 30, 1974, p. 819.
- [18] Page, R., Weertman, J. R., and Roth, M., *Scripta Metallurgica*, Vol. 14, 1980, p. 773.
- [19] Cortesse, P. et al, *Materials Science and Engineering*, Vol. 36, 1978, p. 81.
- [20] Weertman, J. R. in *Nondestructive Evaluation: Microstructural Characterization and Reliability Strategies*, O. Buck and S. M. Wolf, Eds., The Metallurgical Society of the American Institute of Mining, Metallurgical, and Petroleum Engineers, 1980, pp. 147-168.
- [21] Glinka, C. J., Prask, H. J., and Choi, C. S. in *Mechanics of Nondestructive Testing*, W. W. Stinchcomb, Ed., Plenum Press, New York, 1980, pp. 143-164.
- [22] Manjoine, M. in *Critical Issues in Materials and Mechanical Engineering*, J. T. Fong et al, Eds., American Society of Mechanical Engineers, New York, 1981, pp. 210-211.
- [23] Morris, G. E. and Hetter, C. M., "Fractographic Studies of Graphite/Epoxy Fatigue Specimens," in this publication.
- [24] Fong, J. T., Ed., *Fatigue Damage*, ASTM E9.01 Subcommittee Document, American Society for Testing and Materials, to be published.
- [25] Fong, J. T. and Dowling, N. E. in *Fatigue Crack Growth Measurement and Data Analysis, ASTM STP 738*, American Society for Testing and Materials, 1981, pp. 171-193.
- [26] Fong, J. T. and Simmons, J. A., *Archiwum Mechaniki Stosowanej* (Warsaw), Vol. 24, 1972, p. 363.
- [27] Fong, J. T., *Journal of Pressure Vessel Technology*, Transactions of the American Society of Mechanical Engineers, Vol. 97J, 1975, p. 214.
- [28] Fong, J. T. and Penn, R. W. in *Fracture Mechanics and Technology*, G. C. Sih and C. L. Chow, Eds., Sijthoff and Noordhoff, The Netherlands, 1977, Vol. 1, pp. 145-159.
- [29] Fong, J. T. and Smith, J. H. in *Critical Issues in Materials and Mechanical Engineering*, J. T. Fong et al, Eds., American Society of Mechanical Engineers, New York, 1981, pp. 197-217.
- [30] Fong, J. T., *Nuclear Engineering and Design*, Vol. 51, 1978, p. 45.

## **Summary**

## Summary

---

In order to maximize the transfer of information to the reader, and to provide a convenient brief but precise source of information to readers who use this summary as a major source of information from this book, the material that follows will be organized into two major sections. The first section will review each paper specifically in the order of appearance in this volume. The second section will address specific subject areas and attempt to bring the information in the individual papers together to make some collective statement about those subjects. While every attempt will be made to present an objective commentary, the reader is reminded that this summary is an individual effort, and is encouraged to read and study the details in each of the papers.

The parent symposium was organized under a very specific (albeit very long) title. The papers which were presented, and those that appear in this book, were categorized, however, under just two headings, "Damage Mechanisms: Accumulation and Nondestructive Investigation" and "Damage Mechanisms: Tolerance and Characterization." The introductory paper by Mordfin is titled "Toward the Nondestructive Characterization of Fatigue Damage in Composite Materials." The title of that paper makes the point that much of the "damage" referred to in the conference presentations and in this Special Technical Publication is damage that is induced by fatigue loading, and most of the "characterization" to be discussed will be based on nondestructive testing and evaluation schemes. Mordfin develops a number of strong points having to do with the general philosophy of characterizing fatigue damage. But his central theme, briefly, is that people who have specialties in nondestructive evaluation frequently are not directly associated with experts in the mechanical behavior of composites, and even when such an association is present, the two types of expertise often must be combined in very unconventional ways to solve problems. He supports his premise with a case history of a failure analysis of glass-polyester pultruded rods used as guys for towers and arrays. It happens that those rods failed by propagation of hairline cracks that were induced by shock tension followed by an incubation period of considerable length, a fact that was identified only after some very unconventional and interdisciplinary activity.

The paper by Sendeckyj, Maddux, and Porter deals with "Damage Documentation in Composites by Stereo Radiography." The subject method is a laboratory scheme for obtaining three-dimensional information for our radiographs made by translating or rotating the specimen relative to the X-ray source between otherwise identical radiographic exposures. This paper is very thorough and provides an excellent discussion of the technical details involved in the method. A demonstration of the technique also is provided using radiographs of damage around the center hole in  $[(0, \pm 45, 90)_s]_2$  graphite epoxy induced by constant amplitude fatigue loading. The damage was enhanced by an opaque penetrant material, tetrabromoethane (TBE) in this case. Matrix cracks and delaminations were identified, and earlier work in which fiber fractures were detected was cited. A discussion of the manner in which the depth of detail influences the changes in each radiographic image as the specimen is rotated or translated suggests methods for quantifying the spatial distributions observed.

Morris and Hetter address the tedious subject of "Fractographic Studies of Graphite/Epoxy Fatigue Specimens," using scanning electron microscope and fluorescent penetrant methods. Overload and fatigue fracture patterns in graphite/epoxy laminates were examined. A variety of distinctive characteristic topological features were identified and associated with different modes of failure. Perhaps the salient results of the work are the identification of "hackles" which relate to the fracture path (and origin) of overload failure, and the identification and characterization of "striations" or arrest marks which relate to tension-compression fatigue fractures.

Further evidence of fatigue damage is presented in the paper by Masters and Reifsnider, "An Investigation of Cumulative Damage Development in Quasi-Isotropic Graphite/Epoxy Laminates." Fatigue damage development in the off-axis plies of  $[0, \pm 45, 90]_s$  and  $[0, 90, \pm 45]_s$  graphite/epoxy laminates under quasi-static fatigue loading was studied using surface replication and opaque-penetrant-enhanced X-ray radiography. The development of matrix cracks, crack coupling, and delamination was followed as a function of load level and cycles of loading. Stacking sequence was found to have a major effect on the development of all three types of damage observed. The formation of transverse matrix cracks (across the width of the specimens) was found to stabilize when a characteristic crack spacing of cracks had formed in each off-axis ply. That characteristic crack spacing was called the "characteristic damage state," a stable matrix crack arrangement which was determined by lamina properties and thicknesses, and the laminate stacking sequence—a laminate property. The same characteristic damage state was found to form under quasi-static or fatigue loading.

Kriz and Stinchcomb studied "Effects of Moisture, Residual Thermal Curing Stresses, and Mechanical Load on the Damage Development in Quasi-Isotropic Laminates." The same types of laminates and material as those used in the previous paper by Masters and Reifsnider were used for this

study, making comparisons especially meaningful. Moisture was the principal experimental variable in the experiments. Surface replication was used to follow matrix crack and delamination development. Statistical analysis of strength data from quasi-static and residual strength (following fatigue loading) tests was conducted. An extensive analysis of ply and edge stresses was performed using a plane-strain finite element method. Variations in residual stresses and threshold stress levels for crack and delamination formation were calculated by using Young's modulus and shear modulus values which were reduced (by 25 and 27 percent, respectively) in the presence of a 1.2 percent moisture weight gain. It was found that the initiation and development of damage was greatly influenced by moisture, as predicted from the analysis, but that the characteristic crack spacings and the final damage state prior to failure were altered only slightly, also as predicted. Final strengths were influenced in a correspondingly minor way.

The only metal matrix investigation was reported by Johnson, who studied the "Mechanisms of Fatigue Damage in Boron/Aluminum Composites." The paper addresses "shakedown" in 0-deg specimens, saturation damage states, stacking sequence effects, and variable load history effects. Damage was represented collectively by the percent of initial unloading elastic modulus remaining after  $N$  cycles. When that quantity reached a stable value following cyclic loading, no more damage accumulated and fatigue failure did not occur. When that quantity did not change at all, the threshold of damage accumulation was defined. That threshold corresponded to the shakedown limit (fatigue damage initiation stress) below which the matrix strain hardens such that only elastic deformation occurs under subsequent load cycles. Damage was detected by etching off successive layers of material. An elastic-plastic analysis is presented which described these events. For a variable load history it was found that the specimen formed the saturation state which corresponded to the largest stress range.

"Stiffness-Reduction Mechanisms in Composite Laminates" was discussed by Highsmith and Reifsnider. The paper is entirely concerned with the relationship between stiffness changes and crack formation in off-axis plies in a multiaxial laminate. In order to isolate and exaggerate this effect for study,  $[0,90_3]_s$ ,  $[90_3,0]_s$ ,  $[0,90]_s$  and  $[0,\pm 45]_s$  glass epoxy specimens were tested under quasi-static and fatigue loading. Characteristic damage states, as discussed in the paper by Masters, were observed. Changes in  $E_x$ ,  $\nu_{xy}$ ,  $G_{xy}$ , and  $D_{yy}$  were measured. Changes of up to 74 percent were observed. Two analyses were discussed. A shear-lag one-dimensional analysis developed by the authors showed good agreement with the observed  $E_x$  changes as a function of crack density. The more conventional laminate analysis discount method was used to predict maximum changes in all of the tensor values measured with agreement that was satisfactory in some cases but not satisfactory in other situations.

Transverse crack formation, as well as delamination, was studied also by

Crossman and Wang in their paper titled "The Dependence of Transverse Cracking and Delamination on Ply Thickness in Graphite/Epoxy Laminates." The tensile fracture sequence of  $(25, -25, 90_n)_s$  and  $(25_2, -25_2, 90_2)_s$  T300/934 laminates was studied and reported, with the general goal of determining the degree of structural modeling necessary to predict fracture in such laminates. Incremental tensile loading and diiodobutane (DIB) enhanced radiography were used to examine the damage. The onset strain for transverse cracking, delamination, and final fracture all showed a strong dependence on the number of repeated 90-deg plies above a threshold thickness which corresponded to the initiation of edge delamination before failure. Transverse crack initiation levels showed strong dependence over the entire range of 90-deg ply thicknesses and was entirely precluded for  $n = 1/2, 1$ . The authors found that a shear lag model predicted crack densities as a function of strain well, but underestimated maximum crack densities when a characteristic crack spacing was reached. An energy release rate analysis devised by the investigators predicted the dependence of transverse crack initiation on ply thickness but was not as satisfactory for delamination initiation predictions.

O'Brien continues with a thorough discussion of the "Characterization of Delamination Onset and Growth in a Composite Laminate," specifically in  $[\pm 30, \pm 30, 90_2]_s$  graphite/epoxy laminates. DIB enhanced X-ray radiographs were used to follow delamination growth during fatigue loading. Laminate stiffness was observed to change linearly with delamination size. Two analyses (a quasi-three-dimensional finite element analysis and a modified laminate analysis) were used to calculate stiffness loss and total strain energy release rates. A critical energy release rate for delamination growth was calculated and used to predict the onset of delamination in  $[+45_n, -45_n, 0_n, 90_n]_s$  ( $n = 1, 2, 3$ ) laminates with success. A delamination  $R$ -curve was developed to characterize stable growth under monotonic tensile loading, and a power law relationship between the strain energy release rate and fatigue induced delamination growth rate was developed. All relationships were verified with experimental data obtained by O'Brien.

Wilkins, Eisenmann, Camin, Margolis, and Benson also discussed "Characterizing Delamination Growth in Graphite Epoxy." However, they concentrated on the design of test specimens (and methods) to study Mode I and Mode II (forward shear) subcritical delamination growth and related strain energy release rates. A three-dimensional finite element method employing virtual crack closure was incorporated to interpret data from a lap-shear test specimen. A double cantilever beam specimen was used to obtain Mode I data. It was found that the critical release rate  $G_{IC}$  (for a 0/0-deg interface) was about 0.1 of a common value for structural adhesives and about half the  $G_{IIC}$  value. However, for fatigue, the growth rate exponent for Mode I was found to be high; hence, at design levels such delaminations grew slowly. Mode II delamination growth rate exponents were lower (comparable to

Mode I in aluminum), suggesting that it is a predominant fatigue mode. It was found also that constant-amplitude data could be used in a simplified analysis to predict successfully spectrum crack growth.

A third delamination investigation was reported by Ramkumar; his subject was "Compression Fatigue Behavior of Composites in the Presence of Delaminations." Three quasi-isotropic T300/5208 laminates were tested. Delaminations were introduced by imbedding Teflon strips at chosen interfaces at various positions through the specimen thickness. Flaw growth was monitored using DIB enhanced radiography. Half-life residual strength data were recorded. When delaminations were positioned near the centerline of the specimen, no stable growth was observed. (Delamination growth was unstable under static loading in all cases). Delaminations which did grow during fatigue loading were located near a surface and below a 0 or 45-deg ply which "buckled out" in the delaminated region during cyclic load variations. Residual strength values indicated that relatively little strength variation occurred at the half-life of the specimens even when delaminations grew.

Ratwani and Kan discussed "Effect of Stacking Sequence on Damage Propagation and Failure Modes in Composite Laminates." Four different stacking sequences were studied. Tension-compression fatigue loading was applied and damage was followed by DIB enhanced X-ray radiography. The material system was AS/3501-6 graphite epoxy. All specimens had a one-quarter width center hole. Interlaminar stresses were calculated using a finite element program (NASTRAN). For the laminates examined, interlaminar shear stresses seemed to be a more likely source of delamination initiation than interlaminar normal stresses judging from a comparison of the stress analysis and experimental results. Other things being equal, there also seemed to be a preference for delamination to initiate near a surface.

Badaliance and Dill addressed "Damage Mechanism and Life Prediction of Graphite/Epoxy Composites" for compression dominated spectrum loading of center-hole specimens of AS/3501-6 graphite/epoxy laminates dominated by 0 and 45-deg plies. TBE enhanced X-ray radiographs were used to follow damage around the hole. A damage correlation parameter was developed by summing strain energy density factors for each ply under the assumption that fiber-direction matrix cracking dominates the failure mode. The resulting parameter sum was used to correlate data from different laminates tested at different stress ratios. Then the constant amplitude (collapsed) data were used, along with a linear damage rule to predict spectrum fatigue life. Predictions were compared to data for three laminates, also dominated by 0-deg (16 percent) and 45-deg (80 percent) plies. Agreement was satisfactory.

The concluding paper by Fong brings together a number of concepts and attempts to make an assessment of the "state of the art." The paper begins by discussing twelve different damage parameters extracted from the literature, in the context of their sensitivity to damage throughout the life of var-

ious materials and their consistency. Data from the literature for each of the parameters are presented. Several of the damage parameters are based on nondestructive evaluation techniques that are especially sensitive to voids or other micro- (or submicro-) nonuniformities, such as positron annihilation and lifetime measurement, photo-stimulated exo-electron emission, and small angle neutron scattering. The latter method was judged to be particularly promising. Fong also presents an excellent discussion of the general development of fatigue research efforts and presents information from five years of work by Subcommittee E09.01 on Fatigue Research which bears on his topic.

Having reviewed the individual papers, I will close now with a brief summary of the collective document. My remarks will be organized under four topics which I pose as questions to be answered. "What is fatigue damage?" "What new concepts were introduced by this work?" "What can we do with these concepts?" "What opportunities for further work do we have?"

From the papers in this volume, one would have to conclude that fatigue damage consists of matrix damage, that is, matrix cracking parallel to the fibers and delamination. However, interface debonding and fiber fracture were mentioned, so we should include those as secondary damage modes. Based on the present information, however, it is certainly fair to say that matrix cracking and delamination appear to be the types of fatigue damage that are of greatest concern to most investigators. There is also a strong suggestion that those two modes are closely associated, that they are frequently observed together, and that matrix cracking is a precursor of delamination.

A number of important concepts regarding damage are offered in the volume. Throughout the book the point constantly is made that much is to be gained from a truly interdisciplinary study of fatigue damage in composite materials. The physics, chemistry, and mechanics of fatigue damage events are so intimately associated and interdependent that rigid disciplinary studies are, *a priori*, sterile. Nowhere is this more evident than in the efforts to find suitable nondestructive evaluation schemes to follow damage development. A number of more specific concepts also are discussed. The concept of using tensor stiffness changes to follow matrix crack development in polymer and metal matrix composites is discussed, and appears to offer a damage parameter that can be interpreted clearly and measured easily when matrix cracking causes significant changes in one or more of the four in-plane moduli. The concept of shakedown is discussed and directly associated with the threshold for fatigue damage (rather than the endurance limit as had been suggested earlier) in metal matrix composites. Another general concept that emerged is that sequence effects are often sufficiently inconsequential to allow constant amplitude fatigue results to be used successfully to predict the results of spectrum loading. One of the most fertile conceptual fields of discussion in the volume is the use of strain energy release to characterize micro-damage. That quantity was used successfully to describe the effect of ply

thickness on matrix crack and delamination formation, to represent the initiation and growth rate of edge delamination, and to identify the importance of different failure modes in fatigue damage. Other uses of strain energy release are mentioned. It is clear that this concept is an important part of damage representation. Strain energy density also was used as a collective damage parameter and was found to be useful for reducing information from different laminates to a single representation of fatigue behavior.

Another concept (which appears in six of the papers) is that of a characteristic damage state, a stable damage state (consisting mostly of transverse matrix cracks) which develops prior to failure and is uniquely defined by the properties and thickness of each ply and the stacking sequence. Two final generalities are also evident. It is suggested that during fatigue loading, damage development usually occurs in three rather distinct phases: an initial phase which may be dominated by the damage that would have formed at the corresponding quasi-static load level and by the initiation (or incubation) of additional damage; the second phase where damage grows, interacts, and may stabilize; and the third phase where damage combines at an accelerating rate to cause failure. And finally, it appears that compression fatigue damage nearly always involves delamination at interfaces which have high interlaminar stresses. There is also the suggestion that these delaminations show a preference for interfaces near the surface, other things being equal, suggesting that (ply) buckling may play a role in this damage mode.

Now to our question of "What can we do with these concepts?" I will generalize this answer slightly beyond the scope of information in this book. First, it appears that we *can* find fatigue damage and characterize it. Experimental methods have developed to the point where, in my opinion, nearly any type of damage *can* be detected. Of course, we have to look for and analyze it carefully. We also can analyze stresses and strains in damaged and undamaged laminates, approximately, but to a level of useful accuracy. This latter field is still under development, but it is encouraging to find such frequent efforts to conduct meaningful analyses of the mechanical deformations and stresses. We can define parameters which characterize fatigue damage over wide ranges of life; but it does not appear that any parameter yet defined serves this purpose well over the entire range of damage development. And we can associate damage with remaining strength and life. This association is, at present, somewhat tenuous, but strong foundations have been laid for the development of this area.

Finally, we arrive at our question of "What are the opportunities for future work?" This is another way of saying "What do we need to do?" and "What are the remaining obstacles?" While much of the success discussed here, and elsewhere, is based on single damage modes, we do not have a corresponding understanding of mixed modes or combinations of damage. Partly because of that, damage states (or collective conditions) are poorly defined and the analysis of such states is poorly developed. It is also true that

we don't seem to have a damage parameter which we can measure at any given point in the fatigue life and use directly to calculate the consequences of that damage, that is, to specify correctly the remaining strength and life of the specimen or component. And it appears that we are not moving rapidly in that direction; we seem to be more interested and involved in finding correlations than in finding explanations and rigorous descriptions.

However, much progress has been made, and certain aspects of damage can be described with surprising rigor. (Edge delamination in certain special cases is an example.) Perhaps we should say our understanding of fatigue damage can be best described in the same words that Irving Stone used to criticize William Jennings Bryan, "His mind is like a soup dish—*wide and shallow*." It is hoped that this document has added at least a modest increment to both of those dimensions.

*K. L. Reifsnider*

Department of Engineering Science and Mechanics, Virginia Polytechnic Institute and State University, Blacksburg, Va. 24060; symposium cochairman and editor.

# Index

- A**
- Acoustic emission, 203  
Analytical methods (*See* Stress Analysis)
- B**
- Boron-aluminum, 83  
Buckling of laminates, 185
- C**
- Case histories  
  Failure of pultruded rods, 8  
Characteristic damage state  
  For matrix cracking, 40, 63, 69, 103, 134  
Compliance calibration for delamination, 149, 175  
Composite structures, 168  
Compression of laminates, 184  
  (*See also* Fatigue—Testing, Compression-compression)  
Crack initiation, 97, 136, 262  
Crack length, 260  
Crack propagation, 168, 262  
Crack spacings, 47, 103  
  Predicted crack spacings, 56, 69, 108, 134  
Crack tip stresses, 235
- D**
- Damage (*See* specific types such as Delamination, Fiber fracture, Matrix cracks, etc.)  
Damage incubation, 246  
Damage parameter, 245  
Debonding, 247, 249, 261  
Delamination, 24, 32, 73, 121, 136, 142, 153, 169, 189, 233  
  Growth rate, 157, 168, 173  
  Onset prediction, 122, 153, 213  
Diiodobutane (*See* Opaque X-ray penetrants)  
Discount method, 114  
Double cantilever beam specimens, 169
- E**
- Edge effects  
  Edge stress states, 68, 77  
Effective modulus, 92, 148  
Enhanced radiography (*See* Opaque X-ray penetrants)  
Etching of matrix material, 90
- F**
- Fabrication (*See* Laminates—Fabrication of)  
Failure analysis, 27  
Failure criteria, 76, 88  
Fasteners, 230  
Fatigue  
  Damage induced by, 21, 27, 29, 41, 91, 111  
  Limit, 89  
  Testing  
    Compression-compression, 186  
    Tension-compression, 29, 213  
    Tension-tension, 21, 41, 83, 86, 109, 230

Fiber buckling, 247  
 Fiber fracture, 16, 90, 128  
 First ply failure, 42  
 Fractography, 27  
 Fracture  
   Fracture mechanics, 168  
   Fracture modes, 11, 33, 127, 228  
   Fracture surfaces, 9, 11, 32, 96  
   Fracture surface preparation  
     For scanning electron micro-  
     scopy, 32

## G

Glass epoxy, 109, 248  
 Glass-polyester rods, 8  
 Graphite epoxy  
   Laminates, 21, 29, 41, 64, 70, 118,  
   140, 171, 185, 212, 230  
 Growth law, 140  
   Delamination growth, 155, 173,  
   216  
 Guys, 7, 8

## H

Hackles, 27  
 Hairline cracks, 11  
 Hysteresis loops, 86

## I

Interlaminar stresses, 136, 142, 146,  
 220

## L

Laminates  
   Laminated composite specimens  
     Fabrication of, 29, 85, 120, 171,  
     230  
 Life  
   Correlation with strain energy den-  
   sity, 237  
   Fatigue life data, 35, 86, 187, 237  
   Prediction, 233

Linear strength reduction model, 239  
 Load history effects, 98  
 Longitudinal cracking, 44, 95, 127  
 LVDT strain measurement, 143

## M

Manufacture of composites  
   (See Laminates—Fabrication of)  
 Matrix cracks, 23, 40, 64, 74, 90, 103,  
 110, 121, 233, 247  
 Matrix materials (See specific types)  
 Metal matrix composites (See spe-  
 cific types)  
 Microcracks (See Matrix cracks)  
 Microstructure, 243  
 Mixed mode delamination, 173  
 Moisture  
   Absorption, 63  
   Coefficients of absorption, 66  
   Effects on damage development,  
   63  
   Effects on elastic properties, 65

## N

Neutron scattering, 25  
 Nondestructive testing, 7  
   Radiography, 16, 30, 45, 121, 143,  
   212, 233  
   Ultrasonic C-scan, 29  
 Notched specimens  
   Damage induced in, 21, 31, 199,  
   213, 233  
   Strength, 75, 189, 231  
   Stress analysis, 220

## O

Opaque X-ray penetrants  
   Diiodobutane, 45, 121, 143, 186,  
   212  
   Fluorescent penetrants, 32  
   Tetrabromoethane, 16, 24, 30, 233

Optical correlation holographic method, 251  
 Overload failures, 39

## P

Penetrants (*See* Opaque X-ray penetrants)  
 Photo-stimulated exo-electron emission, 251  
 Positron annihilation, 251  
 Properties (*See* specific types such as Stiffness, Strength, etc.)

## Q

Quasi-static loading  
 Damage induced by, 47, 71, 110, 121, 172

## R

Reliability, 168  
 Replication (*See* Surface replication)  
 Residual strength (*See* Strength)  
 Residual stresses  
 Residual thermal curing stresses, 42, 63  
 Resin (*See* Matrix materials)  
 Resistance curve, 140  
 Rods  
 Fiber reinforced, 8  
 Rule of mixtures, 140

## S

Saturation damage state, 83  
 Saturation spacing (*See* Characteristic damage state)  
 Scanning electron microscopy, 32  
 Secant modulus, 86  
 Shakedown stress, 85  
 Shear lag model, 66  
 Shear transfer layer, 65

Shock loading, 12  
 Small angle neutron scattering, 251  
 Specimens (*See* Laminates)  
 Splitting (*See* Longitudinal cracking)  
 Stacking sequence effects, 83, 95, 211  
 Standards  
 For testing of coated pultruded rods, 12

## Stereo

X-ray technique, 16  
 Scanning electron microscopy, 29

## Stiffness

Laminate stiffness, 86, 103  
 Stiffness changes, 87, 93, 110, 147  
 Tensor stiffness and stiffness changes, 115

## Strain

Failure strain, 127  
 Strain energy release rates, 147, 151, 171, 233

## Strength

Laminate strength, 71, 74, 121, 138, 189  
 Residual laminate strength, 71, 197, 209, 239, 248  
 Stress analysis, 59, 65, 79, 105, 133, 146, 161, 220  
 Stress free temperature, 67  
 Stress intensity factor, 235  
 Stress ratio correction, 238  
 Striations, 27, 33  
 Surface  
 Cracks, 11, 97  
 Replication, 43, 64, 71  
 Temperature measurement, 251

## T

## Testing techniques

X-ray, 18  
 Tension testing, 143  
 Tetrabromoethane (*See* Opaque X-ray penetrants)  
 Thermal expansion coefficients, 66

U

Wet strength (*See* Moisture effects)

Ultrasonics

C-scan testing, 29, 85

Unloading elastic modulus, 86

X

X-ray (*See also* Nondestructive testing)

Stereo-radiography, 16

X-ray diffraction, 251

V

Void density distribution, 257

Void volume ratio, 257

W

Weibull representation of strength,  
74

Y

Yield surfaces, 88